technische universität
dortmund

Resonant and non-resonant X-ray emission studies on cobalt bis(o-dioxolene) valence tautomers

Dissertation
for obtaining the academic degree
Doctor rerum naturalium

submitted on 24.07.2022 to the
Fakultät Physik, Technische Universität Dortmund

by

Florian Otte

Referees : Prof. Dr. M. Tolan

Prof. Dr. C. Bressler

Abstract

The study and design of novel molecular materials, miniaturized molecular switches and sensors, is propelled by the investigation of *electronically-labile* systems. This property enables molecules to interconvert between distinct (meta-)stable electronic states. A prominent group of bistable molecular systems is represented by cobalt-based valence tautomer transition-metal complexes, which can be switched between tautomeric forms by external stimuli such as temperature, pressure, or irradiation by light. This transition is characterized by a combined metal-ligand charge-transfer and spin-crossover. The driving force behind valence tautomerism (VT) is the presence of redox-active benzoquinone-ligands, which enable the oxidation and reduction of the central cobalt ion between Co^{2+} to Co^{3+}.

These systems present scientific value not only due to their electronically-labile behavior and their potential application for the development of molecular storage or sensor units but also as model systems for larger, more complicated complexes. Valence tautomers have been investigated since the late 1970s. Despite this, the amount of available element-specific and spin-sensitive X-ray spectroscopic data is very limited. In this thesis, systematic studies on three cobalt valence tautomers were conducted to explore resonant- and non-resonant X-ray emission spectra for the presence of signatures of the VT process. Based on these spectra, time-resolved ultra-fast investigation on a cobalt valence tautomer has been conducted using ultra-short highly-brilliant X-ray pulses, as they are produced by the European X-ray free-electron laser in Hamburg at the *Femtoseconds X-ray Experiments* (FXE) instrument. The obtained X-ray emission results indicate subtle differences between the spectral signatures of the individual valence tautomers, which are enhanced by the application of resonant X-ray emission methods. Time-resolved experiments on a valence tautomer indicate the presence of two ultra-short (sub one picosecond) dynamic processes. The interpretation and correlation with a photocycle for complexes exhibiting VT requires further investigation.

Kurzfassung

Die Untersuchung und Entwicklung neuartiger molekularer Materialien, miniaturisierte molekulare Einheiten, welche schalten oder messen können, wird vorangetrieben von Studien an *elektronisch-labilen* Systemen. Diese Eigenschaft verleiht Molekülen die Fähigkeit, in mehreren (meta-)stabilen Zuständen zu existieren. Eine prominente Gruppe von bistabilen molekularen Systemen stellen die Übergangsmetallkomplexe der Kobalt-Valenztautomere dar, welche sich durch äußere Reize wie Temperatur, Druck oder bei Einstrahlung von Licht zwischen zwei Tautomeren schalten lassen. Dieser Übergang ist durch einen kombinierten Metal-Liganden Ladungstransfer und einen Spin-Übergang charakterisiert. Die treibende Kraft hinter dem Valenz-Tautomerismus (VT) ist die Anwesenheit von redox-aktiven Benzoquinone-Liganden, welche die Oxidation und Reduktion des zentralen Kobaltatoms von Co^{2+} nach Co^{3+} ermöglichen.

Derartige Systeme bieten nicht nur aufgrund ihres elektronisch-labilen Verhaltens als Kandidaten für die Entwicklung von molekularen Speicher- oder Sensoreinheiten einen wissenschaftlichen Mehrwert; ein tiefergreifendes Verständnis der involvierten elektronischen Prozesse ist auch als Modellsystem für andere, größere Komplexverbindungen von Nutzen.

Valenztautomere stehen seit den späten 1970er Jahren im Fokus der Forschung. Trotz dieses Umstandes ist die Verfügbarkeit von elementspezifischen und Spin-sensitiven Röntgenspektroskopie-Ergebnissen stark begrenzt. Im Rahmen dieser Thesis wurden systematische Studien an drei Kobalt-Valenztautomeren durchgeführt, um resonante und nicht-resonante Röntgenemissionsspektren auf Signaturen des VT Übergangs zu überprüfen. Die erhaltenen experimentellen Spektren bilden die Basis für die zeitaufgelöste Untersuchung an Kobalt-Valenztautomeren mithilfe ultra-kurzer Femtosekunden-Röntgenlichtblitze, wie sie an der Großforschungseinrichtung des Europäischen Röntgen-Freie-Elektronen-Lasers in Hamburg am *Femtoseconds X-ray Experiments* (FXE) Instrument verfügbar gemacht werden.

Die erhaltenen Röntgenergebnisse belegen subtile Unterschiede in den spektralen Signaturen der einzelnen Valenztautomere, welche sich durch die Anwendung von resonanter Röntgenemission in vereinfachter Weise zeigen lassen. Die zeitaufgelösten Messungen an einem Tautomersystem weisen Signaturen von zwei ultra-kurzen (Sub-1-Pikosekunden-) dynamischen Prozessen auf, deren Interpretation und Einordnung in einen Photozyklus weiteren Untersuchungen bedarf.

Contents

Chapter 1

Introduction

The quest for novel functional molecular materials, e.g., miniaturized sensors, switches, and storage units on atomic length scales, has been at the heart of modern material research for many decades. *Electronically labile behavior*, i.e., the presence of distinct (meta-)stable electronic states readily accessible by external stimuli, constitutes a fundamental ingredient to the design of such materials. In the center of the periodic table, we find prominent actors in nature's play of molecular bistable behavior: The group of 3d, 4d, and 5d transition metals. The colorful chemistry of these elements – in the truest sense – is witness to the overwhelming number of existing transition metal complexes and has originated numerous promising candidates for switchable molecular design. Some of those complexes have risen to great scientific popularity, such as $[Ru(bpy)_3]^{2+}$ in the field of photo-induced catalysis.

A lesser-known molecular family, cobalt-based dioxolene complexes, is the subject of this thesis. These compounds are characterized by a rare electronic occurrence: The presence of unpaired electron spin on ligand moieties and metal ions, in combination with the ability to exhibit both metal-ligand charge-transfer- and spin-crossover-behavior when switched. These properties constitute an example of valence tautomerism / valence tautomer (VT) behavior. VT complexes have been called the chameleons of chemistry [1] [as cited in 2], as they undergo drastic changes in structure when external conditions (such as temperature) are varied. A fruitful combination of benzoquinone ligand- and metal- frontier orbital energies enables this fortunate constellation and allows these complexes to be switched between the distinct Co^{3+} and Co^{2+} state. Dramatic differences in the optical and magnetic properties of these two states might qualify cobalt-based dioxolene compounds (or derivatives thereof) as molecular sensors.

The obtained information, e.g., about the intricacies arising from spin-coupling between metal and ligands in bistable molecular systems, is not limited to the case at hand. VT compounds constitute important model systems for the investigation of correlated charge-transfer- and spin-crossover-processes in larger or less accessible molecules. Likewise, they reveal more about cobalt chemistry itself; after all, cobalt plays a vital role in many biological processes, such as the metabolism via methylcobalamin (vitamin B12) or as a cofactor in DNA synthesis. Compounds containing cobalt play

essential roles in the functioning of the human nervous system (specifically in the synthesis of myelin) and the maturation of red blood cells in the bone marrow. The study of charge-transfer mechanisms in cobalt complexes is thus not only motivated by material research questions but also aims toward the general elucidation of cobalt coordination chemistry in organic compounds.

How does one study intermolecular charge-transfer processes on the angstrom length scale and interrogates unpaired electron spin in atoms? X-ray spectroscopic methods, by virtue of their sensitivity to the core-level electronic structure of atoms, provide a powerful and element-sensitive tool for the investigation of VT. They complement other experimental techniques, such as optical or magnetic measurements, but can offer special insights due to a unique combination of properties. X-ray spectroscopy in the hard X-ray regime is bulk-sensitive and largely non-invasive, easing the implementation of experiments that require the enclosure of the sample (e.g., in temperature-controlled setups). The combination of multiple spectroscopic disciplines (e.g., the resonant excitation of atoms with simultaneous capture of the emitted X-ray fluorescence) promises to further expand the available information content.

With the onset of free-electron-laser facilities for the generation of highly intense and ultra-short flash duration X-ray pulses, a new dimension to the investigation of these correlated electronic processes has become available. The investigation of ultra-fast switching processes in these molecular systems is motivated by an extended understanding of the dynamic properties of VT. These kinds of experiments are made possible by the stimulation of VT by light.

In this thesis, we will introduce fundamental concepts of transition metal chemistry and the experimental techniques of X-ray emission spectroscopy in chapters 2 and 3. Non-resonant and resonant X-ray emission spectroscopy results on cobalt-based VT complexes will be discussed in chapters 4 and 5. A systematic investigation of two prominent cobalt X-ray emission lines, the Kβ mainline and valence-to-core, is conducted. These sensitive emission features are screened for signatures of the VT process during temperature-induced transition. A different X-ray technique, X-ray Raman Scattering, is proposed for the direct probe of ligand properties in dioxolene VT compounds via interrogation of light elements such as oxygen.

In the closing chapter 6 we will extend the applied spectroscopic methodology extensively to investigate VT in a femtosecond X-ray study at the FXE instrument of the European XFEL facility. We aim to provide the starting grounds for further investigation in complexes exhibiting VT in femtosecond time-resolved X-ray experiments.

Chapter 2

A peek into transition metal complex chemistry

Transition metal (TM) complexes represent a major and important group of chemical compounds of general form MX_aL_b, where *metal ions* M are coordinated to one or more neutral (X) or anionic (L) *ligands* [3]. These complexes possess several prominent properties, among them their often vibrant colors and the large number of existing chemical compounds involving TM ions. Importantly they often exhibit completely different chemical properties as their individual composition partners and some TM complexes have risen to exceptional roles, e.g., as functional units in the biochemistry of living organisms [4], in catalysis and renewable energy applications [5, 6] or in functional material research [7]. A picture of a small subset of cobalt-based TM complexes in solution is given for illustration in figure 2.1.

The starting point to understanding the bonding and coordination behavior of TM complexes is a discussion of the metal d orbitals. The dominant property of these complexes is the existence of valence-active (and often incompletely filled) metal d-shells, which dictate the compound's chemical properties. An isosurface representation of the

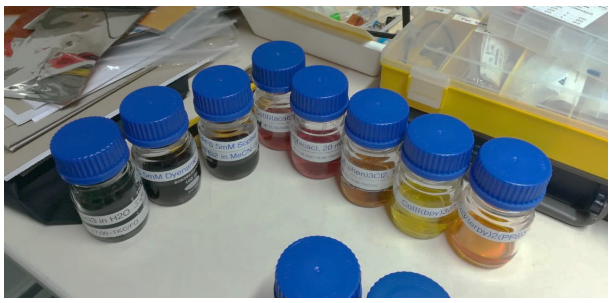

Figure 2.1: A selection of cobalt-based TM complexes in solution. The wide range of observed colors arises due to the properties of the valence electrons, which are, as many chemical properties in these compounds, dictated by the intricacies of the metal d-orbitals and the nature of the ligands (see text).

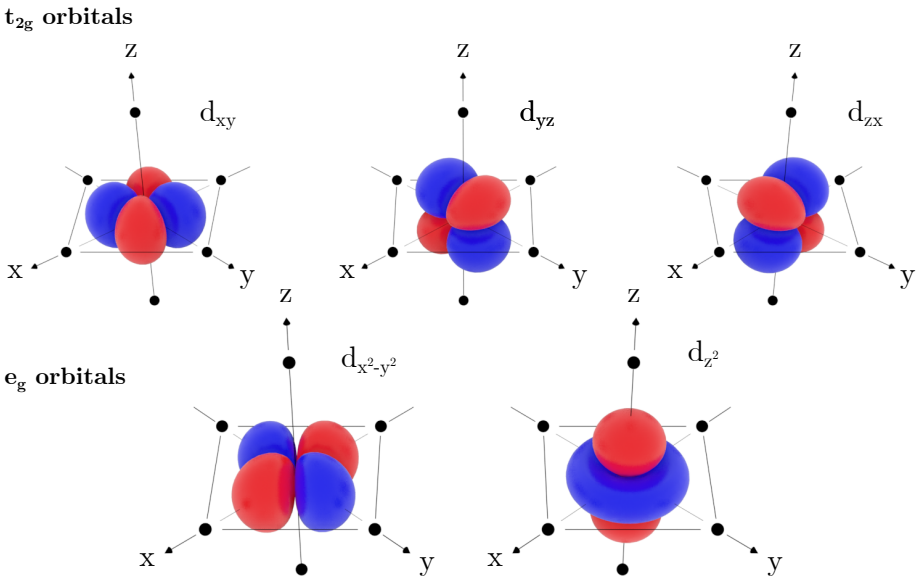

Figure 2.2: Isosurface representations of the 3d orbitals in TM complexes. The corresponding energy levels will depend on the coordination geometry with the ligand atoms along those axes.

five d metal orbitals in 3d TM complexes is shown in figure 2.2. The orbital shapes can be distinguished into two groups within a Cartesian coordinate system (as indicated by the black axes). An orientation of orbital lobes along the coordinate axes characterizes the set of e_g orbitals, $d_{x^2-y^2}$ and d_{z^2}. The remaining d orbitals are oriented between the illustrated axes and are denoted by the t_{2g} set [8]. The coordination with ligand atoms will lead to a lift of the degeneracy of the metal d orbitals. This splitting of the d orbitals is behind many characteristic properties of TM complexes, e.g., their magnetic properties and color, i.e., their absorption bands in UV-visible spectroscopy [3, 9].

How the arrangement of the ligand atoms modulates the corresponding energy levels of molecular orbitals can be discussed in the framework of crystal field theory.

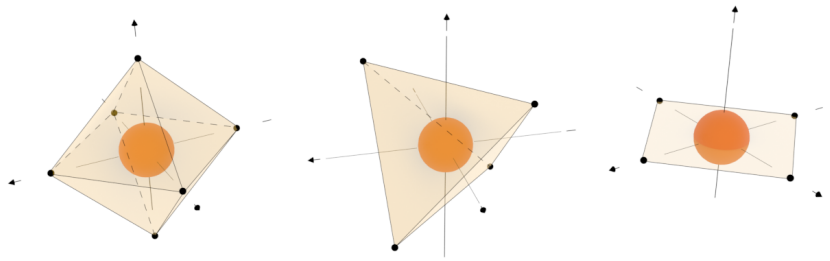

Figure 2.3: Octahedral, tetrahedral and square-planar coordination geometry around a central metal ion. The black vertices mark the position of ligand atoms.

2.1 Crystal field theory and the lift of d orbital degeneracy

Within Crystal field theory (CFT), many properties of TM complexes can be explained by a model based on the electrostatic repulsion and attraction between the metal d-orbitals and negative point charges modeling ligand atoms [3]. In the framework of CFT, electrostatic repulsion between the metal orbital lobes and ligand point charges will depend on the spatial arrangement. The lift of degeneracy of the d orbitals can be explained when positioning ligand point charges at the positions of physical atoms. Generally, metal orbitals that point along the ligand axes will experience an increase in energy due to electrostatic repulsion. In contrast, metal orbitals that fall in between ligand axes are lowered in relative energy. The *coordination* geometry, i.e., the arrangement of ligand atoms around the metal, is a fundamental property of a chemical compound. A convention for the nomenclature of different coordination geometries is the use of polyhedrons (e.g., an *octahedron* describing *octahedral* geometry), whose vertices give the position of coordinate ligand atoms. The common octahedral, tetrahedral, and square-planar coordination geometries for TM complexes are presented in figure 2.3. The number of coordinated ligand atoms (i.e., the number of vertices in the coordination polyhedron) is called the *coordination number*. Intuitively, the orbitals will experience different interactions with coordinated ligand atoms. This is shown schematically for octahedral, tetrahedral, and square-planar coordination geometry in figure 2.4 on the following page.

In octahedral geometry, ligand atoms lie on the vertices of an octahedron (depicted as black dots in figure 2.2). Metal orbitals that exhibit significant contributions along the ligand axes ($d_{x^2-y^2}$ and d_{z^2}) will experience an increase in energy, while the metal

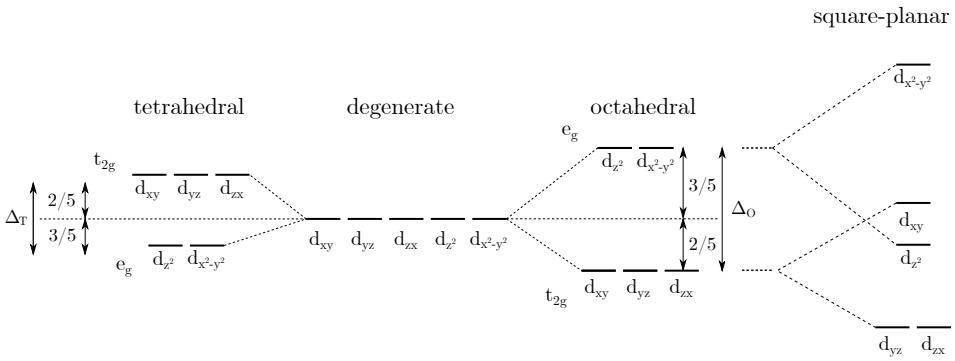

Figure 2.4: The degeneracy of the metal d-orbitals is lifted when a crystal field is introduced: Tetrahedral (left), octahedral (center right) and square-planar (right) coordination geometries.

orbitals d_{xy}, d_{yz} and d_{zx} experience less repulsion and are thus lowered. This leads to the creation of two energy levels, as depicted in the center-right of figure 2.4. The energy splitting between the t_{2g} and e_g levels in octahedral geometry is denoted Δ_0. Due to the center of gravity conservation, the three t_{2g} orbitals will be lowered by 2/5 Δ_0, while the two e_g orbitals are raised by 3/5 Δ_O. The labels t_{2g} and e_g stem from the symmetry properties of the orbitals when subjected to the symmetry operations of the octahedral point group. The degeneracy is given by the letters t (triple) or e (double). The tetragonal distortion of the coordination polyhedron along the z-axis leads to a further breaking of orbital degeneracy (Jahn-Teller effect). Stretching of the metal-ligand distances along z will stabilize orbitals with a z component, while compression will have the opposite effect.

Square-planar coordination can be understood as the edge case of tetragonal distortion, in which the z ligands have been placed at an infinite distance. This lowers the energy for the d_{z^2} orbital and all other orbitals with z contribution, while the $d_{x^2-y^2}$ orbital experiences a relative increase in energy. The remaining ligands are more strongly attracted, and thus all orbitals with components in x and y are raised in energy. The energy diagram for square-planar geometry is shown at the right of figure 2.4.

Finally, for tetrahedral geometry, the ligand atoms lie on the vertices of a tetrahedron. Out of the five orbitals, the d_{z^2} and $d_{x^2-y^2}$ orbitals stay further apart from the ligand atoms. In contrast, the d_{xy}, d_{yz} and d_{xz} orbitals experience an increase in energy, leading to an inverted order of levels compared to the octahedral coordination. The energy diagram for tetrahedral geometry is depicted left in figure 2.4.

Electrons that occupy the t_{2g} orbitals in octahedral geometry lead to stabilization since the t_{2g} orbital energies lie below the mean level of the metal in spherical symmetry. This stabilization is denoted the crystal field stabilization energy (CFSE). In systems with between four and seven metal d electrons, multiple possibilities are available for the occupation of the d levels. Starting with the d^3 configuration, additional electrons might either be added to an already singly occupied orbital in the t_{2g} set (for which a

spin-pairing energy P has to be provided) or added to the e_g orbitals, following Hund's Rule. For a given system, configurations with a low amount of unpaired electron spin in the d orbitals are denoted low-spin (LS). High-spin (HS) on the other hand, indicates a different configuration with a significant number of unpaired electrons. We note that the terms LS and HS are used to describe a relative configuration, and the actual number of unpaired electron spin might vary from system to system. If a LS or HS configuration is reached will depend on the balance between the crystal field splitting Δ and the spin pairing energy P. In relation to the influence of the ligand field, the terms weak-field and strong-field are used synonymously. In tetragonal coordination geometry, the crystal field splitting is around 4/9 O_h, which explains why these compounds primarily exist in HS configuration.

2.2 Ligand field theory and excited states

Aside from the missing description of covalent chemical bond nature, the unmodified crystal field theory (CFT) has a few notable shortcomings, among those the missing prediction of crystal field splitting values for a given ligand (spectrochemical series) and the neglection of the nephelauxetic effect, which describes the delocalization of electrons away from the metal ion into the ligand structures [3]. Additionally, for systems with between two and eight valence electrons, the coupling between electrons has to be considered [9]. This can be treated within a multi-electron picture in the framework of ligand field theory (LFT) as an extension of CFT, which delivers the basis for a quantitative discussion of experimental data, such as UV-visible absorption spectroscopy [10]. The effect of the multi-electron interaction is considered via an LS-Coupling scheme, in which the individual quantum numbers for the angular momentum l_i and spin s_i couple to the total angular momentum L and spin S of the system. This leads to a spectroscopic term symbol $^{(2S+1)}L$ describing a multi-electron state of the system with total angular momentum L (S, P, D) and spin multiplicity $(2S + 1)$ [9]. The degeneracy of these terms is given by (2S+1)(2L+1), leading to single (A), double (E), and triple degenerate states (T). Analogous to the one-electron picture discussed above, a splitting of these states is introduced in the presence of a ligand field, breaking the degeneracy of the terms. The relative energies of the split terms can be determined within the framework of ligand field theory (LFT) in a semi-empirical way with the introduction of the Racah-parameters, which model electrostatic repulsion between electrons [10].

The excited state term energies can be illustrated relative to the ground-state in Tanabe-Sugano diagrams as a function of the normalized ligand-field splitting Δ [9]. The normalization by the ion-specific Racah parameter B universalizes the illustrated diagrams for multiple metals. The Tanabe-Sugano diagrams of d^6 and d^7 configurations (as commonly found in cobalt) are given in figure 2.5. The curves in these diagrams exhibit a kink at medium field splitting values, which stems from a change in the ground state. The left side of the diagram denotes the HS phase and is called the weak-field case. The right side denotes the LS phase and is called the strong-field case. The lowest-lying spin-allowed excited states for a cobalt d^6 configuration in the strong field

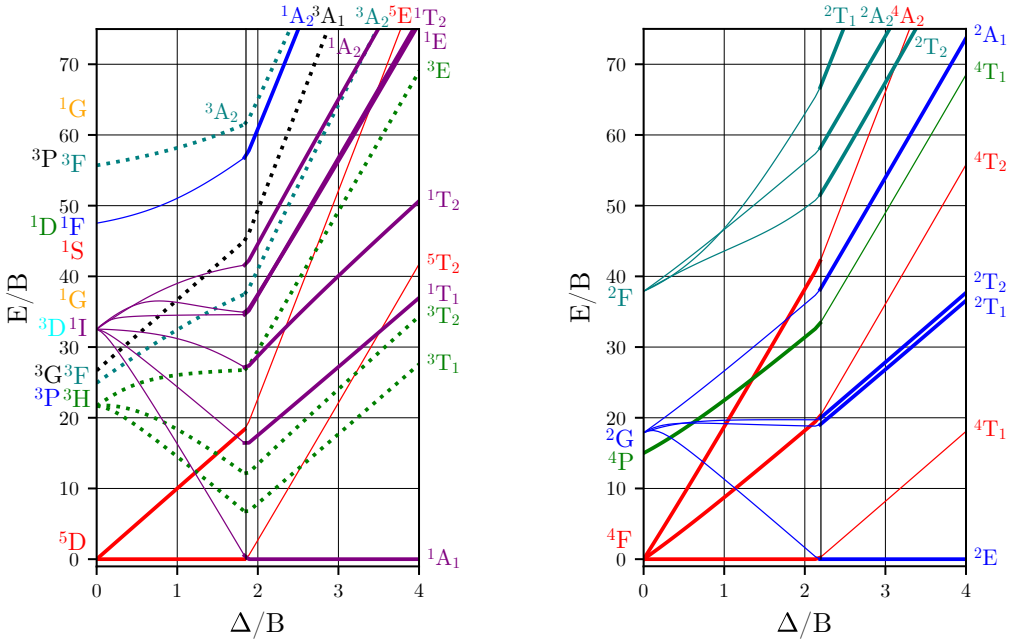

Figure 2.5: Partial Tanabe-Sugano diagrams for a metal ion d^6 (left) and d^7 (right) configuration in octahedral symmetry. Colors indicate the origin term symbol, as shown on the y-axis. Dotted lines indicate excited states which do not share the same spin-multiplicity as the ground state and transitions are thus formally spin-forbidden. Solid thick lines indicate states which are spin-allowed either before or after the spin-crossover indicated by the black vertical line. Based on Ref. [11].

case would be singlet $^1A_1$, and for a cobalt d^7 ion in the weak-field case, a quartet $^4T_1$. The spin-allowed transitions for a cobalt LS-d^6 compound populate the $^1T_1$, $^1T_2$, ^1E and $^1A_2$ state, as indicated in the left panel of figure 2.5. A HS-d^7 compound exhibits the quartet states $^4T_2$ and $^4A_2$ as excited states (right panel in figure 2.5).

2.3 Molecular orbital theory and covalent bonds

The electrostatic picture applied by CFT can not adequately describe covalent chemical bonds. The orbital basis set is comprised of the metal (n-1)d, np, and ns orbitals, which mix with the valence orbitals of the ligands. Generally, orbitals that mix in between ligand and metal will split into bonding and anti-bonding sets. Non-mixing orbitals remain non-bonding. The order of the orbitals will be dictated by the ligand electronic structure, namely the presence of σ and π-donating or accepting orbitals and by the energy overlap with the metal orbitals. This is the explanation behind why some ligands are strong- and other ligands are weak-field ligands. The amount of net

splitting between the t_{2g} levels and the anti-bonding e_g* levels is dominated by whether the ligand π orbitals are close in energy to the metal d orbitals and whether the π orbitals of the ligand are empty (strong splitting, ligand π acceptor) or the energies are far off from the metal d orbitals and the ligand π orbitals are already occupied (ligand π donor). This is illustrated in figure 2.6. Typical electronic transitions in the valence shells of TM complexes are also indicated. Ligand-centered (Lc) transitions (e.g., $\pi \rightarrow \pi^*$) involve a filled or partly-filled and an empty Lc orbital. Metal-centered (Mc) transitions (e.g., d-d transitions) involve a filled or partly-filled and an empty Mc orbital. Metal-to-ligand charge transfer (MLCT) denotes transitions from Mc orbitals to an orbital with predominantly Lc character. Analogous, ligand-to-metal charge transfer (LMCT) describes transitions from ligand-centered orbitals to metal-centered orbitals.

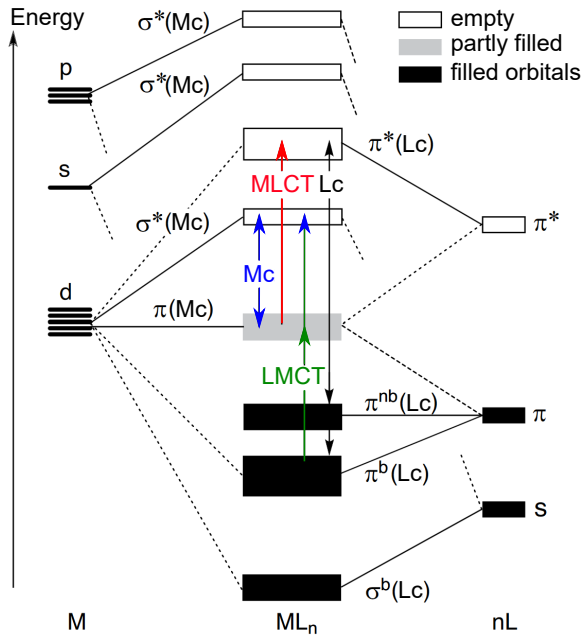

Figure 2.6: A simplified molecular orbital diagram visualizing possible electronic excitations in an octahedral complex. Ligand-centered (Lc) and metal-centered (Mc) orbitals are indicated by solid and dotted lines. Important transitions inside TM complexes are shown as well. Figure adapted from Ref. [9].

2.4 The case of cobalt VT complexes

Fundamentally, several classes of bistable TM compounds are distinguished. Mixed valence compounds (MV) contain metal ions of multiple oxidation states, exhibiting a ligand-mediated metal-to-metal charge transfer [12]. Spin-crossover complexes (SC), on the other hand, present a metal-centered change in spin-multiplicity. This process is driven by entropy, primarily of vibrational origin due to the longer metal-ligand bond distances, which stem from the population of the anti-bonding π^* molecular orbitals of the ligand in the HS form [13].

The third class of bistable behavior, VT, is characterized by both a charge-transfer and spin-crossover of the central metal ion. Tautomers are a group of structural isomers, i.e., chemical compounds which interconvert between multiple related forms, all exhibiting the same number of atoms for each element [2]. VT thus describes a complex, which may exist in two different valence states with the same molecular composition. The phenomenon of VT has been observed in several metal-based complexes, including manganese, copper, and cobalt [14]. The equilibrium for VT in cobalt compounds

$$[\mathrm{Co^{III}}]_{\mathrm{LS}} \rightleftharpoons [\mathrm{Co^{II}}]_{\mathrm{HS}} \tag{2.1}$$

is characterized by the tautomerization from a LS Co^{3+} complex to a related tautomer form with a HS Co^{2+} ion (cf. figure 2.7). This equilibrium can be controlled by external stimuli, such as temperature [15–18], UV-visible light [19, 20], pressure [21, 22] and X-rays [23, 24]. The Gibbs free energy difference

$$\Delta G = \Delta H - T\Delta S, \tag{2.2}$$

describes the balancing factors driving the VT equilibrium [21, 25]: At low (cryogenic) temperatures, the entropy term $T\Delta S$ is practically neglectable, and we are left with just

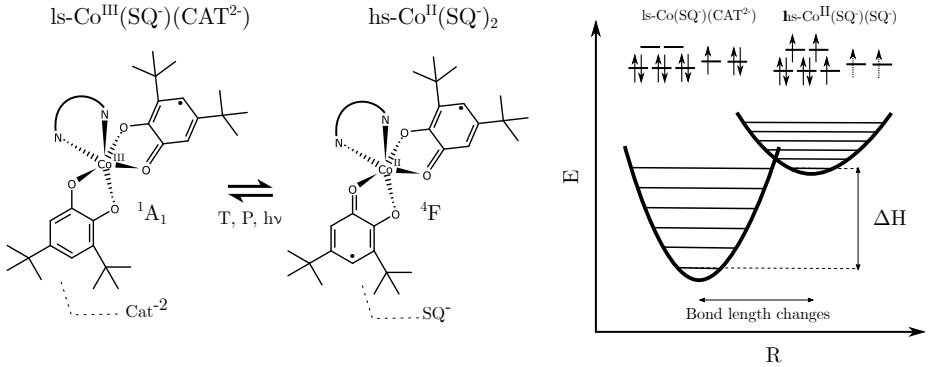

Figure 2.7: The VT transition scheme and potential energy diagram, here shown for cobalt dioxolene VT complexes. SQ and CAT denote the semiquinone or catecholate form of 3,5-di-tert-butyl-o-benzoquinone. The chelating ancillary nitrogen-ligand is indicated by the solid arc at the upper left of the molecular structures. Adapted from Ref. [12].

the enthalpy difference ΔH. The Co^{3+} form is preferred at low-temperatures [26], since the enthalpy of the HS Co^{2+} form appears to be larger [27]. Intuitively this agrees with the increased volume [28] and lower crystal field stabilization energy in HS Co^{2+} d^7 complexes. At elevated temperatures, the entropy term becomes dominant. In cobalt complexes, a large increase in entropy S is assumed by the HS Co^{2+} complex since electrons are placed in the anti-bonding e_g* orbitals of the metal ion, which implies an increase in metal-ligand bond distance and additional vibrational modes. Entropy is further gained by the rise in spin-multiplicity upon transition from Co^{3+} to Co^{2+}, given by the higher degeneracy of the ^4F ground state and spin on the oxidized redox-active ligand moieties [16]. Both effects, together with the increasing temperature factor, will lead to a change of sign [21] for the Gibbs energy at a *critical temperature* $T_{1/2}$ which defines the temperature at which $\Delta H = T\Delta S$ [12]. This dramatic change in ΔG is behind the stabilization of the Co^{2+} HS phase at elevated temperatures.

Experimentally, the critical temperature expresses the temperature at which both tautomer species exist in equal amounts [12]. The Gibbs energy in eq. (2.2) can serve as a starting point for the discussion of many ground state properties of the VT equilibrium. Solvent effects (section 2.4.4) which modulate the critical temperature $T_{1/2}$ and the influence of ancillary ligands (section 2.4.2) will be briefly mentioned in the following sections.

The investigation of VT is motivated by the desire to obtain functional materials which express significant changes in their structural, optical, and magnetic properties. Temperature-dependent magnetic susceptibility measurements and optical absorption data in figure 2.8 illustrate that cobalt-based dioxolene VT complexes exhibit drastic changes upon conversion from the diamagnetic LS-d^6 configuration to paramagnetic

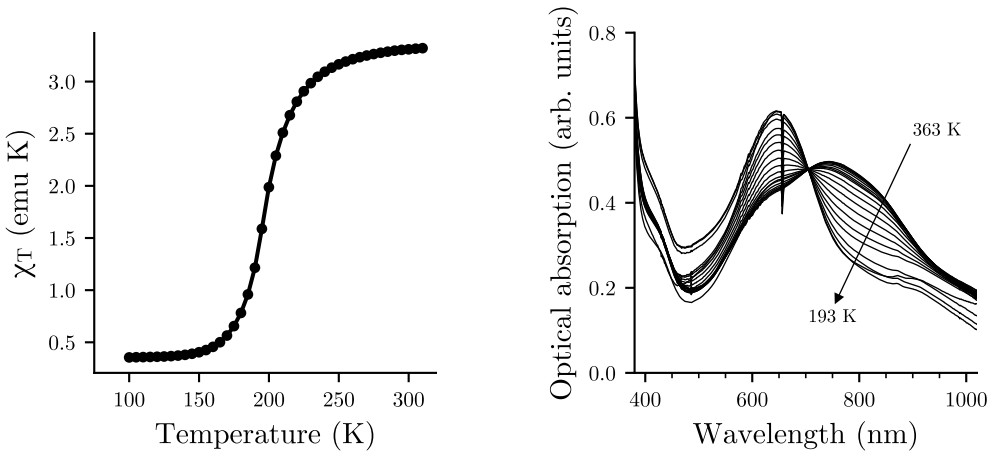

Figure 2.8: Experimental data illustrating VT in cobalt dioxolene complexes. The magnetic susceptibility of $Co(DTB)_2(tmeda)$ (left, DTB = CAT or SQ) exhibits a drastic decrease upon cooling. The optical absorption spectrum on the same compound (right) features the appearance of an isosbestic point and significant changes in the spectral line shape.

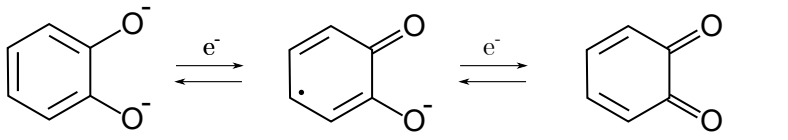

Figure 2.9: The redox-series of o-quinone, exhibiting three different oxidation levels.

HS-d^7. This has led to an increased interest in this family of compounds for the development of possible future applications such as molecular sensors or switches, or spintronic devices [12, 14, 29]. Complexes with dioxolene ligands are the most prominent members of the family of mononuclear cobalt VT compounds [12]. In these octahedral complexes, a ligand variant from the redox-series of o-quinone (Q) with tert-butyl-groups (3,5-di-tert-butyl-o-benzoquinone), either as the single reduced semiquinone (SQ^-) or the double reduced catechol (CAT^{2-}), is coordinated to the cobalt ion. A nitrogen-based ancillary ligand completes the octahedral coordination.

2.4.1 The redox series of o-quinones

Redox-active moieties are crucially important for the manifestation of VT in the investigated metal complexes. The redox-series of Q is illustrated in figure 2.9. For cobalt complexes, dioxolene ligands (3,5/6-di-tert-butyl-benzoquinone) exhibit the correct orbital energies to mix with the metal ions' d orbitals. This happens in a way where the metal d e_g orbitals form anti-bonding σ^* orbitals with the dioxolene lone pair orbitals, and the metal d t_{2g} orbitals mix to a π orbital with the dioxolene π^* orbitals [30]. The participating frontier orbitals are illustrated in figure 2.10.

Upon tautomerization from LS Co^{3+} to HS Co^{2+}, metal anti-bonding d e_g* orbitals are populated by oxidation of CAT [28]. This reconfiguration is accompanied by a metal-ligand bond length increase on the order of 0.16 Å to 0.22 Å [31], leading to a higher

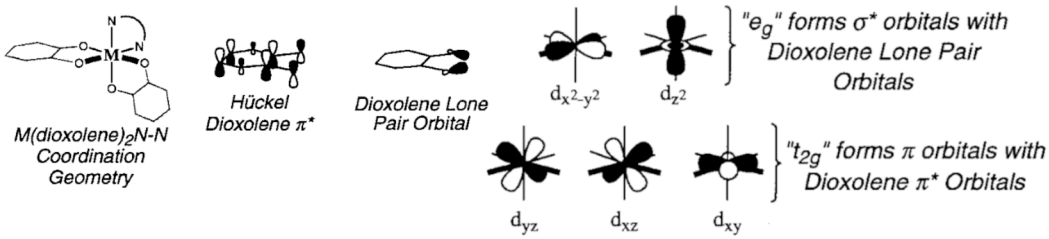

Figure 2.10: Metal d and dioxolene frontier orbitals of cobalt dioxolene VT complexes. Figure adapted from Ref. [12].

density of vibrational states as indicated by the shallower potential well for the Co^{2+} HS phase in the right panel of figure 2.7 [12]. The opposite transition is characterized by the reduction of one of the two SQ ligands. To account for both metal-ligand charge transfer and spin-crossover, metal and ligand orbitals are assumed to stay primarily localized, with moderate interaction. A too-weak metal-ligand interaction does not create bonding- and anti-bonding orbitals as required for spin-crossover. Extensive orbital mixing renders metal-ligand charge-transfer infeasible [12]. The unpaired spins on semiquinone ligands couple antiferromagnetically with the metal d t_{2g} orbitals (π bonds) and ferromagnetically with the e_g levels, whereby the contribution from the antiferromagnetic coupling is substantially larger [12]. The coupling between the unpaired ligand spins has been shown to be metal-mediated in the case of a tridentate radical species [32] but remains unclear in the case of the cobalt-based VT complexes [28]. To accommodate for the possible spin-coupling scenarios, we are introducing the labels Q_{low}, Q_{int} and Q_{high}, which denote ferromagnetic (spin-down), antiferromagnetic, and ferromagnetic (spin-up) coupling between the metal and SQ ligand spins. The subscript stems from the total compound spin after coupling the net ligand spins with the quartet metal ion.

The quinone ligands have also been found to carry the potential for solvent molecule fixation via donor-acceptor interactions [33].

2.4.2 The nitrogen-based ancillary ligand

Despite being not directly involved in the redox-mechanism of VT, the ancillary ligand (also sometimes called the counter-ligand) modulates the transition behavior of the VT complex by influencing the VT equilibrium. The ancillary ligands for the investigated VT compounds in this thesis are illustrated in figure 2.11.

It was found that the critical temperature decreases as a linear function of the increasing reduction potential of the ancillary ligand [30]. It was proposed that this happens due to a favorable decrease of the total energy induced by the acceptance of charge into the co-ligands π^* anti-bonding orbitals [15]. A recent computational study by Janetzki et al. explored DFT-based methods for the prediction of critical VT transition temperatures based on the ancillary ligand electronic structure [34]. The authors of

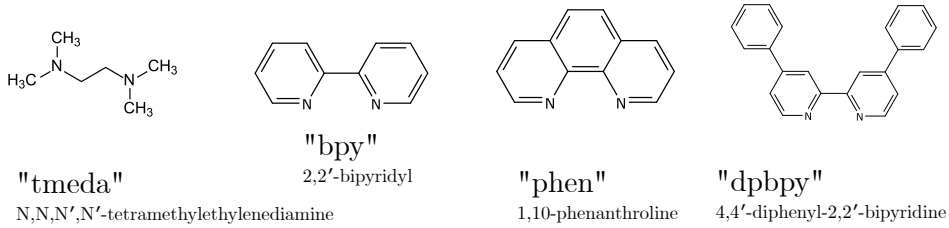

Figure 2.11: The ancillary nitrogen-based ligands for the investigated VT complexes in this thesis and their abbreviated names.

this study found a good correlation between the orbital energy of the ancillary ligands lowest unoccupied molecular orbital (LUMO) and the critical temperature. This not only confirms the above hypothesis of ligand π orbital acceptance but was also proposed as a way to computationally screen potential VT complexes before the experimental investigation in a convenient manner.

2.4.3 Photo-induced VT

In the optical absorption regime of cobalt dioxolene complexes, the presence of both MLCT and LMCT absorption bands has been speculated [25, 35]. By irradiating VT compounds with light of around 600 nm or 800 nm, a shift in the tautomeric equilibrium can be induced [36]. This is illustrated for $Co(DTB)_2(tmeda)$ in figure 2.12.

Early studies investigated photo-induced VT in solution on the picosecond and nanosecond timescale. Adams et al. proposed for the relaxation mechanism on photo-excited $Co(DTB)_2(bpy)$ a rapid intersystem crossing of the excited MLCT state to a HS Co^{2+} state (which occurred faster than the used 90 ps laser pulse width) and back tautomerization within 0.1 ns to 1.0 ns after excitation at around 550 nm [25].

A different body of work has been dedicated to the study of VT complexes at low temperatures, giving rise to long-lived metastable states upon photo-irradiation. This phenomenon has been studied analogous to light-induced excited spin state trapping (LIESST) in iron compounds [37].

Ultra-fast studies, i.e., studies with femto- and pico-second time-resolution, have been undertaken more recently by the use of infrared spectroscopy with sub 40 fs laser pulse widths [38]. In these studies, a sub 200 fs vibrational cooling from the excited LMCT* state to the HS Co^{2+} state was reported for a 1:1 cobalt dioxolene complex [38].

A recent study by Leroy et al. demonstrated the light-induced high-yield excitation of a meta-stable state in a VT crystal, after irradiation with 450 nm blue light.

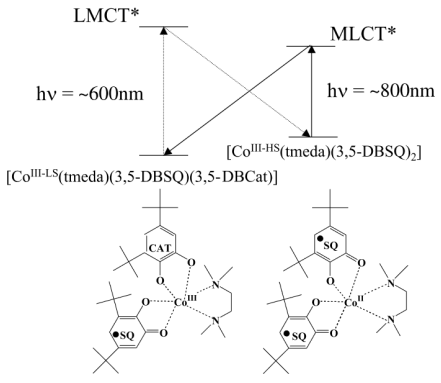

Figure 2.12: Simplified Jablonski diagram for $Co(DTB)_2(tmeda)$, illustrating the concept of photo-induced VT in this complex. Figure from Ref. [36].

2.4.4 Solution and solid samples

Early studies revealed that the presence and nature of solvent molecules in VT compounds significantly modulated VT transition behavior [15, 16]. Significant differences in the critical temperature were found for a series of cobalt-based VT compounds when measured in toluene solution and solid-phase [25]. In many studies, changes in the chemical environment lead to the modulations of VT behavior [26, 39, 40]. Notably, the temperature range over which tautomerization occurred was shown to change drastically for the cobalt VT compound $Co(DTB)_2(phen)$, leading to a sharp transition within 10 K for the solid sample and a more gradual transition over approximately 100 K for the compound in toluene solution [25]. For the tautomer complex $Co(DTB)_2(bpy)$ in the solid crystalline phase, it was found that the toluene solvate is formed by two molecules per unit cell via a pairing of the (bpy) ligands [28].

In a series of publications by Adams et al., the synthesis process of the investigated VT compounds in this thesis was first described [16]. In their work, multiple variants of the tautomer complex $Co(DTB)_2(phen)$ were prepared. In one of the variants, the remaining toluene solvent molecules were removed by evaporation through heating. In subsequent temperature-dependent measurements of the effective magnetic moment, they found no indication of VT in the non-solvated sample. At the same time, variants with remaining toluene or chlorobenzene solvent molecules showed a substantial change in the effective magnetic moment, associated with VT [16]. Based on nuclear magnetic resonance (NMR) measurements, it was further speculated that the presence of the solvent molecules contributes to cooperativity effects in these samples via solvent-based vibrational modes.

Analogous to the terminology used in these works, we will refer to the microcrystalline solid-phase compounds as *solvated*, implying the presence of solvent molecules in the crystalline powder. We refer to the form above if no further specification is given. Contrary, *non-solvated* denotes the complex contains no solvent molecules. Liquid phase measurements in toluene solution are explicitly stated as *in toluene*.

Chapter 3

Basic principles of selected X-ray techniques

A fundamental property of matter, the nature of electronic and geometric structure on an atomic or molecular level, is subject to the field of X-ray spectroscopy and scattering techniques. Photon radiation in the X-ray regime provides wavelengths at atomic length scales and suitable photon energies for probing core transitions in atoms or molecules.

In this chapter, fundamental aspects of X-ray techniques, primarily X-ray emission spectroscopies, are discussed. When appropriate, multiplet [41] and density functional theory (DFT) calculations [42] on model systems will be utilized to provide a descriptive discussion of experimentally observed features and signatures. The chapter closes with a brief overview of X-ray synchrotron and free-electron-laser sources and aspects of the experimental implementation of X-ray emission measurements.

3.1 X-ray absorption

X-rays, electromagnetic waves with wavelengths on the Ångstrom lengthscale (10^{-10} m), fundamentally interact with matter by elastic scattering (Rayleigh scattering and diffraction), inelastic scattering (Raman and Compton processes) and absorption [43]. In the field of spectroscopy on 3d TM complexes, we are concerned with X-ray energies in the $<$ 100 keV regime [44]. In this region, the interaction of matter with X-rays is dominated by photoelectric absorption [45][1].

During the photoelectric effect in X-ray absorption, the energy of an impinging photon promotes a core electron to a higher energy level, leaving a hole. This is depicted in figure 3.1 for the case of 1s (K) absorption. The excited core-hole state is highly unstable and will relax via a cascade of radiative or non-radiative transitions into an energetically more favorable state. The emission of a photon from the atom is termed radiative decay to differentiate from a second process that may occur upon the filling of

[1] The cross-sections of scattering processes become much more significant at higher energies but can still be exploited here as well (potentially at the cost of longer acquisition times), e.g., in X-ray Raman scattering [46]

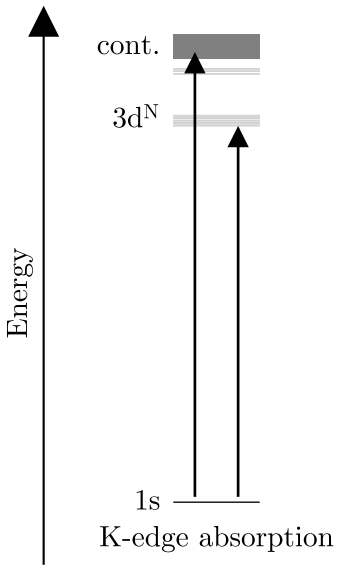

Figure 3.1: X-ray K-edge absorption via promotion of an electron to the valence-levels or continuum states.

a core-hole. X-ray emission spectroscopy (cf. section 3.2) is concerned with the detection of this photons. During non-radiative decay, the excess energy from the relaxing electron is transmitted onto a second electron, which is emitted from a higher-level shell in the atom (Auger-decay). The lifetime τ of the primary core-hole is on the order of a few femtoseconds, which, in spectroscopy terms and by virtue of the Heisenberg uncertainty principle $\tau\Gamma \geq \hbar/2$ introduces a broadening to experimentally observed energies Γ. For elements from the first row of TM complexes, the 1s core-hole lifetime is around 11 fs to 2 fs. This implies an intrinsic broadening on the order of 1 eV [47] for experimentally observed features stemming from the filling of a core-hole.

The absorption process is described via the linear absorption coefficient, μ, in

$$I = I_0 \exp(-\mu d), \tag{3.1}$$

which gives the remaining intensity of a photon beam after transmission of a homogenous medium of thickness d. For an atom of a given element, the absorption coefficient will vary characteristically as a function of energy [43]. Specifically, a sharp rise of the absorption cross-section will be observed when the energy of an incoming photon has exceeded the required energy to ionize a core-shell. This is arguably the essential property of the absorption process and can give X-ray spectroscopic methods a determining advantage over other non-element-sensitive experimental methods.

The overall cross-section for absorption of photons in matter is often given via the linear mass attenuation coefficient μ/ρ. As an example, we plot the linear mass attenuation coefficient as a function of photon energy for cobalt and oxygen in figure 3.2. Oxygen, a comparatively light element, exhibits a jump in the absorption cross-section

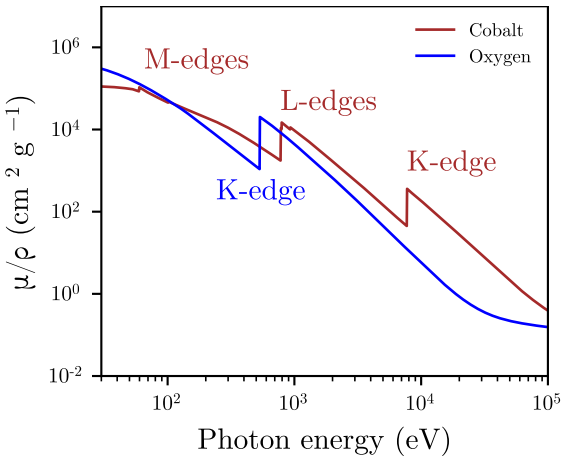

Figure 3.2: Mass attenuation coefficient for oxygen and cobalt. The plotted data has been published by Chantler [48].

at around 543 eV, corresponding to the ionization of the 1s core-level (K-edge). A significantly weaker feature at around 41 eV (L edge ionization) is not shown in the graph. For the TM cobalt, an element with significantly more electrons, three different jumps (K, L, M) in the absorption cross-section are observed since more shells are available for ionization. The systematic study of this behavior in varying elements is subject to the field of X-ray absorption spectroscopy (XAS) [45]. In the following, we discuss X-ray emission, the radiative decay of a core-hole state, in more detail.

3.2 X-ray emission spectroscopy

X-ray emission spectroscopy (XES) offers an essential tool for the exploration of core- and valence-level electronic structure in atoms and molecules [41, 49]. In general, XES is considered element-specific, enabling the targeted investigation of selected atoms inside larger assemblies. In specific cases, valence interactions between the targeted atom and its nearest neighbors are picked up in XES signals, allowing for a sophisticated probe of molecular electronic structure [50–52], see section 3.2.3.

In TM complex chemistry, the spin and oxidation state of metal ions are studied as vital elements in understanding important physical and chemical properties. Those include catalytic activity [53, 54], magnetism [55] or photo-active behavior [56]. The fact that XES provides, in many cases, a sensitive experimental tool for the study of such properties has led to the widespread application of this technique. Today, XES is used as a routine spectroscopic method at many synchrotron and free-electron laser facilities [57–60], and, with the onset of more powerful miniaturized X-ray sources and improved detectors, in sophisticated ways at laboratories [61].

XES is based on the observation of emitted X-ray photons from excited atoms, as they occur during radiative decay of excited core-hole states [49]. In a typical XES experiment, a sample is brought into an excited core-hole state with X-ray radiation.

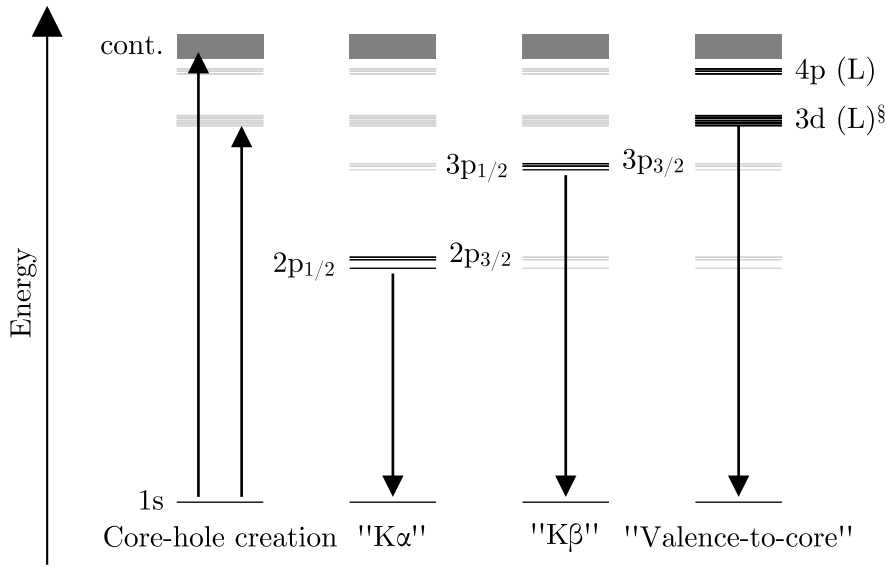

Figure 3.3: X-ray emission, a two-step process: Upon excitation by the creation of a core-hole, multiple radiative transitions are possible. §Quadropole contributions to the formally forbidden 3d → 1s transition are not neglectable in the valence-to-core case. Additionally, significant ligand contributions (L) to the valence levels in coordination compounds can be present.

Upon relaxation, the sample will emit photo-/Auger-electrons and photons, of which the X-ray photons are analyzed by an X-ray spectrometer. Importantly, the emitted photons are analyzed in a wavelength- or energy-dispersive fashion (as opposed to X-ray measurements where the total integrated fluorescence is recorded, for example), allowing for the inspection of individual spectral components in the emission signal.

We will use multiplet and DFT calculations in a simplistic way to discuss the sensitivity of XES towards subtle electronic details and strengths as a spectroscopic method. Calculations will be used marginally and as a tool to explore parameters most commonly identified during X-ray emission spectroscopy experiments. These include splittings (energy differences between features), intensity ratios, line symmetries, and the width of emission lines. We will briefly mention specific challenges in calculating certain spectral signatures to give context to the difficulties manifest when interpreting experimental spectra.

XES can provide a rich footprint of core (and valence) electronic structure. Fundamentally, XES is commonly denoted as a two-step process (figure 3.3), in which an incoming X-ray photon first creates a 1s core-hole[2], either by ionization (non-resonant) or promotion of an electron into a 3d valence level (resonant). For an element from the group of first row TMs, e.g. Ni ($[\mathrm{Ar}]\,3d^8 4s^2$), two dominant decays to the 1s core level are possible: The relaxation of an electron from the L- to the K-shell (2p to 1s),

[2]We will limit ourselves to the discussion of hard X-ray XES on 3d TM complexes.

called Kα emission, and the transition of an electron from the M- to the K-shell (3p to 1s, Kβ emission). These are the most dominant XES features in 3d TM complexes. The transitions from the metal valence-orbitals (potentially carrying significant ligand-character) are denoted valence-to-core. Historically, these transitions have been labeled according to Siegbahn notation, e.g., "$K\alpha_1$", in which the capital Latin and the Greek letters designate the two shells between which the relaxation process takes place, and the running index designates spectral features with increasing energy distance from the main feature [62].

3.2.1 Kα emission lines

We can discuss many essential features in the observed XES signals in a one-electron ionic picture. The Kα ($2p \rightarrow 1s$) XES signal is split into a stronger $K\alpha_1$ and a weaker $K\alpha_2$ line (Figure 3.4). The origin of this splitting is spin-orbit coupling, in which electron spin interacts with the different orbital momenta of the $2p_{3/2}$ and $2p_{1/2}$ subshell [49]. Since the 2p core state is comparatively far away from the valence 3d states of the metal, a secondary effect to the Kα emission line, the 2p-3d exchange coupling, is significantly smaller. Consequently, Kα XES is generally considered less sensitive towards valence-dominated properties, e.g., the spin-state of the metal. It is clear, however, that a variety of subtle electronic effects such as covalency or remaining influence of p-d exchange coupling is encoded in the Kα emission signal and needs to be carefully assessed when attempting to extract electronic structure parameters based on Kα emission [63, 64].

Multiplet theory provides a more detailed understanding of some of the observed phenomena in XES spectra [41]. We see in the right panel in figure 3.4 that a multiplet calculation (here conducted with CTM4XAS [65]) is well suited for reproducing the characteristic features of the Kα emission lines in 3d TMss by including spin-orbit coupling.

A more detailed investigation of the results from the multiplet calculation allows for

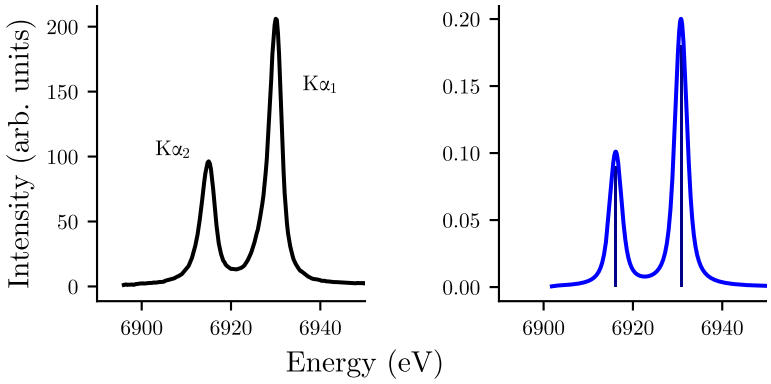

Figure 3.4: The Kα emission lines of cobalt. Left: Experimental spectrum. Right: Multiplet calculation and broadened spectrum without p-d exchange. A full list of calculation parameters is tabulated in appendix H.

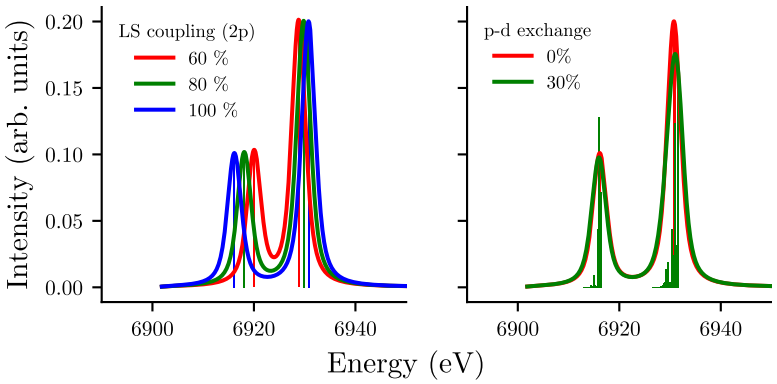

Figure 3.5: Multiplet calculations for a Co^{3+} ion. Left: Spin-orbit (LS) coupling parameter varied between 60% and 100% of their atomic values. Right: Slater integral reduction values varied from 0% to 30%. A full list of calculation parameters is tabulated in appendix H.

a qualitative analysis of common lineshape variations in Kα emission lines for 3d TM complexes. Those variations are characteristic in static Kα measurements (appendix F), but are also important as baseline references during ultra-fast transient measurements (chapter 6). The left panel in figure 3.5 shows the dependence of the Kα lineshape on the reduction of the spin-orbit coupling in a multiplet calculation. It can be observed that the splitting between $K\alpha_1$ and $K\alpha_2$ increases with increasing spin-orbit coupling. Furthermore, the pivot point of movement, i.e., the common center of mass around which the two emission lines are split, lies closer to $K\alpha_1$. This is expected from the higher number of states in the $2p_{3/2}$ subshell for the $K\alpha_1$ emission line but implies that the Kα emission lines split asymmetrically as a function of spin-orbit coupling.

Based on the number of possible states, one might expect the intensity ratio between the $K\alpha_1$ and $K\alpha_2$ feature to be 2:1. In reality, further individual splitting of the underlying transitions in both the $K\alpha_1$ and $K\alpha_2$ leads to asymmetry of the observed emission lines, which in turn modulates the expected intensity ratio [66]. This can be rationalized with another multiplet calculation shown in the right panel of figure 3.5. Here, the p-d direct and exchange slater integral values were changed from 0 to 0.3. We observe no influence on the characteristic splitting of the Kα emission lines. However, the $K\alpha_1$ peak experiences a splitting, leading to an asymmetry often picked up experimentally as a lower-energy shoulder. Since the states of the $K\alpha_1$ line split more strongly than those of the $K\alpha_2$ line as a function of p-d exchange, the intensity ratio $I(K\alpha_1)/I(K\alpha_2)$ decreases with increasing p-d exchange. This simplistic description is entirely consistent with experimental observations. HS complexes (for which the influence of p-d exchange coupling is larger, see chapter 2) exhibit more asymmetric Kα emission lines and a reduced $I(K\alpha_1)/I(K\alpha_2)$ intensity ratio. Contrary, LS complexes commonly present narrower and more symmetric Kα emission lines, with an intensity ratio closer to 2:1 (as expected from the pure number of states in the non-degenerated $p_{3/2}$ subshell when compared to the $p_{1/2}$ orbitals).

3.2.2 Kα emission lines

The influence of the p-d exchange coupling for the Kβ emission feature is significantly larger than for the Kα peaks [41]. While this emission feature does not exhibit an apparent splitting as in the case of the Kα emission lines, it is still highly asymmetric. A pronounced low-energy tail or shoulder (Kβ') next to the main $K\beta_{1,3}$ peak is commonly found. High-spin compounds exhibit a pronounced Kβ' satellite feature, while low-spin complexes present a significantly weaker feature. This behavior was recognized early as a means to study TM spin-state [67]. The Kβ XES sensitivity has been exploited extensively on a large number of chemically relevant species containing ions from the group of TM complexes, especially iron [68]. In some instances, special care has to be taken since, as in the case of the Kα emission lines, metal covalency can influence this region significantly [63, 64].

The left panel in figure 3.6 displays an experimental Kβ XES spectrum on a HS cobalt compound, $[Co(bpy)_3]Cl_2 \cdot 5\,H_2O$, exhibiting the characteristic Kβ' shoulder to the low energy side of the $K\beta_{1,3}$ feature. The right panel shows a multiplet calculation on a Co^{2+} ion with consideration of ligand-field splitting (octahedral geometry). In comparison, the main features are reproduced, namely the shoulder and the split mainline feature. The spin-orbit coupling does play a subordinate role in the general lineshape of the Kβ emission line but does modulate the splitting and thus the asymmetry and width of the $K\beta_{1,3}$ feature. This can again be rationalized with a multiplet calculation as shown in the left panel of figure 3.7. The p-d exchange slater integral values have been reduced to 0 in this calculation. While the overall lineshape behavior does not agree as no Kβ' feature is observed, splittings in the $K\beta_{1,3}$ region become more visible. Varying the spin-orbit coupling value does influence the splitting of the states, due to which the spectroscopic features $K\beta_1$ and $K\beta_3$ arise.

When increasing the parameter for the p-d exchange (right panel in figure 3.7), both

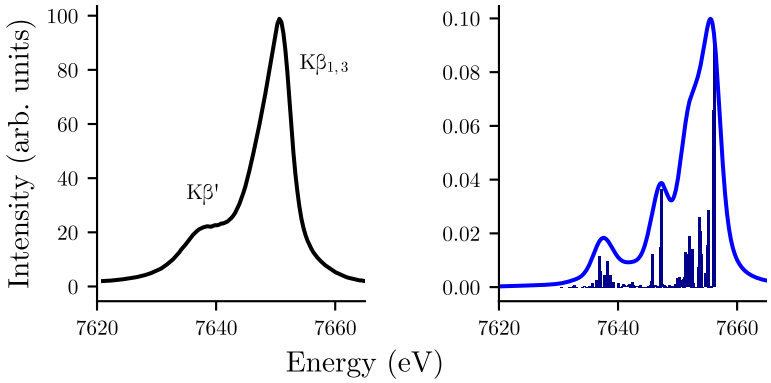

Figure 3.6: The Kβ emission line of a Co^{2+} ion. Left: Experimental spectrum of $[Co(bpy)_3]Cl_2 \cdot 5\,H_2O$. Right: Multiplet calculations and broadened spectrum for a Co^{2+} ion with both spin-orbit coupling and p-d-exchange set to 100 % of their atomic values. A full list of calculation parameters is tabulated in appendix H.

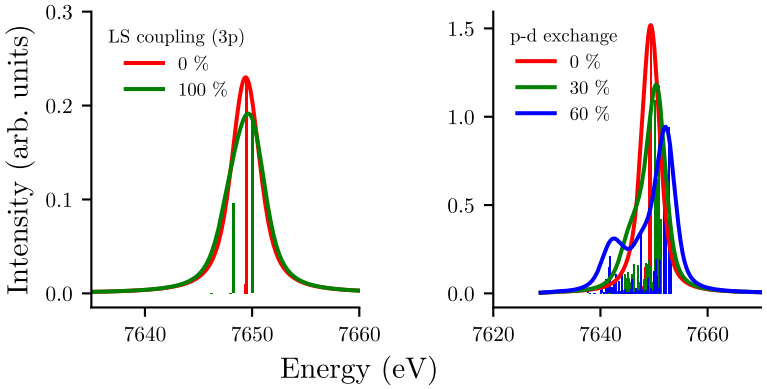

Figure 3.7: Multiplet calculations for a Co^{2+} ion. Left: Spin-orbit coupling (LS) parameter varied from 0 % to 100 %. Right: p-d exchange varied between 0 % and 60 %. A full list of calculation parameters is tabulated in appendix H.

multiplet states start to split, and a tail at lower energies appears. The separation between the main group of states and the satellite peaks is directly influenced by the values for the p-d exchange parameter. Based on this simplistic analysis, we may hold that the asymmetry and width of the $K\beta_{1,3}$ feature are dominated by spin-orbit coupling, and the splitting between the $K\beta_{1,3}$ and Kβ' feature is characterized by the p-d exchange coupling. Due to a large number of involved multiplets, both effects will strongly mix, hardening the extraction of a simple behavior for individual multiplets. As for the splitting of the Kα lines, the origin of p-d splitting in the Kβ feature is the different magnetic coupling of the $3p_{1/2}$ and $3p_{3/2}$. In a molecular level picture, the Kβ' feature will contain those electrons that couple antiferromagnetically with the spin in the 3d levels of the metal (lowering the total energy of the states), while the $K\beta_{1,3}$ feature will contain states that couple ferromagnetically to the metal d spin. This spin-resolved characteristic of the Kβ emission line opens up the possibility for spin-selective X-ray absorption measurements [69]. We will discuss this further in section 5.2.1.

3.2.3 Valence-to-core emission lines

At the higher-energy tail of the 3d metal Kβ feature, the roughly 50 times weaker valence-to-core (VtC) emission signal is observed. The origin of these features stems from ligand s or p orbitals mixing with the valence orbitals of the metal ion, which enables formally dipole-forbidden transitions for the $3d \rightarrow 1s$ decay. The ligand contributions to VtC spectra have attracted interest, as the encoded signatures due to ligand orbital mixing can be significant and may, in some instances, allow claims about the ligand electronic structure and bonding properties [51, 52]. In reality, multiple effects have to be carefully disentangled. Intensity changes due to orbital overlap have to be considered, as subtle variations in the ligand electronic nature may be masked by more extensive absolute intensity changes due to differences in the ligand-metal distance and subsequently changing metal-ligand orbital overlap. This makes the extraction of purely electronic

ligand-based properties challenging.

Using multiplet theory, we discussed fundamental aspects of the Kα and Kβ emission lines in an ionic picture. Experimental VtC XES data exhibits a strong interplay with the ligand environment and coordination structure of the compound. Since the origin of VtC emission features are ligand orbitals mixing into the d-orbitals of the metal (otherwise, no p character would be available for a dipole-allowed transition), and the d levels are strongly coupled to the structure of the compound (see chapter 2.1), this is not a surprising observation. We will turn to DFT for a discussion of selected aspects of VtC emission lines.

The VtC emission region is well accessible via standard one-electron DFT calculations since the 3d levels are well separated from the core-hole [70]. In many cases, VtC calculations with DFT have been shown to match the experimental data well, reproducing relative energies of experimentally observed spectra [51]. The absolute calculated energies are usually off by as many as a few hundred eV, but since relative calculated energies agree [52], calibration is possible. This calibration is commonly undertaken by extracting a mean offset energy shift based on multiple experimental datasets, which demands the collection of sufficiently structured and low-noise VtC spectra for a series of complexes.

The results of a ground-state (GS) DFT calculation on $[Co(acac)_3]$ are presented in the right panel of figure 3.8. For a qualitative analysis and comparison with the experimental spectrum, orbital ligand and metal contributions to the calculated transition intensities were extracted from the results of the calculations. A distinction regarding the orbital nature (s, p, d) has been made. The calculation protocol and analysis methodology are given in section 4.4.4. The analysis reveals that the VtC region for this compound exhibits features with contributions mainly from ligand-based orbitals with 2s and 2p character. We confirm earlier reports about a strong preference of ligand

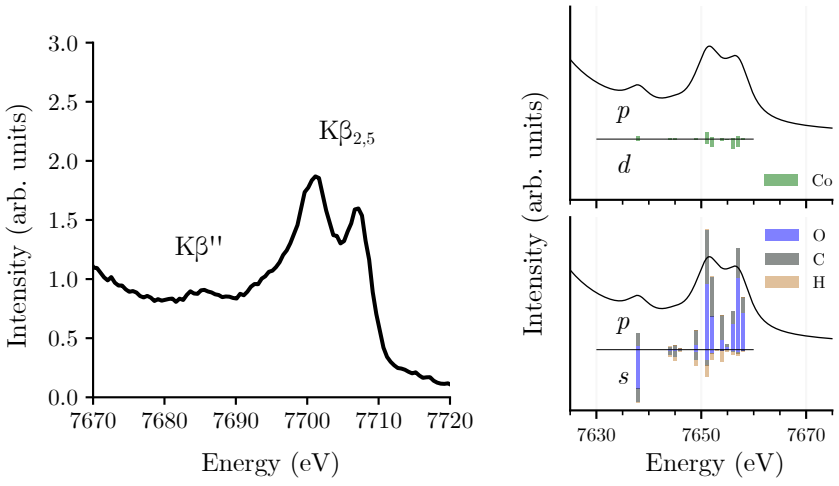

Figure 3.8: Left: Experimental spectrum. Right: DFT calculated VtC emission spectrum on $[Co(acac)_3]$. Clearly visible are different accounts of metal 3d-ligand 2s, and 2p mixing under the different regions of the spectrum.

s orbitals in the Kβ" feature and a general trend towards p character for the $K\beta_{2,5}$ peak [51]. The position of Kβ"as been shown to vary with the ligand identity [50].

3.2.4 Resonant X-ray emission spectroscopy

During resonant X-ray emission spectroscopy (RXES), spectra are measured as a function of the incoming photon energy. In a typical RXES experiment, the incoming photon energy E_{in} is scanned over an absorption edge (hence resonant) of the target element. During scanning, emission spectra might either be collected in a dispersive fashion for multiple emission energies E_{out} at once or sequentially for one emission energy at a time throughout multiple absorption scans. The acquired emission spectra are assembled into a two-dimensional RXES map, which plots the collected intensity I as a function of both the incoming- and emitted energy $I(E_{in}, E_{out})$.

The RXES process can be described with a two-step scheme as depicted in figure 3.9. A 1s core-hole is created by the promotion of an electron to one of the empty 3d valence orbitals $1s^2 3d^n \rightarrow 1s^1 3d^{n+1}$. This state constitutes the intermediate state (IS). From there, an electron from the 2p (or 3p) orbitals decays to the 1s orbital, creating the $1s^2 3p^5 3d^{n+1}$ final state (FS). The final state of the 1s3p RXES process, $3p^5 3d^{N+1}$, is identical to metal M-edge absorption spectroscopy. Due to interactions with the intermediate state in the resonant process, significant line shape variations can arise, which reduce the similarity between the two spectral signatures, despite the identical final state [41].

Spectral signatures in the two-dimensional RXES map will exhibit anisotropic broadening due to contributions by the intermediate and final state lifetimes [69]. Figure 3.10 gives an experimental 1s3p RXES datasets on the Co^{3+} compound $[Co(bpy)_3]Cl_3 \cdot 4\,H_2O$ and the Co^{2+} compound $[Co(bpy)_3]Cl_2 \cdot 5\,H_2O$ (cf. chapter 5). Additional instrumental

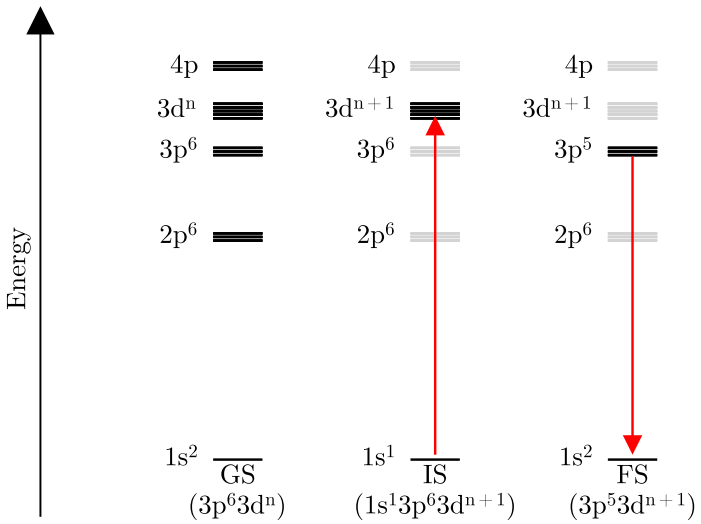

Figure 3.9: The resonant 1s3p X-ray emission process. The case for 1s2p is analogous.

broadening stemming from the finite energy resolution of the monochromator and the X-ray emission spectrometer will also contribute to the final two-dimensional broadening. The individual contributions are illustrated as black arrows in figure 3.10 The directions of the instrumental broadening contributions Γ_{INC} for the monochromator and Γ_{SPEC} for the X-ray emission spectrometer align with the incoming- and emitted energy axes, respectively. The intermediate state lifetime broadening Γ_{INT} acts along the axis of constant energy transfer ($\mathrm{E_{in}}$ - $\mathrm{E_{out}}$), which, in the presented illustration, lies along a diagonal axis. The final state broadening Γ_{FIN} applies along the vertical emission axis. The directionality of the broadening contributions can be exploited by considering just a finite width slice in the RXES map along the incoming energy at selected emission energy. If such a slice reduces the influence of diagonal broadening components onto the line shape and thus results in an improved energy resolution for the XAS spectrum, the measurement is titled high energy resolution fluorescence detected (HERFD) [49, 71].

Related to RXES are measurements in spin-polarized (or spin-selective) fashion. These measurements exploit the separation of final state multiplets in the Kβ line shapes of TM complexes [63, 72], which can allow a distinction between opposite spin-polarizations (spin-up, spin-down) during resonant XES. This concept will be revisited in section 5.2.1.

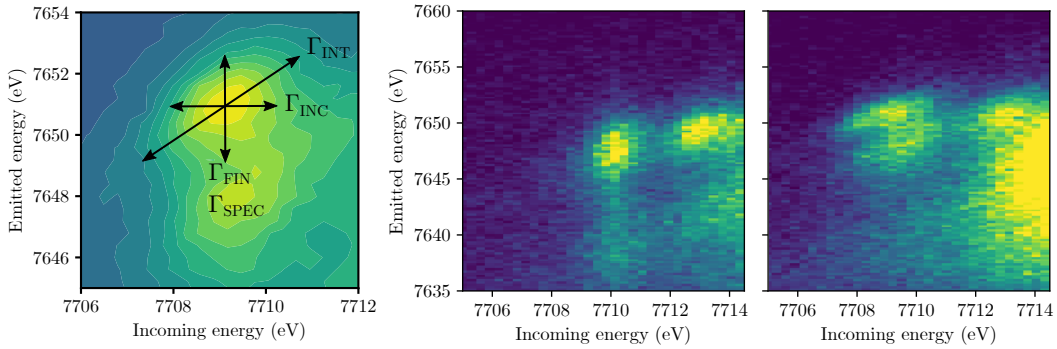

Figure 3.10: Experimental 1s3p RXES data on $[\mathrm{Co(bpy)_3}]\mathrm{Cl_3} \cdot 4\,\mathrm{H_2O}$ (center) and $[\mathrm{Co(bpy)_3}]\mathrm{Cl_2} \cdot 5\,\mathrm{H_2O}$ (right), illustrating broadening contributions from the incoming photon radiation Γ_{INC}, the emission spectrometer Γ_{SPEC}, the core-hole lifetime broadening of the intermedia state Γ_{INT} and the core-hole lifetime broadening of the final state Γ_{FIN} to the total observed peak width (contributions illustrated in the left panel).

3.3 Experimental implementation

In this section, we visit the fundamental experimental concepts behind the study of VT compounds in chapters 4 to 6. Specifically, we will comment on selected properties of FEL radiation and introduce the crystal spectrometers commonly used at synchrotron and free electron laser (FEL) instruments.

3.3.1 X-ray free electron lasers

Third-generation synchrotron facilities can deliver intense X radiation pulses on the order of 100 ps time duration [43]. The *time-resolved* investigation of ultrafast processes on the atomic scale and femtosecond time-duration demands experimental techniques which go beyond the capabilities of synchrotron facilities. Fundamentally, these processes require probing via ultra-short X-ray flashes of similar duration as the observed kinetics since subsequent events in the sample can not be electronically separated in the detector anymore. In other words, the detector exposure times can not be brought down to the femtosecond timescale, which thus leaves the exposure via ultra-short and bright X-ray flashes as a viable alternative. Aside from the short temporal duration, this technique demands a high number of photos.

These requirements have been answered with advances in the field of X-ray FELs, as this type of X-ray source offers highly brilliant photon pulses with durations below 1 ps [73]. The European X-ray free electron laser facility (EuXFEL) in Hamburg, Germany, operates seven instruments for the investigation of ultrafast processes and matter under extreme conditions with soft and hard X-rays [74].

The facility design consists of three fundamental sections. A superconducting accelerator structure achieves electron energies of up to 17.5 GeV. This section constitutes the first of two underground structures, which extend over a distance of approximately 3.4 km from the facility side of the DESY synchrotron at Hamburg, Germany, towards the neighboring city of Schenefeld. The second section comprises three FEL undulator sources. A characteristic property of the FEL undulator design is the facilitation of the self-amplified stimulated emission (SASE) process, with leads to the emission of coherent photon radiation in the up to 200 m long undulator structures [73, 75]. The

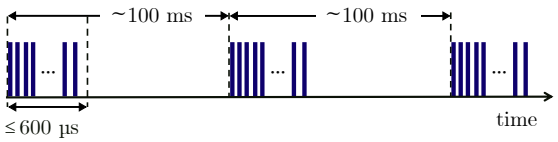

Figure 3.11: X-ray pulse timing-structure at EuXFEL. Pulses are delivered in bursts (*trains*), every 100 ms. The inter-train distance between the pulses can be set to integer fractions of the base repetition rate of 4.5 MHz. The maximal number of pulses per train is 2700, corresponding to a total of 27000 pulses per second.

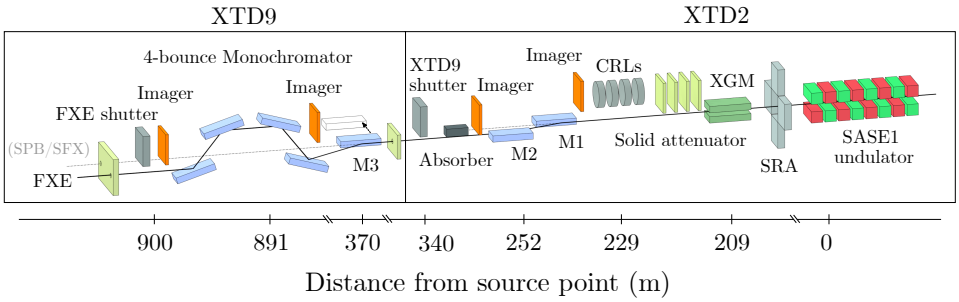

Figure 3.12: Photon beamline at EuXFEL, illustrating important optical components for ultra-fast experiments at the FXE instrument. Based on Ref. [76].

emitted photons are guided to the experimental hall over a multiple hundred meters to allow for a horizontal separation (a spatial requirement due to the accommodation of multiple instruments) and a sufficient increase in beam size to suppress damages to the optical elements due to exceeding heat loads. The experimental hall in the third section houses the six instrument end stations. Contrary to other hard X-ray FEL facilities, EuXFEL features a unique arrival pattern for the delivered X-ray pulses. The timing pattern, which consists of ten bursts of shorter X-ray bunches, is illustrated in figure 3.11.

One of the six end stations, the Femtoseconds X-ray Experiment (FXE) instrument, was used to investigate ultra-fast time-resolved processes in the cobalt complexes investigated in this thesis. The beam transport layout of the FXE instrument is illustrated in figure 3.12 and comprises two photon-tunnel sections labeled XTD2 and XTD9. After emission in the undulator section (right), X-rays pass a diagnostic X-ray gas monitor (XGM) and a solid attenuator unit. A set of compound refractive lenses (CRL) and three mirrors (M1, M2, M3) are used to focus and guide the photon beam toward the FXE instrument hutch. Several diagnostic imagers aid with the alignment of the photon beam. Since the photon beam must be horizontally offset for propagation to the neighboring SPB/SFX instrument, a realignment is required at the beginning of most operational shifts. By simultaneously using all three FEL sources, three instruments can operate in parallel. A 4-bounce monochromator offers the option for monochromatized photon radiation with a bandwidth of $\Delta E/E \approx 10^{-4}$. Selected properties of the FXE instrument itself will be presented in more detail in chapter 6.

3.3.2 Common types of X-ray spectrometers

In the non-resonant case, the initial core-hole is created with incoming photons whose energy is above the target atom's ionization energy. In many cases, the energy of the ionizing photon radiation can be relatively freely chosen since the absorption cross-section of many elements only slowly decays after the ionization edge jump. This means that the efficiency of the emission creation will not significantly change as a function of exact excitation energy. A direct consequence is that non-resonantXES experiments are

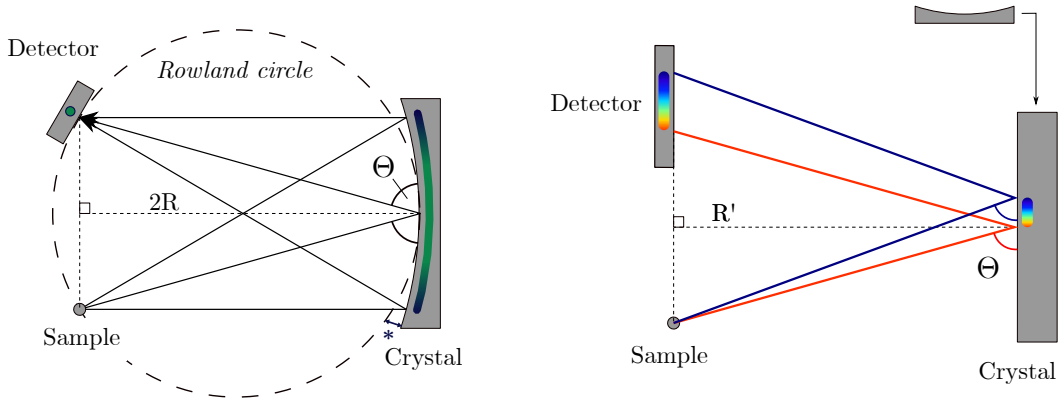

Figure 3.13: Spectrometer geometries for the capture of XES spectra. Rowland geometry (left) and the dispersive von Hámos geometry (right) are discussed in the test.

generally not very sensitive to the precise value chosen for the energy of the incoming photons. Additionally, the bandwidth of the incoming radiation does play a subordinate role. This lifts the requirements of high-resolution monochromators and scanning of the incoming energy, which eases the experimental process and makes this technique accessible to beamlines with broad incoming photon bandwidth, e.g., bending-magnet beamlines.

Modern XES implies the use of specialized instrumentation. Hard X-ray high-energy resolution spectra are commonly acquired with crystal spectrometers. Two fundamental approaches, the scanning- and dispersive spectrometer designs, are available to capture 3d transition metal XES spectra. A scanning analyzer spectrometer is based on the Rowland geometry (as shown in the left panel of figure 3.13). It offers, in principle, the same Bragg angle to all impinging photons. If operated in a 1:1 focussing Rowland geometry (as shown), only photons that fall within the intrinsic bandwidth of the analyzer crystal will be captured by the photon detector. The intrinsic resolution will largely depend on the quality of the bend crystal lattices and less on the inherent Darwin width of the crystal [49]. In Rowland geometry, a whole XES spectrum is acquired by collecting the reflected photon radiation as a function of the scanned Bragg angle for multiple emission energies.

To fulfill the Bragg condition at each point along the spherical analyzer surface, the crystal lattice planes have to follow the radius of the Rowland circle R. The focusing condition, which dictates the crystal surface's shape, requires the analyzer's bending radius to be twice the Rowland circle radius 2 R. A Johansson crystal denotes an analyzer that fulfills both of these conditions [77]. From a manufacturing point of view, a Johansson analyzer is challenging to fabricate, as it involves both bending and grounding [77]. A more straightforward design, in which the crystal lattice planes remain parallel to the crystal surface and follow a 2 R radius, is termed Johann cut [78]. Since the crystal lattice planes will increasingly deviate from the true optimal

orientation in the outer regions of the spherical analyzer (marked as * in figure 3.13), chromatic aberration effects come into play, which diminishes the imaging properties. Experimentally, one can counter this effect by using a suitable aperture (masking) on the analyzer crystal and region of interest (ROI) integration on the detector.

A dispersive or polychromatic type spectrometer (right panel in figure 3.13) records a whole XES spectrum simultaneously. This characteristic is also termed *single-shot* and presents advantages in the field of ultra-fast XES, where the point-to-point normalization in spectra might hold challenges (cf. chapter 6). A typical dispersive analyzer design is based on the von Hámos geometry. It features a radial bend along the non-dispersive direction (leading to a focusing). Along the dispersive direction, a flat crystal surface presents a range of Bragg angles, enabling photons to reflect with multiple X-ray energies within a well-defined bandwidth. Since each energy will be reflected under its corresponding Bragg angle, different X-ray energies will image onto spatially separated parts of the detector. Since the bending for analyzers in the von Hámos geometry is only applied in one direction, the intrinsic energy resolution may be improved. A further step in this direction is the use of sliced analyzers, in which the radial crystal surface is constructed of multiple flat crystal segments [79].

Chapter 4

XES and XRS for the investigation of VT complexes

From the late 1970s, investigations on the interplay between redox-active bis-semiquinone radical anions and TM ions led to the characterization of a novel family of bistable complexes. Those cobalt-based compounds are characterized by their ability to exhibit VT and of general form $Co(N\text{-}N)(DTB)_2$, in which N-N denotes a nitrogen-based diimine ligand and DTB the semiquinone or catecholate form of 3,5-di-tert-butyl-o--benzoquinone [33, 80]. The extensive use of optical absorption spectroscopy, electron paramagnetic resonance (EPR), and magnetic measurements provided experimental evidence for the presence of a combined MLCT and spin-crossover [15, 16, 19]. X-ray crystallography measurements till the early 1990s contributed to the experimental basis for DFT calculations on these systems, which corroborated the assignment of redox-active ligand frontier orbitals and the assessment of spin-coupling between metal and ligand [16, 30].

The rise of synchrotron-based X-ray spectroscopic methods in the 1990s led to a limited number of X-ray absorption studies on these systems, among which the cobalt metal pre-K-edge was investigated during pressure-induced VT [21]. More recent studies extended the application of XAS-based methods to other, newer cobalt-based tautomer systems (differing mainly in the co-ligand) [81, 82].

Despite the more than 40 years of research on VT in cobalt complexes, the implications and delicate electronic nature of combined intermolecular processes, and the overwhelming success of X-ray spectroscopic techniques in the investigation of other TM complexes, only a minimal amount of X-ray studies on VT exist to date. This is especially severe in the case of XES, where, to the best of our knowledge, only single studies on VT in cobalt complexes have been published [18].

In this chapter, we will explore the sensitivity of Kβ and VtC XES towards subtle electronic effects for the study of VT in cobalt complexes. The experimental results are discussed to investigate (i) how the core- and valence-electronic structure of the central metal ion is influenced when external temperature or chemical environment is varied, (ii) and what other, potentially ligand-based properties might be accessible

via the application of these techniques. Another hard X-ray-based method, X-ray Raman scattering (XRS), will be applied to study the K-edge of oxygen atoms in the benzoquinone ligand.

4.1 Collection of reference datasets

To obtain references of cobalt XES signals for the investigation of the VT process, we investigated a benchmark set of cobalt reference compounds via XES and RXES techniques. The investigated compounds were selected to exhibit variations in the spin- and charge-state, coordination geometry, and ligand environment. Their structures are shown in figure 4.1.

Tris-bipyridine and tris-phenanthroline redox couples (**4** and **5** in figure 4.1) present octahedral coordination geometries. They are studied due to their role as electron shuttles, i.e., their ability to accept and donate charge and mediate intermolecular electron transfer, e.g., in light-converting applications [83–86]. In specific ligand environments, $[Co(bpy)_3]Cl_3 \cdot 4\,H_2O$ / $[Co(bpy)_3]Cl_2 \cdot 5\,H_2O$ acts as a spin-crossover compound.

The acetylacetone complexes $Co(acac)_n$ ($n = 1$ or 2, compound **6** in figure 4.1) play a role in catalysis processes [87, 88]. The LS complex $[Co(acac)_3]$ presents octahedral coordination geometry. In the case of $[Co(acac)_2]$, both square-planar and tetrahedral conformation has been found [89, 90].

$[Co(terpy)_2]Cl_2$ (compound **7** in figure 4.1) presents semi-octahedral coordination. This complex has been found to exhibit different LS-HS equilibria, in which HS sites are formed due to a tetrahedral compression of the coordination octahedron. At the same time, a fraction of the molecules undergoes additional perpendicular elongation caused by the Jahn-Teller effect, stabilizing a LS state [91–95]. $[Co(terpy)_2]Cl_2$ was among the first cobalt compounds discovered to undergo a thermal spin-transition and has since been studied due to its molecular bi-stability [95].

The Bis(salicyliden)ethylenediamine (salen) complex (**8** in figure 4.1) is investigated for its catalytic potential during fixation of carbon dioxide or in the reduction of organic halides and the synthesis of cyclic carbonates [96–98]. The compound exhibits square-planar coordination geometry and presents a trivalent LS configuration.

The trivalent octahedral $[Co(en)_3]^{3+}$ compound was first reported by Werner in 1912 and played a role in the understanding of coordination chemistry [99]. In this study, the chloride salt $[Co(en)_3]Cl_3 \cdot 2\,H_2O$ was investigated (compound **9** in figure 4.1).

The CoF3 compound (**10**) has been studied as potential electrode material in Li-ion batteries [100]. Extensive studies on ammonium triflourides also included $(NH_4)CoF3$ [101, 102]. Despite being a Co^{3+} complex, CoF3 exhibits a HS configuration.

The sepulchrate Co^{3+} compound Co(sep) (complex **12** in figure 4.1) is investigated as a pillaring reagent in the synthesis of pillared layered functional materials for catalytic applications [103].

$Co(C_2O_4)$ (**13**), one of the two known cobalt oxides, has been included in the study of VtC spectra. The compound has gained interest in the field of semiconductor research [104].

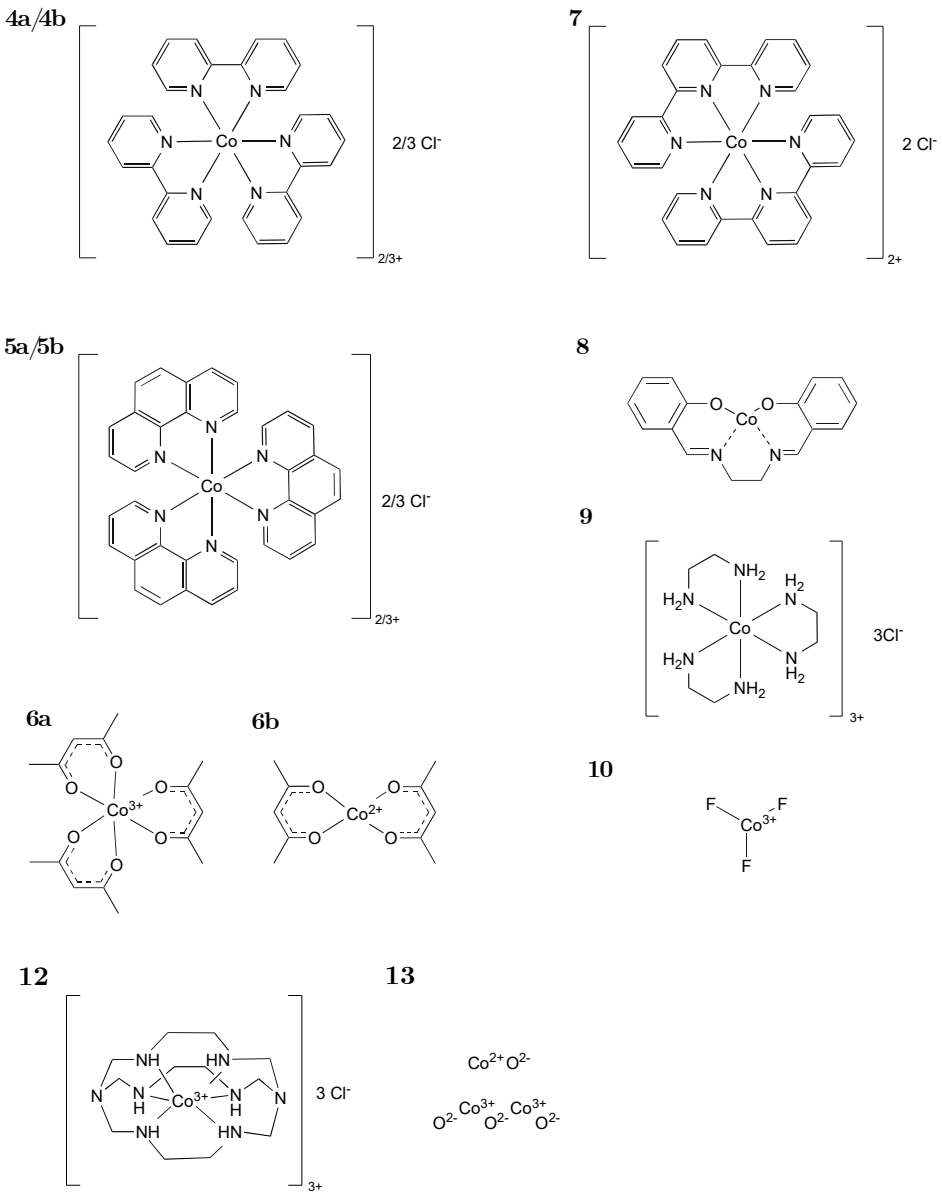

Figure 4.1: Investigated cobalt reference compounds. The numerals indicate identifiers, which are used as shorthand labels. Cobalt VT complexes (not shown here) are labeled 1-3 and 11. Compound names are given in the main text. Not all reference data are presented in this chapter. More experimental spectra are given in appendix F.

4.2 Temperature variation as trigger for VT transition

The control of VT behavior via external stimuli has been discussed in section 2.4. Sample temperature, a well-accessible experimental parameter, has been used extensively in the study of VT. In this section, we are giving the experimental implementation of the sample temperature control for the following measurements. The cryostat solution the CLÆSSbeamline, ALBA, beamline P64, PETRA III, beamline BL9, DELTA and beamline GALAXIES, SOLEIL is given in figure 4.2. In all cases, cryostats operated with liquid nitrogen. The closed-cycle cryostats at CLÆSSand GALAXIES operated in a vacuum, reducing ice buildup. A Linkam temperature stage was used at P64. This stage is also operated in a vacuum to reduce the chance of icing. To address this issue at DELTA, where a nitrogen cryo blower was used, a constant flow of nitrogen was flushing the sample.

The experimentally obtained transition temperatures $T_{1/2}$ are an essential fingerprint of the equilibrium behind the VT process. Table 4.1 lists a survey of published transition temperatures for the compounds investigated in this thesis. Experimentally, the sample temperature was controlled by a liquid nitrogen cryostat directly attached to the sample holder (figure 4.2).

Table 4.1: A survey of transition temperatures (critical temperature) in cobalt VT complexes. A portion of the references in this list was compiled by Shultz [12]. Decimals are given as reported by the cited publication.

Sample		$T_{Lit.}$ (K)	References
$Co(DTB)_2(tmeda)$	solid	195	[36]
	in toluene	280	[105]
	in CH_2Cl_2	~300	[105]
	in MeCN	~340	[105]
	in DMF	363	[105]
$Co(DTB)_2(bpy)$	solid	310	[106]
	in toluene	277.0	[35]
$Co(DTB)_2(phen)$	solid	226.6	[35]
	in toluene	240	[16]
$Co(DTB)_2(dpbpy)$	solid	350.0	[35]

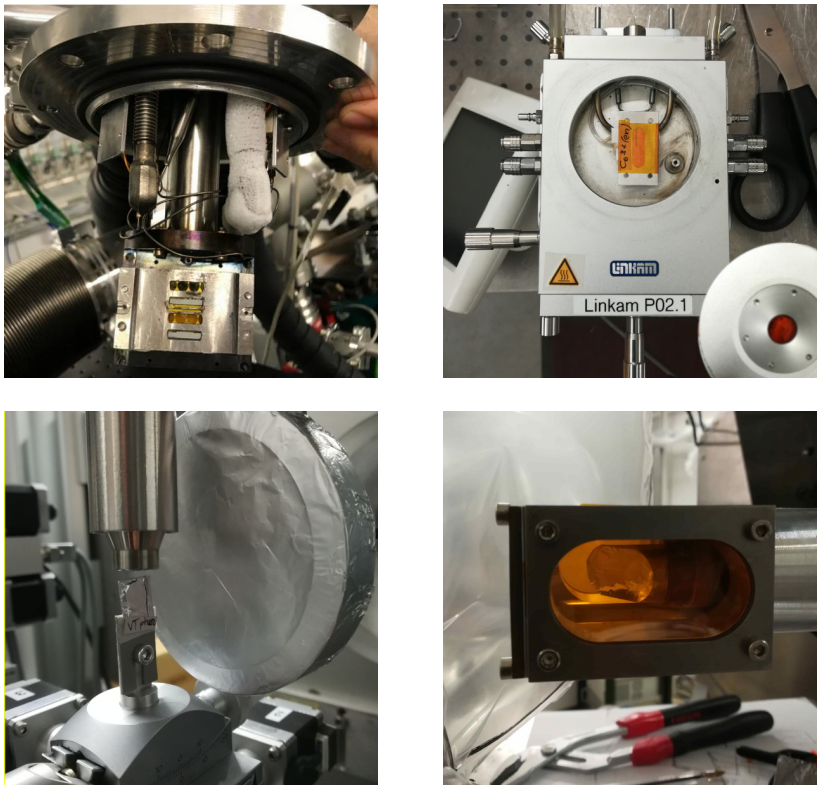

Figure 4.2: Experimental implementation of temperature-induced VT experiments at ALBA, CLAESS (top left), PETRA III, P64 (top right), DELTA (bottom left) and SOLEIL, GALAXIES (bottom right).

4.3 Sample synthesis and characterization

The compounds $Co(DTB)_2(tmeda)$, $Co(DTB)_2(bpy)$, and $Co(DTB)_2(phen)$ are not commercially available and require synthesis and subsequent crystallization via slow evaporation of a toluene solution under an oxygen-free atmosphere [16]. The samples utilized in this study were synthesized by Dr. Sergio A. V. Jannuzzi and Fabian Otto from the Inorganic Synthesis & Spectroscopy group in the Department of Inorganic Spectroscopy of the Max Planck Institute for Chemical Energy Conversion in Mülheim, Germany.

We observed that evaporation rate and storage conditions significantly influenced the synthesis results. Sample characterization turned out to be crucial and was undertaken by UV/Vis and IR spectroscopy, as well as magnetic susceptibility measurements both in the solid phase and in toluene solution [39]. In the following, selected measurements will be discussed, as they also aid the understanding of the VT process.

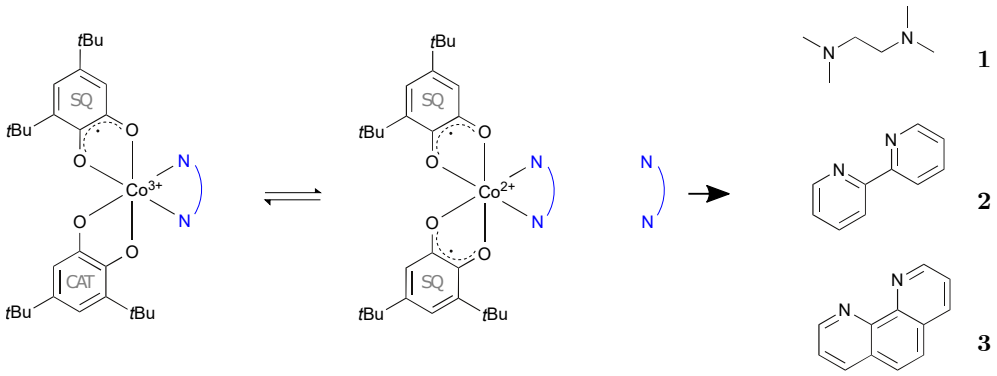

Figure 4.3: Investigated cobalt compounds exhibiting VT. The numerals indicate identifiers, which are used as shorthand labels.

4.3.1 UV/Vis spectroscopy

Optical spectroscopy in the UV/Vis regime (300 nm - 1000 nm) probes valence electronic states, which can allow access to electronically relevant states in VT [36, 107], and corresponding spectra exhibit significant changes upon VT interconversion.

UV/Vis optical absorption measurements on $Co(DTB)_2$(tmeda), $Co(DTB)_2$(bpy) and $Co(DTB)_2$(phen) in toluene solution have been conducted by Dr. Sergio Jannuzzi and Fabian Otto (see above). We performed additional measurements on a fourth VT compound, $Co(DTB)_2$(dpbpy), at EuXFEL. In all experiments, we varied the temperature to control the VT equilibrium. This allowed us to collect optical absorption spectra of both the LS Co^{3+} VT complex and the HS Co^{2+} form. Optical absorption measurements on the first three VT complexes required cooling the sample solution. This was achieved with an Agilent Cary 8454 diode array spectrometer equipped with an Unisoku USP-203 cryostat and inside a 1 cm optical length quartz cuvette. In contrast, the forth VT complex, $Co(DTB)_2$(dpbpy), exists almost exclusively in its LS Co^{3+} form at room temperature [14]. This allowed a simplified measurement setup, in which the sample temperature was controlled by placing the base of the cuvette sample holder in a hot-water bath. Control of the bath temperature gave good temperature stabilization of the sample, verified by simultaneously inspecting both sample and the bath temperature with immersion thermometers. Optical absorption measurements were conducted inside a 1 cm quartz cuvette with an Ocean FX VIS-NIR spectrometer and a DH-2000 deuterium-tungsten halogen light source.

We will begin the discussion with three VT complexes, specifically $Co(DTB)_2$(tmeda), $Co(DTB)_2$(bpy) and $Co(DTB)_2$(phen) in toluene solution. All of these compounds require cooling for tautomerization and are presented in figure 4.4. The optical absorption spectra of these complexes exhibit a strong feature at medium wavelengths in the Co^{3+} LS phase (▼; tmeda: 640 nm, bpy: 600 nm, phen: 600 nm). An increase in sample temperature leads to the appearance of a near-infrared (NIR) feature (▲; tmeda: 740 nm, bpy: 770 nm, phen: 770 nm), while the other peak loses significantly in intensity.

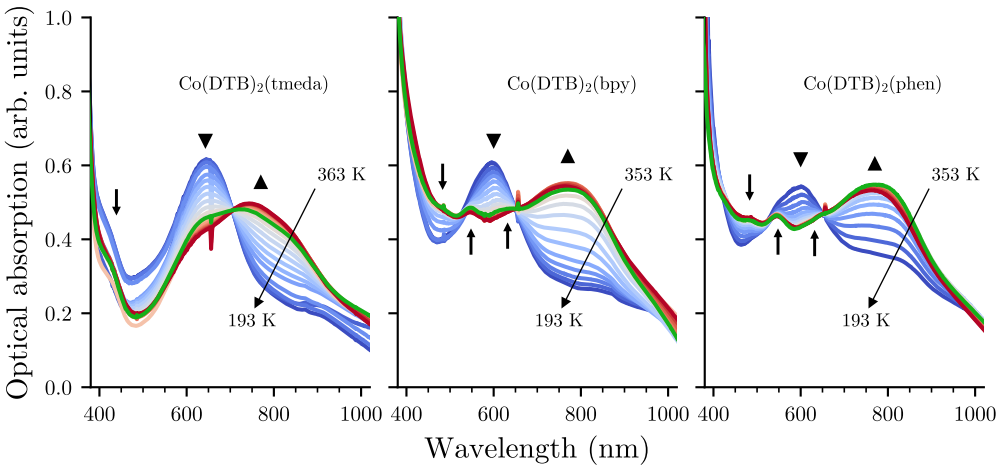

Figure 4.4: Temperature resolved UV/Vis spectroscopy on cobalt VT compounds, plotted for the discussion of line shapes. Green lines represent the room temperature spectrum. The sharp peaks at 485 nm and 565 nm represent glitches, most likely caused by a switch of the internal optics in the spectrometer during acquisition scan.

The general shape of the spectra agrees with published data [16, 105, 108]. At lower wavelengths around 428 nm, a faint shoulder can be observed in the spectrum (downward black arrow).

Three additional weaker bands are observed for the polypyridine complexes in the center and right panel of figure 4.4 at elevated temperatures. The position of these narrow bands is similar for both complexes and found at approximately 484 nm, 544 nm, and 643 nm (marked by thin black arrows). In the low-temperature spectra, these features are not clearly visible. For $Co(DTB)_2(phen)$, the remaining intensity of the central weaker band at 544 nm is found as a shoulder to the main peak at 600 nm. The optical absorption spectra of $Co(DTB)_2(bpy)$ and $Co(DTB)_2(phen)$ exhibit the same general feature shapes, aside from a shift in temperature. This is in good agreement with the reported critical temperatures of these compounds, which differ by approximately 37 K (cf. table 4.1). We note that similar optical absorption spectra are also in line with the fact that the polypyridine co-ligand in $Co(DTB)_2(bpy)$ and $Co(DTB)_2(phen)$ are structurally comparable (cf. section 2.4.2).

Multiple authors have discussed the nature of the main features observed. The broad peak at around 800 nm for the HS-form of $Co(DTB)_2(tmeda)$ has been assigned a MLCT to the semiquinone ligand [19]. A bright band at 640 nm for $Co(DTB)_2(tmeda)$ and at 600 nm for $Co(DTB)_2(bpy)$ in the LS-phase has been associated with a LMCT band [25]. Experimentally, this assignment was supported for $Co(DTB)_2(phen)$ via magnetic measurements, in which the measured magnetic moment was increased when irradiating with 532 nm light and reduced when irradiating with 830 nm light [109]. It should be noted that the bidirectional light-switching of this compound was only possible at sample temperatures below 50 K.

The presence of LMCT and MLCT bands in the optical spectrum has gained interest

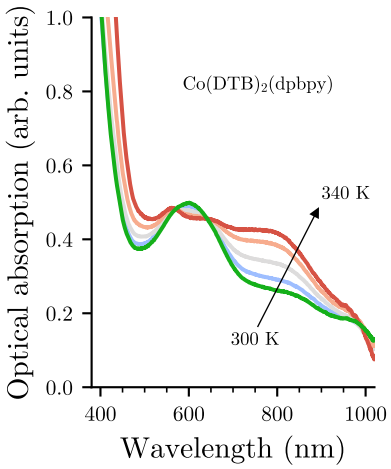

Figure 4.5: UV/Vis spectroscopy on $Co(DTB)_2(dpbpy)$, a cobalt VT compound which has a critical temperature above room temperature.

due to the possibility of light-induced VT. Broad bands have been observed for the photo-excitation, which implies that the exciting one of the mentioned bands inevitably leads to a photo equilibrium, in which neither a full LS nor HS-phase is accessible. Several similar complexes have been reported to present photo-reversible behavior, i.e., switchable by light [19, 110].

As previously mentioned, $Co(DTB)_2(dpbpy)$ represents a particular case among cobalt VT complexes since the critical temperature is higher than for most of the remaining compounds and above room temperature. The optical absorption spectrum is given in figure 4.5. Due to experimental constraints, measurements in toluene had to be undertaken at temperatures well below the solvent boiling point of 383.3 K [111]. Additional details regarding the measurement procedure are given in section 4.1.2 of the Bachelor thesis of Julia Rogalinski [112]. Despite the limited temperature range, similarities with the temperature-resolved UV/Vis spectra of the other VT complexes are observed for $Co(DTB)_2(dpbpy)$. As in the case of the cooled complexes, an intense feature at around 600 nm in the Co^{3+} LS phase loses intensity upon heating and LS to HS interconversion. Around 750 nm, a broad band in the Co^{2+} HS phase starts to appear. The dpbpy co-ligand in $Co(DTB)_2(dpbpy)$ also belongs to the group of polypyridine compounds. As in the case of the bpy- and phen-containing cobalt VT complexes, multiple narrow bands can be observed at around 560 nm and 655 nm in the HS Co^{2+} phase. This corroborates our initial hypothesis that the narrow bands in this region are specific to the cobalt complexes in our study with polypyridine-type ligands. Compared to the spectra in figure 4.4, the feature of $Co(DTB)_2(dpbpy)$ at 800 nm appears weaker at elevated temperatures. A possible explanation is the incomplete interconversion of the compound within the probed temperature range. This is attributed to the constraints mentioned above during the experiment.

In conclusion, we observe a strong and roughly 100 nm wide absorption band at 600-640 nm for the cobalt VT complexes in the Co^{3+} LS form, while the Co^{2+} HS

spectrum is dominated by a broad and asymmetric absorption feature at around 800 nm. The VT compounds with polypyridine type ligands exhibit additional narrow bands in the 550 - 650 nm region.

4.3.2 Bulk magnetic measurements

Prominent changes in the magnetic properties during VT transition is one of the most salient properties of VT complexes. Magnetic measurements on the bulk sample are an invaluable tool in the study of VT [16, 110]. In the present study, magnetic measurements presented implicit evidence that the VT behavior of the synthesized samples occurred as expected. The magnetic data is presented in figure 4.6. The figure shows the magnetic susceptibility for both solid-phase and liquid samples in toluene solution as a function of temperature. Solid lines indicate a fit of the magnetization data undertaken by S. Jannuzzi according to

$$I(T) = A + \frac{A - B}{1 + \exp\left[C\left(\frac{1}{T} - \frac{1}{T_{1/2}}\right)\right]}, \tag{4.1}$$

where A, B, and C are fitted constants, and $T_{1/2}$ the critical Temperature [113, 114]. For the fit on solid-phase $Co(DTB)_2(bpy)$, a fixed value of $T_{1/2}$ of 310 K has been used (cf. table 4.1). More details are given in an article manuscript pending submission [115].

The magnetic measurements indicate a solvent effect on the magnetic properties of the two investigated samples $Co(DTB)_2(tmeda)$ and $Co(DTB)_2(bpy)$. In the case

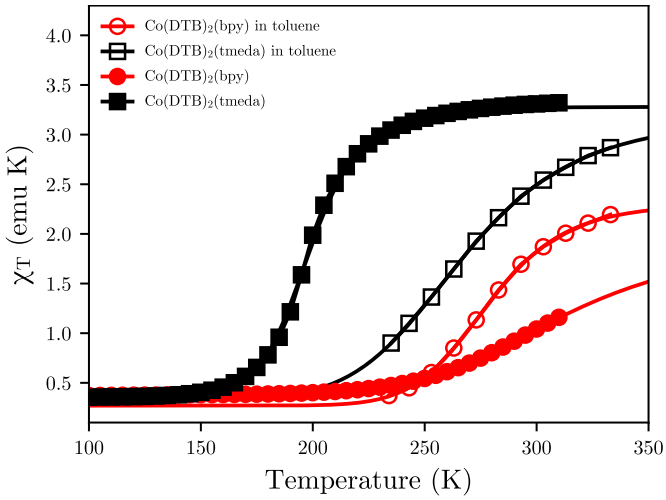

Figure 4.6: Magnetic susceptibility measurements on $Co(DTB)_2(tmeda)$ (red) and $Co(DTB)_2(bpy)$ (black). Both measurements in toluene solution (empty markers) and on solids (filled markers) are plotted. Courtesy of Dr. Sergio Jannuzzi and Fabian Otto from the Max Planck Institute for Chemical Energy Conversion, Mülheim an der Ruhr, Germany.

of $Co(DTB)_2$(tmeda), a shift of the critical temperature (as extracted per the fitting procedure) from 198.5 K to 267.4 K between the solid-phase and liquid sample in toluene solution can be observed. Contrary, for $Co(DTB)_2$(bpy), the critical temperature seems to shift to a lower temperature when in solution, from 310 K to 278.3 K. For $Co(DTB)_2$(tmeda) in toluene-solution, the transition appears to take place more gradually, compared to the solid phase, while the opposite is true for $Co(DTB)_2$(bpy). The observation that solvent effects influence the sample's bulk magnetic properties is essential for studying these compounds via time-resolved XES techniques, as it is likely that the metal spin is modulated by the solvent effect as well.

4.3.3 Concluding remarks on sample synthesis and handling

The synthesized VT samples $Co(DTB)_2$(tmeda), $Co(DTB)_2$(bpy), and $Co(DTB)_2$(phen) exhibit a sensitivity towards oxygen. This effect predominantly occurs when the samples are in solution, but we observed during this study that prolonged storage at ambient atmosphere conditions resulted in degraded (i.e., non-inter-converting) samples. Contributing to this is that the investigated VT samples require a remaining amount of solvent molecules to be present, even in the solid phase, to undergo VT transition [16], as discussed in section 2.4.4. We denote the evaporation of solvent molecules from the sample as a dominating factor of compound degradation during extended storage. In the experimental context, this requires sample storage in sealed containers, with ideally oxygen-deficient atmospheres.

Due to the limited available sample quantity for this study, no precise experimental data could be collected on the survival rate of these systems in air. We note a few qualitative corner points on sample resilience. It was found that low quantities of the studied systems in the solid phase did not exhibit VT anymore after storage in unsealed containers for six months. In toluene solution and when exposed to air, irreversible changes in the samples were noticed after less than 24h. In this case, a change in sample color from dark-green to light-yellow was observed for $Co(DTB)_2$(bpy). On the other hand, storage in N_2 or argon-filled containers with screw caps was sufficient to conserve the samples for more than six months, as implicitly confirmed by Kβ XES and UV/Vis optical spectroscopy.

4.4 Non-resonant X-ray emission spectroscopy

Mainline Kβ XES can deliver detailed information about the metal-covalency and metal spin-state [63, 68]. The dispersive von Hámos spectrometer geometry enables fast acquisition of complete experimental spectra, even on radiation-sensitive samples. To our knowledge, this promising experimental approach has not yet been used significantly to investigate the VT phenomena. In fact, an article by Liang et al. seems to be the only published experimental study reporting Kβ XES on cobalt-based VT complexes to date [18]. To investigate the potential for a XES study on VT complexes, we collected temperature resolved Kβ emission signals on the three cobalt VT complexes $Co(DTB)_2$(tmeda), $Co(DTB)_2$(bpy) and $Co(DTB)_2$(phen). An overview of the structure for these compounds is given in figure 4.3.

4.4.1 Experimental details

All experimental data in this section were recorded by use of Bragg-type X-ray spectrometers at synchrotron beamlines. Non-resonant X-ray emission spectroscopy (XES) data were collected under similar conditions at all beamlines. Namely, the monochromatic incident X-ray energy was initially calibrated against a cobalt foil and subsequently set to 8100 eV or 8300 eV depending on the beamline, corresponding to values well above the Co K-edge (7709 eV), thus avoiding any possible resonances. In the collection of Co Kβ XES data at CLÆSS, the spectrometer [116] was equipped with two Si(333) crystals set to Bragg angles around 50.8°, and a MYTHEN strip detector was used for photon detection. Inspection of the elastic line profiles at CLÆSS indicated a resulting energy resolution of about 1.3 eV. The XES measurements at PIPOXS were performed using a multi-crystal Johann-type spectrometer equipped with five Si(533) analyzers set to a Bragg angle of about 78.1°. The emitted photons were collected by a PILATUS 100K detector, and the resulting energy resolution was determined, also by inspection of elastic lines, to be approximately 1.5 eV. A multi-crystal dispersive spectrometer operating in von Hámos geometry was employed in the XES measurements at P64, [58] with a total of 8 Ge(444) analyzers placed in a Bragg angle of about 82.9°. A PILATUS 100K detector was used to detect the emitted X-rays and the elastic line profiles showed a final energy resolution of about 0.5 eV. This improved energy resolution is due to the larger Bragg angle in which the spectrometer operated. However, it does not significantly affect the comparison of non-resonant XES data. The collected XES data were corrected by the incoming intensity, and the energy was calibrated by inspecting the position of elastic reflections at different emitted energies. In the case of dispersive spectrometers, spectra were obtained by integrating the detector area along the non-dispersive direction. This step of the data-reduction process is similar to the time-resolved XES measurements in chapter 6 and has been described in more detail there. All XES spectra were normalized by setting the area under the curve between 7630 eV and 7680 eV to 1000. Datasets were binned to have a common energy step-size of 0.25 eV around the Kβ mainline and 0.48 eV in the VtC region, yielding slightly improved statistics for the weak-intensity features.

All VT complexes in this section were investigated in solid phase as powders, as obtained after recrystallization in toluene (cf. section 4.3).

4.4.2 Kβ XES on cobalt references

The Kβ line of cobalt exhibits an asymmetric main peak ($K\beta_{1,3}$) with a lower energy tail (Kβ'). In HS complexes, unpaired spin in the metal 3d orbitals increases the intensity in the Kβ' feature due to p-d exchange coupling (cf. section 3.2). We are beginning our discussion of mainline Kβ XES on the cobalt VT complexes with a survey of reference line shapes for a distinction of more subtle spectral properties.

Figure 4.7 shows the Kβ spectra of all reference compounds, grouped according to the strength of their Kβ' feature. As expected from their HS Co^{2+} configuration, $[Co(bpy)_3]Cl_2 \cdot 5\,H_2O$, $[Co(phen)_3]Cl_2 \cdot 2\,H_2O$ and $[Co(acac)_2]$ present a pronounced Kβ' feature at around 7637.5 eV. Similarly, CoF3, a Co^{3+} HS complex, presents this feature as well by virtue of the increased influence of the p-d exchange coupling for the HS d^6 configuration. $[Co(acac)_2]$ presents the most pronounced Kβ' feature, while $[Co(bpy)_3]Cl_3 \cdot 4\,H_2O$ and $[Co(phen)_3]Cl_3 \cdot 5\,H_2O$ exhibit the weakest intensity in this region. In the mainline region, an approximately 6.7 eV broad asymmetric peak is observed at around 7650.5 eV. The polypyridine-ligand complexes show almost overlapping line shapes and appear at approximately 0.5 eV lower energies than CoF3.

For the LS Co^{3+} compounds in the center panel, no pronounced Kβ' is observed. Instead, two weak features are visible for $[Co(acac)_3]$ (black arrows). This compound exhibits an octahedral coordination geometry as in the other complexes but was recorded with a slightly higher instrumental resolution due to the use of Ge(111) analyzer crystals in fourth-order reflection. The $K\beta_{1,3}$ mainline peak of all complexes appears significantly narrower (4.8 eV) and shifted towards lower energies (7649.6 eV).

The right panel in figure 4.7 displays LS Co^{3+} compounds of different coordination geometry. In the two spectral regions around 7638 eV and 7646 eV (marked by blue arrows), subtle line shape differences are observed. The LS Co^{2+} compound $[Co(terpy)_2]Cl_2$

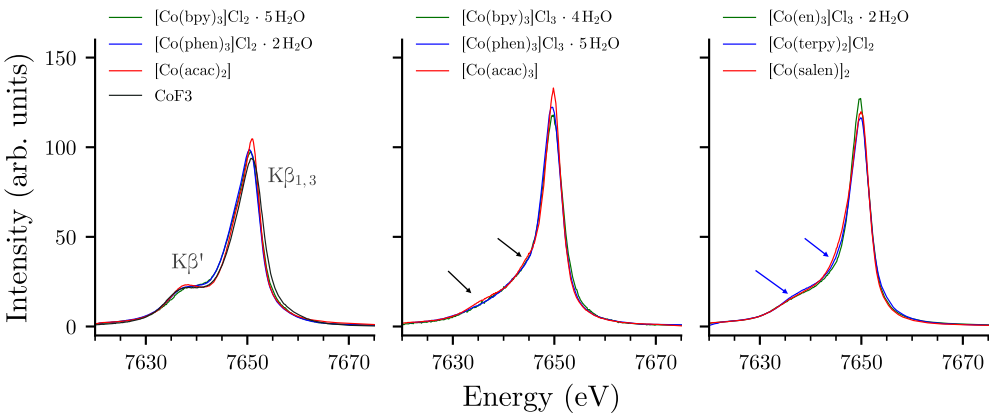

Figure 4.7: Kβ XES line shapes of cobalt compounds.

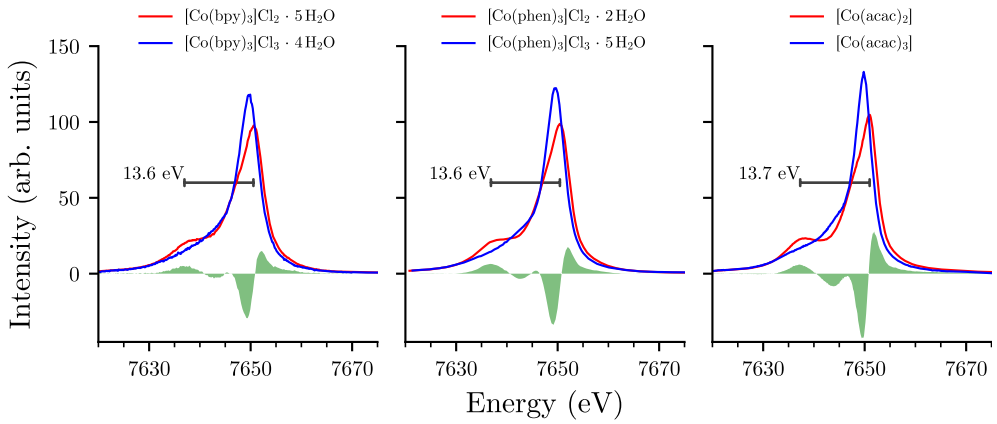

Figure 4.8: Kβ XES on reference sets of LS Co^{3+} and HS Co^{2+} compounds.

exhibits significant intensity in the Kβ' region.

Since we obtained the (bpy-), (phen-), and (acac-) compounds as pairs of samples with both Co^{3+} and Co^{2+} oxidation states, we are comparing the line shape differences in figure 4.8. The value for the Kβ'-$K\beta_{1,3}$ splitting of the HS curves is around 13.6 eV, as determined by inspection of the first feature of the difference signal, and the position of the $K\beta_{1,3}$ maximum in the Co^{2+} data. No reliable splitting values for the LS curves can be extracted by this method. While the separation of the Kβ' feature visually appears more pronounced for $[Co(acac)_2]$, the extracted value for the Kβ'-$K\beta_{1,3}$ splitting agrees within the energy step size of the reported spectra with the remaining complexes. It is plausible that the reasons behind the more pronounced Kβ' peak are rooted in the square-planar coordination geometry of this complex. The two tris-bpy and tris-phen datasets exhibit both a clear and pronounced Kβ' shoulder feature, albeit slightly weaker.

The difference curves for the investigated samples are shown in green in figure 4.8. Interestingly, in the difference curve for the (acac) compound in the right panel at around 7647.7 eV, we observe no intensity above zero. A possible explanation for this behavior is a different distribution of multiplet states in the lower energy region of the $K\beta_{1,3}$ peak.

4.4.3 Investigation of VT with temperature-resolved Kβ mainline XES

After we have outlined the general behavior of the Kβ mainline region in cobalt complexes, we are equipped for a discussion of the temperature-resolved measurements on complexes exhibiting VT.

From variable-temperature magnetic measurements, significant differences in the critical temperature $T_{1/2}$ of the VT complexes are known (cf. table 4.1). As introduced in section 2.4, the reduction potential of the co-ligand has been speculated to be a contributing factor to these differences. Additionally, unpaired electron spin in the redox-active ligand orbitals will couple with the metal d orbitals. The effect of these properties on the metal XES spectrum has not yet been extensively investigated for

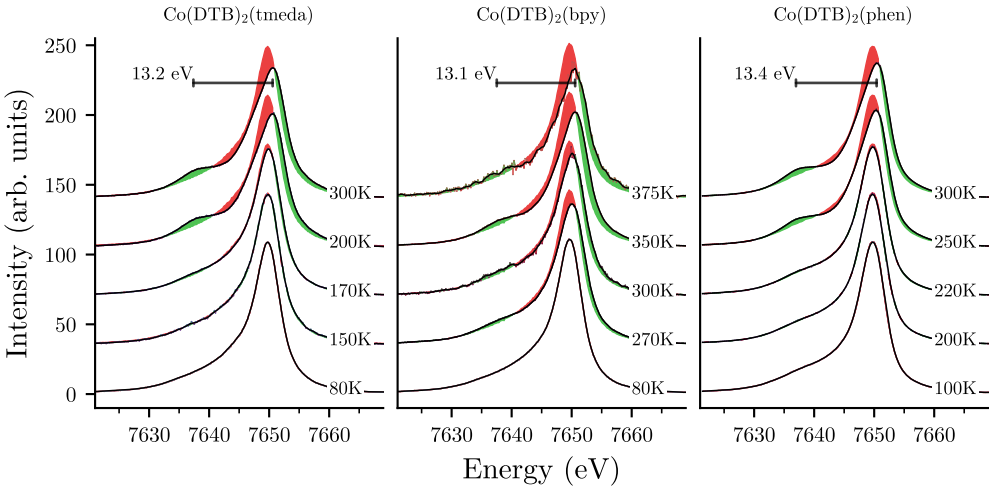

Figure 4.9: Temperature dependent Kβ XES on tautomer complexes. Solid line represents savitzky-golay filtered curves, the shaded area visualizes the difference to the lowest temperature curve recorded on each sample. Green shaded areas correspond to an increase in spectral intensity with respect to the reference spectrum, red areas signify a decrease. Spectra have been offset vertically for visual clarity.

complexes exhibiting VT.

Temperature-dependent Kβ mainline spectra for $Co(DTB)_2$(tmeda), $Co(DTB)_2$(bpy) and $Co(DTB)_2$(phen) are presented in figure 4.9. Upon cooling, similar behavior is observed for all three VT complexes. A characteristic decrease in intensity in the Kβ' region is accompanied by a shift toward lower energies of the $K\beta_{1,3}$ mainline peak, similar to the series of low-spin complexes presented earlier and in the literature [18]. The shift of the $K\beta_{1,3}$ mainline feature to lower energies is about 0.5 eV and goes along with an asymmetric reduction of the mainline width by about 2 eV. The extracted values for the Kβ'-$K\beta_{1,3}$ splitting are between 13.2 and 13.4 eV and approximately 0.4 eV smaller than for the cobalt references.

If a series of XES spectra S_j has been recorded as in the present case, changes in the Kβ line shape are regularly described via the integrated area difference (IAD) [68],

$$\mathrm{IAD}_j = \int_{E_1}^{E_2} |S_j(E) - S_{\mathrm{ref}}(E)|\, dE, \tag{4.2}$$

where a reference spectrum $S_{\mathrm{ref}}(E)$ is selected. To follow the evolution of the Kβ XES signature more intuitively, we are plotting the in figure 4.10, where the lowest recorded temperature spectrum was chosen as reference $S_{\mathrm{ref}}(E)$. The lowest value of each IAD curve was subtracted to reduce the influence of varying statistical noise. The magnetic susceptibility measurements from section 4.3.2 have been overlapped with the obtained IAD values. Due to the experimental requirements of X-ray emission spectroscopy, only a limited number of temperature points could be collected for each VT sample. The transition temperatures can thus not exactly be pinpointed based

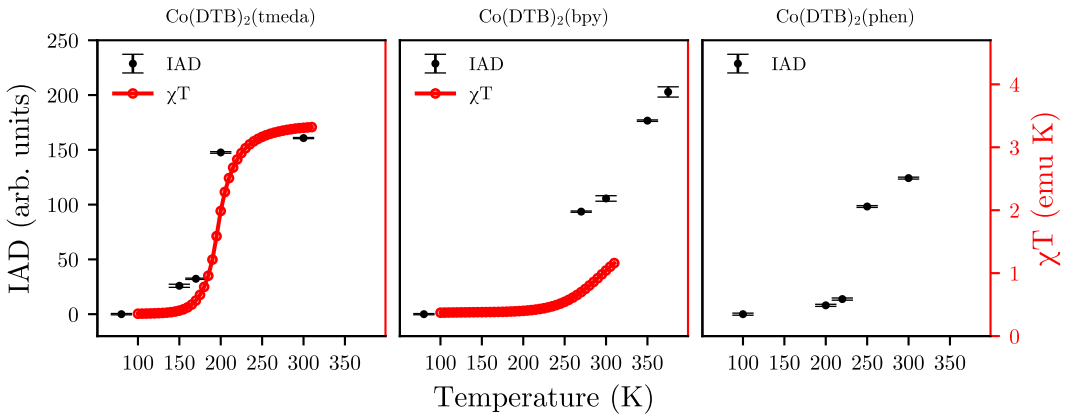

Figure 4.10: IAD of Kβ spectra on $Co(DTB)_2$(tmeda) (left), $Co(DTB)_2$(bpy) (center) and $Co(DTB)_2$(phen) (right). The IAD reference was chosen to be the lowest recorded temperature spectrum. Magnetic susceptibility measurements are plotted in red. IAD- (black) and susceptibility-values (red) are to scale, respectively.

on these data; for $Co(DTB)_2$(tmeda) however, the critical temperature as indicated by the IAD seems to agree with previously published experimental values [12] and are close to the transition behavior indicated by the magnetic susceptibility data. The IAD values of $Co(DTB)_2$(bpy) exhibit a clear deviation from the magnetic susceptibility measurement. The origin of this deviation is under investigation by extended-range magnetization measurements. We attribute this effect to either excess volatile toluene solvent molecules in the newly synthesized sample powder (potentially influencing the VT equilibrium) or differences in the method sensitivity towards VT. The smaller slope of the transition curve for $Co(DTB)_2$(bpy) observed in the magnetic susceptibility data is clearly present in the IAD values as well, indicating that the general VT behavior of the compound is correctly captured.

Both IAD and magnetization data verify that the transition between the two states in VT does not partake continuously, which, in addition to the published literature Adams et al. and Jung and Pierpont [16, 106] and the collected Kβ line shapes, provides own evidence that the observed process is indeed the targeted transition and distinct from purely structurally induced processes triggered by the lowered sample temperature.

A complimentary component-fitting-based assessment of the temperature behavior in these XES datasets was conducted in a Bachelor thesis by Julia Rogalinski [112]. The analysis agrees with the non-continuous transition shape mentioned above. Furthermore, comparison of Kα and Kβ XES data verified experimentally that the transition can be tracked via both emission lines, and agreement within approximately 30 K was found for $Co(DTB)_2$(bpy).

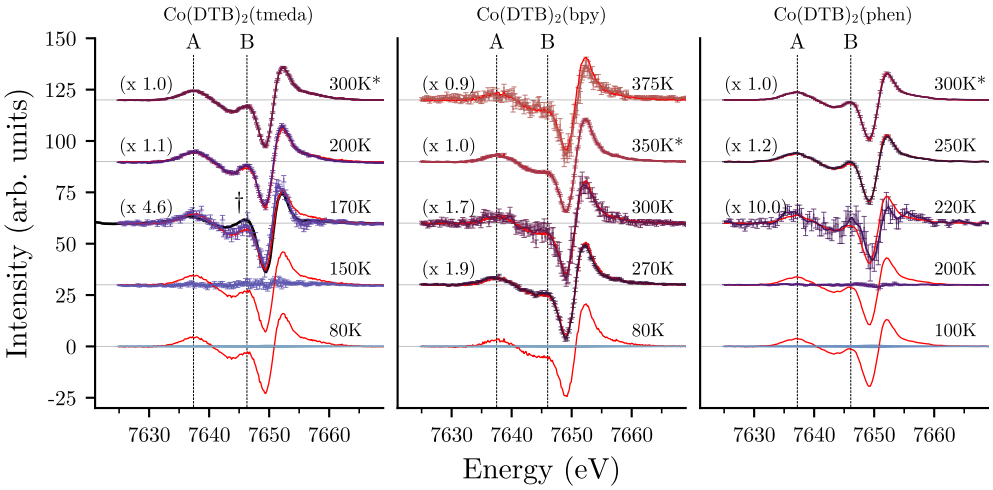

Figure 4.11: (Scaled) Kβ difference curves for $Co(DTB)_2(tmeda)$, $Co(DTB)_2(bpy)$ and $Co(DTB)_2(phen)$. Spectra recorded at different temperatures are offset vertically for clarity. Featured difference curves have been scaled to minimize the residual difference to a reference from the same set (red curve, *). The applied scaling factor is given in the plot. The black reference curve (†) is calculated with the tetragonally distorted compound $[Co(terpy)_2]Cl_2$ (see text).

While the inspection of the transition behavior via the IAD value is important for the verification of the temperature-resolved X-ray experiment, more information can be drawn from the inspection of the individual HS-LS difference curves, presented in figure 4.11. The overall line shapes of the Kβ difference curves follow the same general behavior for all VT complexes. A rise of the difference signal in the region of the Kβ' feature around 7637 eV (A) is accompanied by the signature of the $Kβ_{1,3}$ shift and broadening at around 7650 eV. We note variations between the Kβ differences curves of the VT compounds at around 7646 eV (B), where the $Co(DTB)_2(bpy)$ complex exhibits a slightly lower difference intensity, with no return above the zero line. The complexes $Co(DTB)_2(tmeda)$ and $Co(DTB)_2(phen)$ exhibit a more prominent feature in the discussed region. To investigate, if individual spectral regions of the Kβ difference curves vary during the temperature-induced VT transition, those spectra in figure 4.11 which exhibited significant (i.e. larger than uncertainty) features were scaled to fit a HS-LS reference from the same set. This was done with an optimization fit, which minimized the residual values between the reference curve and the scaled data by applying a constant scaling factor without offset. In the case of $Co(DTB)_2(tmeda)$ and $Co(DTB)_2(bpy)$, scaled differences agree in most cases with their references, as indicated by the overlap with the red curves within the measurement uncertainty. For $Co(DTB)_2(tmeda)$, a weak but significant deviation is observed in the 170 K curve, where the intensity in the high-energy tail of the $Kβ_{1,3}$ peak underestimates the reference. This is noteworthy since the Kβ' region of the remaining curve shows good agreement with the reference. The main peak signature instead seems to indicate a slight shift to lower energies. This

indicates that subtle electronic effects are picked up by Kβ XES during VT, which can not be explained by a simple two-state transition model. The presence of a Co^{2+} LS metal configuration state in VT, a natural potential explanation behind changes in the Kβ lineshape, has been previously speculated [30], but was not observed in the only other published Kβ XES study on $Co(DTB)_2(tmeda)$ [18]. A different curve between the Co^{2+} LS compound $[Co(terpy)_2]Cl_2$ and the HS Co^{2+} curve of $[Co(phen)_3]Cl_2 \cdot 2\,H_2O$ has been added to the plot (†). $[Co(terpy)_2]Cl_2$ is formal of octahedral coordination geometry but has been reported to exhibit a tetrahedral compression of the coordination octahedron. The obtained difference curve qualitatively agrees in the high-energy region of the $K\beta_{1,3}$ peak but fails to reproduce the remaining signal at lower energies. We hold that structural distortion of the coordination octahedron might be at work in this compound, as hinted by the black difference curve, and further investigation (e.g., via crystallography methods) is needed. In the case of $Co(DTB)_2(phen)$, overlap for the 200 K curve with the reference was less optimal than for the remaining set but within the reported measurement uncertainty. The fact that the scaled spectra overlap in the majority of cases indicates that no spectroscopically identifiable intermediate states for $Co(DTB)_2(bpy)$ and $Co(DTB)_2(phen)$ are populated by temperature conversion. In the context of the reported sensitivity of the Kβ XES emission lines towards the metal spin state, we conclude that intermediate metal spin states for these compounds are unlikely [18]. This agrees with the notion that the VT process is a chemically driven equilibrium between two species. The temperature-transition behavior for $Co(DTB)_2(tmeda)$ is under further investigation.

4.4.4 Ligand identity via valence-to-core spectroscopy

In the past decades, increasing interest in the VtC region of TMs has emerged. The use of VtC spectroscopy was further propelled by advances in the interpretation of these spectra, also based on theoretical calculation methods, enabling extensive experimental and theoretical studies revealing significant ligand character in the obtained data [51, 117, 118]. Multiple studies demonstrated scientific cases in which VtC spectra exhibited sensitivity towards ligand identity, the protonation state of neighboring dimers and the degree of bond activation [69, 70, 119–123]. The benefits of VtC spectroscopy have also been exploited in time-resolved experiments [124, 125].

Since the Kβ measurements presented in the previous section demonstrated that the capture of comparatively weak XES signals on sensitive VT complexes prove possible within the current measurement conditions, we investigated if a potential ligand identity in the VtC signal could be extracted in VT. For that, we recorded VtC spectra under identical conditions as described in section 4.4.1 for the cobalt VT complexes $Co(DTB)_2(tmeda)$, $Co(DTB)_2(bpy)$ and $Co(DTB)_2(phen)$.

Experimental spectra

As in the case of the $K\beta_{1,3}$ mainlines, we are beginning our discussion with an inspection of the VtC spectra of cobalt reference compounds. Co^{2+} and Co^{3+} complexes are shown in the left and center panels in figure 4.12. The right panel contains spectra from complexes with varying coordination geometry. In the VtC region, substantial variations in line shape can be observed. This spectral region is strongly influenced by both geometric effects, which modulate orbital overlap, as well as the electronic properties of neighboring ligand atoms (cf. chapter 3).

The VtC spectra for the polypyridine (phen-, bpy-) complexes appear similar, as expected, due to the comparable ligand environment. In the Co^{3+} LS form, both compounds exhibit a faint Kβ" feature and a strong, almost symmetric $K\beta_{2,5}$ peak. The HS Co^{2+} spectra contain no visible $K\beta_{2,5}$ feature and weaker, split $K\beta_{2,5}$ peaks.

The VtC regions of the (acac) complexes exhibit a strongly structured $K\beta_{2,5}$ double-peak structure, which shows an inverted ratio of peak intensities when compared to the (bpy) and (phen) complexes. In the LS Co^{3+} form, we observe a pronounced Kβ" feature at around 7685 eV. In the HS Co^{2+} form, the Kβ" is not clearly visible. Here, the $K\beta_{2,5}$ peak appears broader and weaker.

The VtC spectra of the octahedral Co^{3+} LS compound $[Co(en)_3]Cl_3 \cdot 2\,H_2O$ (right panel) exhibits a clear Kβ" feature. The Kβ" feature has been reported to generally arise due to overlap between ligand oxygen, nitrogen and carbon 2s and metal p orbitals [50, 119]. An increase of the Kβ" feature strength with an increasing metal oxidation state is thus rationalized by the shorter bond distances between the metal and ligand atoms. The $K\beta_{2,5}$ peak appears significantly narrower than the remaining complexes. In the same panel, the $K\beta_{2,5}$ region is very structured for $[Co(terpy)_2]Cl_2$, with a much stronger higher energy feature and a weaker intensity feature at slightly lower energies. The VtC spectrum of $[Co(salen)]_2$ is of lower intensity in general. In terms of shape, the spectrum

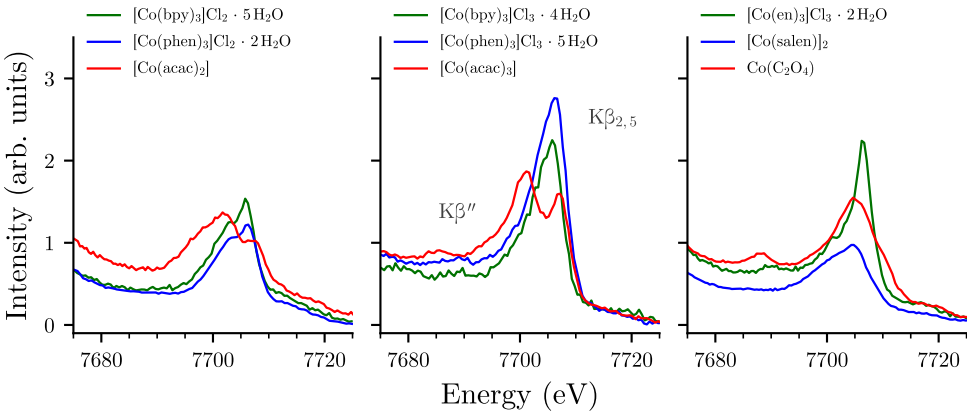

Figure 4.12: VtC XES line shapes of cobalt reference compounds. Spectra are grouped according to formal oxidation state (Co^{2+}, left panel; Co^{3+}, center panel) and by different coordination (right panel), cf. figure 4.1.

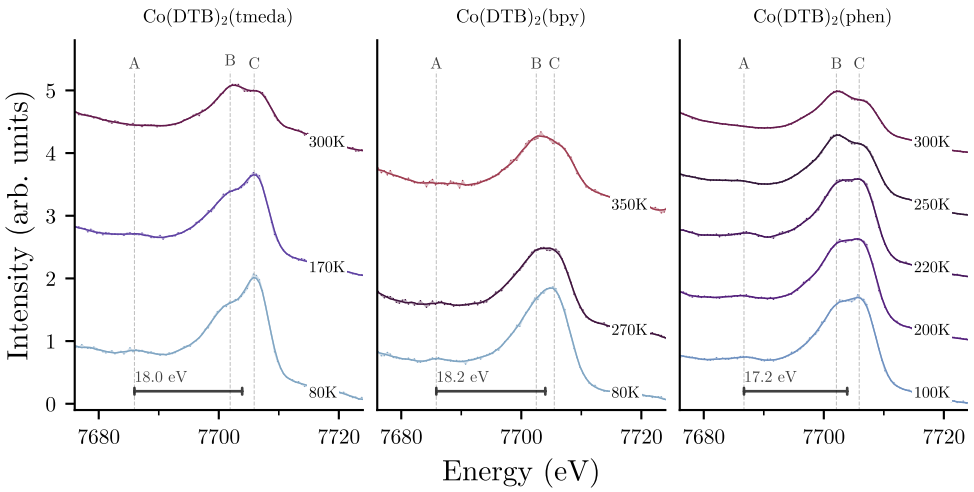

Figure 4.13: Experimental variable-temperature VtC XES on $Co(DTB)_2(tmeda)$, $Co(DTB)_2(bpy)$ and $Co(DTB)_2(phen)$. Curves have been offset for visual clarity.

follows the behavior of the remaining samples (except $[Co(acac)_3]$ / $[Co(acac)_2]$) and exhibits a more substantial higher energy feature in the $K\beta_{2,5}$ region, accompanied by a weaker intensity feature at slightly lower energies. The VtC region of the investigated samples exhibit 2 or 3 resolved features.

Equipped with a general overview of cobalt VtC line shapes, we are moving to the discussion of the experimental spectra in cobalt VT samples. The VtC spectra of $Co(DTB)_2(tmeda)$, $Co(DTB)_2(bpy)$ and $Co(DTB)_2(phen)$ at different temperatures are shown in figure 4.13. The VtC spectrum of $Co(DTB)_2(tmeda)$ resolves at least three distinct features (A, B and C) in the LS-phase. A weak Kβ" satellite feature, labeled as A, is visible at around 7685.95 eV. The $K\beta_{2,5}$ main peak in the VtC region of $Co(DTB)_2(tmeda)$ is composed of at least two features, situated at 7701.9 eV and 7705.9 eV. Notably, the intensity ratio between the two features in the high energy peak inverts when undergoing VT transition. The splitting between the A feature and the mean position of B and C is around 18.0 eV.

The separation of the main feature in the $K\beta_{2,5}$ region of $Co(DTB)_2(bpy)$ appears to be smaller compared to the splitting observed for the remaining VT complexes. At least two features are present as well, with energies at around 7702.5 eV and 7705.5 eV. The inversion of intensity ratio is observed as well. A weak lower energy peak is visible at 7685.9 eV in the LS-phase. Here, the A-BC splitting is around 18.2 eV.

The temperature-resolved VtC spectra of $Co(DTB)_2(phen)$ follow the same behavior as for the former two VT complexes. A weak Kβ" peak is visible in the low-temperature spectra at 7686.7 eV. The main peak at higher energies is composed of at least two features at 7702.1 eV and 7705.9 eV. As in the case of the other VT complexes, the intensity ratio in the high energy peak inverts upon transition. The splitting between A and the two higher energy features is 17.2 eV.

DFT calculated VtC spectra of VT compounds

VtC spectra are in general well reproduced via DFT calculations [51, 120]. DFT calculations on the cobalt VT systems investigated in this thesis were carried out by Esma Boydas from the group of Prof. Michael Römelt, Arbeitsgruppe Theoretische Chemie, Humboldt University Berlin, Germany, as part of a collaboration project. Details regarding the calculations are described by Otte and Boydas et al. in an article manuscript [115]. For the calculations, the ORCA software package version 4.2.1 was used [126].

For the analysis of the calculation results, we employed two major strategies. For the calculated molecular orbitals (MOs), a Mulliken orbital population analysis [127] can be requested in the ORCA output file. This provides a decomposition of each MO into its individual percentage atomic contributions. Since the element and coordinates of each atom are known, MO contributions can be sorted by ligand moiety (i.e., SQ, CAT or co-ligand). This distinction constitutes the first analysis step and is visualized with different rows in the following figures. The applied DFT approach further yields a set of transition intensities of the calculated VtC spectrum, for which the contributing MOs[1] are given. Together with the sorted list of individual atomic contributions to each MO, a complete decomposition of each calculated transition intensity can be constructed. We do this by multiplying the atomic percentage contributions with the corresponding MO contribution to the total intensity. This yields, in principle, absolute individual atomic contributions to each transition intensity (as extracted by Mulliken population analysis). For visualization, we group the results by ligand moiety and chemical element. Finally, we apply a 1 eV binning along the calculated energy axis. A further distinction by orbital character (s, p, or d type orbital) is also applied.

The MO analysis for the singlet d^6 Co^{3+} configuration (LowT) of compounds $Co(DTB)_2$(tmeda), $Co(DTB)_2$(bpy) and $Co(DTB)_2$(phen) is shown in figure 4.14. Upon comparison with the experimental spectra at low temperatures (solid black line), the overall spectral shape is found to be well reproduced. As typical in DFT calculations, the absolute energy axis is not accurately calculated and must be calibrated against experimental data [128]. In the present case, the spectra were shifted by a constant energy offset of 49.32 eV in order to align the low-temperature $K\beta_{2,5}$ peak feature.

The described weak Kβ" peak around 7686 eV (feature A) is reproduced in the calculations and identified to consist of transitions from SQ/CAT oxygen 2s MOs. Small contributions from carbon and the nitrogen atoms on the co-ligand are also present. The theoretical values for the splitting between the A feature and the two higher energy features are 16.8 eV for $Co(DTB)_2$(tmeda), 16.2 eV for $Co(DTB)_2$(bpy) and 16.1 eV for $Co(DTB)_2$(phen). These values are around 10 % smaller than the experimentally observed splittings.

The intensity ratio between the B and C features is qualitatively well reproduced, with the C feature exhibiting the highest intensity in the low-temperature state. As

[1] In this DFT approach for the calculation of VtC spectra, the donor orbitals are allowed to vary, while the acceptor orbital is fixed to the 1s shell. The fundamental approach is described in more detail in the ORCA manual [127].

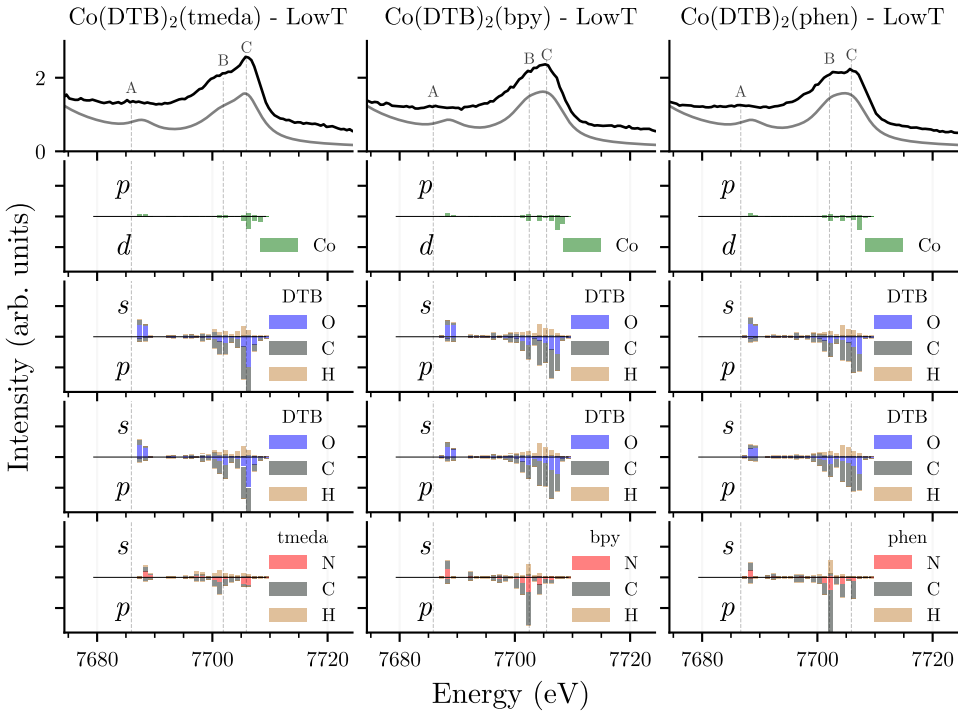

Figure 4.14: MO analysis of LowT state contributions to transition intensities in the VtC region of $Co(DTB)_2(tmeda)$, $Co(DTB)_2(bpy)$ and $Co(DTB)_2(phen)$. The dark grey line visualizes the total broadened calculated spectrum (all moieties, elements and shells), black solid lines give the experimental data (vertically offset for clarity). The intensity axis of all calculation results has the same range. The DTB ligand label refers to either the SQ or CAT form of 3,5-di-tert-butyl-o-benzoquinone. DFT calculation data courtesy of Esma Boydas, Humboldt University of Berlin.

in the experimental spectrum, the B feature of $Co(DTB)_2(tmeda)$ is of slightly lower relative intensity when compared to the other VT complexes. In the bottom row of figure 4.14 we find a reason for this in the varying influence of the co-ligand. Specifically, a strong contribution to the B / Kβ_2 feature is observed for the polypyridine complexes, which is absent for $Co(DTB)_2(tmeda)$. We conclude that the VtC region in the LS-state thus exhibits a moderate specificity toward the co-ligand, which might be exploited in further experiments (e.g., in VtC-detected XAS). The redox-active DTB ligand in figure 4.14 denotes either the SQ or CAT form of 3,5-di-tert-butyl-o-benzoquinone. For these two ligands, significantly more intensity is found in the C / Kβ_5 region. This coincides with cobalt 3d orbital character at similar energies (as depicted in green), and we hold that the Kβ_5 feature might present a sensitivity toward a coupling between the redox-active ligand and the metal d orbital set t_{2g} / e_g. We note, however, that the experimental distinction of coupling schemes based on VtC XES seems unlikely. The energy-splitting of the different spin-coupling states between the metal and redox-active ligands has been predicted to be low, consequently leading to a simultaneous population

of all states [16].

Finally, we note that there is no clear distinction between the intensities calculated for the two redox-active ligands, even though, as seen in crystallography experiments, one ligand should exist in CAT form while the other remains SQ [16]. The reasons behind this are under further investigation.

We are continuing our discussion with calculations for the HS Co^{2+} case. As introduced in section 2.4, the different spin-coupling states of the cobalt VT complexes are labeled according to their central metal ion spin-state[2] (either doublet D or quartet Q). The calculated spectra for the metal quartet d^7 Co^{2+} states (Q) of $Co(DTB)_2(tmeda)$ are given in figure 4.15. In agreement with the experiment, intensities in the VtC region are weaker overall. This agrees with the notion that bond distances between the metal ion and the ligand atoms are larger in Co^{2+} complexes, and the orbital overlap,

[2]The analysis in this section will be concerned with the Q states only. Graphs for the D states are given in the appendix D.

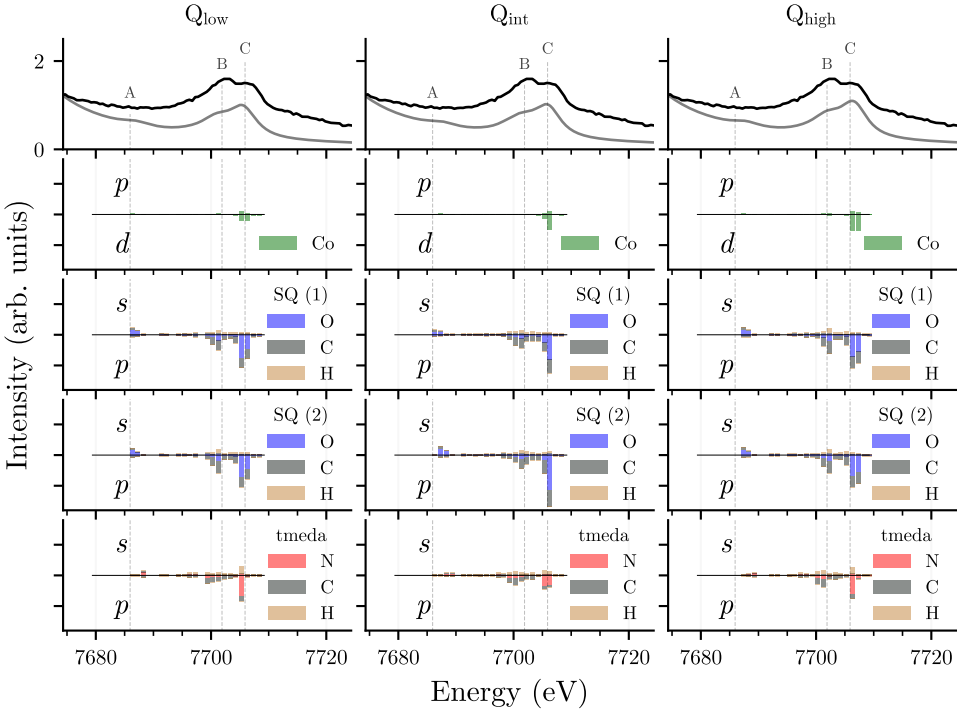

Figure 4.15: Analysis of contributions to transition intensities in the VtC region of $Co(DTB)_2(tmeda)$ for a quartet (Q) metal configuration. Low, int and high describe the ligand spin coupling with the metal. The dark grey line visualizes the total broadened calculated spectrum (all moieties, elements and shells), black solid lines give the experimental data (vertically offset for clarity). The intensity axis of all calculation results has the same range. DFT calculation data courtesy of Esma Boydas, Humboldt University of Berlin.

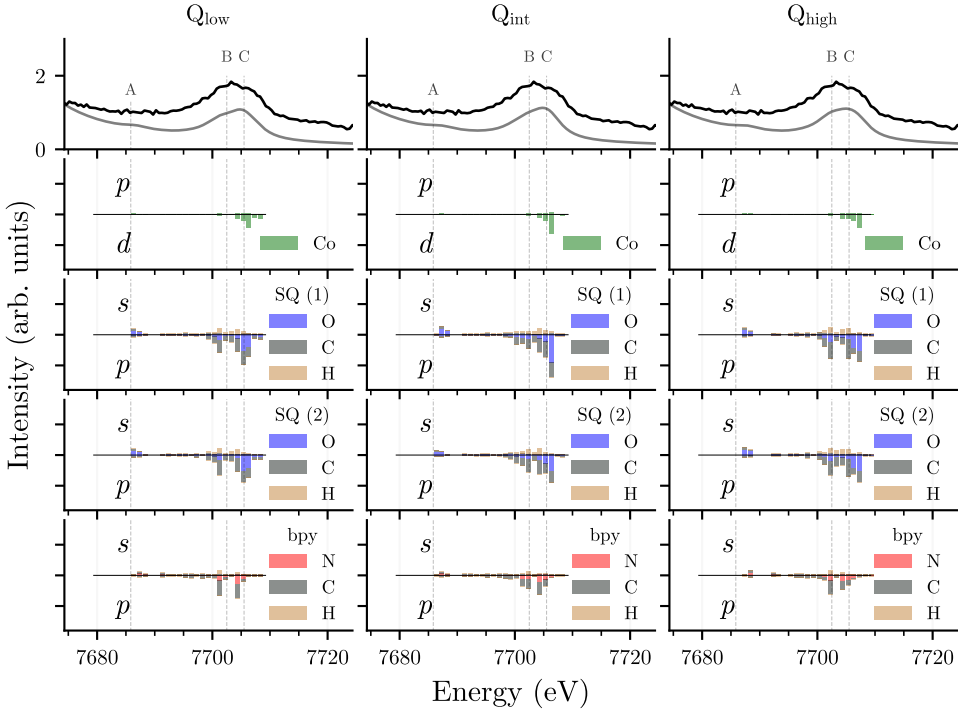

Figure 4.16: Analysis of contributions to transition intensities in the VtC region of $Co(DTB)_2(bpy)$ for a quartet (Q) metal configuration. Low, int and high describe the ligand spin coupling with the metal. The dark grey line visualizes the total broadened calculated spectrum (all moieties, elements and shells), black solid lines give the experimental data (vertically offset for clarity). The intensity axis of all calculation results has the same range. DFT calculation data courtesy of Esma Boydas, Humboldt University of Berlin.

contributing to the Kβ" and $K\beta_{2,5}$ features, is decreased. As described earlier, we experimentally observe an inversion of intensity for the features in the $K\beta_{2,5}$ region. Interestingly, this trend is not reproduced in the DFT calculations. We note that the reproduction of correct relative intensity ratios can not be expected for this method, and other studies with a similar DFT-based methodology on iron complexes exhibited similar deviations [120]. However, we hold that the calculated intensity for the SQ ligands is still predominantly found in the C feature region. The differences in calculated line shape for the different spin-coupling schemes turn out to be minimal. Intuitively, this agrees with the previously discussed prediction of minor energy differences between the spin-coupling states, which are thus unlikely to correspond to vastly different molecular structures (and hence spectra). Finally, we find, as for the LS spectra, that intensities in the Kβ" region carry mostly 2s ligand character, while the $K\beta_5$ peak seems to be dominated by ligand 2p and cobalt d character.

The calculated HS spectra of $Co(DTB)_2(bpy)$ and $Co(DTB)_2(phen)$ are shown in figures 4.16 and 4.17. Structurally, the main difference is the presence of the polypyridine

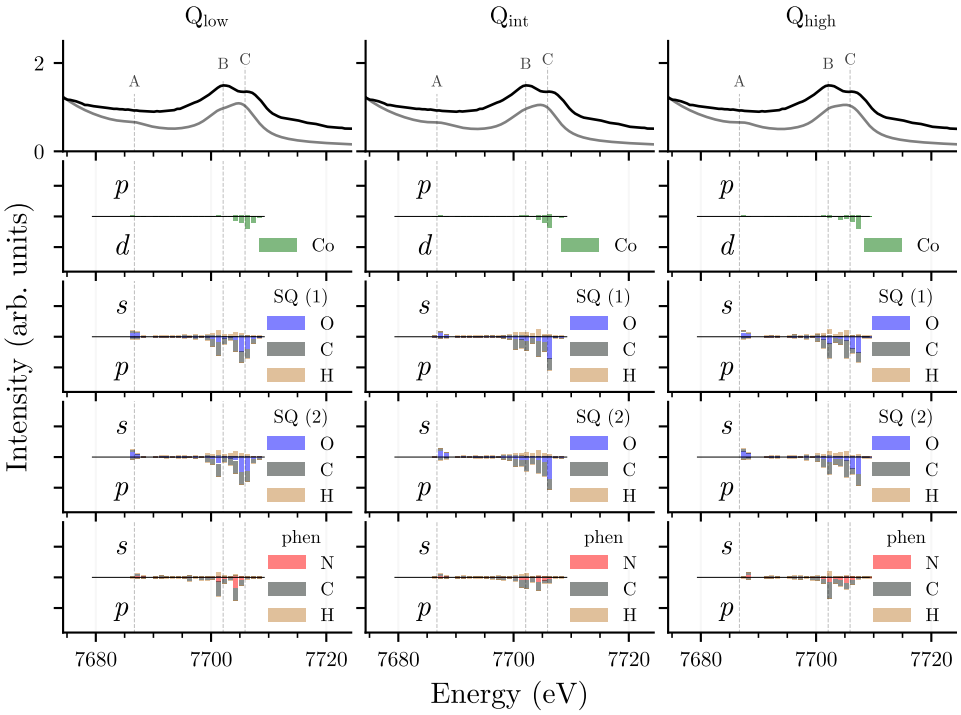

Figure 4.17: Analysis of contributions to transition intensities in the VtC region of $Co(DTB)_2(phen)$ for a quartet (Q) metal configuration. Low, int and high describe the ligand spin coupling with the metal. The dark grey line visualizes the total broadened calculated spectrum (all moieties, elements and shells), black solid lines give the experimental data (vertically offset for clarity). The intensity axis of all calculation results has the same range. DFT calculation data courtesy of Esma Boydas, Humboldt University of Berlin.

co-ligand instead of (tmeda). In the LS spectra, we found transitions involving the co-ligand predominantly in the B feature region. This trend is not reproduced here. The reasons behind this are currently under investigation and require further analysis of the optimized molecular structures.

The low-temperature calculations hinted toward a separation of orbital contribution (features B and C) in the main $K\beta_{2,5}$ feature of the VtC region. This prediction might be accessible experimentally by using VtC RXES in the way of more elaborate studies on the ligand electronic structure. A study by Hall et al. on Mn compounds successfully demonstrated the use of this technique [117].

4.5 Targeting oxygen in redox-active ligands

In the case of the investigated cobalt dioxolene VT complexes, redox-active ligand forms of 3,5-di-tert-butyl-o-benzoquinone are coordinated via two oxygen atoms to the central cobalt ion. As introduced in section 2.4.1, the LUMO with π^* character accepts charge during the redox-series from the electronically neutral quinone Q to the singly reduced semiquinone SQ^{-1} to CAT^{-2}

$$Q \overset{e^-}{\leftrightarrow} SQ \overset{e^-}{\leftrightarrow} CAT. \tag{4.3}$$

The LUMO of these compounds has been reported to exhibit significant (inter-ligand) delocalized character, with electronic charge residing on the oxygen and carbon atoms of the central benzoquinone ring [30]. MO analysis by Adams, Noodleman, and Hendrickson and [129] still showed that a considerable amount of contributions to the LUMO in benzoquinones stems from the oxygen atoms. We note that the only coordinated oxygen in the studied VT complexes is situated in the first coordination shell of the cobalt ion and attributed to the described ligand variants (assuming no significant amount of oxygen is present in the solvent as in the case of toluene). We are investigating how targeting oxygen via element-specific methods could provide a sensitive probe toward the ligand electronic structure and VT state during transition. The premise is that the oxygen atoms indirectly indicate the state of the vacant quinone π^* orbital [28]. An experimentally well-studied spectral signature can be found at the oxygen K-edge at around 530 eV studied by XAS [130]. The general K-edge structure of oxygen in molecules follows a separation of the oxygen π^* type orbitals and the main σ^* feature [130]. We utilized electronic structure calculations to predict oxygen K-edge spectra in the benzoquinone ligands.

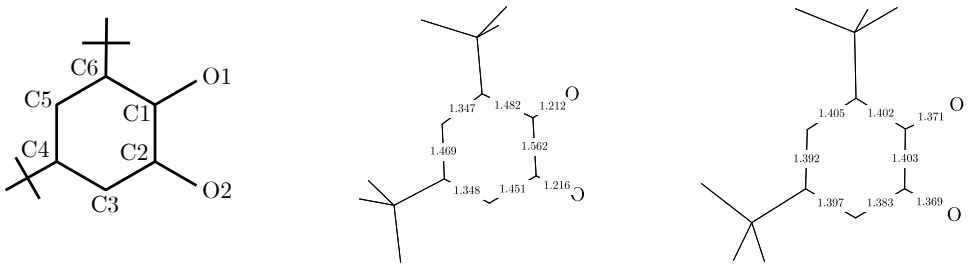

(a) Atomic labels **(b)** Q **(c)** CAT

Figure 4.18: Atomic labels used in the description of Q/CAT (a) and bond lengths (in Å) for DFT-optimized structures on Q and CAT (b, c). Hydrogen atoms are not shown. Importantly, two additional hydrogens are bound to the oxygen atoms in the model for the catecholate (CAT) form.

4.5.1 TD-DFT calculations of the oxygen K-edge

The electronic structure and general DFT procedures on benzoquinones and 3,5-di-tert-benzoquinones have been described by Adams, Noodleman, and Hendrickson and Wheeler, Rodriguez, and McCusker [30, 129]. Wheeler, Rodriguez, and McCusker benchmarked DFT calculations on 3,5-di-tert-butyl-o-benzoquinone using the B3LYP functional and found that it reproduced the experimentally obtained crystal structure for the related 1,2-benzoquinone compound (absent tert-butyl groups) satisfactorily.

We used the ORCA software package to optimize the molecular structures of 3,5--di-tert-butyl-o-benzoquinone (Q) and 3,5-di-tert-butylcatechol (CAT) with DFT for a subsequent calculation of the K-edge of oxygen. The starting geometries were obtained from X-ray crystallography measurements conducted on 1,2-benzoquinone [131] and edited with the Avogadro molecular editor [132] to include the tert-butyl groups. The optimized structures are presented in figure 4.18 together with the interatomic distances of relevance. Upon reducing the quinone form to catechol, characteristic changes in the C-C and C-O bond lengths have been observed experimentally. These changes are characterized by increased C-O distances and the carbon ring's overall more aromatic nature. The optimized structures reflect this behavior well, with the CAT form having more uniform bond lengths in the carbon ring, which fit the aromatic nature of the catechol, and elongated single-bound-like C-O distances. Since no crystallographic data was reported for CAT by Macdonald and Trotter, we report the average deviations between the optimized structures of Q. The average deviation of calculated structures from the experiment data is 0.004 Å for the C-O bond distances and 0.013 Å for the C-C bond lengths. A complete list of the obtained bond lengths and the molecular structure coordinates are given in table 8 in the appendix.

MO obtained from a GS DFT calculation in the optimized structure of 3,5-di-tert--butyl-o-benzoquinone are shown in figure 4.19. The orbital character of the inspected valence orbitals is in good agreement with the previously reported MOs on benzoquinone complexes [129]. This gives us confidence that the optimization converged to a sensible

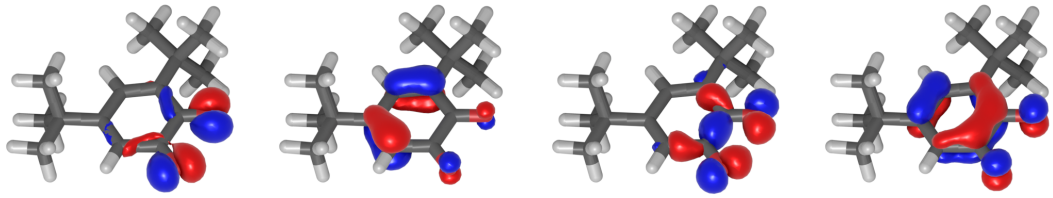

(a) σ (HOMO-2) **(b)** π (HOMO-1) **(c)** σ (HOMO) **(d)** π^* (LUMO)

Figure 4.19: Frontier orbitals of 3,5-di-tert-butyl-o-benzoquinone, calculated with DFT. The orbital character was assigned analogously to the electronic structure of o-butyl-benzoquinone reported by Adams, Noodleman, and Hendrickson and Wheeler, Rodriguez, and McCusker [30, 129].

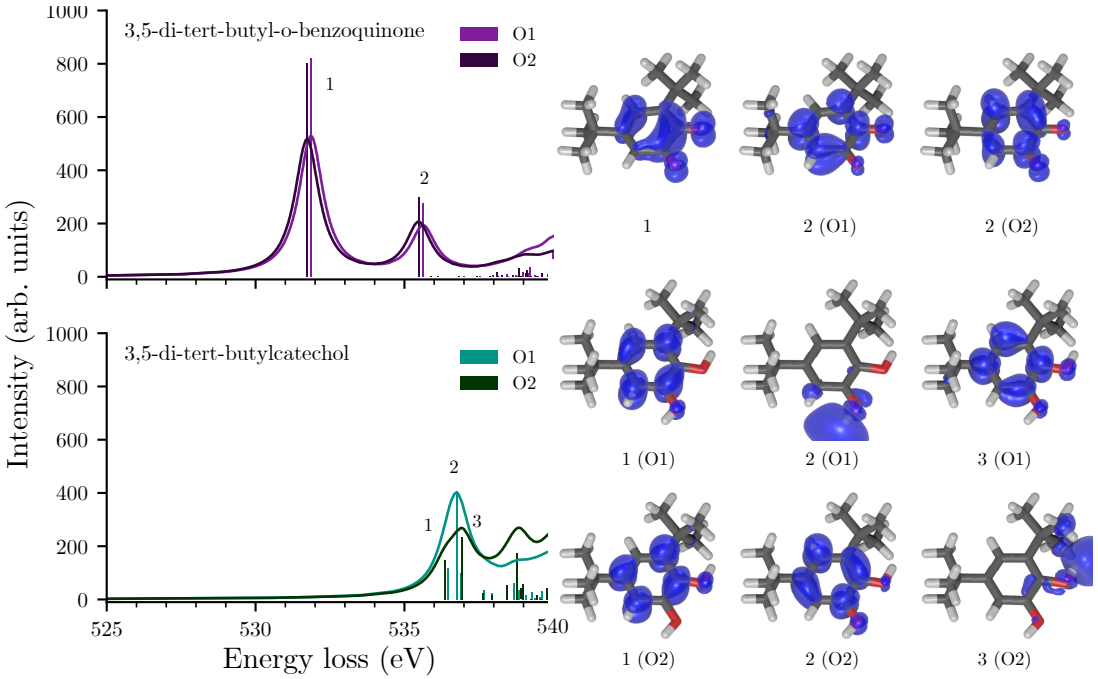

Figure 4.20: TD-DFT calculations on 3,5-di-tert-butyl-o-benzoquinone and 3,5-di-tert-butylcatechol at the oxygen 1s absorption edge. MO isosurfaces illustrate the electron density differences of the first excited states. The energy axis of the calculated spectra has been shifted by a constant offset of 16.6 eV.

GS electronic and molecular structure. The MO of the CAT form exhibited a similar structure and did not exhibit significant differences in electronic charge distribution besides the shift in highest occupied molecular orbital (HOMO)-LUMO assignment. This behavior agrees with the observation by Wheeler, Rodriguez, and McCusker that the spatial distribution of the MOs does not change significantly with increasing oxidation and the Aufbau principle holds. Atomic contributions and orbital energies change slightly. More details regarding the DFT and subsequent time-dependent density functional theory (TD-DFT) calculations are given in appendix J.

We undertook four separate TD-DFT calculations on the individual oxygen atoms of Q and CAT using the B3LYP functional. The calculated intensities and the broadened spectra are presented in figure 4.20, next to the corresponding electron density difference maps on the right. The calculated pre-edge region of 3,5-di-tert-butyl-o-benzoquinone (top panel in figure 4.20) exhibits two distinct features (labeled 1 and 2). An intense peak at 531.7 eV is accompanied by a weaker peak at ca. 3.6 eV higher energies. The corresponding electron density difference map for the first peak feature does not exhibit significant differences between the two oxygen atoms and is associated with a transition into the compound's π^* LUMO orbital (cf. figure 4.19). The electron density difference maps of the second feature appear similar but mirrored. As expected from the fully occupied π^* orbital ion 3,5-di-tert-butylcatechol (lower panel of figure 4.20),

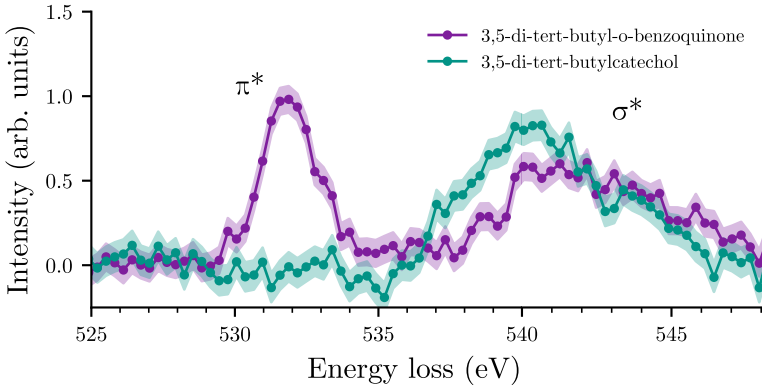

Figure 4.21: X-ray Raman scattering energy-loss spectra of ligand systems at the oxygen 1s absorption edge. A Voigt peak has been fitted to the pre-edge region and subtracted as Compton background. Shaded areas give the standard error of the mean of all averaged scans.

no feature around 531.7 eV is observed. The inspection of a family of transitions around 536.5 eV indicates that those transitions resemble those originating feature (2) on the Q compound. The electron density difference maps for (2) in O1 and (3) in O2 have no equivalent in inspected density differences of 3,5-di-tert-butyl-o-benzoquinone.

Based on the TD-DFT results, we expect the oxygen K-edge to provide a sensitive probe of the redox state for the benzoquinone derivates and thus the overall VT state of the coordination complex.

4.5.2 Oxygen K-edge energy-loss spectra via X-ray Raman scattering

In the field of Earth sciences, studies on the oxygen K-edge are commonly undertaken via X-ray Raman scattering (XRS) [133]. The XRS experiment records the energy of scattered photon radiation from the sample as a function of incoming photon energy, commonly with an X-ray spectrometer [46]. An energy-loss (EL) spectrum is then obtained by tuning the spectrometer to fixed energy at a specific EL value below the incoming energy, which covers the investigated energy domain during scanning (e.g., the oxygen 1s core level excitation). This allows the use of hard X-ray radiation to capture light element absorption edges, which fall into the soft X-ray realm. One benefit of using hard X-ray radiation for measurement is the possibility to record both XES and XRS on the metal complexes simultaneously [133]. This dual acquisition can be achieved by selecting the incoming photon energy and the acquisition of the EL spectra to be above the metal absorption edge. We investigated the feasibility of an XRS experiment on the cobalt-based VT complexes by exploratory oxygen K-edge energy-loss spectra on 3,5-di-tert-butyl-o-benzoquinone and 3,5-di-tert-butylcatechol. Experimental spectra were collected at the GALAXIES beamline, SOLEIL, Paris, France [134] and are shown in figure 4.21. The general experimental layout and details regarding the sample environment are given in appendix K.

The oxygen pre-edge region of 3,5-di-tert-butyl-o-benzoquinone exhibits a distinct peak structure at 531 eV. The intensity does not fully return to the baseline level after the peak, hinting at a second weaker feature in the region around 536 eV. The intrinsically low signals in XRS measurements the signal statistics and the relatively modest resolution obtained by the measurements with around 10 keV incident energy (simultaneous cobalt XES measurements required the incoming energy to be above the Co K-edge at 7709 eV) does not allow us to identify this second peak unequivocally. Future experiments with improved resolution and higher counting statistics could address this. The oxygen K-pre-edge region of 3,5-di-tert-butylcatechol does not exhibit any distinct structures until the onset of the main rising edge at around 537 eV. Based on the previously presented TD-DFT calculations, we interpret our XRS spectra as having 1s-LUMO transitions in the pre-edge region of the Q compound. The absence of the feature in the energy-loss spectrum for 3,5-di-tert-butylcatechol corroborates this notion. The capture of XRS spectra on the full cobalt VT is foreseen for a future experimental campaign. The use of XRS in a combination of XES allows tracking the spin-state of the cobalt metal ion via Kβ emission (thus confirming the temperature-induced transition) while capturing the variation in LUMO occupation on the benzoquinone redox-active ligands as a function of temperature.

The measurement of the oxygen K-edge is also possible with soft XAS. Experimentally, the study of VT complexes with X-ray photon energies in the sub 1 keV regime implies severe restrictions on the sample environment and requires careful setup planning. Generally, air atmosphere under ambient pressures is not feasible. Moreover, windows and other sample environment components must be sufficiently transparent to the soft X-ray photons. Additionally, since the cross-section for X-ray photons in the soft X-ray regime is larger than for hard X-rays, increased care has to be taken in not inadvertently converting the compound via X-ray induced VT [135]. Nevertheless, soft X-ray techniques still present a promising approach to studying the oxygen and nitrogen electronic structure in these compounds [136].

For completeness, we mention that electron energy loss spectroscopy (EELS) offers another possibility for the experimental acquisition of oxygen K-edge spectra [137].

4.6 Chapter summary and outlook

In this chapter, non-resonant XES studies on a family of cobalt dioxolene VT complexes were presented. In the $K\beta_{1,3}$ difference curves, variations in the line shapes, most dominantly at emission energies around 7646 eV, were observed among the VT complexes.

The influence of the solvent nature in VT complexes has been previously discussed in the literature [26, 40, 105]. Evangelio et al. and Caneschi, Cornia, and Dei indicated that the solvent environment most likely modulates the entropy factor as given in eq. (2.2) for the Gibbs free energy, as introduced in section 2.4 [26, 138]. A systematic study on XES line shape variations as caused by the solvent-induced modulation of the thermodynamic VT equilibrium should allow for more insight into the interplay between chemical (solvent) environment and metal configuration for the important Kα (1s2p) and Kβ (1s3p) X-ray emission signatures. This holds especially true for TM complexes, where Kβ XES is used extensively to assess metal spin-state. Furthermore, the influence of the solvent environment on the metal-ligand spin-coupling and the ligand-ligand coupling has not been targeted with suitable XES methods to our knowledge.

As presented in the last section, TD-DFT calculations on the oxygen K-edge of the benzoquinone redox-active ligands indicate a sensitivity towards the occupation of the LUMO of the benzoquinone ligands. XRS energy-loss spectra recorded on the ligand models 3,5-di-tert-butyl-o-benzoquinone and 3,5-di-tert-butylcatechol revealed that a similar feature is captured experimentally, and the general behavior is well reproduced by the TD-DFT calculation results. A combined XES and XRS experiment on the complete complex would provide a complementary picture of the VT process: while Kβ emission lines are most sensitive toward the localized metal (spin-)configuration, measurements on the oxygen K-edge may provide direct access to charge (de-)localization on the redox-active ligands. Due to the low cross-section of the XRS process and the resulting increased integration times, this would require solving multiple experimental challenges. A well-planned and efficient sample scanning technique will drastically reduce the radiation exposure per molecule. A fast photon-beam shutter and a continuously scanning monochromator would further reduce the deposited radiation dose while maintaining the same signal statistics. A challenge arises if both sample and monochromator need to be scanned during the data acquisition. Monochromator scanning is commonly required during the acquisition of energy-loss spectra in XRS experiments since the crystal analyzers are tuned to a fixed energy [46]. This technique sets high requirements for normalizing individual scan points since the insufficient correction of inhomogeneities in the sample volume will lead to a distortion of the experimental spectrum.

An alternative approach to collecting inelastic scattering spectra using a von Hámos spectrometer has been presented by Szlachetko et al. [139]. The fundamental concept of the collection of XRS spectra with a von Hámos spectrometer is shown in figure 4.22. The benefit of dispersive acquisition of IXS spectra lies in the single-shot nature of the obtained spectra, which allows for the collection of complete IXS spectra for each detector acquisition step without the need to scan the monochromator, albeit at a significantly worse signal-to-noise ratio. These benefits also have implications for potential applications in time-resolved experiments, where the von Hámos geometry has

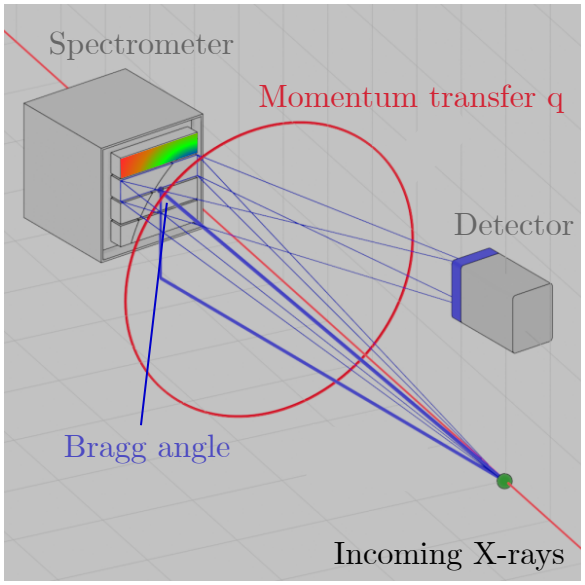

Figure 4.22: An XRS experiment with a four-analyzer von Hámos spectrometer in forward scattering geometry. The blue triangle indicates the vertical Bragg reflection plane for the energy-dispersive selection of X-radiation. The red circle visualizes a constant momentum transfer q on the scattering cone, which intersects with the crystal analyzer surface and leads to a radial gradient of q values.

already proven to ease the collection of non-resonant XES spectra [139, 140]. In the context of IXS studies on cobalt VT complexes, this approach allows collecting oxygen K-edge energy-loss spectra without the need for monochromator scanning.

Chapter 5

Temperature-induced VT via RXES and XAS

X-ray absorption spectroscopy (XAS) measurements in combination with TD-DFT calculations have been used extensively for the elucidation of chemical properties in TM complexes [128, 141, 142]. The TD-DFT method is helpful in calculating transition intensities for metal absorption edges and allows the interpretation of experimental spectra based on a molecular orbital model picture, as described in the previous chapter. The metal K-pre-edge exhibits great value for the probing of valence electronic properties such as metal d-level configuration and splitting, as well as distortions of the coordination polyhedron [143]. In the following, we investigate this important spectroscopic region for the previously introduced cobalt VT complexes. We will first introduce the applied methodology by discussing the XAS spectra of cobalt reference compounds. Subsequently, measurements of the cobalt VT complexes will be presented. Combining conventional XAS with the energy-dispersive detection of emitted X-ray emission signals (resonant X-ray emission spectroscopy (RXES)) may offer an increased resolution of close or overlapping spectral features. To explore the sensitivity of 1s3p RXES toward several broad and overlapping pre-edge features identified in conventional XAS, pre-edge RXES maps will be presented in the second half of the chapter.

5.1 X-ray absorption spectroscopy

We recorded experimental XAS spectra at the cobalt K-pre-edge on a series of cobalt reference compounds at the CLÆSS beamline at ALBA synchrotron, Barcelona, Spain [116], and at the PIPOXS beamline, CHESS, Ithaca, United States [144]. The incident photon energy was selected by a double-crystal monochromator equipped with either Si(111) crystals (PIPOXS) or Si(311) crystals (CLÆSS). A cobalt foil scan was used for the initial calibration of the incoming photon energy. XAS measurements were taken in transmission mode with two ionization chambers placed in front and behind the sample.

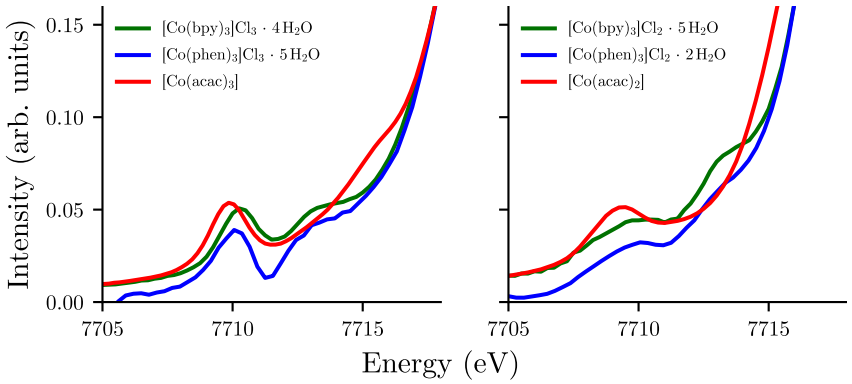

Figure 5.1: Cobalt K-pre-edge spectra on cobalt reference compounds. Co^{3+} LS spectra (left) and Co^{2+} HS spectra (right) are shown.

Metal K-pre-edge spectra on $Co(bpy)_3$, $Co(phen)_3$ and $Co(acac)_{2/3}$[1] are presented in figure 5.1. The experimental spectra exhibit a sharp peak at around 7710.1 eV for the Co^{3+} LS compounds (left panel). The Co^{2+} HS compounds (right panel) present an asymmetric split feature with two peaks for the polypyridine-type complexes at around 7708.4 eV and 7709.8 eV. The (acac)-compound exhibits a more asymmetric peak, with a maximum at around 7709.4 eV. Here, the position of a weaker secondary feature at lower energies, as in the case of the two former compounds, is hinted at but not clearly observable within the experimental resolution. Interestingly, both polypyridine-type complexes exhibit a prominent feature at around 7712.8 eV, which is present in both Co^{3+} and Co^{2+} forms. Due to the edge position being at higher energy, this feature appears more pronounced in the Co^{3+} LS compounds. No such feature is observed for the (acac)-compounds.

To assess the underlying electronic structure, TD-DFT calculations have been carried out by Esma Boydas, Humboldt University Berlin. The TD-DFT protocols for calculating metal pre-edges followed the standard methodology pioneered by DeBeer et al., which has been described elsewhere [128, 141] and lies outside the scope of this thesis. The TD-DFT calculation results on $Co(bpy)_3$ and $Co(acac)_3$ are shown in figure 5.2. To assess the nature of the calculated transitions, we are reverting to the inspection of natural difference orbitals (NDOs), which visualize the difference in electronic charge density induced by a corresponding transition. The sharp feature at 7710 eV in the Co^{3+} $[Co(bpy)_3]Cl_3 \cdot 4\,H_2O$ and $[Co(acac)_3]$ spectra is well reproduced by the calculations. NDOs of the transitions in this feature exhibit metal e_g character (representative NDOs are shown in the right panel of figure 5.2). This is rationalized by the LS Co^{3+} d^6 configuration, which does not support transitions into the fully occupied metal t_{2g} levels. The secondary feature in the Co^{3+} spectrum of $[Co(bpy)_3]Cl_3 \cdot 4\,H_2O$ at higher energies is reproduced in the calculations as well, albeit shifted to higher energies by roughly 3 eV. The inspection of the corresponding NDOs reveals significant charge

[1] The structures of the investigated compounds are visualized in figure 4.1

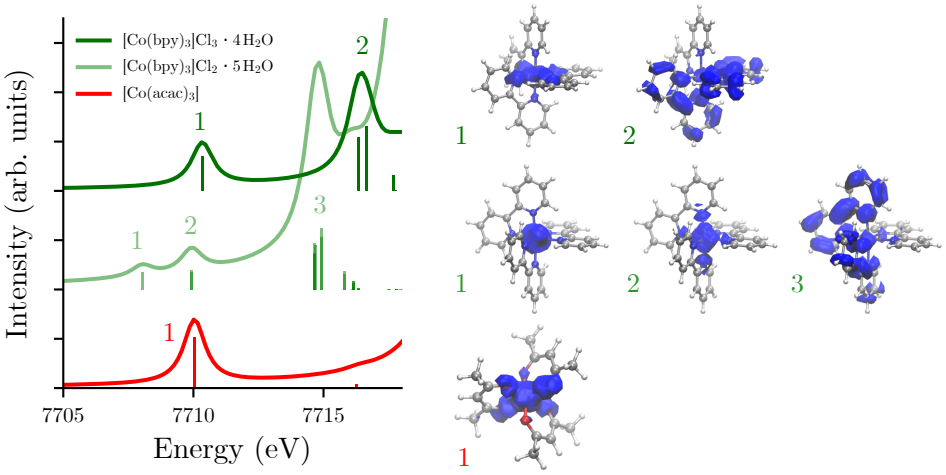

Figure 5.2: TD-DFT calculated cobalt K-pre-edge spectra on $[Co(bpy)_3]Cl_3 \cdot 4\,H_2O$, $[Co(bpy)_3]Cl_2 \cdot 5\,H_2O$ and $[Co(acac)_3]$. Representative natural difference orbitals (NDOs) are shown on the right for the dominant transitions.

density on the (bpy)-ligand, which is indicative of a 1s metal to ligand charge-transfer (MLCT). The position of MLCT features calculated with DFT methods has been shown to shift as a function of the utilized DFT functional, and is thus method dependent [141]. The calculated pre-edge of the Co^{2+} compound $[Co(bpy)_3]Cl_2 \cdot 5\,H_2O$ reproduces the double-peak structure of the experimental spectrum. Inspection of the corresponding NDOs indicates that the two features carry metal d orbital t_{2g} (1) and e_g (2) character and thus correspond to the degenerated cobalt d orbitals. As in the cobalt LS case for $[Co(bpy)_3]Cl_3 \cdot 4\,H_2O$, a secondary feature at higher energies is correctly predicted. The corresponding NDOs indicate that this peak arises due to (bpy-)MLCT transitions as well. As in the experimental spectra of the (acac)-compound, no transition is observed around 7714 eV in the calculated spectrum. Inspection of the pre-edge feature at around 7710 eV agrees with the previous finding that the sharp, intense feature arises due to transitions into a metal-centered orbital with e_g character.

After we have established that the cobalt metal pre-edge reveals information about both the local metal configuration and 1s to ligand charge transfer in these complexes, we are applying the same methodology to the investigated cobalt VT compounds during temperature-induced VT transition. The experimental XAS spectra are plotted in figure 5.3. The pre-edge spectra of these compounds follow the same general behavior of the previously discussed references. A sharp peak at 7710 eV characterizes the Co^{3+} LS spectra. Contrary to the polypyridine reference compounds in figure 5.1, we observe no pronounced charge-transfer peak at 7713 eV. In the low-temperature spectra of the VT complexes, an intensity trend with (phen) > (bpy) > (tmeda) at 7713 eV is found, which might hint toward the presence of a weaker and not clearly visible MLCT peak in the VT complexes with polypyridine co-ligands. While $Co(DTB)_2(bpy)$ exhibits similar behavior in the Co^{2+}, high-temperature spectrum in the sense of displaying a

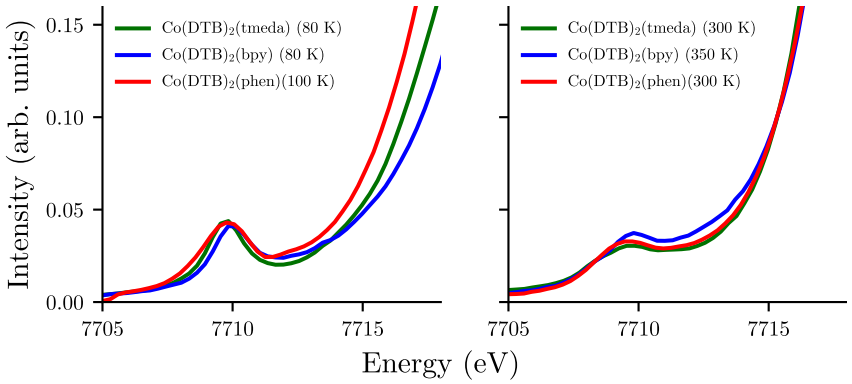

Figure 5.3: Cobalt K-pre-edge spectra on cobalt VT complexes. Cryogenic (left) and elevated temperature (right) spectra present the samples in their Co^{3+} and Co^{2+} phase.

weak, however noticeable pre-edge feature at about 7713 eV, this trend is not as clearly visible for $Co(DTB)_2(phen)$. Following the methodology applied for the cobalt reference compounds in figures 5.1 and 5.2, we are turning to TD-DFT calculation results on the cobalt VT samples.

The discussion of the TD-DFT calculation results is divided into the inspection of LS Co^{3+} and HS Co^{2+} spectra. We begin with results on the LS Co^{3+} d^6 compounds presented in figure 5.4. The sharp feature at around 7710.2 eV is well reproduced, similar to the reference spectra previously discussed. At higher energies around 7713.4 eV and 7714.7 eV, two additional distinct groups of transitions are observed for the polypyridine complexes. The (tmeda)-compounds exhibit only the first transition at around 7713.0 eV.

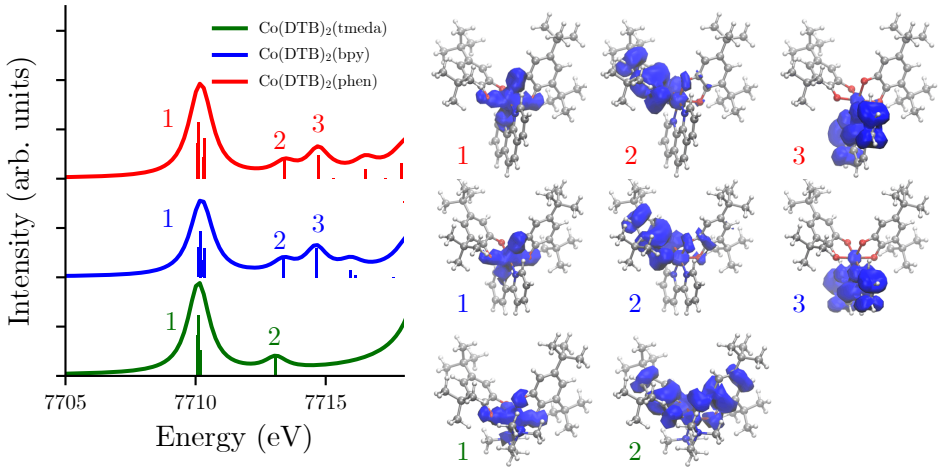

Figure 5.4: TD-DFT calculations on the cobalt K-pre-edge of the low-temperature LS phase of cobalt VT complexes. Representative natural difference orbitals (NDOs) are shown on the right for the dominant transitions.

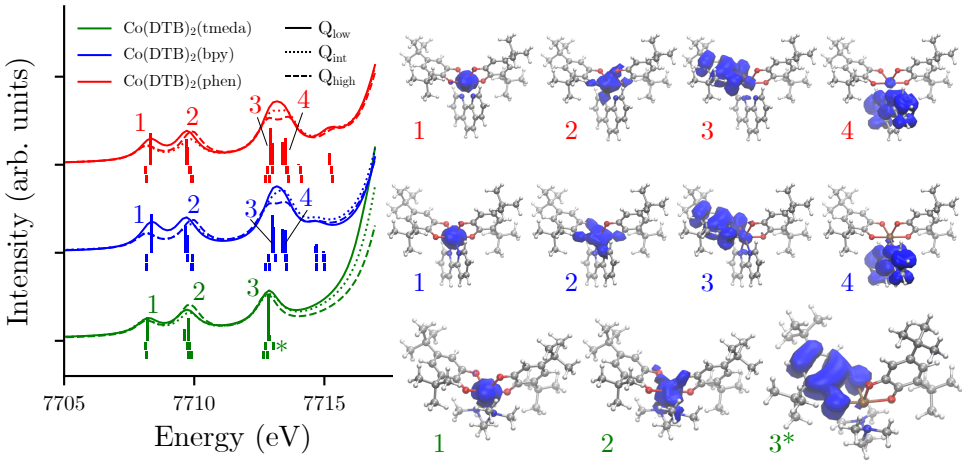

Figure 5.5: TD-DFT calculations on the cobalt K-pre-edge of the high-temperature HS phase of cobalt VT complexes.

Corresponding representative NDOs are visualized in the right panel of figure 5.4. The orbital shape for feature (1) indicates a metal-centered transition with e_g character for all three complexes. For feature (2), the electron density is found predominantly on the redox-active SQ ligand moieties, signifying a cobalt 1s to ligand charge transfer. This behavior is observed for all three complexes as well. The additional feature (3) at slightly higher energies in the two polypyridine compounds is assigned a cobalt 1s to (bpy/phen-) ligand charge transfer, based on orbital shape. We note that the calculated separation between the MLCT transitions into the (bpy/phen-) and redox-active SQ ligands is on the order of 1.3 eV.

In the investigated complexes, the Co^{2+} form exhibits a metal HS d^7 configuration. With the unpaired spin on the redox-active SQ ligands, multiple spin-coupling scenarios with the metal quartet state are possible. This is reflected by three HS-calculations per compound, which are labeled Q_{low}, Q_{int} and Q_{high}, as in the previous chapter. The spin-coupling cases have been described in section 2.4 and are visualized by solid, dashed, and dotted lines in the 5.5. The observed transitions in the HS spectra agree with the general behavior identified in figure 5.4. Contrary to the LS results, metal centered transitions around 7710 eV appear split due to holes in both the t_{2g} and e_g d levels. The splitting between the t_{2g} and e_g levels is on the order of 1.3 eV. The metal-centered transitions are accompanied by cobalt 1s to ligand-orbital transitions at around 7712.9 eV (SQ) and 7713.4 eV (bpy, phen).

We hold that transitions into the co-ligand and SQ orbitals in cobalt VT complexes are only separated by an energy splitting on the order of 1 eV, which is comparable with the metal 1s core-hole lifetime broadening [47]. In the following, we will explore how resonant XES methods, which have been shown to deconvolute transitions not distinguishable in conventional XAS, might assist in the investigation of the metal pre-edge in VT compounds.

5.2 Resonant X-ray emission spectroscopy

The use of resonant XES techniques has been shown to provide enhanced insight into the pre-edge structure of TM complexes. Al Samarai et al. successfully utilized 1s3p RXES to elucidate multiple electronic details in the pre-edge region of cobalt oxide and sulfide complexes not visible in conventional XAS [145]. A related and instructive example of the benefits of RXES techniques in the soft X-ray regime can be found at Vaz da Cruz et al., where the overlapping 1s absorption spectra of nitrogen in VT complexes were deconvoluted by RXES measurements [146].

RXES data acquisition in our study was conducted concomitantly with the XAS measurements presented in the previous section. For the collection of resonant XES data at CLÆSS, a crystal spectrometer [116] equipped with two Si(333) crystals was utilized and set to Bragg angles around 50.8°. This spectrometer is semi-dispersive and can capture a band of multiple emission energies of around 30 eV. The full RXES map was collected by recording three overlapping sections at offset emission energies. Inspection of the elastic line profiles indicated an energy resolution of about 1.3 eV. At the PIPOXS beamline, a scanning Johann-type spectrometer equipped with five Si(533) analyzers was used, set to a Bragg angle of about 78.1°. The resulting energy resolution was determined by inspection of elastic lines to be approximately 1.5 eV.

5.2.1 Spin-selectivity in 1s3p RXES

Spin-selective, spin-polarized or Kβ-detected XAS presents a way of enhancing spectral signatures in experimental data by probing electronic transitions in the metal pre-edge via specifically selected HERFD slices at Kβ emission energies. The Kβ emission line of HS metal complexes exhibits strong p-d exchange coupling (cf. section 3.2), which leads to transitions in the Kβ' region arising due to transitions of a spin-up electron to the 1s core-hole [72]. By capturing a HERFD slice at the position of the $K\beta_{1,3}$ and Kβ' position, spin-up and spin-down decay channels can be selectively probed [147].

The fundamental idea is to exploit that those configurations in which each metal d

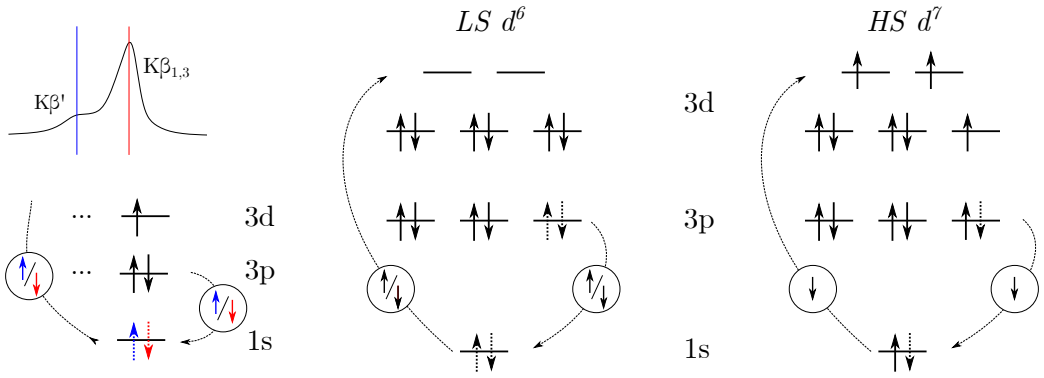

Figure 5.6: Spin-polarized 1s3p RXES.

orbital is occupied at least once do not allow the promotion of a 1s spin-up electron into the d orbital. This is illustrated in the right panel of figure 5.6. In this case, only spin-down transitions into the metal orbitals are possible, as illustrated in figure 5.6 for a LS d^6 and HS d^7 complexes. To open the discussion of our data to a potential spin-selective interpretation, we selected the 1s3p emission region for the investigation of the metal pre-edge structure via RXES.

5.2.2 RXES on cobalt reference compounds

As an introduction to the discussion of resonant XES maps, we begin with analyzing two cobalt reference datasets. For this, RXES maps on the Co^{2+} and Co^{3+} variants of $Co(bpy)_3$ and $Co(acac)_{2/3}$ are presented.

In figure 5.7 for $[Co(acac)_3]$, a single pre-edge feature can be found at approximately 7710 eV incoming energy (A), which exhibits a strong lower energy tail (◆) and pronounced asymmetry along the emitted energy axis till around 7635 eV. In the same region of the 1s3p RXES map of $[Co(acac)_2]$, two features in the pre-edge region are observed (a, b). They appear at similar incoming energy but are separated by approximately 2.5 eV along the emission energy axis. We will see in the following that these transitions are typical for the investigated Co^{2+} HS compounds and represent a case where features would appear at very close energies in conventional XAS but are well separated by resonant XES measurements. The $Co^{2+}-Co^{3+}$ difference map in the right panel of figure 5.7 visualizes the existence of intensity in the lower emitted energies regions for $[Co(acac)_3]$ (◆) as compared to $[Co(acac)_2]$. The single peak-like feature of the Co^{3+} form (A) appears at slightly lower emitted energies than a similar feature in

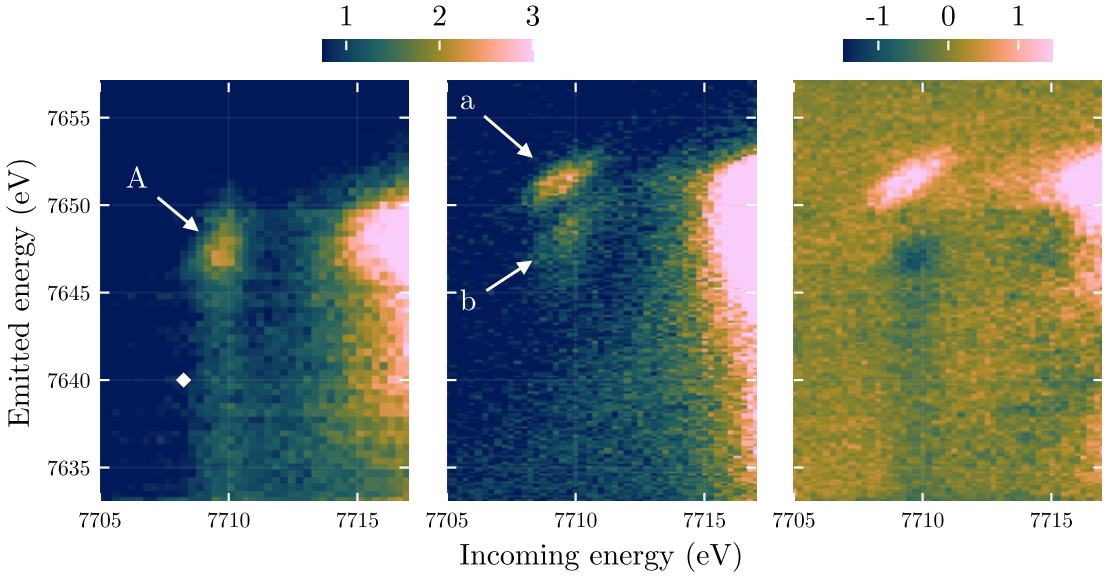

Figure 5.7: 1s3p RXES maps of $[Co(acac)_3]$ (left) $[Co(acac)_2]$ (center) and difference (right). Alphabet labels and (◆/∗) mark features discussed in the text.

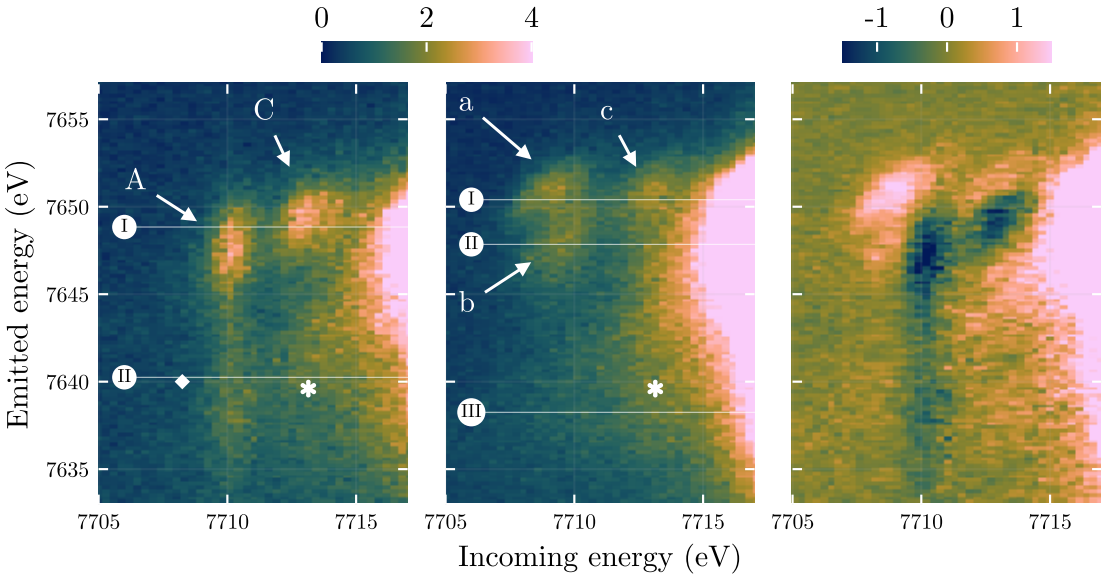

Figure 5.8: 1s3p RXES maps of $[Co(bpy)_3]Cl_3 \cdot 4\,H_2O$ (left) $[Co(bpy)_3]Cl_2 \cdot 5\,H_2O$ (center) and difference (right). Alphabet labels and (◆/∗) mark features discussed in the text. The enumerated lines indicate slices discussed in figure 5.9.

the Co^{2+} form (a). In the Co^{2+} compound, weak intensity (∗) is found in the region of the Kβ' emission energies, starting at around 7710 eV incoming energy.

RXES data on the second cobalt reference, $Co(bpy)_3$, is presented in in figure 5.8. The spectra exhibit for the Co^{3+} form a single pre-edge peak at 7710 eV incoming energy (A) and, notably, an additional satellite feature at 7713 eV incoming energy (C). Based on the analysis in the previous section, we assign a 1s metal to (bpy-)ligand charge transfer to this feature. We note that this transition appears well separated from the main edge intensity and can be accurately described by a peak at 7713 eV incoming- and 7649.3 eV emitted energy. This demonstrates how recording complete RXES spectra can highlight the existence of features otherwise obscured in regular XAS experiments. Moreover, the HERFD obtained by slicing for given emission energy along the incoming energy axis improve the spectral resolution. This extraction of the marked slices at constant emitted energy (CEE) will be discussed in the next paragraph. The main feature (A) at 7710 eV follows a similar behavior as in the case of $[Co(acac)_3]$ and presents a broad tail towards lower emission energies (◆) with strong asymmetry. In the pre-edge region of the HS-compound $[Co(bpy)_3]Cl_2 \cdot 5\,H_2O$, a split pre-edge feature can be observed (a, b), with a similar additional satellite peak at 7713 eV incoming energy (c) as just discussed. The difference map unveils that the satellite peak seems to shift to slightly lower emission energies for the Co^{3+} form but essentially remains in the same spectral region. As before, we invoke the TD-DFT calculation results presented in the previous section to assign a 1s metal-to-ligand charge transfer to this feature. The broad tail of the singular pre-edge feature in the LS spectrum (◆) is absent for the HS spectrum. Instead, a faint rise of intensity in the region below the MLCT feature (c)

is observed, which exhibits a similar broad character and extends over a comparable energy range of ca. 15 eV along the emission energy axis (∗).

The quantitative interpretation of RXES maps is commonly undertaken by the extraction of slices along constant incoming energy (CIE) and CEE at feature positions of interest. Slices at the position of the main emission peak along incoming energy are presented in figure 5.9. Since the influence of the diagonal broadening along constant energy transfer is reduced by the extraction of a finite width slice (cf. section 3.2.4), a line-sharpening effect can be achieved compared to conventional XAS. This effect is well demonstrated by now clearly marked features at approximately 7713 eV in the Kβ HERFD slices I and II, associated with the 1s metal-to-ligand CT transitions in $Co(bpy)_3$, as shown with the blue curves in figure 5.9. By selecting the emission energy of the CEE slice, the two underlying features in the pre-edge region for the $Co(bpy)_3$ HS-compound can be selectively accessed (blue and light-blue curves in the right panel of figure 5.9). The red curve represents a CEE slice at the position of the Kβ' on the emission energy axis. The absence of a pre-edge feature for the HS compound indicates that the transition channels for spin-up electrons (cf. section 5.2.1) are not present due to the HS d^{7+1} configuration. The red curve for the LS spectrum exhibits a clear peak at the position of the pre-edge feature. This is in line with the resonantly excited LS d^{6+1} configuration of the cobalt ion and a demonstration of spin-selectivity in Kβ RXES. We note that capturing a whole RXES map can significantly ease selecting a suitable CEE slice, especially if the pre-edge structure is not experimentally known.

Based on the observation that 1s3p RXES data on the investigated cobalt reference compounds deliver both a line-sharpening effect to the absorption spectra and support the description of distinct pre-edge features signifying 1s-to-ligand charge transfer transition states, we applied the same experimental methodology to the study of the electronic structure in cobalt VT complexes during the temperature-induced transition.

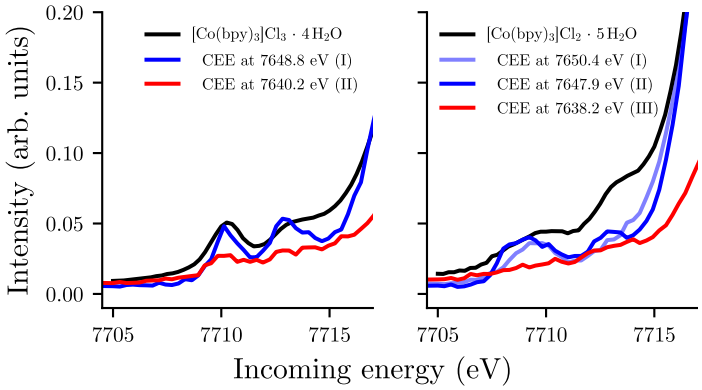

Figure 5.9: Line-sharpening effect achieved by slicing the resonant XES data on the cobalt K-pre-edge region. Co^{3+} (left) and Co^{2+} (right) data of $Co(bpy)_3$ has been sliced at positions indicated by the enumerated labels in figure 5.8. Black curves correspond to the conventionally collected XAS spectrum in transmission mode.

5.2.3 Temperature-resolved RXES on VT complexes

We will begin by inspecting the RXES maps on $Co(DTB)_2(tmeda)$, $Co(DTB)_2(bpy)$ and $Co(DTB)_2(phen)$ and continue the analysis by a discussion of slices of the presented data at selected incoming- and emitted energies (CIE, CEE).

The 1s3p RXES maps on $Co(DTB)_2(tmeda)$ are shown in figure 5.10. The displayed figures contain labeled markers for the subsequent discussion of slices at CIE and CEE. We are presenting both cryogenic and elevated temperature data and the difference map (elevated minus cryogenic temperature spectra). At cryogenic temperatures (80 K), a single feature can be observed in the pre-edge region at ca. 7709 eV incoming energy (A). This feature exhibits a broad tail (◆) along the emitted energy axis, which extends from 7648 eV to approximately 7635 eV, similar to the cobalt LS references presented in the previous section. For the room temperature data, two distinct pre-edge features at 7709.5 eV incoming energy are observed (a, b), which again qualitatively agrees with the observed behavior in the Co^{2+} HS references. The difference map indicates that the lower emission-energy feature in the Co^{2+} HS map (A) and the intense feature in the Co^{3+} LS data (a) appear at similar emitted energies. As expected from the slight reduction in ionization energy upon conversion from the Co^{3+} form to a Co^{2+} complex, an increase in energy for the main edge position is hinted by the recorded RXES data. Since the RXES measurements were undertaken on concentrated samples for suitable signal statistics, further interpretation of the main edge is hardened by self-absorption effects [148]. The region around 7712 eV incoming energy exhibits a broad feature (*)

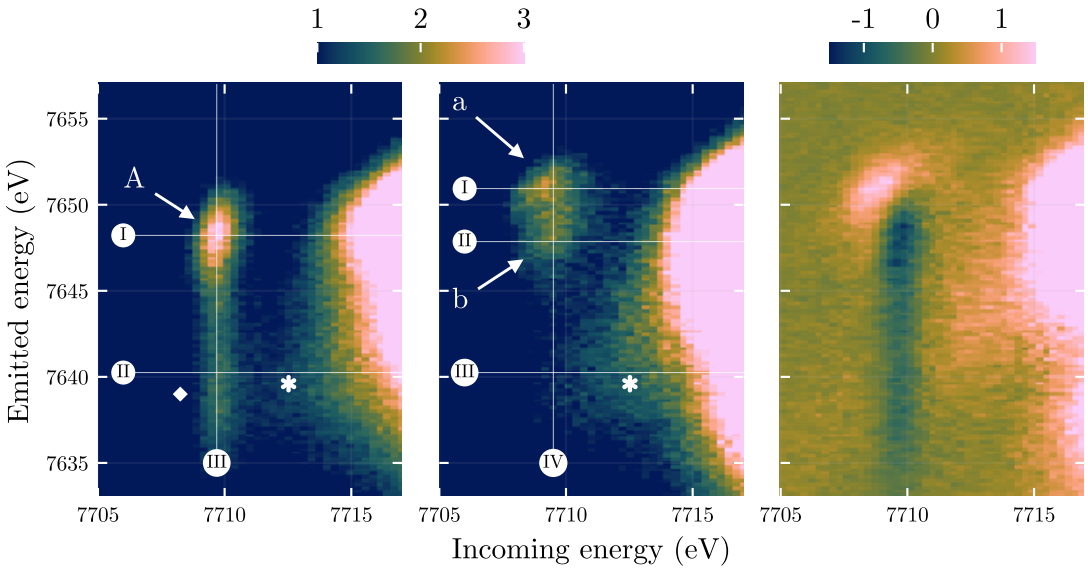

Figure 5.10: RXES maps of $Co(DTB)_2(tmeda)$, recorded both at cryogenic (*left*) and room temperature (*center*). The right panel displays the difference between both states (high temperature - low temperature). Alphabet labels and (◆/∗) mark features discussed in the text. The enumerated lines indicate slices shown in figures 5.13 and 5.14.

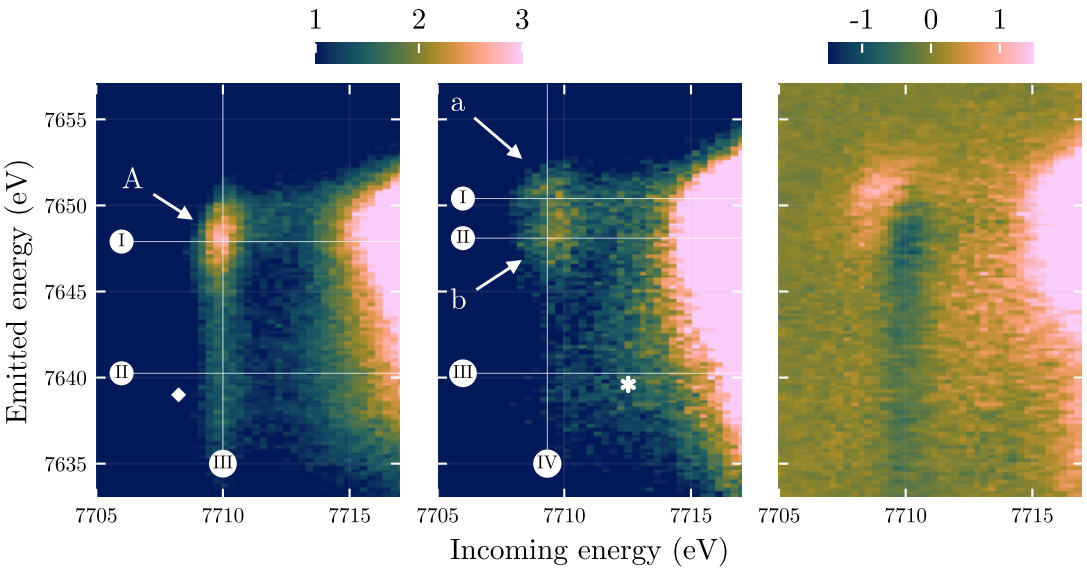

Figure 5.11: RXES maps of $Co(DTB)_2(bpy)$, recorded both at cryogenic (*left*) and elevated temperatures (*center*). The right panel displays the difference between both states (high temperature - low temperature). Alphabet labels and (◆/∗) mark features discussed in the text. The enumerated lines indicate slices shown in figures 5.13 and 5.14.

between 7635 eV and 7645 eV emitted energy in both VT states.

The temperature-resolved RXES maps of $Co(DTB)_2(bpy)$ are presented in figure 5.11. For this compound, a chemically related complex with a similar ligand environment ($[Co(bpy)_3]Cl_3 \cdot 4\,H_2O$ / $[Co(bpy)_3]Cl_2 \cdot 5\,H_2O$) was presented in figure 5.8. Contrary to the reference RXES data, we do not observe a marked charge-transfer peak at 7713 eV for the cobalt VT compound. Despite the absence of a strong, localized feature as in the tris-bipyridine complex, we still note a slight increase in intensity at 7713 eV incoming energy. We find the same general behavior for the remaining pre-edge structure as in the latter VT complex. A strong peak at 7709.8 eV incoming energy (A) in the LS spectrum turns into a split pre-edge feature (a, b) upon heating. In this complex, significantly more intensity for the HS compound is found in the diffuse region at the position of the Kβ' feature (∗). As before, no tail to the main pre-edge feature around 7710 eV (◆) is observed.

We finish the discussion of RXES maps with the temperature-resolved spectra on $Co(DTB)_2(phen)$ presented in figure 5.12. This dataset was acquired with a scanning-type Johann spectrometer and features a slightly reduced background in the presented pre-edge region. This is most likely due to the non-dispersive acquisition mode, which reduced the influence of the scattering background. The sharp and intense feature at 7709.9 eV in the LS data (A) and two peaks in the HS spectrum (a, b) are observed. Again, as in the case of the previously discussed polypyridine VT complex, weak intensity is observed at 7713 eV incoming energy. For this compound, we observe a satellite structure at slightly higher emission energy above the main peak in the low-

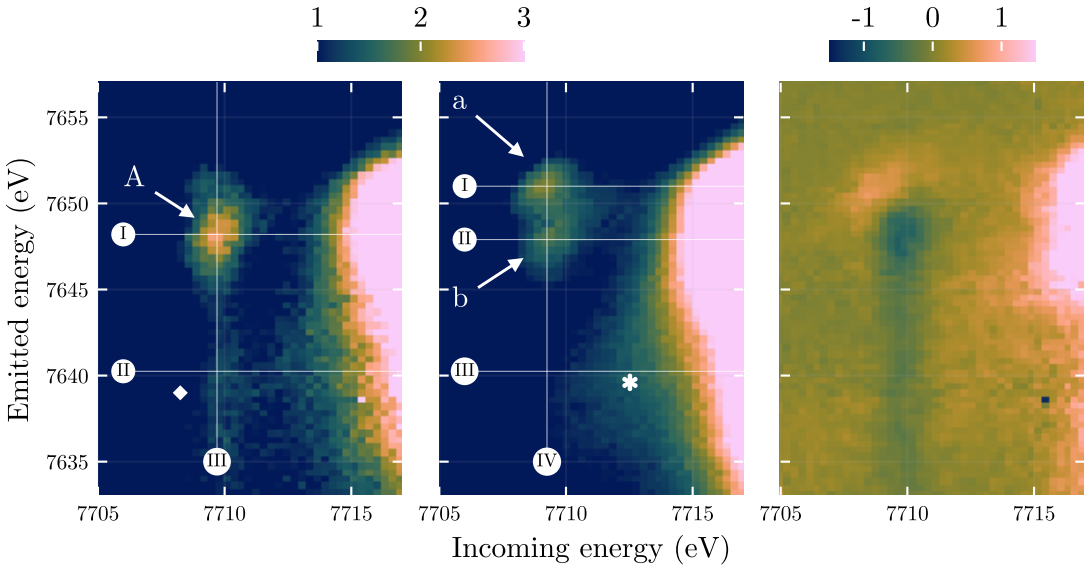

Figure 5.12: RXES maps of $Co(DTB)_2(phen)$, recorded both at cryogenic (*left*) and room temperature (*center*). The right panel displays the difference between both states (high temperature - low temperature). Alphabet labels and (◆/∗) mark features discussed in the text. The enumerated lines indicate slices shown in figures 5.13 and 5.14.

temperature RXES map, which is likely caused by incomplete temperature conversion caused by a less optimal thermal contact of the sample with the utilized cryostat.

For a discussion of conventional XAS and the Kβ HERFD spectra as indicated by the horizontal CEE slices, we are turning towards figure 5.13, where a comparison of the three investigated cobalt VT complexes is presented. We first note that the RXES slices exhibit slightly sharper peak shapes compared to the conventional XAS data, which was also observed previously. In the low-temperature LS-phase (bottom curves), the single almost symmetrical feature of the first RXES slice (I) agrees well with the transmission mode XAS data. A second slice at the emission energy of the Kβ' (II, red) indicates that a clear peak is observed at 7710 eV. Moving on to the high-temperature data (top curves), we again observe that slices (I) and (II) reveal how the pre-edge features exhibit slightly different centroid energies. In the case of $Co(DTB)_2(bpy)$ (center panel), a very faint second feature at ca. 2 eV above the main pre-edge peaks can be observed (blue arrows). This feature is also visible in the HS-phase spectrum of $Co(DTB)_2(phen)$.

With the current instrumental resolution and counting statistics, no further distinction can be made between potentially present ligand-specific MLCT features in the presented experimental data. Higher resolution RXES measurements on these compounds might reveal additional structure, especially in the region between 7710 eV and 7713 eV incoming energy for the polypyridine complexes. Additionally, higher instrumental resolution along the incoming energy axis might contribute to elucidating the discussed broad diagonal feature (*) since no significant structure can be extracted under current measurement conditions.

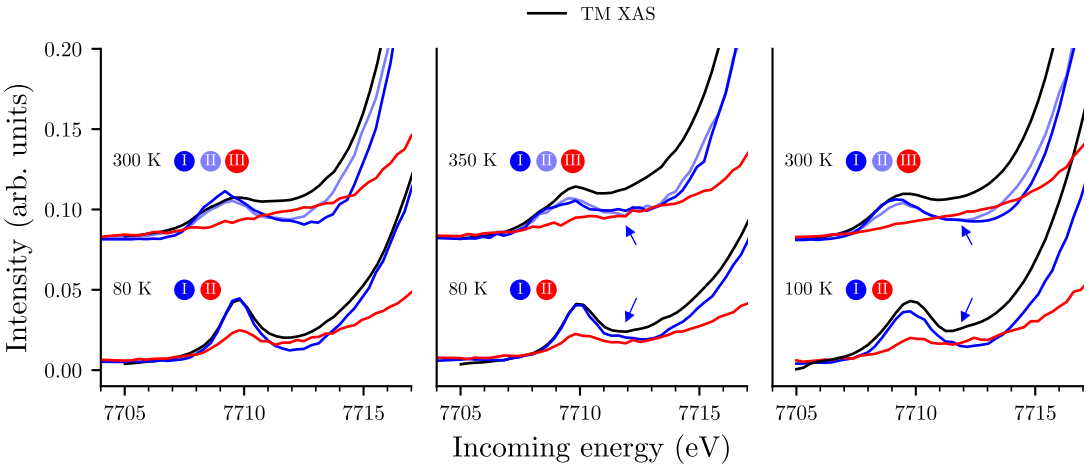

Figure 5.13: CEE slices of the cobalt VT complexes $Co(DTB)_2(tmeda)$ (*left*), $Co(DTB)_2(bpy)$ (*center*) and $Co(DTB)_2(phen)$ (*right*). Black lines indicate conventional transmission-mode XAS spectra at the same temperature.

A selection of CIE slices, corresponding to the labeled markers in figures 5.10 to 5.12, are shown in figure 5.14. For the high-temperature HS-phase spectra, we observe a splitting of the higher energy peak into two features (2) and (3). The splitting between those features is around 3 eV. In the LS-phase, feature (3) disappears. For both LS and HS spectra, a weak maximum around 7639 eV, about 11 eV from the main peak(s) can be observed (1). The absence of significant intensity in the (1) feature around 7640 eV indicates that the orbitals remain localized, and the amount of charge sharing is moderate. This is experimental evidence of one of the fundamental requirements for VT, the presence of a sufficiently low degree of covalency [27].

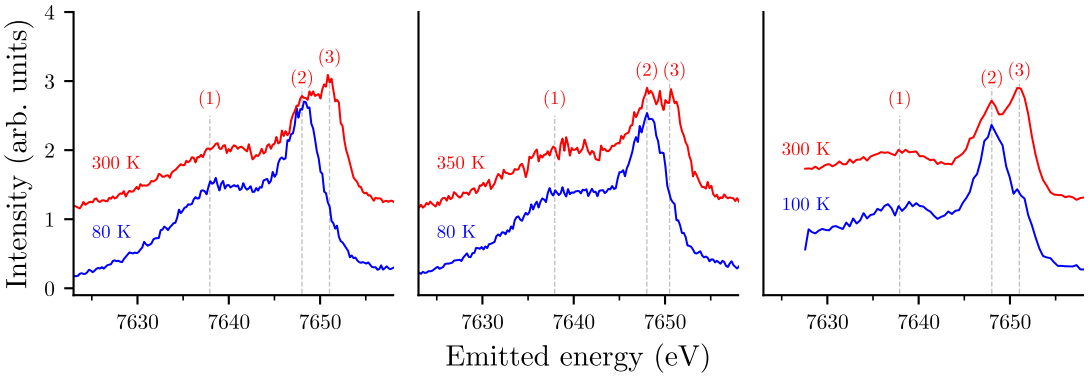

Figure 5.14: CIE slices of the cobalt VT complexes $Co(DTB)_2(tmeda)$ (*left*), $Co(DTB)_2(bpy)$ (*center*) and $Co(DTB)_2(phen)$ (*right*) at cryogenic and elevated temperatures.

5.3 Summary and Outlook for RXES measurements on cobalt VT complexes

The usage of X-ray emission spectrometers for the recording of Kβ detected HERFD XAS in the form of whole RXES maps allowed for the extraction of HERFD slices at selected energies. In the pre-edge region of the K-edge on octahedral cobalt complexes, a strong feature with a broad delocalized tail was identified in the LS spectrum. The HS data exhibited a split pre-edge spectrum with no observable lower energy tail. Using a higher-resolution monochromator and further optimized spectrometer alignment might increase the benefit of the Kβ-HERFD method in probing specific transitions in cobalt VT compounds due to the resulting instrumental energy resolution further below the core-hole lifetime. Proper dilution of the sample might also reveal features that currently lie within the edge region. The presence of such features could be motivated by the prediction of the ligand-specific MLCT states in the TD-DFT calculations. Alternatively, the intensity of such features might appear weaker than expected. In this case, higher resolution measurements might also be beneficial since the distinction of transition features in the pre-edge region from the main-edge background should be eased by a potential sharpening of the observed effect. The incoming energy bandwidth of around 1 eV is most likely also large enough to simultaneously excite multiple groups of electronic transitions, which clouds the analysis of individual pre-edge features.

M-edge spectroscopy, in which a 3p electron is promoted to 3d energy levels, exhibits the same final state as 1s3p RXES ($3p^5 3d^{N+1}$). It is important to note that multiplet effects with the intermediate state of the RXES process can introduce significant complications in the analysis of the observed experimental line shapes [41]. A comparison with experimental M-edge data on cobalt complexes might still provide valuable insights into the electronic nature of the described spectral features.

While the recording of resonant X-ray emission spectra is predominantly undertaken with scanning-type spectrometers [149], this study achieved comparable data quality with a semi-dispersive spectrometer. This suggests that dispersive von Hámos type spectrometers have further potential for recording whole RXES maps when the incoming energy resolution is sufficiently small. This brings significant advantages if the sample has to be scanned in the beam (as in the case of the presented cobalt VT complexes) due to radiation damage. For the dispersive collection of complete RXES maps per scan, the challenging normalization of individual scans is less critical or may even be dropped entirely.

The recording of temperature resolved XAS datasets would allow for a more profound discussion of valence properties by providing an assessment of the metal charge-state via the cobalt K-edge position and line shape. In the presented measurements, concentrated samples were used to improve the signal yield in the less intense pre-edge region, which can cause self-absorption effects in the recorded X-ray spectra [148]. A set of XAS measurements with proper dilution to avoid self-absorption effects is thus needed if the discussion of the complete X-ray absorption near edge structure (XANES) region or extended X-ray absorption fine structure (EXAFS) signals is desired.

Chapter 6

Transient X-ray spectroscopy on cobalt VT compounds

Transient or time-resolved X-ray spectroscopy experiments aim to elucidate the dynamical behavior of matter by combining the sensitivity of X-rays toward atomic and molecular length scales with the ultrafast flash duration required for resolving electronic and structural processes on their respective temporal domains, i.e., femto- and picosecond timescales [56, 150]. A standard scheme for the measurement of time-resolved spectroscopy is the pump-probe technique. A pump-probe experiment features a synchronized pair of a pump- and a probe-pulse (e.g., a split laser beam arriving at the sample position or a synchronized optical pump-laser and a pulsed X-ray probe source with varying temporal delay). The pump-pulse promotes the sample into an excited state. The decay of the excited state is then probed via the probe pulse after a given delay time has passed. Different states of the sample during decay can be probed by varying the pump-probe delay. Making the delay negative (meaning that the probe pulse comes before the pump pulse) probes the unexcited sample. In general, the pump pulse does not have to be an optical pulse but can also be, e.g., a magnetic pulse or a chemical trigger.

Using synchrotron radiation sources, picosecond timescale kinetic processes became available. With the advent of femtosecond hard X-ray sources, FEL in the X-ray regime, the range of accessible kinetic processes with X-rays has been extended towards the domain of even shorter intramolecular electronic processes.

Hard X-ray spectroscopies in the ultrafast regime provide photon energies comparable to the 1s core-level ionization energies of 3d TMs, enabling time-resolved XES. In the case of cobalt VT complexes, the decay times of the photo-induced Co^{3+} phase have been previously studied chiefly with optical spectroscopy methods. On a variety of cobalt VT compounds, the total decay time into the GS was found to be mostly on the nanosecond timescale [25, 38, 151–153]. Only a limited number of studies addressed the shorter timescales. Studies with transient infrared spectroscopy on related cobalt VT complexes revealed kinetics on the femtosecond and low picosecond timescales [38]. This can be rationalized since, due to their intramolecular nature, characteristic

spin-crossover and charge-transfer processes of the VT transition likely pass on the femtosecond and low picosecond timescales, as was shown on a cobalt VT model system[1] by Beni et al. and Gentili et al. [152, 153]. Understanding combined charge-transfer and spin-crossover in cobalt complexes should provide an important stepping stone for studying more complex or larger systems exhibiting correlated transition mechanisms. With the decommissioning of most slicing sources worldwide, early picosecond timescales are not accessible at a synchrotron, and the elucidation of these processes requires X-ray pulses of femtosecond pulse length.

Transient XES spectroscopy is a demanding experimental technique that requires the careful preselection of investigated timescales. This chapter presents a time-resolved X-ray spectroscopic study on $Co(DTB)_2(tmeda)$. $Co(DTB)_2(tmeda)$ has been shown to exhibit general robustness in previous studies involving repeated VT interconversion after pulsed laser irradiation [37] and in the X-ray beam [18]. Since the solubility of $Co(DTB)_2(tmeda)$ in toluene is only moderate, higher sample concentrations as typical for other TM complexes [150, 154, 155] are not achievable. This increases the need for a precise definition of the targeted timescales as the required integration time for the collection of satisfactory data is extended.

6.1 Transient optical absorption spectroscopy

To identify dominant kinetic timescales during the VT process in $Co(DTB)_2(tmeda)$, transient optical absorption spectroscopy (TOAS) has been conducted at the laboratory of Prof. Andrea Cannizzo at the Institute of Applied Physics in Bern, Switzerland. The experimental setup following a laser-pump laser-probe methodology has been described by Nazari Haghighi Pashaki et al. [156]. For the excitation, a wavelength of 840 nm was chosen. This was based on the assignment of the MLCT transition to a broad band centered at around 800 nm, as discussed in section 4.3.1. After laser-excitation, absorption difference spectra were collected for pump-probe delays in the range of 0.2 to 500 ps. The sample was prepared as a 5 mM toluene solution under conditions as described in section 4.3.3. During the measurement, the sample was run through a 500 µm flow cell. Details regarding the data analysis of the recorded transient optical data are given in chapter 4 of Ref. [157]. The transient absorption map (figure 6.1, left) reveals two distinct spectral regions with notable kinetic activity. At around 380 nm, strong excited state absorption (ESA) [157] is observed. At slightly higher wavelengths at 435 nm, a narrow feature with negative intensity is observed and attributed to a ground-state bleach (GSB) [157]. Two additional weaker features with negative intensity are found at around 600 nm and at 750 nm, which are attributed to GSB as well. The observed features occur at pump-probe delay times below 20 ps. As visible in the logarithmic (upper) portion of the left panel in figure 6.1, no significant transient intensity is found at later delays until the end of the observed time window at 500 ps. The overall transient signal strength is on the order of 0.3 to 1.0 Δ mOD. The transient spectra at selected pump-probe delays are displayed in the center panel of figure 6.1.

[1] Co^{3+}(CAT-N-BQ)(CAT-N-SQ), whereas Q is a quinone, CAT catecholate, and SQ semiquinone.

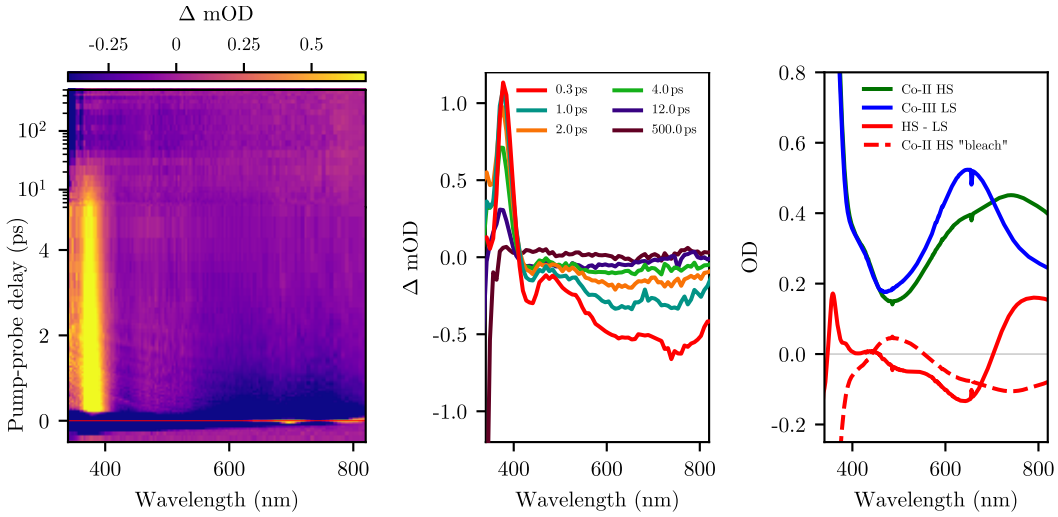

Figure 6.1: Optical transient absorption spectroscopy on a 5 mM toluene solution of $Co(DTB)_2(tmeda)$, pumped at 840 nm. The pump-probe delay axis is on a logarithmic scale starting with 5 ps. Left: Transient difference map. Center: Extracted transient difference spectra at selected pump-probe delays. Right: Steady-state UV/Vis spectra recorded at low and high temperatures and difference.

In comparison with the difference between steady-state LS and HS phase spectra of $Co(DTB)_2(tmeda)$ obtained from temperature-dependent UV/Vis-measurements, structural similarities are observed for the aforementioned features. The dashed curve in the right panel of figure 6.1 illustrates a hypothetical bleach signature as it might occur in the case of Co^{2+} depopulation without an immediate rise of a Co^{3+} line shape in the UV/Vis spectrum.

For the extraction of timescales from this dataset, we fit exponential decay functions to the dominant ESA transient feature at 380 nm and the GSB region around 630 nm. Satisfactory fits are obtained with a one-exponential decay model at 380 nm and a two-exponential decay model for 630 nm, which incorporates the slower decay constant obtained from the fit at 380 nm as a fixed parameter

$$I_{380\,\mathrm{nm}}(t) = A \exp\left(-\frac{t}{\tau_{380\,\mathrm{nm}}}\right) \tag{6.1}$$

$$I_{630\,\mathrm{nm}}(t) = A \exp\left(-\frac{t}{\tau_{630\,\mathrm{nm}}}\right) + B \exp\left(-\frac{t}{\tau_{380\,\mathrm{nm}}}\right). \tag{6.2}$$

A non-linear optical effect called cross-phase modulation is active at early delay times in TOAS data. This effect is based on changes in the refractive index caused by the electric field of the laser, which leads to a modulation of sample transmittance [157]. The region of cross-phase modulation in the presented data extends towards 0.9 ps at 380 nm and up to 0.3 ps at 600 nm. This region was determined by the inspection of the two-dimensional data and has been excluded from the fitted dataset, as no reliable amplitude information can be extracted from that region. The fitting results are plotted

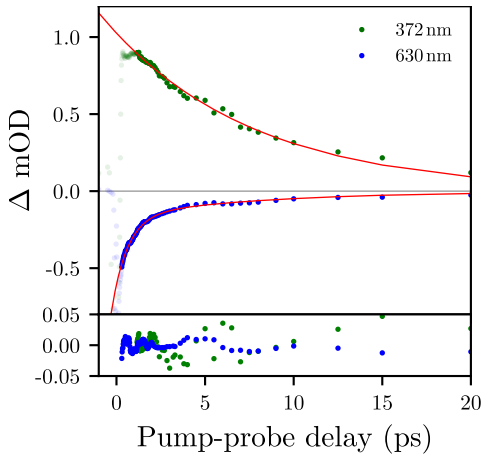

Figure 6.2: Kinetic traces at relevant wavelength extracted from optical TOAS measurements. The bottom panel indicates the fitting residuals.

in figure 6.2. The corresponding extracted time constants in table 6.1 indicate that at least two dominant timescales within the first 20 ps occur. A fast decay of around 0.9 ps is found for the GSB transient feature at around 630 nm, while a longer lived and more intense ESA feature at 372 nm decays with a time constant of roughly 8.3 ps. Another fit to a trace extracted at 700 nm yielded the same time constant as at 630 nm.

Notably, a strong absorption band around 390 nm is observed in the ligand spectrum of 3,5-di-tert-butyl-o-benzoquinone as shown in figure 6.3. This feature has been assigned to a $\pi - \pi^*$ band [158]. The difference spectrum between mixtures of 3,5-di-tert-butyl-o-benzoquinone and 3,5-di-tert-butylcatechol is presented in the right panel of figure 6.3. A very similar structure is observed in the transient maps, where a GSB is found at 437 nm, next to the strong ESA at 380 nm. Based on the ligand spectra, we conclude that the transient signature in this spectral region stems from the transition of SQ moieties to the catecholate form and thus constitutes the decay of a MLCT state, in which charge from the 3d metal orbitals is transferred to a redox-active ligand.

The observed timescales provide the basis for the further analysis of the dynamics in cobalt VT complexes. The transient XES measurements presented in the following will be focused on the investigation of the dynamics taking place in the first 8 ps after laser excitation.

Table 6.1: Dominant time constants extracted by exponential fitting in TOAS on a 5 mM toluene solution of $Co(DTB)_2(tmeda)$.

Wavelength	Time constant τ	
380 nm	8.33 $\pm$ 0.56	ps
630 nm	0.88 $\pm$ 0.05	ps

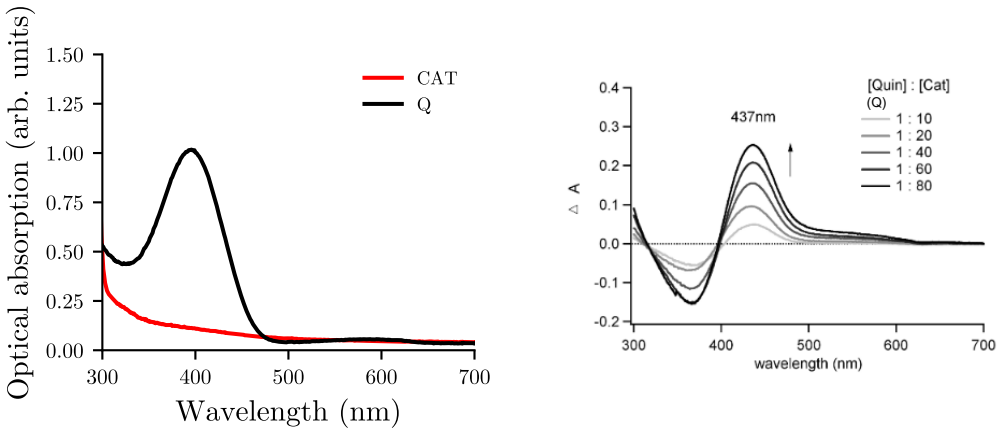

Figure 6.3: UV/Vis ligand spectra and difference curves of 3,5-di-tert-butyl-o-benzoquinone (Q) and 3,5-di-tert-butylcatechol (CAT) in toluene. The figure in the right panel has been taken from the supporting information of Ref. [158].

6.2 A preface about multi-color XES experiments

Before we turn to the discussion of time-resolved XES, a brief overview of the experimental implementation of multicolor XES is given.

While the combination of XES and XAS methods has been shown to be a powerful combination for the investigation of TM charge- and spin-state, their experimental implementation may be hindered by the fact that both techniques intrinsically require different instrument setups and sample preparation.

XAS requires a monochromatic photon beam to be scanned along the energy of an investigated absorption feature. In the context of time-resolved measurements, using monochromators can pose a challenge since the synchronization between pump- and probe-pulse relies on constant path lengths for both beams. Scanning a monochromator can influence the arrival time of the X-ray pulse when the position of reflection on the monochromator crystals changes during Bragg angle variation. While the variation of X-ray pathlength (e.g., by thermal distortion of X-ray mirrors or movement of the beam along optical components) may not be as critical during experiments with picosecond time-resolution, path variations on the order of micrometers can quickly introduce deviations to the arrival time on the order of tens or hundreds of femtoseconds[2]. These variations in arrival time have to be compensated during energy scanning to avoid the loss of temporal overlap between the pump- and probe pulse. Furthermore, sample absorption length and thickness commonly have to be carefully balanced for recording undistorted spectra.

Contrary, (non-resonant) XES typically does not depend on a monochromatized incoming photon beam and is well suited for pink-beam (i.e., broader photon energy bandwidth) or even white-beam (non-monochromatized) experiments. Additionally,

[2] A hypothetical change in pathlength of 50 µm introduces a variation of 167 fs in vacuum.

XES may benefit from highly concentrated samples.

As discussed in section 3.2, different X-ray emission lines, e.g., Kα, Kβ and VtC in 3d TMs, provide complementary information to the experimentalist since they are influenced by different amounts of p-d exchange, spin-orbit coupling, and ligand-orbital mixing. An experimentally more accessible combination of spectroscopies is thus the collection of multiple emission lines with non-monochromatic (e.g., pink or SASE) X-rays. XES may not yield the same sensitivity towards the metal charge state as XAS; however, it can still present valuable information for the analysis of correlated dynamic effects. While the metal spin-state is commonly interrogated via Kβ XES, in the context of transient X-ray experiments, the additional collection Kα XES signals offers multiple benefits. The emission signal from the latter is not only about ten times stronger (and can thus be used for normalization purposes if the signal yield is weak) but also offers two distinct and separated features, which stem from the different spin-orbit coupling. This allows for targeted analysis of the $K\alpha_1$ and $K\alpha_2$ features. Additionally, the lineshape characterization and decomposition of Kα features do tend to be less cumbersome compared to Kβ line shapes because of the more symmetric peak-like structure of the emission line.

The von Hámos spectrometer geometry is especially suited for this multicolor approach since no scanning of the analyzer components is required. The constraints for collecting multiple emission signals are thus relaxed since a suitable arrangement, once found, allows for the collection of all energies at once due to the dispersive nature of the analyzer shape.

Fundamentally, two options for the simultaneous collection of multiple emission lines in dispersive mode may be considered. Firstly, if accessible within the constraints given by spectrometer geometry and the size of the active area of the detector, multiple emission signals may be collected by the same detector. This has the advantage that measured XES data is intrinsically correlated in time, and other influencing factors, such as detector background, are identical. The simultaneous capture of, e.g., nickel Kα, Kβ and VtC XES signals with two sets of 500 mm bending radius von Hámos analyzer crystals is presented in the right panel of figure 6.4. A different combination of analyzer crystals allows for the simultaneous collection of the same set of emission lines on iron. While the analyzer bandpass allows for the VtC signal to be collected by the detector, too, the Bragg angle for the Kβ signal is smaller this time than the Bragg angle for the Kα emission line. This leads to the Kβ signal collected at the higher end of the detector and the VtC region being cut in this configuration, analyzer bending radius, and detector choice. The use of smaller bending radii drastically increases the window of captured photon energies but decreases the resolution on the detector. This is the case since a larger solid angle element is imaged onto the detector pixel.

A suitable spectrometer configuration for simultaneously capturing multiple emission lines by the same detector is not always accessible at a given analyzer bending radius. The left panel in figure figure 6.4 illustrates an example of the simultaneous collection of cobalt Kα and Kβ emission signals by use of two JungFrau detectors, which are stacked along a vertical line above the sample position. The benefit of this approach is that the optimal analyzer crystal can be chosen for both emission signals. Depending on

the investigated energy range, an analyzer with a higher Bragg angle and, thus, better efficiency and higher energy resolution might be available. This is illustrated for the cobalt Kβ XES signal, which was recorded with the best germanium analyzer available at that specific energy, Ge(1,1,1) in fourth-order reflection.

For the planning of XES experiments in von Hámos geometry, we developed a web-based tool. The tool allows easy access via a web-hosted interface and aids experimentalists in the setup of multicolor configurations. More details are given in appendix G.

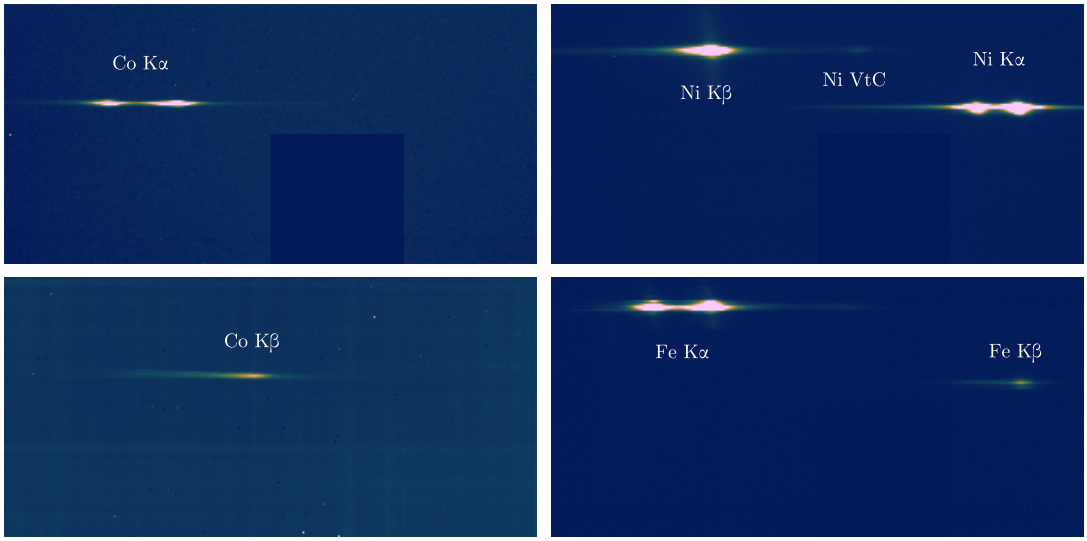

Figure 6.4: Examples of multicolor XES on TM complexes at the FXE instrument, recorded with JungFrau detector(s) ($77.25 \times 38.55\,\mu m^2$ active area, 75 µm pixel pitch) [159] and von Hámos spectrometer [160]. Left column: Simultaneous capture of cobalt Kα and Kβ XES signals with two detectors, utilizing Si(5,3,1) and Ge(4,4,4) crystal analyzers at Bragg angles of 77.01° and 82.91° respectively. Right column, top: Single-detector capture of nickel Kα, Kβ and VtC XES signals (top), recorded with Si(5,3,1) and Ge(1,1,1) crystal analyzers at Bragg angles of 64.56° and 66.70°. Right column, bottom: Iron Kα and Kβ XES captured by use of Ge(4,4,0) and Si(5,3,1) crystal analyzers at Bragg angles of 75.43° and 73.09°.

6.3 Experimental implementation of the XES experiment

The time-resolved investigation of TM complexes at the FXE instrument at EuXFEL follows the same basic methodology described at the beginning of this chapter. An overview of the complete instrument is given in the left panel of figure 6.5. For the realization of the pump-probe scheme, an optical laser is guided from the instrument laser hutch (ILH) toward the sample position (S). A fundamental requirement for pump-probe experiments is the replenishment of sample volume at the position of the

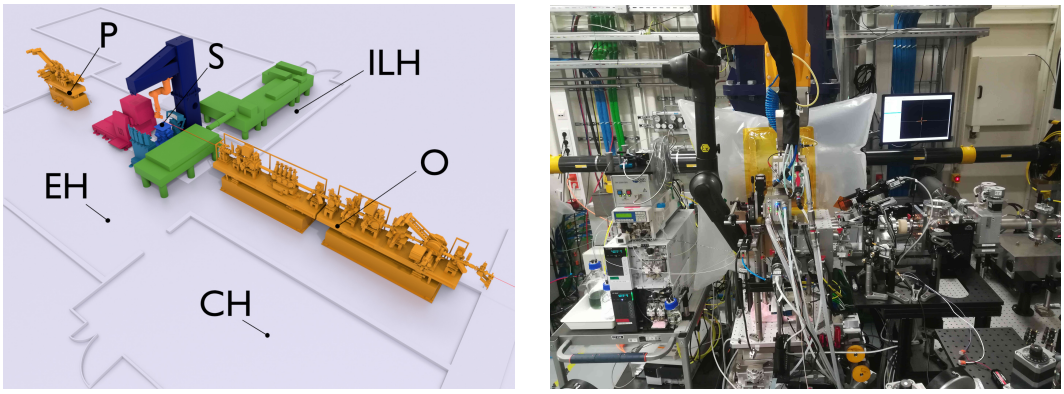

Figure 6.5: Left: Schematic view of the FXE instrument at European XFEL listing the laser-, experimental-, and control-hutch (ILH, EH, and CH), the upstream optical tables (O) and post sample diagnostics (P) as well as the sample position (S). Right: Liquid chemistry pump-probe setup for the investigation of cobalt VT compounds.

X-ray beam within the arrival time of the following pump- and probe pulses. This is most commonly achieved by dissolving the sample in a solvent and the use of a high-speed liquid jet for sample injection (cf. section 6.3.1). To validate the sample integrity during measurement, an online UV/Vis spectrometer flow-through setup is commonly realized. X-ray signals are detected utilizing the detectors at the sample position (area detectors for emission and scattering measurements) and via post-sample diagnostics (P), including an X-ray gas monitor and a crystal-based spectrum analyzer. The focusing of the X-ray beam is achieved with a stack of compound refractive lenses (CRL) on the optics section just upstream of the sample position (O).

The number of X-ray photons per pulse N_{pulse} at the EuXFEL instruments can be calculated from the pulse energy E_{ph} and pulse power P

$$N_{\text{pulse}} = \frac{P}{E_{\text{ph}}}. \tag{6.3}$$

During the acquisition of the presented XES data, the photon energy was set to 9300 eV and a pulse power of around $P_{\text{pulse}} = 2\,\text{mJ}$ was determined. This yields an estimated value for the number of photons per pulse of $N_{\text{pulse}} = 12.5 \times 10^9 \,\frac{\text{ph}}{\text{pulse}}$. Assuming a bunch filling pattern of 200 pulses per train (cf. section 3.3.1), we can additionally give the number of photons per second as $N = 2000 \cdot N_{\text{pulse}} = 2.5 \times 10^{13} \,\frac{\text{ph}}{\text{s}}$.

The following sections will describe selected aspects of the experimental implementation in more detail. Experimental results will be presented in section 6.4.

6.3.1 The liquid-jet sample environment at the FXE instrument

Due to the required replenishing of the sample at the position of the X-ray beam, a liquid jet setup was utilized. For this, the investigated sample is dissolved in the desired solvent. Aside from practical factors like solubility and experimental hazards, the choice

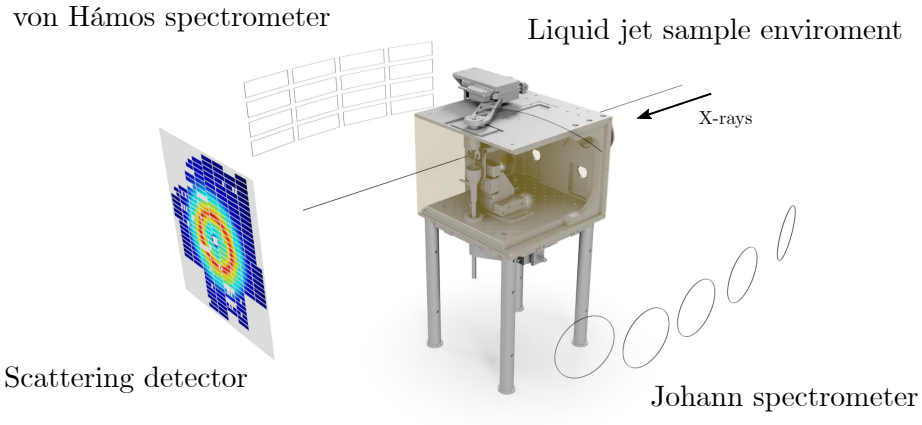

Figure 6.6: Scheme of the sample cell at the FXE instrument, visualizing all three main experimental techniques available at the instrument. During transient XES measurements on cobalt VT complexes, the Johann (hinted, front) and the scattering detector (colored panel) were not utilized. XES was recorded with the von Hámos spectrometer (hinted, back).

of solvent is, in many cases, part of the scientific case, e.g., in the investigation of solvent (dynamic) effects [161]. In any case, influences of the solvent on the dynamic behavior of the system have to be anticipated and carefully inspected [162]. For this experiment, $Co(DTB)_2(tmeda)$ was prepared in batches a 80 mL toluene solution with a concentration of 5 mM to allow for a sufficient recirculation time before refilling due to evaporation was required.

Cobalt XES measurements on $Co(DTB)_2(tmeda)$ 5 mM in toluene were undertaken at the FXE instrument at EuXFEL, Hamburg, Germany [76, 160]. The sample was delivered by a cylindrical jet using high-performance liquid chromatography (HPLC) pumps, which supplied two separate circulating lines with the sample and one optional refilling line. The two circulating lines led the sample to the point of X-ray sample interaction and a flow-through UV/Vis spectrometer, respectively, allowing online sample monitoring. The refilling line drew from a reservoir of clean solvent and injected into the primary sample reservoir when needed. For volatile solvents, this is necessary regularly since a measurable amount of sample solution can evaporate during measurement.

The sample was run with a liquid jet of 100um diameter and at an average speed of ca. 60 m/s. This speed stems from the requirement that the sample at the point of interaction with the laser and X-ray beam must be replaced within the machine repetition rate (see section 3.3.1). For an accelerator repetition rate of f_{rep} and beam sizes of s_{L} and s_{X} for the optical pump and X-ray beam, respectively, the required jet speed v_{lim} can be estimated as

$$v_{\mathrm{lim}} = \max(s_{\mathrm{L}}, s_{\mathrm{X}}) f_{\mathrm{rep}}. \tag{6.4}$$

This yields a theoretical lower limit of 56.4 $\frac{\mathrm{m}}{\mathrm{s}}$ for the jet speed at an accelerator repetition

Table 6.2: Spectrometer properties for the capture of cobalt Kα and Kβ XES data on $Co(DTB)_2(tmeda)$ at the FXE instrument.

Element	Cobalt	
Emission line	Kα	Kβ
Analyzer material	Silicon	Germanium
Diffraction case	(5,3,1)	(4,4,4)
Crystal lattice constant	5.431 Å	5.658 Å
Bragg angle	77.01°	82.91°
Detector height	231 mm	124 mm
Analyzer radius	500 mm	

rate of 0.564 MHz and a larger laser beam size of 150 µm. For a 100 µm jet, a theoretical flow rate of 26.6 ml/min is required. The small nozzle diameter, in combination with the large values for the required jet speed (and thus up-build of line pressure) as well as flow rate, motivates the choice of high-performance HPLC pumps for the operation of the sample environment.

Two X-ray area detectors were used simultaneously to capture XES spectra at both cobalt Kα and cobalt Kβ emission energies (figure 6.5). The von Hámos spectrometer configuration consisted of two sets of Ge(111) and Si(531) analyzer crystals aligned to capture both emission lines simultaneously. Details regarding spectrometer configuration are given in table 6.2. Since recording both emission lines on the same detector was not possible geometrically, two different JungFrau detectors were positioned on top of each other. The X-ray pulse energy during the experiment was on average 1.5 mJ per pulse, with 200 pulses per train at a repetition rate of 0.564 MHz.

Due to a sensitivity of the dissolved samples towards oxygen (cf. section 4.3.3), a dedicated sample environment was used, which allowed an oxygen-reduced atmosphere around the sample jet. Figure 6.6 shows the sample chamber used during the experiment. The inside of the sample chamber was flushed with a continuous flow of helium for two reasons. For once, the helium atmosphere reduced the absorption of the fluorescence signal emitted from the sample. Additionally, the presence of a slight helium overpressure atmosphere reduced the exposure of the sample to oxygen. The cell enclosure is manufactured from 150um Kapton and is mostly transparent to high-energy X-ray photons.

6.3.2 Pump-probe scheme and optical excitation

The pump-probe laser at the FXE instrument has been described by Palmer et al. [163]. A 800 nm laser with an average pulse energy around 65 µJ was used. Since the integration time of the JungFrau detectors is technically limited to be above 500 ns [159], no individual X-ray pulses can be resolved. The timing pattern of the EuXFEL has been described in section 3.3.1. At a time duration of 222 ns x 8 (4.5 Mhz / 0.5625 Mhz) = 1.776 µs in between photon bunches, the whole train takes 1.776 µs x 200 =

355 µs. The detector integration time was set to 360 µs to accommodate for the whole train, with an integration period of 0.1 s (ten images per second, i.e., one image per train). The pump laser repetition frequency was set to 0.5625 Mhz, but only every second train was laser-pumped. This led to five laser-pumped and five laser-unpumped images per second.

6.3.3 Data reduction pipeline

The time-resolved XES data collected at the FXE instrument requires data reduction steps. A short overview of the required processing steps is given. The basic reduction pipeline is illustrated in figure 6.7. Not all reduction steps are necessarily required in the presented order; depending on the acquisition mode and foreseen usage of the datasets, several steps may be omitted. The reduction steps discussed in the following correspond to eponymous python scripts, which are made accessible in a GitHub repository (appendix B).

The beginning of all further data reduction work is given by the Filter step. During high-repetition-rate acquisition, detector images are commonly partially over- or underexposed. This is shown graphically in figure C.1 in the appendix. When the detector is underexposed, only a small number of fluorescence photons has been collected, and the integration of the detector area leads to an unfavorable ratio of background noise and actual extracted signal counts. Underexposure is usually rooted in experimental conditions, such as weak incoming photon flux, unstable sample jet delivery, or low sample concentration. In overexposed parts of the detector image, the linear relationship between detected photons and electronic readout signal might no longer be obeyed. For the determination of lower- and upper cut-off thresholds, a correlation between the $K\alpha_1$ and the weaker (assumed linear) $K\beta$ emission line peak intensities can be inspected. This correlation is shown for the presented experimental data in appendix C. Based on the determined thresholds, under- and overexposed image regions are identified and masked during the filter step.

During the Calibrate step, offset (dark) images are subtracted from the detector data. Since the JungFrau detector operates in a gain-switching mode, raw data must be corrected by applying the correct gain constant for each pixel and gain level. The gain state of each pixel is saved with the ADC values in the experimental file. More details are described by Redford et al. [164].

During this experiment, the JungFrau detector continuously collected images with a frequency of 10 Hz. When experimental parameters such as the pump-probe delay or the laser power were scanned during an acquisition, the timestamps and values of these scanned parameters were also collected. During the Sort step, images collected at the same scanned parameter position are averaged.

Specific pixels of the detector can be identified as bad pixels. This is possible, e.g., via a bad-pixel map provided by the detector or via inspection of the standard deviation of readout values of each pixel. Bad pixels are masked and usually discarded in the subsequent data reduction process. If required, masked values can be replaced by the mean of the closest neighboring pixel values. This can become necessary if the pixel lies

in a region of high intensity, and masking the bad pixel would result in a significant deviation from the estimated actual intensity during integration. This task is undertaken during the FILL step.

The INTEGRATE step averages each ROI along the non-dispersive direction. Adjacent to the signal ROI, two background regions are selected and subtracted from the final signal ROI to reduce the influence of the common scattering background on the final spectra.

Since the pixel size of the detector in the presented experiments was significantly smaller than the instrumental resolution, neighboring pixels were binned to improve statistics. This step is undertaken in the BIN module.

The pixel-to-energy calibration presents an essential step in the data reduction pipeline. In the presented datasets, the incoming photon beam was monochromatized with a four-bounce Si(1,1,1) monochromator and tuned to different energies around 6930 eV and 7650 eV in separate measurements. The incoming photons were scattered from a solid target, and the position of quasi-elastic reflection was collected with the same detector setup used for the presented XES measurements. For the scanned energy value and the recorded position of the reflection on the detector, a functional relationship between incoming energy and position can be assumed. For this relationship, the model

$$E = \frac{h_{eV} c \frac{d}{\sqrt{h^2+k^2+l^2}}}{\sqrt{\left(\frac{p}{2R}\right)^2 + 1}} \tag{6.5}$$

is fitted to the data, where E is the photon energy, h_{eV} the Planck constant in eV units, c the speed of light, R the working distance of the bend analyzer crystal, p the pixel position, d the lattice parameter of the installed analyzer crystal material and h, k, l the miller indices of the applied reflection. Values for R, d and h, k, l are listed in table 6.2 for both the Kα and Kβ diffraction case. The obtained relationship allows the conversion of pixels to energy within the ENERGY module.

To obtain transient differences between the pumped and unpumped XES spectra, difference curves are calculated in the SUBTRACT step. Uncertainties of the acquired spectra are propagated via the general formula of error propagation with the help of the UNCERTAINTIES python module [165].

The final ASSEMBLE step applies an area normalization and collects all results from previous steps of the reduction process into one file for further analysis.

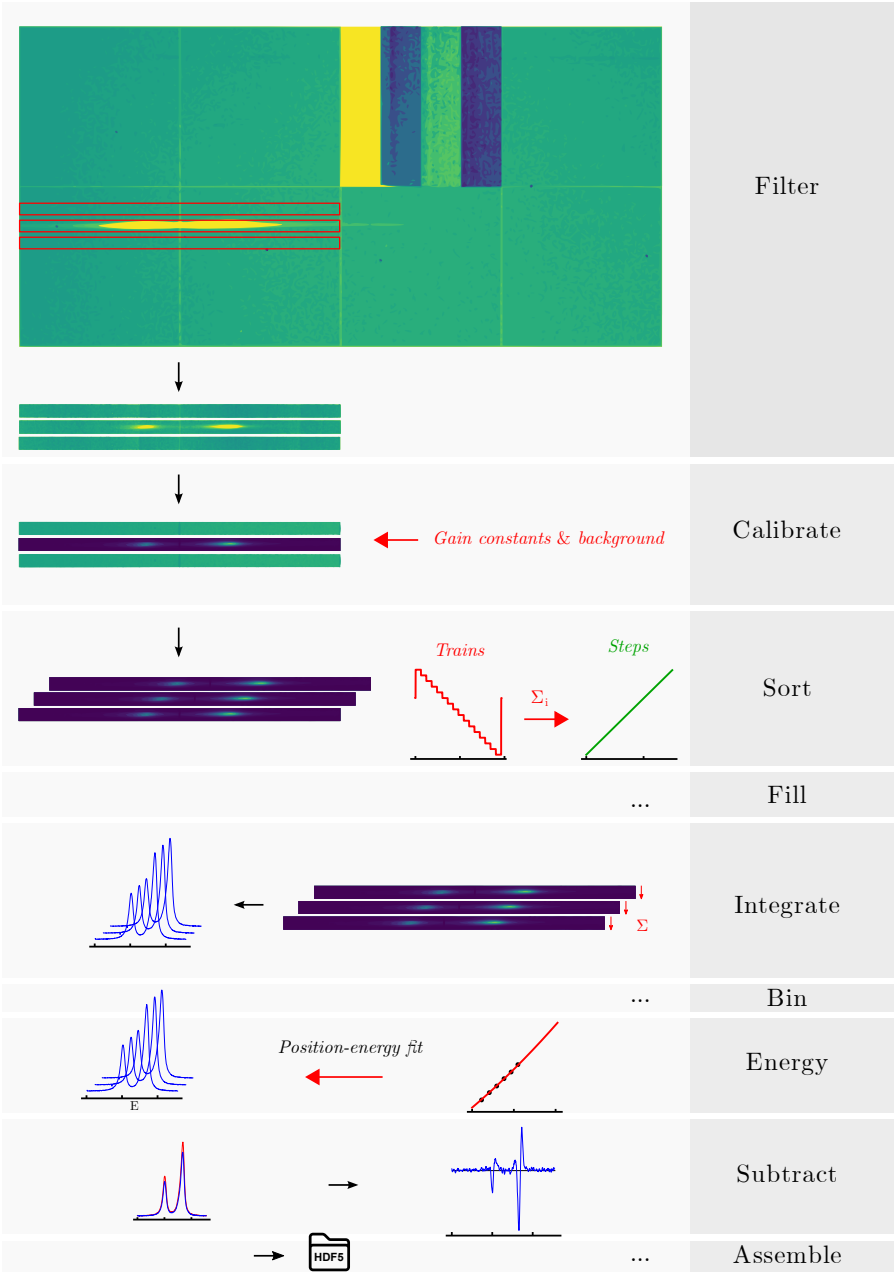

Figure 6.7: Data reduction pipeline for the transient XES data recorded at the FXE instrument at European XFEL.

6.4 Experimental results on $Co(DTB)_2(tmeda)$

This section reports on time-resolved experimental XES results on $Co(DTB)_2(tmeda)$ recorded at the FXE instrument. This section opens with a discussion on the solvent effect for cobalt VT complexes in toluene solution. Experimental parameters regarding the optical excitation laser power and the correction of timing drifts are reported in the subsequent paragraphs. Absolute transient Kα and Kβ spectra are presented and described in section 6.4.4. Transient difference spectra and kinetic traces are discussed next. Modeling approaches to the kinetic behavior observed in the transient data are presented in sections 6.4.7 to 6.4.9.

6.4.1 Solvation effects in cobalt VT compounds

Due to the nature of the time-resolved experiment and the requirement for a liquid jet sample delivery, $Co(DTB)_2(tmeda)$ was measured in toluene solution (cf. section 6.3.1). Solvent effects have been previously reported for a number of cobalt VT complexes [26, 40, 105, 166]. Experimentally, a systematic shift of the critical temperature going from acetonitrile - ethanol - methylene chloride - acetone - toluene for dissolved $Co(DTB)_2(bpy)$ was observed. As was noted by Evangelio et al., the shift of the critical temperature does not follow the sequence of dielectric constants of the investigated solvents. In general, the shift in the critical temperature has been attributed to a change in the entropy factor as described in eq. (2.2), which is influenced by the solvent [26, 138].

To experimentally verify the effect of the toluene solvent environment on the Kβ XES lineshape, measurements on both solid phase and a 5 mM toluene solution of $Co(DTB)_2(tmeda)$ were conducted at beamline GALAXIES at SOLEIL synchrotron, Saint-Aubin, France. The sample solution was prepared inside a cuvette and scanned vertically during the data acquisition in order to avoid radiation damage. Figure 6.8 displays the Kβ XES data on both solid and liquid phase sample. The solid-phase Kβ XES lineshapes measured at 80 K and 300 K show good agreement with previously recorded spectra from the ALBA synchrotron (cf. section 4.4.3), shown as solid lines in the left panel of figure 6.8. This confirms the validity of further results by showing that the sample did undergo the HS to LS tautomerization. Due to the significantly reduced sample concentration in the liquid phase, counting statistics of the acquired spectrum are too low for conventional analysis. A qualitative discussion of the recorded data can be conducted despite this limitation. The gray curve in the right panel of figure 6.8 illustrates an X-ray-induced change in the Kβ lineshape, which became apparent when the sample was irradiated for more than 10 minutes. A strong change in the optical absorption spectrum of the sample was observed during the measurement. The toluene solution featured the characteristic dark blue-green color of dissolved $Co(DTB)_2(tmeda)$ at shorter exposure times. After the measurement with longer integration times, an inspection of the sample by eye and UV/Vis spectroscopy revealed an almost transparent solution with no significant absorption bands in the visible region. Based on these findings, and since the change of lineshape was captured during the experiment, we

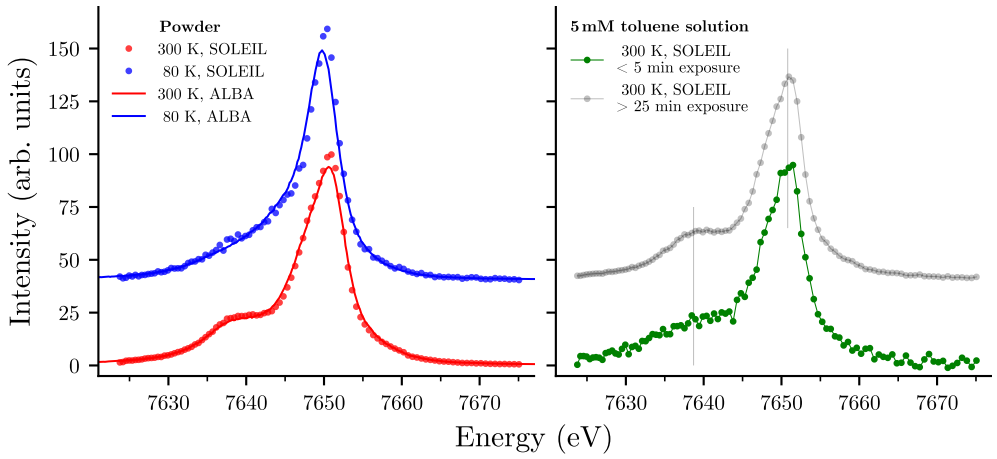

Figure 6.8: Static XES spectra of $Co(DTB)_2(tmeda)$ in solid powder from (left) at two temperatures and in 5 mM toluene solution (right). The gray spectrum on the right illustrates how the liquid sample line shape changes when the exposure threshold is exceeded.

attribute the spectrum marked in green in the right panel of figure 6.8 to the intact dissolved $Co(DTB)_2(tmeda)$ complex, while the gray curve likely corresponds to a decomposition of the metal complex, with changed cobalt configuration.

A qualitative comparison of the intact liquid phase Kβ curve (green curve in the right panel of figure 6.8) with data collected on the solid sample unveils significant differences in the Kβ' area. Here, the intensity of the dissolved sample in that region is lower than in the solid phase counterpart, while the position of the $K\beta_{1,3}$ remains similar. Following the notion of spin-sensitivity in Kβ XES emission signals, two fundamental conclusions might be discussed. Either the individual electronic configurations of the LS and HS phase VT species deviate from their counterparts in the solid sample. Alternatively, the electronic configuration of the individual species might stay as in the solid sample, but the VT equilibrium is shifted towards a higher fraction of Co^{3+} molecules in the dissolved sample. Based on the aforementioned influence of the solvent on the entropy factor as described by Evangelio et al. the second possibility seems more likely.

6.4.2 Determination of the instrumental t_0 parameter and the IRF

In pump-probe spectroscopy, a lower limit for the observable timescales of kinetic processes is given by the instrument response function (IRF). The IRF in pump-probe experiments stems from multiple sources of timing uncertainty. In the linear excitation regime, the convolution of the pump- and probe pulse introduces a temporal broadening to the observed kinetic timescales [167]. Additional components to the IRF commonly arise from uncertainties in the arrival times of the pump- and probe-pulse itself, e.g., due to temporal jitter between the pump- and probe pulse, as well as the group velocity

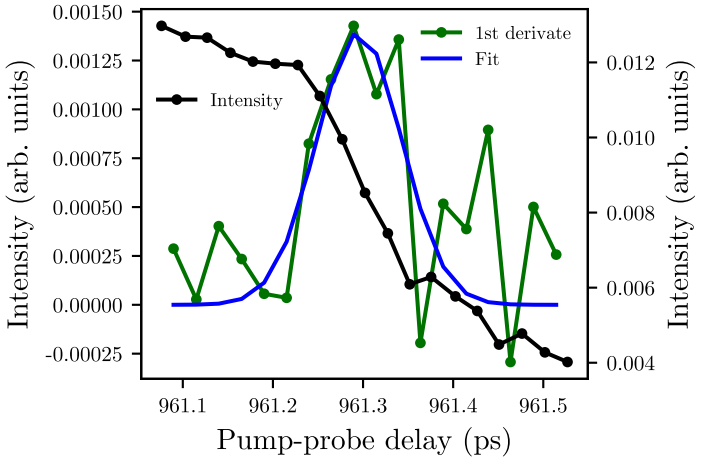

Figure 6.9: Fit of a Gaussian to the first derivative of the total Kα XES difference trace on $[Co(acac)_3]$ 5 mM in water.

mismatch and relative timing drifts. The IRF is commonly modeled with a Gaussian

$$\mathrm{IRF}(t, \sigma, \mu) = \frac{1}{\sigma\sqrt{2\pi}} \exp\left[-\frac{1}{2}\left(\frac{t-\mu}{\sigma}\right)^2\right]. \tag{6.6}$$

For practical reasons, the full width at half maximum (FWHM) of the Gaussian curve,

$$\mathrm{FWHM} = 2\sqrt{2\ln 2}\sigma, \tag{6.7}$$

will be given whenever the width of the IRF is discussed in the following.

For the determination of the IRF, a dataset collected on $[Co(acac)_3]$ 5 mM in water is inspected. A Gaussian function is fitted to the first derivative of the total trace extracted from the Kα XES transient difference signal. Based on the fit in figure 6.9, a FWHM value of

$$\mathrm{FWHM} = (112 \pm 26)\,\mathrm{fs} \tag{6.8}$$

is determined. This value is consistent with the previously reported IRF width at the FXE instrument [76].

The pump-probe delay during the experiment at the FXE instrument is controlled by a pump-probe optical delay line (PPODL), which allows the control of the absolute arrival time of the optical excitation laser-pulse at the sample position [163]. Since both the X-ray pulses and the optical laser pulses are subject to drifts in time[3], and jitter, absolute value settings for the PPODL line have to be adjusted for each experiment, and occasionally even in between individual data acquisition runs. As a result, values

[3]The reasons for these drifts in time are manifold and occur on multiple timescales. Discrete but large jumps in absolute arrival time are typically associated with setup changes (e.g., in the laser beam path) or variations in the electron orbit after FEL accelerator tuning. For more details, see [168].

for the time-delay between pump- and probe pulse are not given as relative differences but as absolute value settings for the pump-probe delay control mechanism, for which a common offset mode with no physical meaning needs to be subtracted. The subtraction value is denoted t_0 ("time zero") and must be determined. During the experiment, a rough estimation of the value for t_0 is possible by using a timing-diode at the sample position, whose electrical readout signal can be inspected on an oscilloscope. This method allows setting the relative laser/X-ray arrival time with an accuracy on the order of 20 ps. For a more precise determination of the t_0 value, fine delay-scans are recorded in the region of the previously estimated value. For those scans, the total integrated trace of the Kα region is fitted with an error function model

$$I(t, t_0, A, w) = A\left[1 + \mathrm{erf}\left(\frac{t - t_0}{\frac{w}{2\sqrt{2\log(2)}}}\right)\right], \tag{6.9}$$

where A and w are the amplitude and IRF FWHM width, and t_0 the determined relative delay between optical and X-ray pulse. The obtained value for t_0 is subtracted from the absolute values read from the PPODL delay control. Values for the pump-probe delay reported in the following have been corrected by this method to yield an estimate for the true relative delay. For the dataset of scans presented in the following, the standard deviation of the fitted t_0 was 0.083 ps. The integrated kinetic traces (cf. section 6.4.6) before and after t_0 correction are shown in figure 6.10. While the standard deviation of the fitted value for t_0 indicates that detectable drifts of the relative pump-probe delay occurred between the measurements, no major drifts in timing are observed. Based on figure 6.10 we conclude that the fitting method described above provides a good method for correcting timing drifts during this experiment. For spectra recorded at fixed delays, the trace fitting method for determining t_0 is not available. For these datasets, a valid t_0 estimate from the closest delay scan was taken.

6.4.3 Correlation of pump-laser power and transient signal strength

During this experiment, the pump laser power at the sample position was controlled via a motorized waveplate. To obtain the laser power for a given motor setting, a calibration measurement is required. For this, a power meter was illuminated with varying laser intensities. The calibration scan data is shown in appendix A. A polynomial fit to the calibration scan data provides the laser power for intermediate waveplate motor settings.

A linear relationship is imperative for the correlation between the pump laser power and the strength of the transient signal response captured via time-resolved XES. A non-linear transient signal response of the system may indicate two- or multi-photon absorption processes, which do not promote the system into the desired excited state. The relationship between pump-laser power and the integrated Kα transient signal strength for this experiment is shown in figure 6.11. Since the sample solubility was comparatively low (5 mM), the laser power in this experiment was set to be in the 55 - 70 µJ regime to still obtain satisfactory transient signal statistics in the weaker Kβ

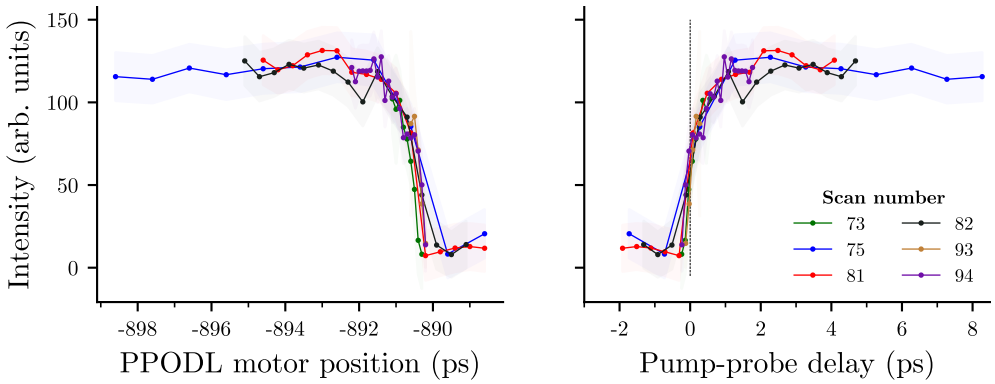

Figure 6.10: Total integrated kinetic traces extracted from transient Kα XES difference curves on $Co(DTB)_2(tmeda)$. Left panel shows the traces before t_0 correction with their respective absolute motor positions. The right panel shows the time-corrected kinetic traces. The standard deviation of the fitted t_0 parameter was 0.083 ps. The axis of the absolute motor positions is inverted due to technical reasons. Shaded areas indicate the measurement uncertainty of each curve.

region. In comparison with other studies on TM complexes, the molar extinction of $Co(DTB)_2(tmeda)$ at 800 nm is relatively low ($1700\,\frac{1}{\mathrm{cm\,M}}$), which decreased the ability for the creation of a significant portion of excited molecules when using lower laser power. A comparison of scaled transient difference curves recorded at increasing laser power is displayed in the right panel of figure 6.11.

An important parameter is the ratio of exciting laser photons and molecules inside the irradiated sample volume. From the molar extinction ϵ, the attenuation cross-section and the Avogadro constant N_A,

$$\sigma = \ln(10)\frac{10^3}{N_A}\epsilon \tag{6.10}$$

can be calculated. The attenuation cross-section is a measure of the probability of interaction with an impinging photon. From steady-state UV/Vis spectroscopy data of $Co(DTB)_2(tmeda)$ 5 mM in toluene, a molar extinction value of $1700\,\frac{1}{\mathrm{cm\,M}}$ at 800 nm was determined (cf. appendix E). The laser fluence Φ is given as the number of photons per unit area and is calculated from the total energy per laser pulse E and the energy of an individual photon with a wavelength λ as well as the beam size A according to

$$\Phi = \frac{E}{A\frac{hc}{\lambda}}. \tag{6.11}$$

In this equation, c denotes the speed of light, and h is the Planck constant. For a laser pulse energy of 50 µJ and a beam size of $A = 100 \times 100\,\mu m^2$, the fluence for 800 nm photons $\Phi = 1.6 \times 10^{18}\,\frac{\mathrm{ph}}{\mathrm{cm^2\,pulse}}$ is determined. The resulting ratio of laser photons per attenuation cross-section is $10\,\frac{\mathrm{ph}}{\sigma}$. This value is discussed in combination with the simulation approach presented next.

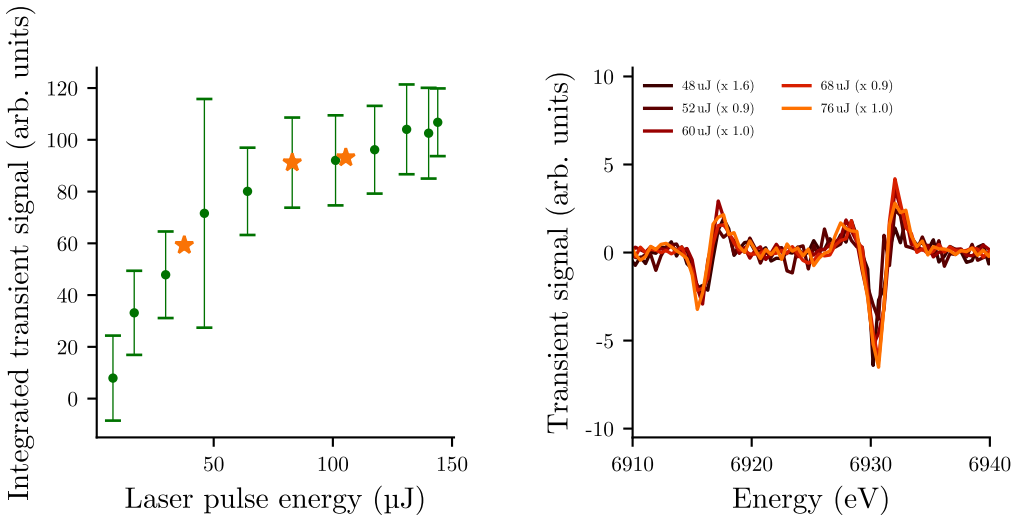

Figure 6.11: Correlation between integrated transient signal strength and pump-laser power. The pump-probe time-delay was set to 1 ps. Stars give values at which datasets in this study were collected.

We are discussing a different way of estimating the ratio of absorbed photons and molecules under consideration of jet geometry. Due to absorption of the impinging light in the sample and solvent according to the Beer–Lambert law, an exponential decrease of intensity inside the liquid jet is expected. Additionally, in the case of round jets, a lensing effect for transmitted light contributes to the inhomogeneous distribution. A raytracing routine with subsequent rasterization was utilized to evaluate the ratio of laser photons and sample molecules inside a round jet. The position and size of the pump laser source, the jet diameter and position, and the focal point of the laser source were used in this raytracing simulation. Specifically, absorption inside the sample and diffraction at the jet boundary via the Fresnel equations were considered. In a second step, the simulation domain was divided into smaller cuboidal subdomains (voxels[4]). For each voxel, the path of all intersecting rays was calculated. The intensity decay of the individual rays along this path was added to the total voxel intensity. The rays' total intensity was reduced by the same amount. This procedure was repeated until all rays had been traced to the opposite side of the simulation domain or no intensity was left. For calculating the ratio between absorbed photons and molecules, a homogeneous sample concentration within the jet diameter was assumed. For each voxel, the individual number of absorbed photons was divided by a constant fractional amount of sample molecules. The absorption of a ray passing along a path l inside a voxel was calculated via

$$I_{\text{out}}(l_{\text{voxel}}) = I_{\text{in}} \cdot 10^{\epsilon c l}, \tag{6.12}$$

[4]We are using the term voxel in its most general scope here, i.e., a gapless three-dimensional arrangement of small regular cubes is described.

Table 6.3: Parameters values for raytracing simulations on a round liquid jet

Property	Case 1	Case 2	Unit
Laser wavelength	800	800	nm
Laser spot size	100 x 100	300 x 100	μm^2
Laser power	55	55	µJ
Sample concentration	5	5	mM
Molar extinction	1700	1700	$\frac{1}{\text{cm M}}$

with the molar extinction ϵ and the sample concentration c.

The results of the simulations are displayed for two focal sizes of the laser beam in figure 6.12. To exclude influences from the voxel cell size and the number of traced rays, both values were increased until a plateau was reached. For the final simulation, 64 x 64 x 64 (262144) voxels, and 10^6 rays were used per case. The calculated ratio for both cases lies above the one photon per molecule threshold. This effect is mitigated by the fact that the probing X-ray pulse impinging the sample from the right in the simulations mostly interrogates molecules that lie outside the region with elevated ratios. The simulation parameters are listed in table 6.3. In the simulations, a larger spot size leads to a generally lower absolute absorption inside the sample since the laser power is distributed over a larger source size, and thus only a fraction of photons is impinging on the smaller jet surface. These simulations offer a conservative estimation of the ratio between absorbed photons and sample molecules. Since the laser footprint is not

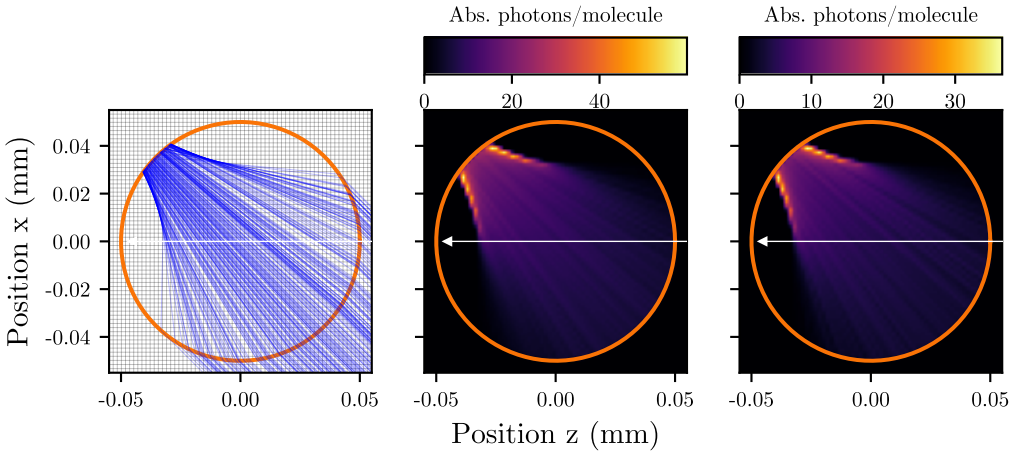

Figure 6.12: Estimation of absorbed optical photons per molecule inside a 100 µm diameter liquid jet. Raytracing step (left), visualizing a small subset of the simulated optical paths. The grey grid indicates the size of the voxels used in the rasterization step. The center and right panels show two cases with different laser spot sizes after rasterization. Parameter values for the simulation are given in table 6.3. The laser enters the simulation domain from the bottom right.

much larger than the jet diameter, small fluctuations in the jet can quickly lead to significantly reduced fractions of excited molecules. Based on the simulation results, a mean ratio between absorbed laser photons and molecules in the X-ray beam path of 1 - 10 is estimated. This value is in agreement with the number of photons per attenuation cross-section determined above and with the onset of a plateau-like level in figure 6.11 at slightly higher energies. Control by online UV/Vis spectroscopy during the experiment did not reveal any changes in the UV/Vis spectrum, which supports the hypothesis that no permanent photo-degradation did occur despite the increased photon flux.

6.4.4 Description of XES line shapes

We begin the discussion of time-resolved XES data on Co(DTB)$_2$(tmeda) in toluene solution with a description of the collected Kα and Kβ emission signals. A selection of spectra recorded at different time-delays is shown in figure 6.13. The curves are divided into optically-excited (laser-pumped, P) and non-excited (laser-unpumped, U) GS spectra. In both the Kα_1 and Kα_2 emission lines, a reduction of peak intensity with increasing time-delay is observed. Additionally, the Kα_1 peak exhibits a shift to higher energies. Similarly, the K$\beta_{1,3}$ emission feature presents a shift to higher energies with increasing time-delay. Since the magnitude of the observed photo-induced line shape changes is on the order of 1 %, a more detailed analysis of spectral changes is saved for the discussion of the transient difference curves in the following section. The laser-unpumped spectra recorded at different time-delays agree within the reported measurement uncertainty. This is an important indication that the filtering and normalization process during data reduction was successful, and the subsequent difference curves are indeed descriptive of actual changes in the laser-pumped spectrum.

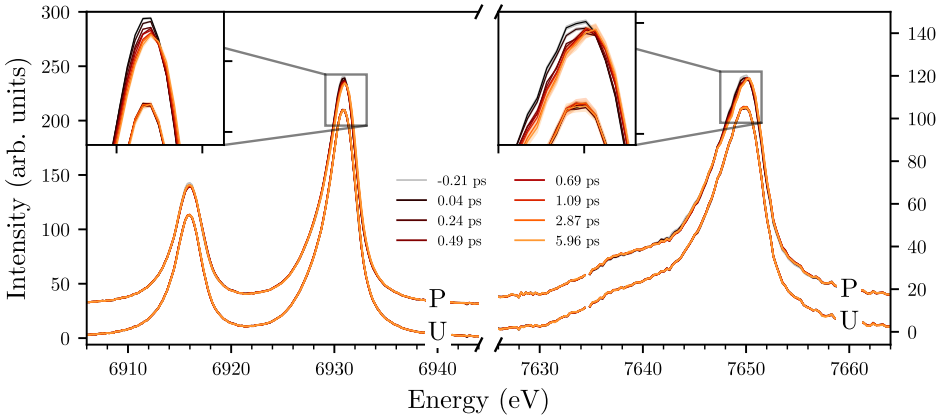

Figure 6.13: Transient XES data on Co(DTB)$_2$(tmeda) in toluene solution, displaying unpumped (non-excited) spectra (U) and pumped (laser-excited) spectra (P). A vertical offset has been added to the pumped spectra for visual clarity. The inset illustrates the magnitude of typical line shape changes observed during this experiment. The measurement uncertainty is given as shaded areas.

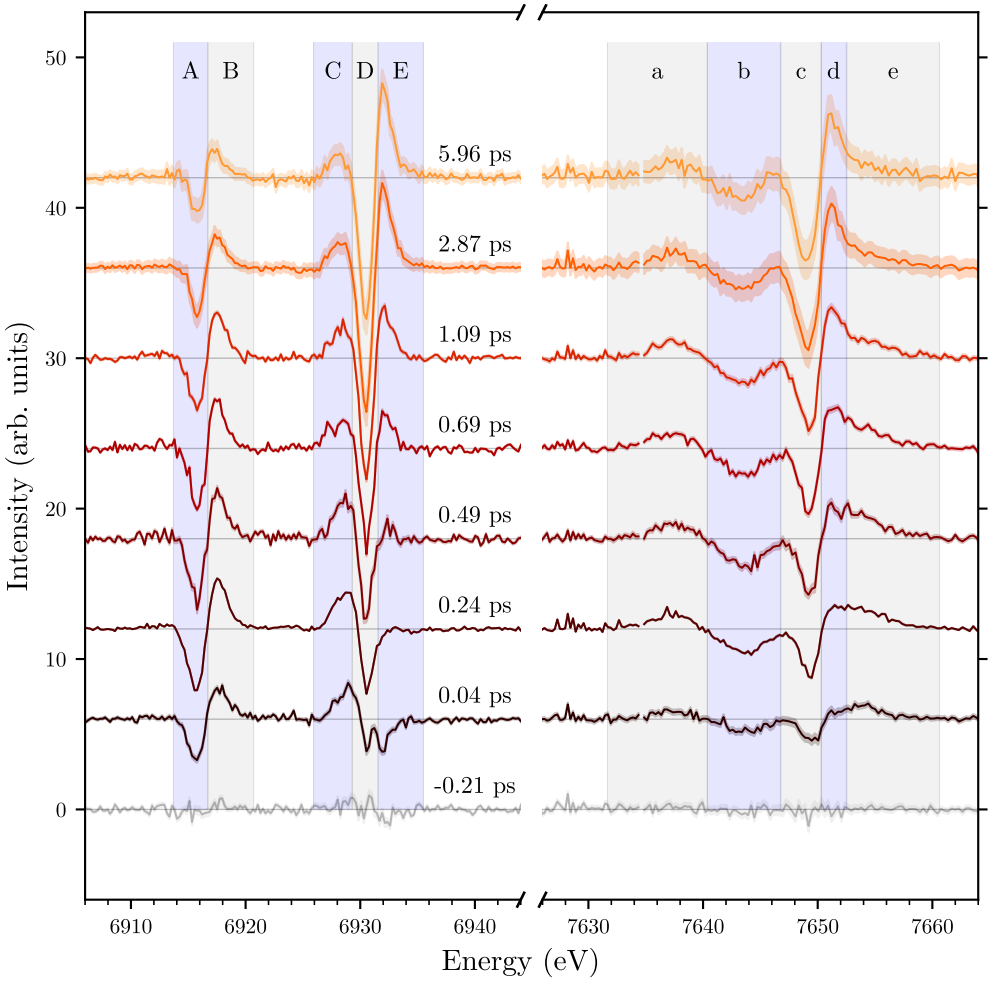

Figure 6.14: Transient Kα (left) and Kβ (right) XES difference curves (P - U) on $Co(DTB)_2(tmeda)$ in toluene solution. Selected time-delays are shown. Transient features are labeled in increasing energy order. Spectra recorded at different pump-probe delays are shifted vertically for visual clarity. Colored shaded areas indicate the propagated measurement uncertainty.

6.4.5 Discussion of transient difference spectra

For the extraction of subtle line shape changes, transient difference curves are calculated for each time-delay as the difference between laser-pumped and laser-unpumped spectra. Positive values at given emission energy in the transient line shape thus correspond to an increase in the laser-pumped excited emission intensity and vice-versa. A selection of transient difference curves from simultaneously collected Kα and Kβ XES spectra on $Co(DTB)_2(tmeda)$ are shown in figure 6.14. The presented transient lineshapes correspond to the absolute spectra given in figure 6.13. Curves in the right panel exhibit a gap in the data at 7634.5 eV, which stems from a detector module border.

The transient Kα emission signal exhibits five regions of individual temporal behavior. For further analysis, these regions are labeled A-E. The Kα_2 region around 6915 eV exhibits a quasi-instantaneous transient signal of two almost point-symmetric features at 6915.7 eV (minimum at A) and 6917.5 eV (maximum at B). No significant differences in the temporal evolution of regions (A) and (B) can be identified. Due to the high degree of symmetry and the similar timescales, a shift of the Kα_2 peak centroid towards higher energies is assumed as the dominant explanation for the occurrence of the early transient signature. At later time-delays, both the (A) and (B) transient features decrease in intensity, and a small amount of asymmetry is introduced. A subtle change in Kα_2 peak shape seems likely, combined with a partial return towards the original energy position.

The Kα_1 transient line shape in the region around 6930 exhibits three regions with distinct temporal evolution. A weak shifting maximum at ca. 6928.5 eV (C) appears almost instantaneously and undergoes a weak decay in intensity with increasing pump-probe time-delay, coupled with a centroid shift of around 0.5 eV. The weak decay and energy shift stabilize between 1 ps to 2 ps. Over the same period, a strong minimum at 6930.5 eV (D) exhibits a much slower gradual rise in intensity, with a similar stabilization behavior within 2 ps. A third, initially negative feature is found at the higher energy tail of the Kα_1 emission region (E). After roughly 200 fs, the sign of the feature inverts, and a positive signal with a slow, gradual rise in intensity starts to appear. This feature exhibits similar kinetic behavior as the (D) feature. In general terms, significant differences between the temporal behavior of the Kα_1 and Kα_2 emission lines are observed in that the Kα_2 region dominantly exhibits very fast and monotonic temporal behavior. In contrast, the Kα_1 region presents two distinct temporal components with different timescales.

The transient Kβ XES difference curves exhibit five distinct spectral regions. A fast quasi-instantaneous rise of a broad maximum with no significant temporal evolution until 5 ps is found at 7637.3 eV (a). A slightly less broad minimum at 7643.5 eV (b) presents a similar quasi-instantaneous rise in intensity but exhibits a weak decay towards higher pump-probe time-delays, accompanied by a subtle shift towards lower energies of about 0.5 eV. A second strong minimum at 7649.3 eV displays a slower, gradual rise in intensity combined with a widening and a shift of around 0.3 eV towards lower energies. As in the case of the Kα_1 emission feature, a plateauing effect appears towards higher time-delays. An asymmetric maximum at 7651.2 eV (d) exhibits a similar gradual rise in intensity as (c), but no significant shift in position is observed. The tail in the spectral region covering the emission energies just above (d) at 7655.3 eV (e) presents a fast rise and a subtle decay towards higher time-delays.

While spectral changes can easily be accessed via inspection of the entire transient line shapes as in figure 6.14, analysis of the temporal evolution is more instructive when undertaken with the help of kinetic traces, which are constructed from integrating the discussed spectral domains along the energy axis. This reduces the dimensionality of the dataset and eases the comparison of temporal behavior between different regions of the transient spectrum. As in the case of the transient Kα emission signal, significant differences in the temporal evolution of the individual Kβ spectral regions are identified. This underlines the need for a careful inspection of the transient line shapes before

spectral integration, especially if an analysis of the particular timescales involved in the photo process is required. A downside to the trace integration method is its susceptibility toward transient intensity shifting in or out of the integration domains. An example of this effect can be observed in the transition region between features (C) and (D) in the $K\alpha_1$ transient signal, where a shift of the zero-crossing hardens the choice of a sensible integration border. In this specific case, we deem the intensity of the neighboring features to be sufficiently high for a meaningfully integrated trace. After discussing the kinetic traces, a different analysis approach via model-based fitting is pursued.

6.4.6 Analysis of kinetic traces

Different options for the numerical integration of transient difference curves are available. Integrating transient signals with both positive and negative parts requires a decision regarding the treatment of opposing signal signs. Either the targeted region is partitioned into sub-parts of equal signs (with a subsequent sum over the absolute integral values), or a single integral over the absolute or squared signal can be carried out. While the latter requires less manual intervention and is usually faster to implement, care has to be taken in regions where the transient signal amplitude is of similar or smaller magnitude as the intrinsic noise level (relevant commonly in regions of small transient signal). Counter-intuitively, the summation of absolute values in these regions can impair the resulting integrated trace's statistical quality since the noise distribution is not preserved. This renders the error-canceling effect of summation or averaging over multiple values in a spectral region inactive. In this work, we are pursuing the partition approach, i.e., with *integration* a simple numerical sum is denoted.

Since the laser-pumped and laser-unpumped spectra are normalized before subtraction, the *total* integrated signed trace area should remain constant around zero. If deviations from zero are observed, either noise or failing area normalization of the individual absolute spectra can be suspected. The signed (pure sum) and absolute integrated transient signals are shown in comparison in appendix A. In light of the estimated measurement uncertainty of the displayed traces, no significant deviation of the signed signal sum from zero is found in the $K\alpha$ nor $K\beta$ spectral region. Since this indicates the conservation of area for the laser-pumped and laser-unpumped spectra, we can assume that the normalization of all experimental spectra was successful. The direct comparison between the two total integrated kinetic traces from the $K\alpha$ and $K\beta$ transient XES region indicates diverging temporal behavior, which underlines the benefit of collecting multiple XES emission lines simultaneously. The rise of the $K\alpha$ emission feature occurs roughly 240 fs earlier. As we see from figure 6.15, this quick rise mainly stems from the $K\alpha_2$ region and the low energy tail of the $K\alpha_1$ peak.

For the shaded regions around (A-E) and (a-e) in figure 6.14, traces are shown in figure 6.15. Since the selection of the integration borders for each spectral region was based on the previous inspection of the transient lineshape behavior, we are assuming that the temporal evolution of spectral components is the dominating signature in the kinetic traces, and cross-correlating effects due to shifting intensity between integration regions can be neglected. Since the visual analysis of the transient lineshapes revealed

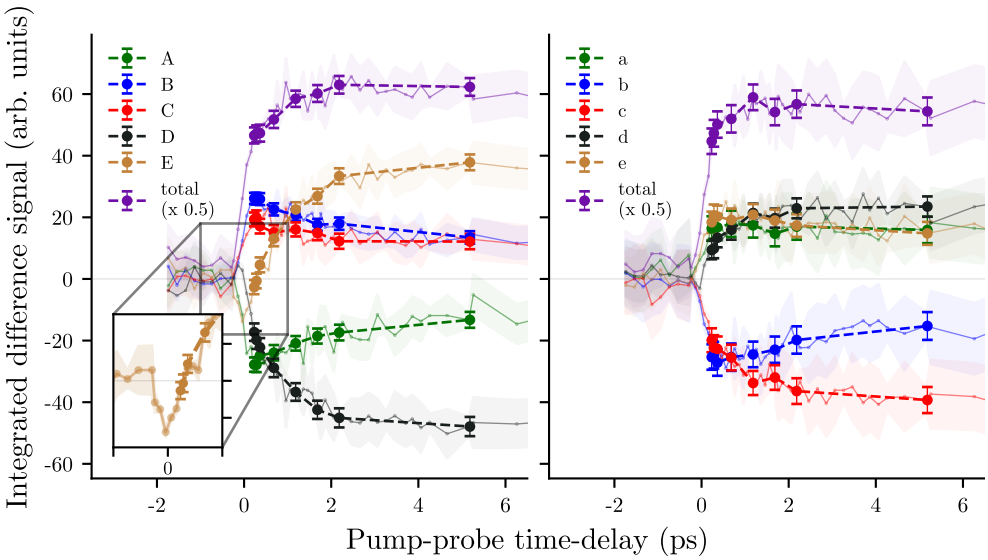

Figure 6.15: Integrated Kα (left) and Kβ (right) XES difference curves (traces). Error bars (fixed delay) and shaded areas (delay scans) give the standard error of the mean as an indication of measurement uncertainty.

a slower and at least one very fast kinetic component, we are expecting evidence of at least two different timescales in the integrated traces. This is confirmed by the Kα XES traces, which exhibit at least two different temporal components. A fast rise is visible in the traces (A-C) and a change in sign at times below 500 fs for the (E) feature. The components (D) and (E) exhibit a slow exponential rise in intensity at pump-probe time-delays above 500 fs, with a simultaneous decay in intensity for features (A-C). Within the experimental uncertainty, no clear distinction can be made about the possibility of a multi-exponential decay at later times. A very weak decay of the total absolute summed trace (purple trace in figure 6.15) as well as in the traces for (A) and (B) may indicate a third slow exponential decay component that is not captured within the observed time window.

The traces for the Kβ XES region exhibit a fast sub 200 fs rise, with an additional slower time component observed in the (c) and (d) traces. A weak exponential decay is hinted at for (a) and (e) and clearly observed for (b). The integrated traces generally indicate at least one exponential rise component during the observed time frame and a fast sub 200 fs increase in initial intensity.

The comparison of trace intensities in figure 6.15 well illustrates a commonly exploited experimental fact: Relative XES line shape changes in the $K\beta_{1,3}$ region are stronger than for Kα features, and integrated trace signals are thus comparable despite the roughly tenfold smaller Kβ XES signal.

As mentioned above, total integrated sum traces for the Kα and Kβ spectral regions exhibit variations in the exponential rise behavior, which hints at potentially different sensitivity toward the underlying kinetic processes (cf. figure 6.16). We will attempt

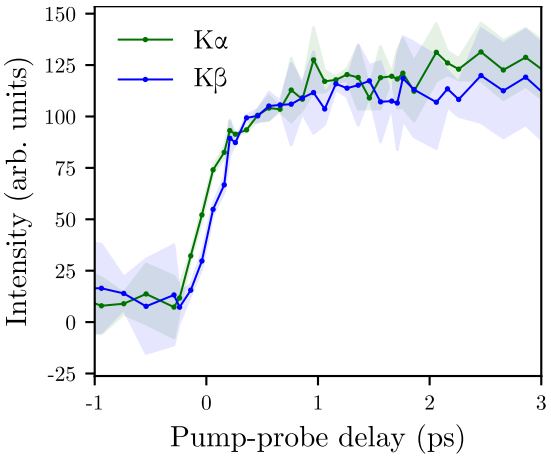

Figure 6.16: Difference in the temporal behavior of the normalized total integrated kinetic traces from the Kα and Kβ transient XES region.

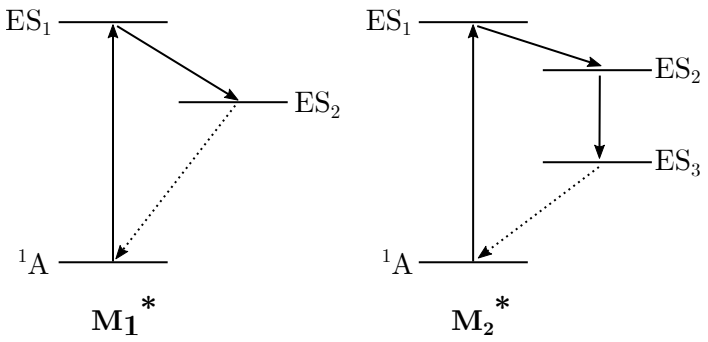

Figure 6.17: Abstract term schemata visualizing the two applied fitting models M_1^* and M_2^*.

quantification of these processes in the following sections.

6.4.7 Cobalt transient XES data modeling

For the extraction of time constants and the description of the temporal behavior of laser-excited $Co(DTB)_2(tmeda)$ in toluene solution, a kinetic model-fitting approach based on the exponential decay of excited state populations is pursued [167].

Derivation of one- and two-exponential decay models

Since the photocycle of $Co(DTB)_2(tmeda)$ at timescales on the order of picoseconds or shorter is not known, a generic excitation model based on the $^1A_1$ GS and two or three excited states [ES] was chosen (cf. figure 6.17).

The model equations are derived by starting with the differential rate equations. If the return into the $^1A_1$ ground state is much slower than the observed timescales, a one-exponential decay model for the sequential population of two excited states [ES$_i$]

$$[ES_1] \longrightarrow [ES_2] \quad (\longrightarrow {}^1A_1) \tag{6.13}$$

is described by the differential rate equations

$$\frac{d[ES_1]}{dt} = -k_1[ES_1], \tag{6.14}$$

$$\frac{d[ES_2]}{dt} = k_1[ES_1]. \tag{6.15}$$

$$\tag{6.16}$$

Variation of parameters solves the differential equations and gives the time-dependent populations [150]

$$[ES_1] = [ES_1]_0 \exp(-k_1 t), \tag{6.17}$$

$$[ES_2] = [ES_1]_0 [1 - \exp(-k_1 t)]. \tag{6.18}$$

The one-exponential decay model M_1 is then described by the sum of the individual populations, scaled by amplitudes A_i, which take the individual spectral footprints of the excited states into account

$$M_1 = A_1[ES_1] + A_2[ES_2]. \tag{6.19}$$

Adding one excited state with an exponential decay component

$$[ES_1] \longrightarrow [ES_2] \longrightarrow [ES_3] \quad (\longrightarrow {}^1A_1), \tag{6.20}$$

the differential rate equations become

$$\frac{d[ES_1]}{dt} = -k_1, \tag{6.21}$$

$$\frac{d[ES_2]}{dt} = k_1[ES_1] - k_2[ES_2], \tag{6.22}$$

$$\frac{d[ES_3]}{dt} = k_2[ES_2]. \tag{6.23}$$

From there, variation of parameters yields the following time-dependent populations

$$[ES_1] = [ES_1]_0 \exp(-k_1 t), \tag{6.24}$$

$$[ES_2] = [ES_1]_0 \frac{k_1}{k_2 - k_1} [\exp(-k_1 t) - \exp(-k_2 t)], \tag{6.25}$$

$$[ES_3] = [ES_1]_0 \left(1 - \frac{k_2 \exp(-k_1 t) - k_1 \exp(-k_2 t)}{k_2 - k_1}\right). \tag{6.26}$$

As for the one-exponential decay, the two-exponential decay model M_2 is described by the sum of the individual populations

$$\mathrm{M}_2 = A_1[\mathrm{ES}_1] + A_2[\mathrm{ES}_2] + A_3[\mathrm{ES}_3]. \tag{6.27}$$

If the observed timescales are comparable to the width of the IRF, the kinetic model has to be convolved with the IRF. Taking M_2 as an example and utilizing the distributivity property of the convolution ($*$), we may account for the IRF as

$$\mathrm{IRF} * \mathrm{M}_2 = \mathrm{IRF} * A_1[\mathrm{ES}_1] + \mathrm{IRF} * A_2[\mathrm{ES}_2] + \mathrm{IRF} * A_3[\mathrm{ES}_3]. \tag{6.28}$$

We are describing the IRF with a Gaussian. The convolution $C := G * D$ of a Gaussian G with an exponential decay D

$$G(t, \sigma, \mu) = \frac{1}{\sigma\sqrt{2\pi}} \exp\left[-\frac{1}{2}\left(\frac{t-\mu}{\sigma}\right)^2\right], \tag{6.29}$$

$$D(t, k) = \exp(-kt), \tag{6.30}$$

is given by the exponentially modified Gaussian (EMG) [169]

$$C(t, k, \mu, \sigma) = \frac{1}{2} \exp\left[-k\left(t - \mu - \frac{\sigma^2 k}{2}\right)\right] \cdot \left[1 + \mathrm{erf}\left(\frac{t-\mu}{\sqrt{2}\sigma} - \frac{\sigma k}{\sqrt{2}}\right)\right]. \tag{6.31}$$

For the convolved model $M_1^* := G * M_1$ this yields

$$[\mathrm{ES}_1]^* = [\mathrm{ES}_1]_0 \; C(t, k_1, \sigma, \mu) \tag{6.32}$$

$$[\mathrm{ES}_2]^* = S - [\mathrm{ES}_1]^* \tag{6.33}$$

$$M_1^* = A_1[\mathrm{ES}_1]^* + A_2[\mathrm{ES}_2]^* \tag{6.34}$$

and for $M_2^* := G * M_2$

$$[\mathrm{ES}_1]^* = [\mathrm{ES}_1]_0 \; C(t, k_1, \sigma, \mu) \tag{6.35}$$

$$[\mathrm{ES}_2]^* = [\mathrm{ES}_1]_0 \frac{k1}{k2 - k1} \left[C(t, k_1, \sigma, \mu) - C(t, k_2, \sigma, \mu)\right] \tag{6.36}$$

$$[\mathrm{ES}_3]^* = S - [\mathrm{ES}_1]^* - [\mathrm{ES}_2]^* \tag{6.37}$$

$$M_2^* = A_1[\mathrm{ES}_1]^* + A_2[\mathrm{ES}_2]^* + A_3[\mathrm{ES}_3]^*. \tag{6.38}$$

The function

$$S(t, \sigma) := [\mathrm{ES}_1]_0 H(t) * G(\sigma) = [\mathrm{ES}_1]_0 \left[1 + \frac{1}{2}\,\mathrm{erf}\left(\frac{t}{\sqrt{2}\sigma}\right)\right] \tag{6.39}$$

in eqs. (6.33) and (6.37) is needed to model the step-like rise in initial population of the first excited state and stems from the convolution of a Gaussian with the Heaviside function. The kinetic evolution of both models is visualized in figure 6.18. An abstract term scheme is given in figure 6.17.

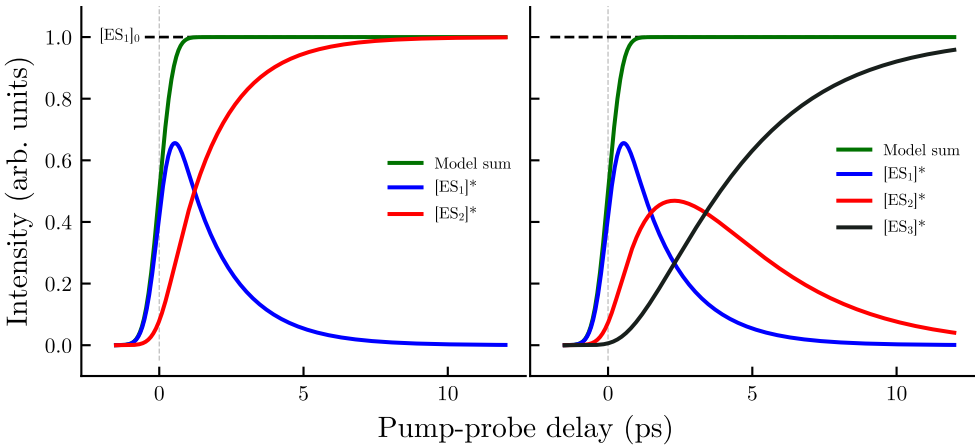

Figure 6.18: Kinetic models used for the description of transient XES data. Left: One-exponential decay model, with two excited states. Right: Two-exponential decay model with three excited states. Example values have been chosen for the model parameters: $t_1 = 1.7\,\text{ps}$, $t_2 = 3\,\text{ps}$ and $\text{FWHM}_{\text{IRF}} = 1\,\text{ps}$. The value for the width of the IRF has been strongly exaggerated.

Global fitting approach

The in section 6.4.7 introduced individual amplitudes A_i allow the relative weighting of the temporal model components i when modeling a dataset. This approach can be extended towards the fitting of multiple datasets at once (Global fitting [167]), where each dataset D_k is modeled by an individual set of component amplitudes A_i^k. The global time constants t_i and the width of the IRF are constrained to be identical for all datasets.

6.4.8 Model-based analysis of kinetic traces

We begin the model-based analysis of the transient XES data on $Co(DTB)_2(tmeda)$ with a one- and two-exponential global fitting approach to the kinetic traces illustrated in figure 6.15. To investigate if a one-exponential decay model can adequately describe the data, all ten kinetic traces are fitted simultaneously by the M_1^* model described in eq. (6.34). The variable fitting parameters contain the individual component amplitudes A_i^k for each temporal component i and each kinetic trace dataset k. In the one-exponential decay case, one time constant t_1 is fitted. The parameter value for the width of IRF of 112 fs is held fixed (cf. section 6.4.2).

The fitting results for the one-exponential decay are visualized in figure 6.19. The top panels display the experimental values and the fitting model evaluated for each trace dataset, based on the individual component amplitudes and the global optimized time constant parameter. The bottom panel gives the fit residuals, with shaded areas indicating the propagated measurement uncertainty of each dataset. Since more data points were collected in the vicinity of the kinetic trace rise around t_0, better counting

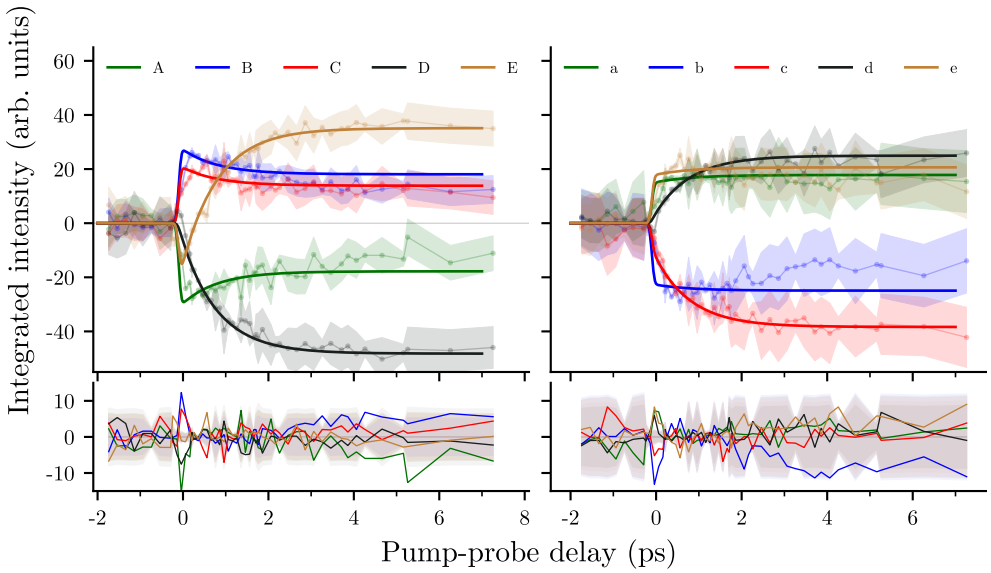

Figure 6.19: One-exponential decay global fit of traces A-E (Kα, left) and A-D (Kβ, right). Top panels display the experimental data and fitted kinetic components. Bottom panels indicate the fitting residual (lines) and experimental uncertainty (shaded areas).

statistics and smaller uncertainties in that region are expected. At later pump-probe time-delays, both lower total integration times and coarser scan step size lead to an increase in measurement uncertainty. The increase in measurement uncertainty from smaller time-delays to larger times is not constant because delay scans with different step sizes and integration times were merged for the complete fitted dataset. The individual datasets which entered this analysis are displayed in figure 6.10 in section 6.4.2. The reduced χ^2_{red} value is commonly inspected as an estimate for the goodness of fit. For the optimized fit result, a value of $\chi^2_{\mathrm{red}} = 0.68 < 1$ was obtained. This can be explained by the fact that large measurement uncertainties are present in the Kβ traces and, for both Kα and Kβ traces, at negative pump-probe time-delays. This indicates that while, intuitively speaking, data with small measurement uncertainty around t_0 may be well captured by the model, remaining data with much larger uncertainties decrease the χ^2 value. The simple χ^2_{red} metric might thus not be sufficiently sensitive for this dataset, and a careful inspection of the fitting residuals is imperative. No significant correlations between fitting parameters is reported.

The agreement between the fitted one-exponential decay model and the experimental traces for the Kα XES region is satisfactory at pump-probe delays between 0.5 and 2 ps. The fit residuals exhibit a significant exceedance of the experimental uncertainty around t_0, which is explained by the absence of a fast time component required to model the earlier pump-probe time-delays. At later delay times, the fitted decay constant given in table 6.4 describes the dominant temporal behavior of the Kα trace significantly better, with no significant deviation of the model from the experimental data within the measurement uncertainty. At pump-probe delays around 2.5 ps, the temporal

Table 6.4: Fitted time constant for the one-exponential decay model on kinetic traces extracted from the transient differences in the Kα and Kβ region.

Property	Fitted value	
t_1	0.83 ± 0.09	ps

behavior is not captured sufficiently anymore, which is indicated by the exceedance of the measurement uncertainty for the (A) component in the Kα trace. The slower rise, which the fitted model describes well, dominates in the components (D) and (E), which explains the smallest residual values for this datasets. The integrated trace components (D) and (E) correspond to the central peak and high-energy tail of the $K\alpha_1$ emission line.

In the Kβ traces, the model satisfactorily describes only the (c) and (d) components. As in the case of the Kα traces, this is caused by the absence of a faster time component needed to explain the early pump-probe time-delays after t_0. This is further illustrated by the significant deviations from the experimental data observed for all traces at t_0. The two trace components which are sufficiently described correspond to the $K\beta_{1,3}$ main peak region. The faster traces which are not well captured constitute the Kβ' region and the high-energy tail of the Kβ mainline peak. Based on the observation that significant deviations between the one-exponential decay model and the experimental data are present at both short time-delays around t_0 and later delays, a two-exponential decay model is attempted next.

In the two-exponential decay model M_2^*, two time constants t_1 and t_2 model the sequential population of three excited states. With this, an additional individual component amplitude A is introduced (cf. eq. (6.38)). As in the previous case, the parameter value for the width of the IRF is fixed.

The optimized model parameters are illustrated in figure 6.20. Compared with the above model, significant improvement in overall agreement with the experimental traces is observed. The reported χ^2_{red} value for this fit is 0.24. As discussed above, we add the discussion of the fitting residuals for a more reliable analysis of fit quality since large variations of the experimental uncertainty of the fitted data points hinder the conventional interpretation of the χ^2_{red} value. As in the previous case, no significant correlation between fitting parameters is observed. The improved agreement between experimental data and optimized model parameters is indicated by the absence of significant structure in the fitting residuals, as shown in the lower panels of figure 6.20. The optimized parameter values for the time constants are given in table 6.5.

As in the case of the one-exponential decay fit, a slower time constant of around 1 ps is found. Additionally, a very short time constant of ca. 250 fs is found for t_1, which corresponds to a very fast decay of the first modeled excited state, with an almost immediate subsequent population of the second modeled excited state. As supported by the residual plots and the agreement between the evaluated model components in both the bottom and top panels of table 6.5, this enables good modeling of the observed

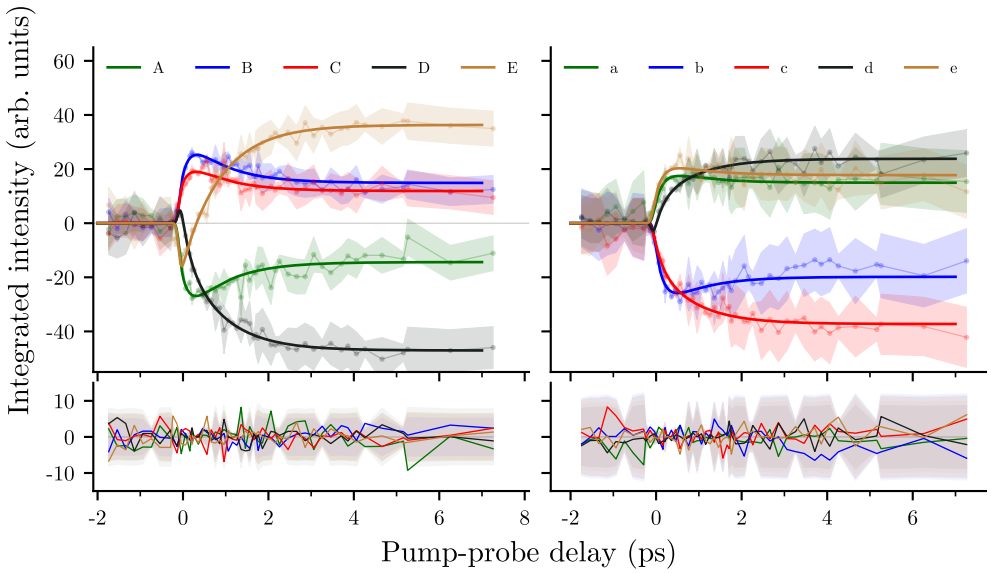

Figure 6.20: Two-exponential decay global fit of traces A-E (Kα, left) and A-D (Kβ, right). The top panels display the experimental data and fitted kinetic components. The bottom panels indicate the fitting residual (lines) and experimental uncertainty (shaded areas).

experimental traces. Specifically, the fast initial inversions of sign for the kinetic traces (D) and (E) in the Kα region are picked up by the inclusion of a second time constant in the fitting model. The general agreement along the whole recorded pump-probe delay region is within the experimental uncertainty, with a slight overestimation of the transient intensity for the (A) trace in the Kα region. The agreement with experimental data for the Kβ traces is satisfactory, albeit the assessment of significant deviation is harder due to the increased measurement uncertainty. Notably, the model successfully picks up a small change of sign in the Kβ (d) trace. The presence of these subtle kinetic details underlines the importance of analyzing individual spectra regions in transient cobalt XES spectra. The observation that these features are successfully reproduced in the global kinetic modeling approach supports the initially chosen sequential decay model.

Two time constants are found based on the optimized parameter values from the

Table 6.5: Fitted time constants for the two-exponential decay model on kinetic traces extracted from the transient differences in the Kα and Kβ region.

Property	Fitted value	
t_1	0.24 ± 0.03	ps
t_2	0.94 ± 0.05	ps

modeling approach on kinetic traces. A very short-lived decay component of around 250 fs is followed by a second component with around 0.9 ps lifetime. To explain the observed experimental traces, no additional temporal components are required within the reported experimental uncertainty. For comparison, results on the separately fitted Kα and Kβ traces are presented in appendix M. For the shorter time component t_1, the obtained values are comparable within the estimated parameter uncertainty, i.e., (0.19 ± 0.04) ps for Kα, (0.28 ± 0.09) ps for Kβ. For the longer time component t_2, the Kα traces exhibit a slightly shorter time component of (0.82 ± 0.09) ps, compared to (0.97 ± 0.04) ps for Kβ, but follow the general behavior of predicting a very fast sub 200 fs component, and a slower 0.8 ps to 1 ps time constant. A potential interpretation of underlying electronic states of the extracted timescales will be undertaken after the global fitting results from the full transient spectra presented in the next section.

6.4.9 Model-based full transient difference spectra analysis

The comparison of the total integrated trace with the individual traces in section 6.4.6 already hinted toward the necessity of treating different regions of the XES transient spectra individually. Otherwise significant differences in the kinetic behavior of the spectral regions are not detected. Several drawbacks remain even with the manual selection of spectral regions (A–E, a–e). The segmentation of the integrated area into fixed spectral regions suffers from the need for a manual selection of sensible integral borders, which is not always possible. This is illustrated by the fact that the fitted traces (C, D, E) in figure 6.15 do not fully capture the kinetic behavior of their respective regions since the position of the transient line shape zero-crossing slightly shifts with increasing pump-probe time-delay. In comparison, the (A) and (B) regions describe the temporal evolution of the corresponding spectral regions satisfactorily since the transient line shape zero-crossing position stays nearly constant for all probed time-delays.

In this section, we are applying the global fitting approach to the complete time-resolved XES spectrum (cf. figure 6.21). Intuitively speaking, each point in the transient difference XES spectrum is now treated as an individual trace. To refine the kinetic timescales on the full transient Kα and Kβ XES difference datasets, we are again employing the M_1^* and M_2^* models introduced in section 6.4.7. Several spectral regions were excluded from the data before fitting to avoid regions with low signal and unfavorable signal-to-noise ratios. The excluded spectral regions span all emission energies up until 6914 eV, energies between $K\alpha_1$ and $K\alpha_2$ (6920 eV until 6926 eV) and above 6937 eV for the Kα dataset. For the Kβ dataset, all energies outside the 7633 eV to 7658 eV window are excluded.

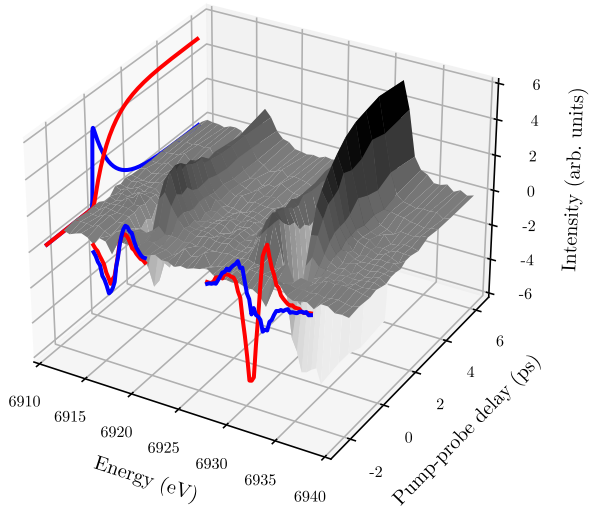

Figure 6.21: Schematic view of the global fitting approach for the full transient difference spectra. Fitting components (red, blue) are shown along the time axis (temporal evolution) and energy axis (individual per-energy component amplitudes A_i).

Table 6.6: Fitted time constant for the one-exponential decay model on full transient difference maps.

Property	One-exponential decay model	
t_1	0.91 ± 0.05	ps

As in the previous section, we are beginning our analysis with the optimized parameter values of the M_1^* model. The fitted parameter value for the time constant t_1 is given in table 6.6. The extracted time constant agrees within the estimated parameter variance with the decay time found from the one-exponential decay fit on the kinetic traces in section 6.4.8, indicating that the slower kinetic rise has been captured by the global fitting approach on the full transient difference map.

For an assessment of fit quality, the residual map of the fit and reconstructed transient difference line shapes for the more intense Kα region were given in figure 6.22. These reconstructions have been created by selecting a set of experimental transient line shapes at given pump-probe time-delays, and calculating the model-predicted spectra. The reconstructed transient difference spectra in the center and right panel of figure 6.22 exhibit notable differences in the $K\alpha_2$ region as well as at the higher energy tail of the difference signal from the $K\alpha_1$ emission line. The general intensity evolution of the $K\alpha_1$ line and the slight shift in centroid energy of the lower energy shoulder of the $K\alpha_1$ feature are captured by the fit.

An interesting property of the global fitting approach on the full transient difference maps is the availability of decay associated difference spectra (DADS), which are given by the individual component amplitudes for each excited state model component at

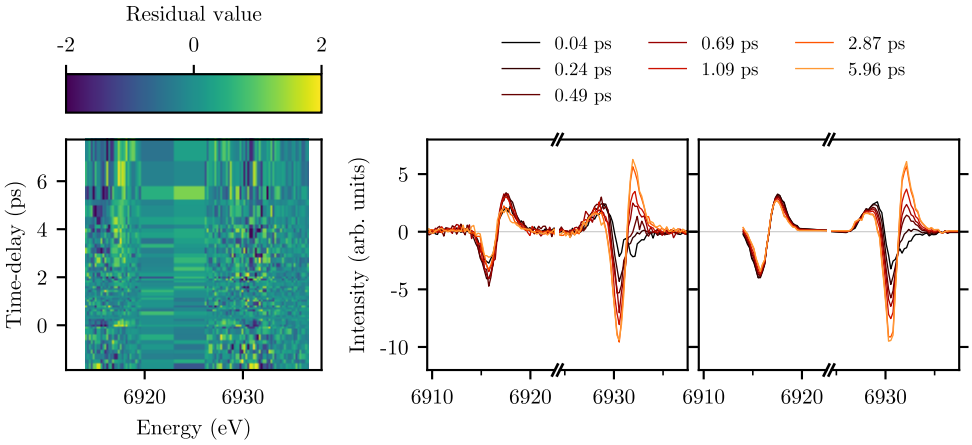

Figure 6.22: Residual values for the global fitting approach on full transient difference maps with a one-exponential decay model (left). Experimental transient Kα difference spectra (center) and reconstructed transient line shapes based on the one-exponential decay model (right) used in the global fitting analysis.

each energy [167]. Below, we will compare the obtained DADS component spectra with static reference difference spectra. The temporal evolution of the fitted kinetic components and the DADS are given in figure 6.23. Since the amplitude of the obtained kinetic components is an individual parameter for each energy point in the spectrum, a normalized portrayal (i.e., $A_i \equiv 1$) has been chosen to visualize the obtained fitting parameters in the left panel.

The first component DADS exhibits an almost point-symmetric feature in the lower energy $K\alpha_2$ region and a second feature of similar amplitude but of reduced symmetry in the $K\alpha_1$ region. As in the analysis of the experimental transient lineshapes, the two features are of opposite sign. The DADS of the second component exhibit a feature of unchanged shape but reduced intensity in the $K\alpha_2$ XES region. The feature's shape in the $K\alpha_1$ region is significantly different. Here, a feature with two-zero crossings is observed.

Notably, similarities of the presented DADS with steady-state difference spectra from cobalt reference compounds are observed. Six static difference spectra calculated from the line shapes of $[Co(bpy)_3]Cl_3 \cdot 4\,H_2O$ (Co^{3+}) and $[Co(bpy)_3]Cl_2 \cdot 5\,H_2O$ (Co^{2+}) are presented in figure 6.24. The top row panels illustrate difference spectra created by a relative energy shift of the $K\alpha_1$, $K\alpha_2$ and $K\beta$ peaks on only the Co^{2+} compound. Here, a small relative energy shift of 0.3 eV leads to an almost point symmetric difference curve for the $K\alpha_2$ line (upper left panel). The relative energy shift for the $K\alpha_1$ region was chosen to be negative, which leads to a less symmetric signature with a notable deflexion around 6934 eV. In comparison with the DADS in figure 6.22, a comparable $K\alpha_1$-$K\alpha_2$ amplitude ratio for the opposing energy shift, and a similar deflexion at the high-energy tail of the $K\alpha_1$ emission peak are observed. Based on these similarities, the dominating spectral line shape upon photo-excitation on the fast timescale (component 1) is thus

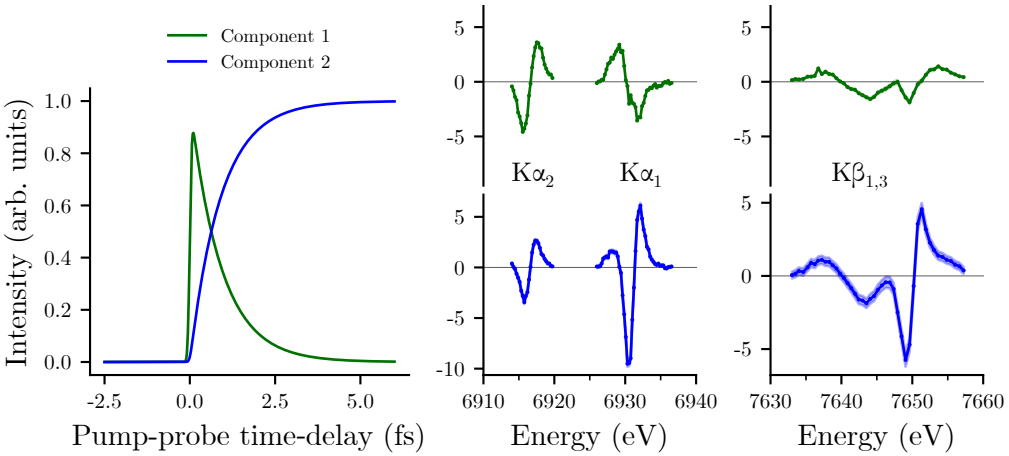

Figure 6.23: Kinetic model with one-exponential decay component used during the fitting analysis. Normalized kinetic components (left) and corresponding DADS (right), for $K\alpha_1$, $K\alpha_2$ and $K\beta_{1,3}$ respectively. Parameter uncertainties are given as shaded intervals.

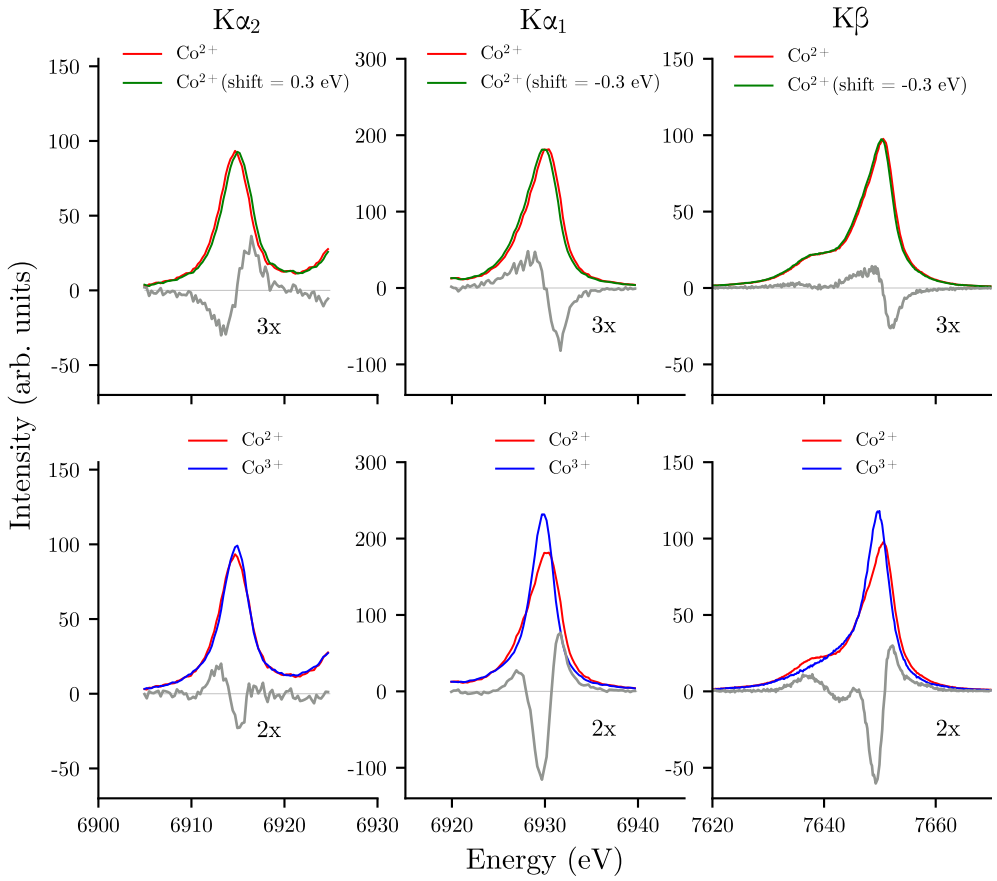

Figure 6.24: Difference lineshape synthesis from Kα and Kβ XES spectra of reference compounds $[Co(bpy)_3]Cl_3 \cdot 4\,H_2O$ (Co^{3+}) and $[Co(bpy)_3]Cl_2 \cdot 5\,H_2O$ (Co^{2+}). Top: Difference spectra created from shifted curves of the same compound. Bottom: HS-LS difference curves.

hypothesized to be a shift towards lower energies for the Kα$_1$ peak. Based on the static reference difference spectra for the Kα$_2$ emission line, a simultaneous energy shift towards higher energies leads to an overall decreased splitting between the Kα peaks.

The panels in the lower row of figure 6.24 illustrate differences obtained by subtracting the Co^{3+} LS spectra from Co^{2+} HS. A commonly observed HS-LS difference line shape in the Kα$_1$ region exhibits similarity with the DADS of the second component. Specifically, they exhibit the same characteristic asymmetric inverted w shape with a weaker intensity peak at the lower energy side of the Kα$_1$ region and a sharp, increased intensity peak at the higher energy side of the feature. The dominating spectral property leading to the creation of the described difference curve is the change in Kα$_1$ peak width and intensity, which is generated by the increased peak symmetry for the Co^{3+} form. For the transient line shape behavior at slower timescales captured by the second component DADS, we thus hypothesize an increase in peak width upon photo-excitation on the 1 ps timescale.

The DADS of the Kβ feature exhibit similar parameter uncertainties as the Kα components. No steady-state equivalent of the first DADS component could be generated. The second Kβ DADS component resembles the steady-state line shapes of the HS-LS difference, e.g., as found in section 4.4.3 for the temperature induced spectra of solid-phase $Co(DTB)_2(tmeda)$.

The analysis of the integrated kinetic traces in the previous section indicated that a two-exponential decay model led to a significantly better capture of the early temporal behavior of photo-excited $Co(DTB)_2(tmeda)$. Analogous to the approach described above, we apply the global fitting model M_2^* to the complete transient difference dataset. To inspect the agreement with the actual transient difference curves recorded at selected pump-probe time-delays, the comparison with experimental data is given in figure 6.25. The amount of structure in the residual map displayed in the left panel is slightly reduced. The reconstructed transient difference spectra in the right panel of figure 6.25 indicate a better agreement with the experimentally observed line shapes, specifically concerning the slow decay of the $K\alpha_2$ transient feature and the shape of the early pump-probe time-delay spectra for the $K\alpha_1$ emission line.

The extracted timescales are given in table 6.7. The slower decay time constant is recovered. In comparison with the time constants extracted from the trace fits and the one-exponential fit, the obtained value for t_2 is slightly smaller, and the observed deviation lies just outside the estimated parameter uncertainty. Compared with the earlier temporal component extracted from the kinetic trace fits, the global fitting approach on the full transient difference spectra exhibits a faster time constant of around 140 fs.

The corresponding DADS are visualized in figure 6.26. Increased estimated parameter uncertainty is found for the aforementioned fast time constant, but structural components

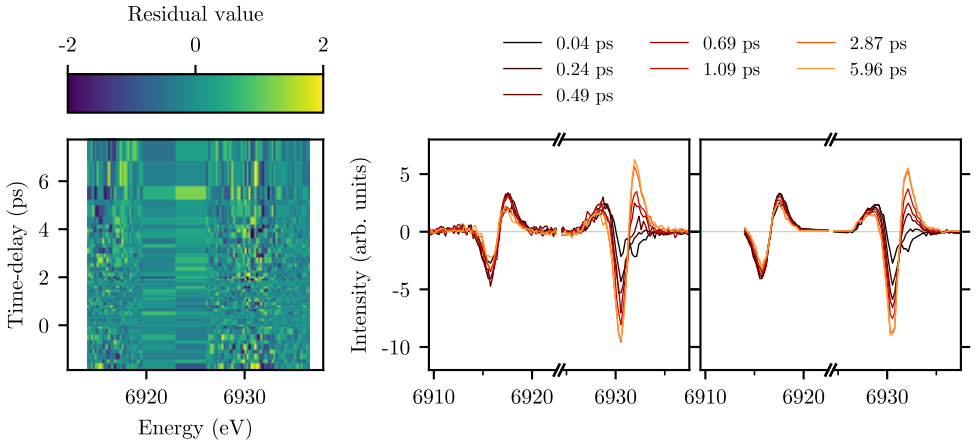

Figure 6.25: Residual values for the global fitting approach on full transient difference maps with a two-exponential decay model. Experimental transient Kα difference spectra (center) and reconstructed transient line shapes based on the one-exponential decay model (right) used in the global fitting analysis.

Table 6.7: Fitting results for the one-exponential decay model for the description of transient Kα XES data on a 5 mM toluene solution of Co(DTB)$_2$(tmeda).

Model	Two-exponential decay model	
t_1	0.14 ± 0.01	ps
t_2	0.78 ± 0.06	ps

in the Kα$_1$ region remain significant. Here, a sharp minimum at 6933 eV and a broader maximum at 6929 eV are found. Contrary to the second temporal model component, only weak intensity is observed in the Kα$_2$ region, which indicates that the first DADS exhibits reduced sensitivity towards the Kα$_2$ region. The remaining DADS exhibit similar behavior as in the case of the one-exponential fit and are interpreted along the same notion. Specifically, we invoke the static differences in figure 6.24 to assign a shift of the Kα$_1$ and Kα$_2$ peak at fast times, and a broadening at slower timescales. The first temporal model component in the Kβ region exhibits no significant structure. As above, only for the slowest DADS in the Kβ region static reference differences could be created by subtracting reference compounds spectra.

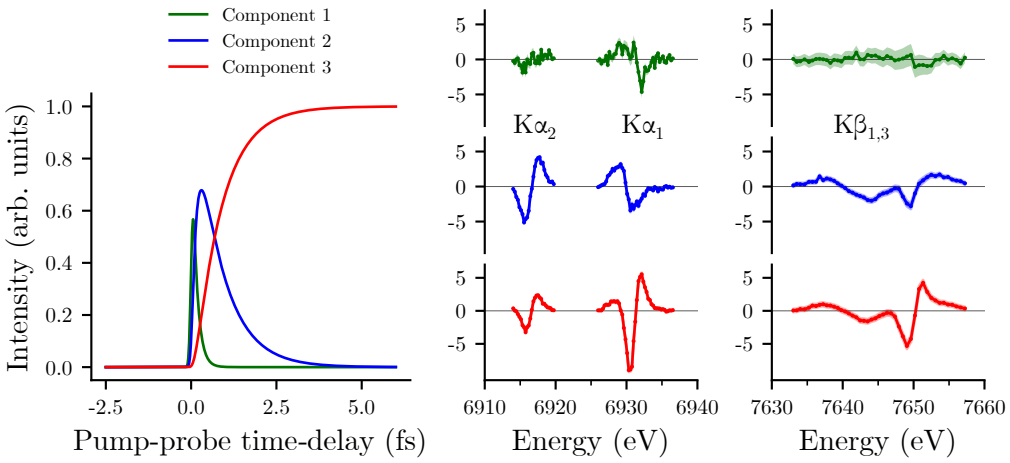

Figure 6.26: Kinetic model with two-exponential decay components used during the fitting analysis. Normalized kinetic components (left) and corresponding DADS (right). Parameter uncertainties are given as shaded intervals.

6.5 Discussion of time-resolved measurements and outlook

In this chapter, the kinetic behavior on femtosecond and picosecond timescales for the laser-excited VT compound $Co(DTB)_2(tmeda)$ in toluene solution was investigated. The fundamental concepts of multicolor time-resolved XES measurements at the FXE instrument at EuXFEL have been illuminated.

Magnetic susceptibility measurements revealed a strong solvent effect, which led to shifts of the critical temperature $T_{1/2}$. In going from the solid-phase sample to a 5 mM solution of $Co(DTB)_2(tmeda)$ in toluene, a ca. 25 % reduced room-temperature magnetic susceptibility value was found. Correspondingly, in cobalt Kβ XES measurements, a weaker Kβ' feature on $Co(DTB)_2(tmeda)$ upon solution in toluene was observed. These findings hint at a different solution GS as in solid-phase. We list three scenarios for the GS of this VT complex in solution. First, a shift in the VT species equilibrium leads to a higher amount of molecules in the Co^{3+} LS phase in the dissolved sample. This behavior has been observed for other cobalt VT complexes in solution [26, 138]. Alternatively, a metal doublet state, i.e., Co^{2+} $(t_{2g})^6(e_g)^1$, would lead to a reduced spin-population on the central metal ion. In the picture of crystal field theory, a significant increase of the d-orbital energy splitting by modulation of the crystal field and distortion would be required to stabilize this – for cobalt uncommon – LS Co^{2+} $(t_{2g})^6(e_g)^1$ configuration. Structurally, modulation of the crystal field can be caused by reduced bond distances, which would be detectable by X-ray scattering techniques on samples in toluene solution. Lastly, bulk magnetization measurements will also be sensitive to the unpaired spin density on the redox-active ligands. A change in the metal-ligand spin-coupling (effectively changing the net spin per molecule) upon solution in toluene might thus also lead to a reduced magnetic susceptibility value.

Based on the argument that the solvent effect influences the entropy factor in the VT equilibrium in eq. (2.2) and thus shifts the critical temperature [26], a plausible mechanism for the GS in solution has been presented. A study on VT complexes in multiple solvents with a metal-sensitive method, such as XES, might yield further evidence about the metal spin state. Furthermore, to our knowledge, the influence of ligand-spin coupling with the metal ion onto the Kβ XES line shape of cobalt has not been extensively investigated.

For a discussion of the temporal evolution in transient difference spectra, kinetic traces were extracted from the experimental data. Since significant variations in the behavior of different regions in the spectrum are present, individual kinetic traces for these spectral regions were analyzed. The analysis revealed a swift transient response for the cobalt $K\alpha_2$ XES region, while the $K\alpha_1$ region presented different, multi-component temporal behavior. For the lower energy side of the transient features in the $K\alpha_1$ emission region, a fast rise with subsequent slow decay was found, as in the case of the $K\alpha_2$ peak. Conversely, a much slower appearance of a transient feature at the higher energy tail of the $K\alpha_1$ transient feature was observed, which led to a more complicated evolution of transient line shapes in this spectral region.

An overview of the extracted time constants from global fitting approaches and optical spectroscopy is given in table 6.8. A slower time constant (t_3) of 8.33 ps is

Table 6.8: Overview of extracted timescales on $Co(DTB)_2(tmeda)$ after excitation with a 800 nm optical laser pump-pulse.

Method	t_1 ps	t_2 ps	t_3 ps
Optical spectroscopy		0.88 ± 0.05	8.33 ± 0.56
Trace fitting		0.83 ± 0.09	
	0.24 ± 0.03	0.94 ± 0.05	
Full transient fitting		0.91 ± 0.05	
	0.14 ± 0.01	0.78 ± 0.06	

observed in the optical spectroscopy data only, where a longer time window could be investigated. All methods yield a shorter time constant around 0.8 ps to 0.9 ps (t_2), which is accompanied by a secondary, significantly faster, time constant of 0.14 ps to 0.24 ps (t_1) on XES data. Fits on the optical transient absorption spectroscopy data gave a slightly larger value for the second timescale t_2 of around 1.4 ps.

In addition to validating extracted timescales via a second analysis route, the global fitting approach on the full transient differences delivered DADS which exhibit similarities with the steady-state differences from cobalt reference compounds. Based on the comparison of DADS with these static reference difference spectra, two predominant effects in the laser-excited Kα spectra were described. At early sub 300 fs delays, both Kα peaks shift toward a common centroid, effectively reducing the $K\alpha_1$-$K\alpha_2$ splitting. For $K\alpha_1$, a subsequent broadening with a time constant of around 0.9 ps takes place. For the temporal evolution of the Kβ line shapes, similarity with HS-LS static differences was found for the slowest of the extracted DADS components.

Due to the comparatively low solubility of the sample resulting in weak XES signals and the hypothesized mixed GS, multiple experimental challenges arise. The observed absolute line shape changes in figure 6.13 are on the order of 1 %, which we attribute to the fact that only a fraction of the molecules in toluene solution are present in the Co^{2+} GS (and thus susceptible to optical pumping at 800 nm). Additionally, a large laser fluence proved to be necessary to resolve the weak line shape changes in the transient difference spectra, despite the high FEL photon flux of around $2.5 \times 10^{13} \frac{\text{ph}}{\text{pulse}}$ (cf. section 6.3). Furthermore, collection efficiency with the dispersive von Hámos spectrometer, i.e., the number of photons collected per energy increment, was lower than for a scanning spectrometer. In addition, due to the MHz timing-structure of EuXFEL, very high jet speeds were required, which led to additional challenges during the delivery of the sample. The main effect was decreased jet stability at the high pressures associated with running thin jets at very high speeds.

In future time-resolved measurements on this type of system, using a timing tool at the beamline might allow access to a more detailed picture of the electronic timescales

at early pump-probe time-delays [168], especially by resolving the identified fast time component around 200 fs.

Importantly, as in the temperature-dependent measurements, XAS at the cobalt K-edge should provide crucial additional information regarding the oxidation state of the metal ion. Pressure-induced VT has been studied on a similar system with XANES at the cobalt K-edge before [21]. In the context of time-resolved measurements, at least two prime objectives should be addressed by future XAS studies. For once, we hypothesized a MLCT state based on TOAS measurements. This charge-transfer should be quantifiable with XAS techniques. Furthermore, a targeted investigation of the potential presence of LS Co^{2+} should be more accessible in XAS, e.g., by inspection of the rising edge position in comparison with spectra recorded on solid-phase VT samples.

Chapter 7

Conclusion and thesis outlook

We reported on the application of optical and X-ray spectroscopies to study bis-(o-dioxolene) cobalt complexes, a family of cobalt compounds exhibiting VT, i.e., electronically labile behavior.

Temperature-resolved UV/Vis optical absorption measurements on the cobalt complexes $Co(DTB)_2(tmeda)$, $Co(DTB)_2(bpy)$, $Co(DTB)_2(phen)$ and $Co(DTB)_2(dpbpy)$ in toluene solution present features characteristic of Co^{3+} at lower temperatures and of Co^{2+} at elevated temperatures. As has been previously reported, this is indicative of VT, which involves the tautomerization between a LS Co^{3+} and HS Co^{2+} form [16]. The presence of isosbestic points in the spectra indicates that those two states are the only spectroscopically identifiable species involved in the VT transition for the studied compounds. For cobalt VT compounds in this study except for $Co(DTB)_2(tmeda)$, three additional faint bands were identified in the region between 480 nm to 650 nm. We associate the presence of these bands with a polypyridine-type co-ligand. The computational assessment of these bands, potentially via TD-DFT-based methods, should provide further insight into the intricacies of co-ligand to metal interaction in VT complexes.

Magnetic susceptibility measurements revealed a strong solvent effect of the VT equilibrium, which led to shifts of the critical temperature $T_{1/2}$, and, subsequently, the magnetization curve. In going from the solid-phase sample to the solution in toluene, variations of the magnetization for the high-temperature HS-phase were observed. Solution yielded a ca. 25 % *reduced* room-temperature magnetic susceptibility value for $Co(DTB)_2(tmeda)$, and a ca. 60 % *increase* for $Co(DTB)_2(bpy)$. The extracted critical temperatures agree with previously reported values. The solvent effect was further corroborated by Kβ XES measurements on $Co(DTB)_2(tmeda)$ in solution and in solid-phase, where a significantly weaker Kβ' feature was observed for the tautomer in toluene. This behavior has been associated with a smaller p-d exchange interaction, which leads to a reduced splitting between the Kβ' and $K\beta_{1,3}$ mainline peak [67]. Three hypotheses, a change in the metal spin state, ligand-metal spin-coupling or a shift in the VT equilibrium, were discussed.

The main focus of this work was the application of resonant- and (time-resolved) non-

resonant X-ray emission spectroscopy. On solid-phase samples, a series of temperature-resolved Kβ XES spectra were collected. Two dominant spectral regions in the HS-LS difference curves have been identified, in which subtle differences between the investigated complexes are present.

Intermediate-temperature spectra of $Co(DTB)_2(tmeda)$ do not exhibit the same line shape around 7655 eV (high-energy tail of the $K\beta_{1,3}$ peak) as the difference reference, even when scaled by a constant factor. This hints at the presence of subtle electronic or structural effects in the transition phase of VT, which are picked up by Kβ XES. The origin of these line shape variations might lie in cooperative effects, which are known to be operative in these compounds, and vary as a function of the co-ligand [37].

Additionally, we discussed a deviation of the difference curves of $Co(DTB)_2(bpy)$ in the region around 7646 eV, where this complex exhibits less intensity compared to the remaining tautomer complexes. We note that, contrary to $Co(DTB)_2(tmeda)$ and $Co(DTB)_2(phen)$, tautomerization has been reported to be weaker and occur over a much wider temperature range in the solid-phase of this compound [17].

We hold that Kβ XES on cobalt VT compounds might provide signatures that go beyond the assessment of 3d spin-momentum and could even signify that a simple two-state model supported by the UV/Vis spectroscopy results is not fully sufficient to explain XES line shapes. The electronic interpretation of these signatures will have to rely on multi-reference calculation methods due to the complicated multiplet structure of the cobalt Kβ emission line [63] involving open-shell ligands and remained outside the scope of this thesis.

To explore ligand-specific signatures and hints regarding the spin-coupling between metal and ligand in VT complexes, cobalt VtC XES was conducted. Based on TD-DFT calculations, we attribute oxygen, nitrogen, and carbon 2s orbital character to the Kβ" feature in the VtC spectra. Since the calculations hint toward an oxygen-dominated Kβ" region, VtC emission might allow for selective probing of the lone-pair dioxolene oxygen orbitals of redox-active ligands (such as benzoquinones) during temperature-induced tautomerization. Furthermore, in the low-temperature calculation results, a separation of transition intensities into predominantly co-ligand-based carbon and nitrogen contributions at the position of the $K\beta_2$ feature and mostly oxygen and carbon contributions at the $K\beta_5$ feature is observed. This, following the same rationale as above, might allow the targeted investigation of co-ligand-based properties. We conclude that the separation of transition intensities motivates a study with resonant X-ray excitation, in which VtC-detected XAS is applied. This would provide quasi-direct access to ligand atom properties, with significantly larger cross-sections than in XRS (discussed below). The comparison of TD-DFT-calculated spectra did not allow any distinction for the spin-coupling between metal and redox-active ligand since calculated line shapes exhibited only minor differences.

Exploratory XRS measurements on the oxygen K-edge of redox-active benzoquinone ligand variants, 3,5-di-tert-butyl-o-benzoquinone (Q) and 3,5-di-tert-butylcatechol (CAT) revealed a pre-edge feature for Q only. Based on TD-DFT calculations, we assigned quinone π^* LUMO orbital character, implying that the redox-state of the ligand can be fingerprinted by the recording of oxygen pre-edge XAS. This hints toward the oxygen

K-edge being well suited for the targeted investigation of VT.

The application of XRS for capturing oxygen K-edge spectra offers the advantage of options for simultaneous XES on these compounds. This is possible since the energy of the incoming X-ray photons can be chosen to lie above the ionization energy of the cobalt 1s absorption edge, and thus non-resonant excitation for XES and energy-loss spectroscopy can be carried out in parallel [133], e.g., with Si(2,2,0) analyzers in 6th order reflection and a scanned incoming photon energy around 10 210 eV (around 530 eV above the elastic energy, i.e., the bandpass at around 90° Bragg angle of the analyzer).

Since all studied tautomers are prone to radiation-induced changes, samples need to be scanned in the X-ray beam during data acquisition. Due to the challenges of combined sample scanning and temperature control with a cryostat, as well as the integration times of typically several hours required for the collection of XRS spectra at the oxygen edge (as caused by the small cross-sections), XRS on the full cobalt VT samples remained inaccessible during this study. The successful experimental implementation of XRS on cobalt VT samples will depend on the reduction of dead times (i.e., to only expose the sample while a detector image is being taken) during motor scanning, e.g., by use of continuous monochromator scanning or fast-shutters, and a large scannable sample area offering a sufficient amount of measurement spots.

We further investigated the cobalt metal K-pre-edge region with conventional XAS and resonant XES (RXES) methods. For the tris-bipyridine reference complexes $[Co(bpy)_3]Cl_3 \cdot 4\,H_2O$ / $[Co(bpy)_3]Cl_2 \cdot 5\,H_2O$, a metal 1s to ligand charge-transfer feature at around 7713 eV was identified via TD-DFT calculations. Calculations on the metal pre-edges of the VT compounds indicated a similar charge-transfer feature originating from the co-ligand and, additionally, the redox-active ligand. These features could not be experimentally resolved in conventional XAS. To investigate if additional pre-edge features could be differentiated, we applied RXES. Temperature-resolved 1s3p RXES did unveil the appearance of a second pre-edge feature in the region around 7710 eV incoming energy, which we attribute to the Co^{3+} d^6 to Co^{2+} d^7 conversion and the presence of holes in both the t_{2g} and e_g 3d sets in the HS phase. TD-DFT-predicted charge-transfer features at higher incoming energies were not experimentally observed. We hypothesize that transitions in the experimental spectrum are either higher in energy and thus obscured by the edge-rise, much broader in reality due to local inhomogeneities in the sample and subsequent variations in transition energies, or incorrectly predicted by the calculation due to shortcomings of the DFT-method in calculating metal main K-edges.

The combined spin-crossover and charge-transfer processes in bis(o-dioxolene) VT complexes had not been previously targeted by ultrafast X-ray emission techniques. We conducted time-resolved experiments on $Co(DTB)_2(tmeda)$ in toluene solution at the FXE instrument, EuXFEL. Fully-correlated Kα and Kβ XES spectra were collected after laser-excitation with optical light (800 nm) in the sub 5 ps range. The analysis of transient difference spectra (i.e., the difference between spectra recorded from the laser-excited and non-excited sample) revealed that the simultaneously recorded $K\alpha_1$, $K\alpha_2$ and $K\beta_{1,3}$ emission lines follow distinctly different temporal behavior on these timescales. Qualitatively, spectral signatures in the $K\alpha_2$ region follow a fast transient

rise, with subsequent weak decay, while the $K\alpha_1$ peak exhibits both a rapid rise in the lower energy region and a slower time component at higher energies. We used a global-fitting approach to model the individual temporal kinetics of the spectral features and identified a fast signature between 140 fs to 240 fs and a slower component between 780 fs to 940 fs. These values are complemented by a component on the 8.3 ps timescale as extracted by TOAS.

The extension of the global-fitting approach to the whole non-integrated Kα and Kβ XES regions allowed for the discussion of DADS, spectral model components. Comparison of these components with synthetic differences obtained from the steady-state spectra collected in chapter 4 revealed that the temporal evolution of the Kα line shapes is characterized by first a rapid decrease in $K\alpha_1$-$K\alpha_2$ splitting, and subsequent broadening of the $K\alpha_1$ peak. For the series of 3d TM complexes, the $K\alpha_1$-$K\alpha_2$ splitting, as caused by the spin-orbit coupling, correlates with the absolute 2p level energies [44]. It can be hypothesized that an increased $K\alpha_1$-$K\alpha_2$ splitting in cobalt signifies a shift in the 2p level, as would be caused by a change in the oxidation state of the metal ion, e.g., due to a MLCT.

The general line shape behavior indicated an increase of HS molecules in the laser-excited sample, which differs from the steady-state picture of VT, where optical excitation in the MLCT-band would decrease the fraction of HS molecules since a Co^{2+} d^7 configuration converts to Co^{3+} d^6 (LS).

These measurements denote the first steps toward ultrafast hard X-ray spectroscopies on complexes exhibiting VT. They provide the basis of further experimental studies by unveiling multiple sub ps temporal components and providing estimates for the sample behavior in the hard X-ray FEL beam, as well as experimental reference for electronic structure calculations. The collection of time-resolved XAS pre-edge/XANES spectra constitutes an important next step, which would allow the unambiguous assignment of the cobalt oxidation state during the tautomerization transition.

Appendix

A Waveplate calibration for laser-power and traces

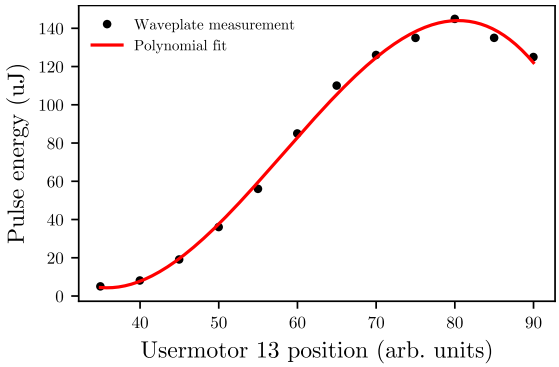

Figure A.1: Power meter scan for the calibration of the waveplate laser attenuation mechanism and polynomial fit for the determination of pump-laser power at the sample position.

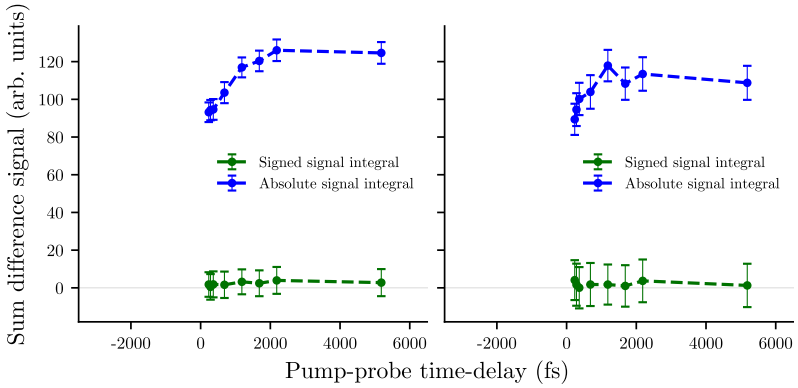

Figure A.2: Signed and absolute integrated Kα (left) and Kβ (right) XES difference curves (traces).

B Github repository with analysis code

The analysis code used for the reduction of FXE data in this thesis can be found in the following Github repository:

- `https://github.com/flmiot/euxfel_reduct`

C Signal linearity

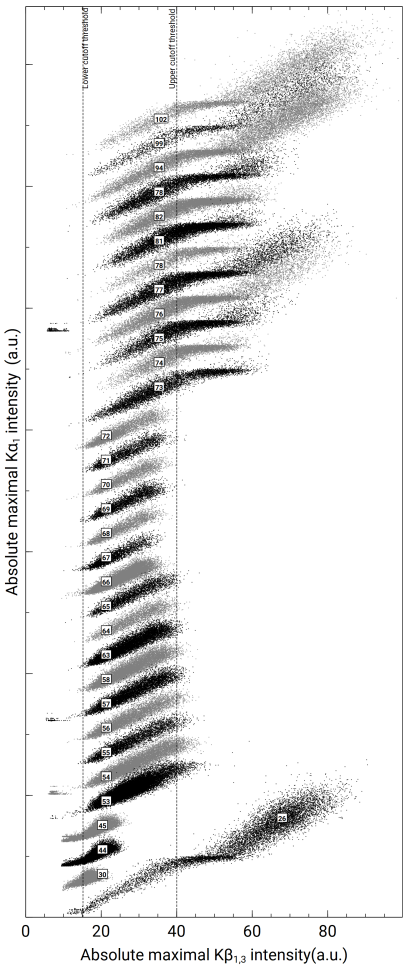

Figure C.1: Investigation of signal linearity and determination of a cut-off threshold. Kα peak intensity vs Kβ peak intensity for non-excited (laser off) shots during the time-resolved XES experiment at FXE, EuXFEL. The increasing number label refers to individual experimental acquisition runs.

D Molecular orbital analysis of VtC spectra

This section gives the MO analysis according to section 4.4.4 in metal doublet configurations.

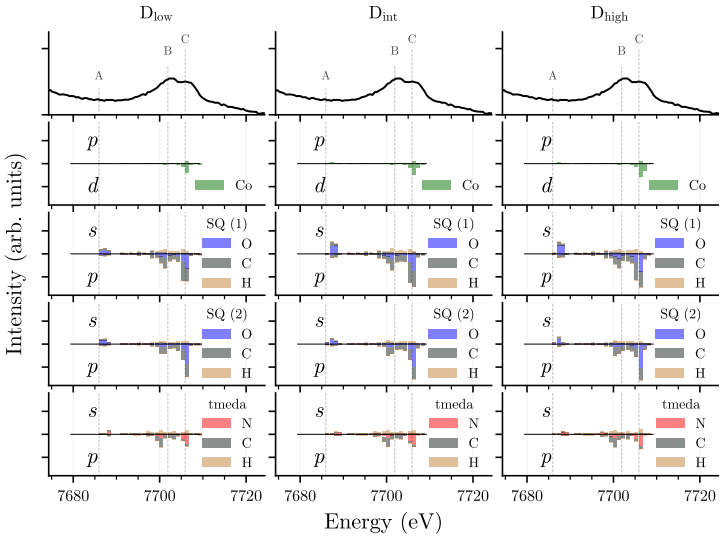

Figure D.1: Analysis of ligand-based D state contributions to transition intensities in the VtC region of $Co(DTB)_2(tmeda)$.

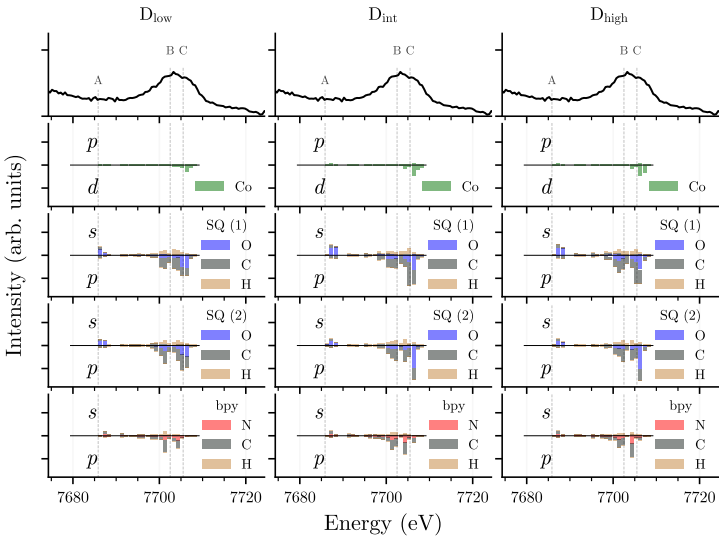

Figure D.2: Analysis of ligand-based D state contributions to transition intensities in the VtC region of $Co(DTB)_2(bpy)$.

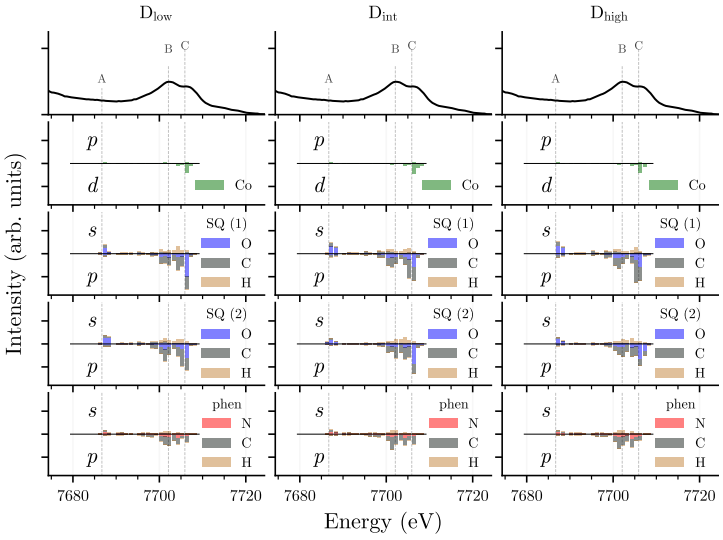

Figure D.3: Analysis of ligand-based D state contributions to transition intensities in the VtC region of $Co(DTB)_2(phen)$.

E Sample characterization

The molar extinction of $Co(DTB)_2(tmeda)$ 5 mM in toluene was measured by use of a Shimadzu UV-3600 Plus spectrophotometer. 1 mg of $Co(DTB)_2(tmeda)$ were dissolved in 2.5 mL of toluene and measured in a 5 mm optical path quartz cuvette.

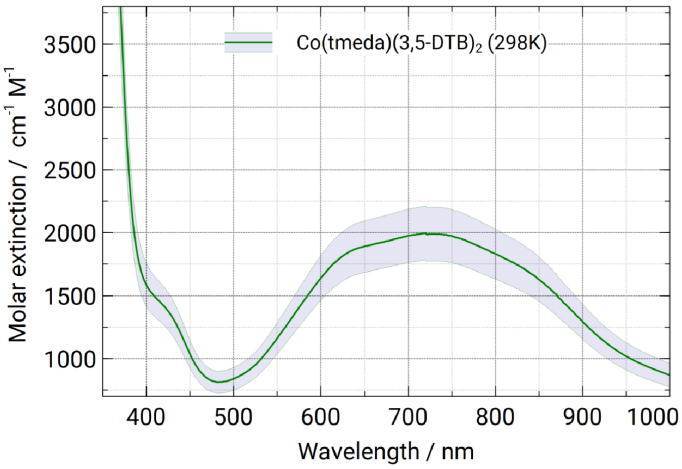

Figure E.1: Molar extinction of $Co(DTB)_2(tmeda)$ 5 mM in toluene. Shaded areas indicate the total uncertainty due to uncertainty in the measured sample mass and solvent volume.

F XES measurements on $Co(DTB)_2(bpy)$ and cobalt references

Cobalt Kα XES is not as sensitive as the Kβ enission line toward valence electronic structure of transition metal complexes, since the p-d exchange integral is smaller. Since the Kα emission presents the most intense emission line in cobalt, we start our investigation with the discussion of Kα XES data on $Co(DTB)_2(bpy)$. The temperature resolved spectra are plotted in figure F.1. Upon sample cooling, a reduction in lineshape width can be observed for the $K\alpha_1$ line, which is accompanied by an increase in intensity. This behavior is common for the Co-II to Co-III transition and has been discussed in section 3.2. The IAD values exhibit a gradual transition, as expected from the magnetic measurements (cf. section 4.3.2) and published literature on $Co(DTB)_2(bpy)$. The difference line shape displayed in figure F.1 exhibits an almost symmetrical shape in the $K\alpha_1$ region and a roughly 80% weaker difference feature in the $K\alpha_2$ region.

The Kα datasets presented above were investigated with a multi-component fitting approach for the determination of peak positions, areas and widths. The extracted values are listed in table 1.

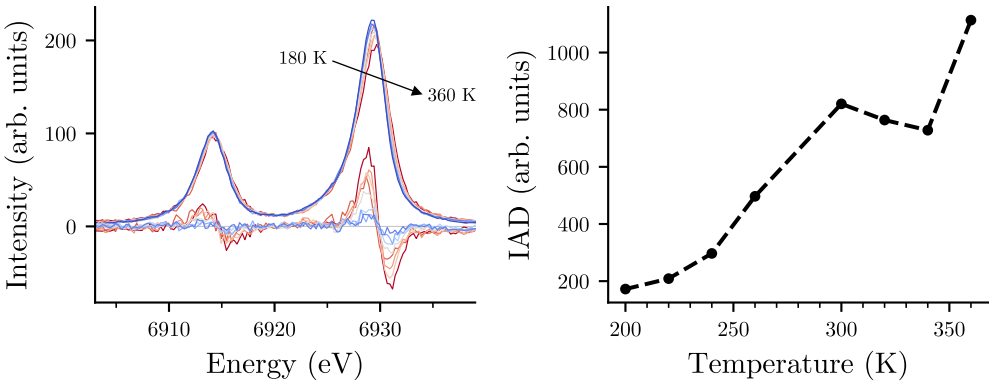

Figure F.1: Temperature dependent Kα XES on $Co(DTB)_2(bpy)$ (left). IAD values for different sample temperatures (right). The IAD reference was chosen to be the spectrum collected at lowest temperature (180 K). A fitting-based analysis of this dataset is presented in the Bachelor thesis of Julia Rogalinski [112].

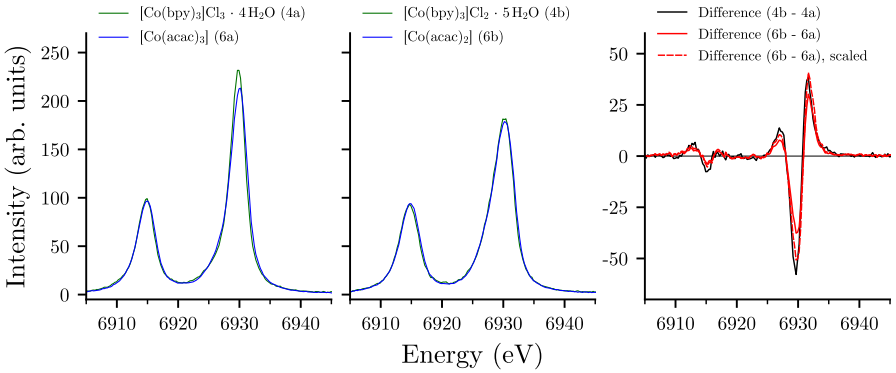

Figure F.2: Comparison of Kα low-spin (*left*) and high-spin spectra (*right*) of $[Co(bpy)_3]Cl_3 \cdot 4\,H_2O$ / $[Co(bpy)_3]Cl_2 \cdot 5\,H_2O$ and $[Co(acac)_3]$ / $[Co(acac)_2]$. The difference spectra are shown in the right panel. The dashed line represents the scaled difference curve of $[Co(acac)_2]$ and $[Co(acac)_3]$.

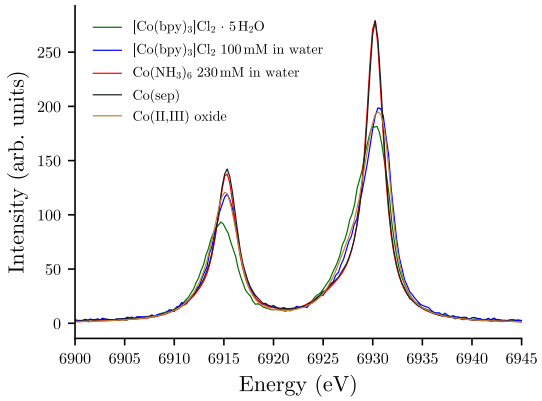

Figure F.3: XES study on liquid cobalt reference compounds

The strong correlation between the Kα line shape width and the energy splitting between the Kα$_1$ and Kα$_2$ peak position are visualized in figure F.4.

Table 1: Selected properties of Kα XES spectra for cobalt complexes

Compound	Splitting[1]		I-Ratio[2]		FWHM	
	Max.	IWAE	Max.	Area	Kα$_1$	Kα$_2$
	(eV)				(eV)	
$[Co(bpy)_3]Cl_3 \cdot 4\,H_2O$	15.0	14.8	2.4	2.4	3.0	3.4
$[Co(bpy)_3]Cl_2 \cdot 5\,H_2O$	15.6	15.1	2.0	2.5	4.3	3.8
$[Co(bpy)_3]Cl_2$ 100 mM in water	15.4	15.0	1.7	1.8	3.7	3.3
$[Co(acac)_3]$	15.1	14.9	2.2	2.1	3.4	3.7
$[Co(acac)_2]$	15.5	15.3	1.9	2.2	4.5	3.9
Co(sep) 21 mM in water	15.0	14.7	1.9	1.6	2.3	2.6
$Co(C_2O_4)$	15.4	14.8	1.7	1.8	3.6	3.3
$Co(NH_3)_6$ 230 mM in water	14.8	14.7	2.1	1.8	2.1	2.7
Co foil	15.0	14.6	2.2	1.7	2.4	3.1

[1] Energy difference between the Kα$_1$ and Kα$_2$ emission line, as extracted from the fitted component positions. Computed for both the difference between maximum positions and the difference between the intensity weighted average energy (IWAE) values for each emission peak.

[2] Intensity ratio between the Kα$_1$ and Kα$_2$ emission line. Computed for both the ratio of peak heights and the ratio of summed component area.

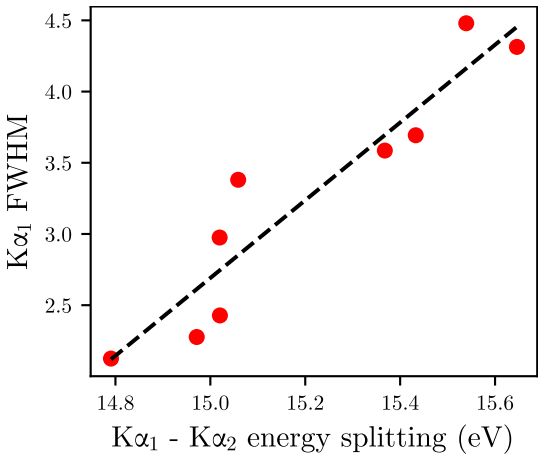

Figure F.4: Correlation between Kα lineshape parameters in cobalt complexes.

Table 2: Pearson correlation coefficient between the parameter values in table 1.

	Splitting		I-Ratio		FWHM	
	Max.	IWAE	Max.	Area	$K\alpha_1$	$K\alpha_2$
Splitting						
Max.	1.0					
IWAE	0.8	1.0				
I-Ratio						
Max.	−0.5	−0.3	1.0			
Area	0.5	0.6	0.4	1.0		
FWHM						
$K\alpha_1$	0.9	0.9	−0.3	0.6	1.0	
$K\alpha_2$	0.7	0.8	0.1	0.8	0.9	1.0

G XES analyzer configurations

A webtool for the planning of XES experiments with the von Hámos spectrometer has been developed. Suitable analyzer and spectrometer configurations can be requested in a comfortable manner. The tool features sorting and options for the planning of two-color experiments (cf. figure G.1) has been optimized for mobile devices (e.g., during the setup inside an experimental hutch or laboratory) and is made available at `http://where-are-my-photons.com/xtals.html`.

The calculated multicolor configurations in tables 3 to 6 were calculated with the developed framework. An API documentation is available online via the footer of the website.

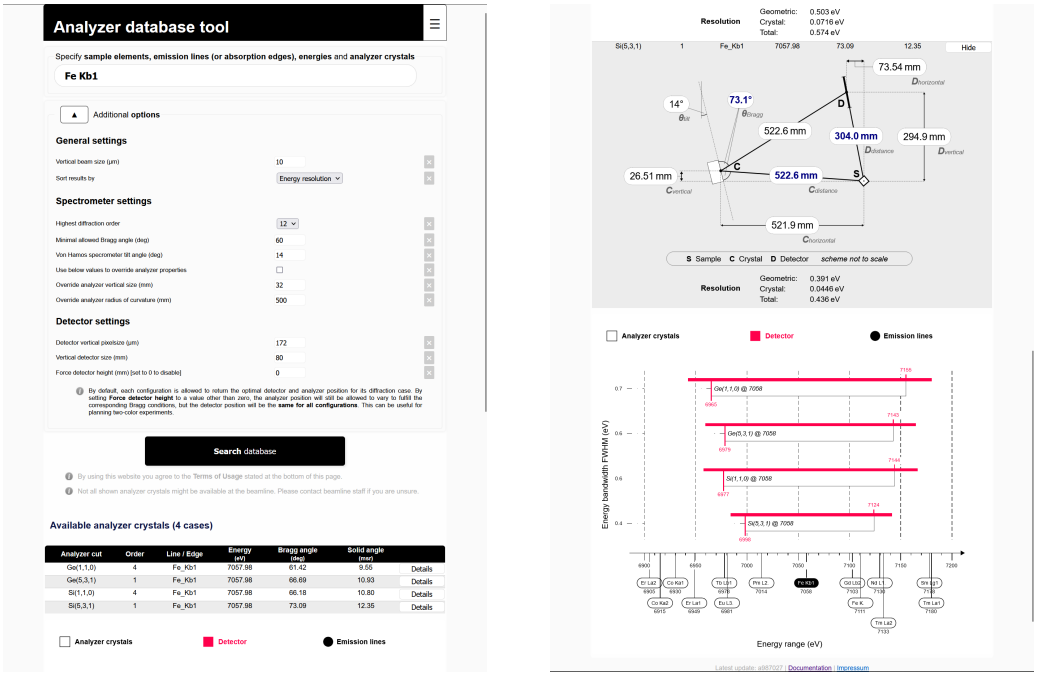

Figure G.1: A web-based tool for the planning of XES experiments with a von Hàmos spectrometer.

Table 3: Transition metal emission lines. Cross-chart for multicolor XES experiments.

A / B	Sc Kα	Sc Kβ	Ti Kα	Ti Kβ	V Kα	V Kβ	Cr Kα	Cr Kβ	Mn Kα	Mn Kβ	Fe Kα	Fe Kβ	Co Kα	Co Kβ	Ni Kα	Ni Kβ	Cu Kα	Cu Kβ	Zn Kα	Zn Kβ
Sc Kα	X																			
Sc Kβ		X	1			2											3			
Ti Kα		4	X																	5
Ti Kβ				X	6 7						8 9	10	11		12	13			14 15	
V Kα				16 17	X						18 19	20	21		22 23	24			25 26	
V Kβ		27				X	28			29							30			
Cr Kα						31	X			32										
Cr Kβ								X		33 34	35 36	37 38			39		40 41 42			
Mn Kα									X			43	44 45 46			47 48				
Mn Kβ						49	50	51 52		X	53 54				55	56 57	58 59 60			
Fe Kα				61 62	63 64			65 66		67 68	X	69	70		71 72	73	74		75 76	
Fe Kβ				77	78			79 80	81		82	X	83 84 85		86				87 88	
Co Kα				89	90				91 92 93		94	95 96 97	X	98 99					100 101	
Co Kβ													102 103	X	104			105		
Ni Kα				106	107 108			109		110	111 112	113		114	X			115	116 117	
Ni Kβ				118	119				120 121	122 123	124					X	125			
Cu Kα		126				127		128 129 130		131 132 133	134					135	X			
Cu Kβ														136	137			X		
Zn Kα				138 139	140 141						142 143	144 145	146 147		148 149				X	
Zn Kβ			150																	X

Table 4: Two-color configurations for XES experiments (1/3)

Case	Analyzer	Bragg angles
1	Ge(1,0,0) / Ge(1,0,0)	79.3° / 76.5°
2	Ge(1,0,0) / Ge(2,1,1)	79.3° / 81.5°
3	Ge(1,0,0) / Si(1,1,1)	79.3° / 79.7°
4	Ge(1,0,0) / Ge(1,0,0)	76.5° / 79.3°
5	Ge(1,0,0) / Ge(1,1,0)	76.5° / 76.2°
6	Si(1,0,0) / Si(1,0,0)	67.8° / 67.3°
7	Ge(1,0,0) / Ge(1,0,0)	62.7° / 62.3°
8	Si(1,0,0) / Si(1,1,1)	67.8° / 68.0°
9	Ge(1,0,0) / Si(2,1,1)	62.7° / 60.9°
10	Si(1,0,0) / Si(1,1,0)	67.8° / 66.2°
11	Si(1,0,0) / Si(1,1,0)	67.8° / 68.9°
12	Ge(1,0,0) / Ge(5,3,1)	62.7° / 60.2°
13	Ge(1,0,0) / Si(5,3,3)	62.7° / 64.9°
14	Si(1,0,0) / Si(1,1,1)	67.8° / 66.4°
15	Ge(1,0,0) / Si(5,3,3)	62.7° / 60.2°
16	Si(1,0,0) / Si(1,0,0)	67.3° / 67.8°
17	Ge(1,0,0) / Ge(1,0,0)	62.3° / 62.7°
18	Si(1,0,0) / Si(1,1,1)	67.3° / 68.0°
19	Ge(1,0,0) / Si(2,1,1)	62.3° / 60.9°
20	Si(1,0,0) / Si(1,1,0)	67.3° / 66.2°
21	Si(1,0,0) / Si(1,1,0)	67.3° / 68.9°
22	Si(1,0,0) / Si(5,3,1)	67.3° / 64.7°
23	Ge(1,0,0) / Ge(5,3,1)	62.3° / 60.2°
24	Ge(1,0,0) / Si(5,3,3)	62.3° / 64.9°
25	Si(1,0,0) / Si(1,1,1)	67.3° / 66.4°
26	Ge(1,0,0) / Si(5,3,3)	62.3° / 60.2°
27	Ge(2,1,1) / Ge(1,0,0)	81.5° / 79.3°
28	Ge(2,1,1) / Ge(2,1,1)	81.5° / 82.8°
29	Ge(2,1,1) / Si(1,1,0)	81.5° / 84.2°
30	Ge(2,1,1) / Si(1,1,1)	81.5° / 79.7°
31	Ge(2,1,1) / Ge(2,1,1)	82.8° / 81.5°
32	Ge(2,1,1) / Si(1,1,0)	82.8° / 84.2°
33	Si(1,1,1) / Si(1,1,0)	85.9° / 84.2°
34	Ge(1,1,1) / Ge(1,1,0)	73.2° / 72.7°
35	Ge(1,1,1) / Ge(1,1,0)	73.2° / 75.7°
36	Ge(2,1,1) / Ge(1,1,1)	64.5° / 62.9°
37	Si(2,1,1) / Si(5,3,1)	70.1° / 73.1°
38	Ge(2,1,1) / Ge(5,3,1)	64.5° / 66.7°
39	Ge(1,1,1) / Ge(5,3,3)	73.2° / 74.1°
40	Si(2,1,1) / Si(5,3,3)	70.1° / 68.6°
41	Ge(1,1,1) / Ge(1,1,1)	73.2° / 70.8°
42	Ge(2,1,1) / Ge(5,3,3)	64.5° / 63.4°
43	Ge(1,1,1) / Si(5,3,1)	75.0° / 73.1°
44	Si(2,1,1) / Si(1,1,0)	71.6° / 68.9°
45	Ge(1,1,1) / Si(5,3,1)	75.0° / 77.3°
46	Ge(2,1,1) / Ge(1,1,0)	65.6° / 63.5°
47	Si(2,1,1) / Si(1,1,1)	71.6° / 73.1°
48	Ge(2,1,1) / Ge(1,1,1)	65.6° / 66.7°
49	Si(1,1,0) / Ge(2,1,1)	84.2° / 81.5°
50	Si(1,1,0) / Ge(2,1,1)	84.2° / 82.8°

Table 5: Two-color configurations for XES experiments (2/3)

Case	Analyzer	Bragg angles
51	Si(1,1,0) / Si(1,1,1)	84.2° / 85.9°
52	Ge(1,1,0) / Ge(1,1,1)	72.7° / 73.2°
53	Ge(1,1,0) / Ge(1,1,0)	72.7° / 75.7°
54	Ge(1,1,1) / Ge(1,1,1)	61.3° / 62.9°
55	Ge(1,1,0) / Ge(5,3,3)	72.7° / 74.1°
56	Si(1,1,1) / Si(5,3,3)	66.0° / 64.9°
57	Ge(1,1,1) / Ge(5,3,3)	61.3° / 60.4°
58	Si(1,1,1) / Si(5,3,3)	66.0° / 68.6°
59	Ge(1,1,0) / Ge(1,1,1)	72.7° / 70.8°
60	Ge(1,1,1) / Ge(5,3,3)	61.3° / 63.4°
61	Si(1,1,1) / Si(1,0,0)	68.0° / 67.8°
62	Si(2,1,1) / Ge(1,0,0)	60.9° / 62.7°
63	Si(1,1,1) / Si(1,0,0)	68.0° / 67.3°
64	Si(2,1,1) / Ge(1,0,0)	60.9° / 62.3°
65	Ge(1,1,0) / Ge(1,1,1)	75.7° / 73.2°
66	Ge(1,1,1) / Ge(2,1,1)	62.9° / 64.5°
67	Ge(1,1,0) / Ge(1,1,0)	75.7° / 72.7°
68	Ge(1,1,1) / Ge(1,1,1)	62.9° / 61.3°
69	Si(1,1,1) / Si(1,1,0)	68.0° / 66.2°
70	Si(1,1,1) / Si(1,1,0)	68.0° / 68.9°
71	Si(2,1,1) / Ge(5,3,1)	60.9° / 60.2°
72	Ge(1,1,0) / Ge(5,3,3)	75.7° / 74.1°
73	Ge(1,1,1) / Ge(5,3,3)	62.9° / 60.4°
74	Ge(1,1,1) / Ge(5,3,3)	62.9° / 63.4°
75	Si(1,1,1) / Si(1,1,1)	68.0° / 66.4°
76	Si(2,1,1) / Si(5,3,3)	60.9° / 60.2°
77	Si(1,1,0) / Si(1,0,0)	66.2° / 67.8°
78	Si(1,1,0) / Si(1,0,0)	66.2° / 67.3°
79	Si(5,3,1) / Si(2,1,1)	73.1° / 70.1°
80	Ge(5,3,1) / Ge(2,1,1)	66.7° / 64.5°
81	Si(5,3,1) / Ge(1,1,1)	73.1° / 75.0°
82	Si(1,1,0) / Si(1,1,1)	66.2° / 68.0°
83	Si(1,1,0) / Si(1,1,0)	66.2° / 68.9°
84	Ge(1,1,0) / Ge(1,1,0)	61.4° / 63.5°
85	Ge(5,3,1) / Ge(5,3,1)	66.7° / 69.4°
86	Si(1,1,0) / Si(5,3,1)	66.2° / 64.7°
87	Si(1,1,0) / Si(1,1,1)	66.2° / 66.4°
88	Ge(1,1,0) / Ge(1,1,1)	61.4° / 61.6°
89	Si(1,1,0) / Si(1,0,0)	68.9° / 67.8°
90	Si(1,1,0) / Si(1,0,0)	68.9° / 67.3°
91	Si(1,1,0) / Si(2,1,1)	68.9° / 71.6°
92	Si(5,3,1) / Ge(1,1,1)	77.3° / 75.0°
93	Ge(1,1,0) / Ge(2,1,1)	63.5° / 65.6°
94	Si(1,1,0) / Si(1,1,1)	68.9° / 68.0°
95	Si(1,1,0) / Si(1,1,0)	68.9° / 66.2°
96	Ge(1,1,0) / Ge(1,1,0)	63.5° / 61.4°
97	Ge(5,3,1) / Ge(5,3,1)	69.4° / 66.7°
98	Si(5,3,1) / Si(5,3,3)	77.3° / 78.1°
99	Ge(5,3,1) / Ge(5,3,3)	69.4° / 69.9°
100	Si(1,1,0) / Si(1,1,1)	68.9° / 66.4°

Table 6: Two-color configurations for XES experiments (3/3)

Case	Analyzer	Bragg angles
101	Ge(1,1,0) / Ge(1,1,1)	63.5° / 61.6°
102	Si(5,3,3) / Si(5,3,1)	78.1° / 77.3°
103	Ge(5,3,3) / Ge(5,3,1)	69.9° / 69.4°
104	Si(5,3,1) / Si(5,3,1)	62.0° / 64.7°
105	Si(5,3,1) / Si(1,1,1)	62.0° / 62.6°
106	Ge(5,3,1) / Ge(1,0,0)	60.2° / 62.7°
107	Si(5,3,1) / Si(1,0,0)	64.7° / 67.3°
108	Ge(5,3,1) / Ge(1,0,0)	60.2° / 62.3°
109	Ge(5,3,3) / Ge(1,1,1)	74.1° / 73.2°
110	Ge(5,3,3) / Ge(1,1,0)	74.1° / 72.7°
111	Ge(5,3,1) / Si(2,1,1)	60.2° / 60.9°
112	Ge(5,3,3) / Ge(1,1,0)	74.1° / 75.7°
113	Si(5,3,1) / Si(1,1,0)	64.7° / 66.2°
114	Si(5,3,1) / Si(5,3,1)	64.7° / 62.0°
115	Si(5,3,1) / Si(1,1,1)	64.7° / 62.6°
116	Si(5,3,1) / Si(1,1,1)	64.7° / 66.4°
117	Ge(5,3,1) / Si(5,3,3)	60.2° / 60.2°
118	Si(5,3,3) / Ge(1,0,0)	64.9° / 62.7°
119	Si(5,3,3) / Ge(1,0,0)	64.9° / 62.3°
120	Si(1,1,1) / Si(2,1,1)	73.1° / 71.6°
121	Ge(1,1,1) / Ge(2,1,1)	66.7° / 65.6°
122	Si(5,3,3) / Si(1,1,1)	64.9° / 66.0°
123	Ge(5,3,3) / Ge(1,1,1)	60.4° / 61.3°
124	Ge(5,3,3) / Ge(1,1,1)	60.4° / 62.9°
125	Ge(5,3,3) / Ge(5,3,3)	60.4° / 63.4°
126	Si(1,1,1) / Ge(1,0,0)	79.7° / 79.3°
127	Si(1,1,1) / Ge(2,1,1)	79.7° / 81.5°
128	Si(5,3,3) / Si(2,1,1)	68.6° / 70.1°
129	Ge(1,1,1) / Ge(1,1,1)	70.8° / 73.2°
130	Ge(5,3,3) / Ge(2,1,1)	63.4° / 64.5°
131	Si(5,3,3) / Si(1,1,1)	68.6° / 66.0°
132	Ge(1,1,1) / Ge(1,1,0)	70.8° / 72.7°
133	Ge(5,3,3) / Ge(1,1,1)	63.4° / 61.3°
134	Ge(5,3,3) / Ge(1,1,1)	63.4° / 62.9°
135	Ge(5,3,3) / Ge(5,3,3)	63.4° / 60.4°
136	Si(1,1,1) / Si(5,3,1)	62.6° / 62.0°
137	Si(1,1,1) / Si(5,3,1)	62.6° / 64.7°
138	Si(1,1,1) / Si(1,0,0)	66.4° / 67.8°
139	Si(5,3,3) / Ge(1,0,0)	60.2° / 62.7°
140	Si(1,1,1) / Si(1,0,0)	66.4° / 67.3°
141	Si(5,3,3) / Ge(1,0,0)	60.2° / 62.3°
142	Si(1,1,1) / Si(1,1,1)	66.4° / 68.0°
143	Si(5,3,3) / Si(2,1,1)	60.2° / 60.9°
144	Si(1,1,1) / Si(1,1,0)	66.4° / 66.2°
145	Ge(1,1,1) / Ge(1,1,0)	61.6° / 61.4°
146	Si(1,1,1) / Si(1,1,0)	66.4° / 68.9°
147	Ge(1,1,1) / Ge(1,1,0)	61.6° / 63.5°
148	Si(1,1,1) / Si(5,3,1)	66.4° / 64.7°
149	Si(5,3,3) / Ge(5,3,1)	60.2° / 60.2°
150	Ge(1,1,0) / Ge(1,0,0)	76.2° / 76.5°

H Multiplet calculations

Parameter values for the multiplet calculations in chapter 3 are given in table 7.

Table 7: Parameter values for multiplet calculations on cobalt ions.

Fig.	Case	Ion	Spectrum	f2dd %	f4dd %	ls3d %	ls2p %	f2pd %	g1pd %	g3pd %	10Dq eV
3.4	1	Co3+	1s2p XES	0	0	100	100	0	0	0	0.00
3.5	2	Co3+	1s2p XES	0	0	100	60	0	0	0	0.00
3.5	3	Co3+	1s2p XES	0	0	100	80	0	0	0	0.00
3.5	4	Co3+	1s2p XES	0	0	100	100	0	0	0	0.00
3.5	5	Co3+	1s2p XES	0	0	100	80	0	0	0	0.00
3.5	6	Co3+	1s2p XES	30	30	100	100	30	30	30	0.00
3.6	7	Co2+	1s3p XES	100	100	100	100	100	100	100	2.00
3.7	8	Co2+	1s3p XES	80	80	0	0	50	0	0	1.90
3.7	9	Co2+	1s3p XES	80	80	0	0	50	30	30	1.90
3.7	10	Co2+	1s3p XES	80	80	0	0	50	60	60	1.90
3.7	11	Co2+	1s3p XES	0	0	0	0	0	0	0	1.90
3.7	12	Co2+	1s3p XES	0	0	100	100	0	0	0	1.90

I Full RXES maps on cobalt VT compounds

The visualized RXES maps discussed in chapter 5 focus on the cobalt K-pre-edge region. The full RXES maps are given in figure I.1.

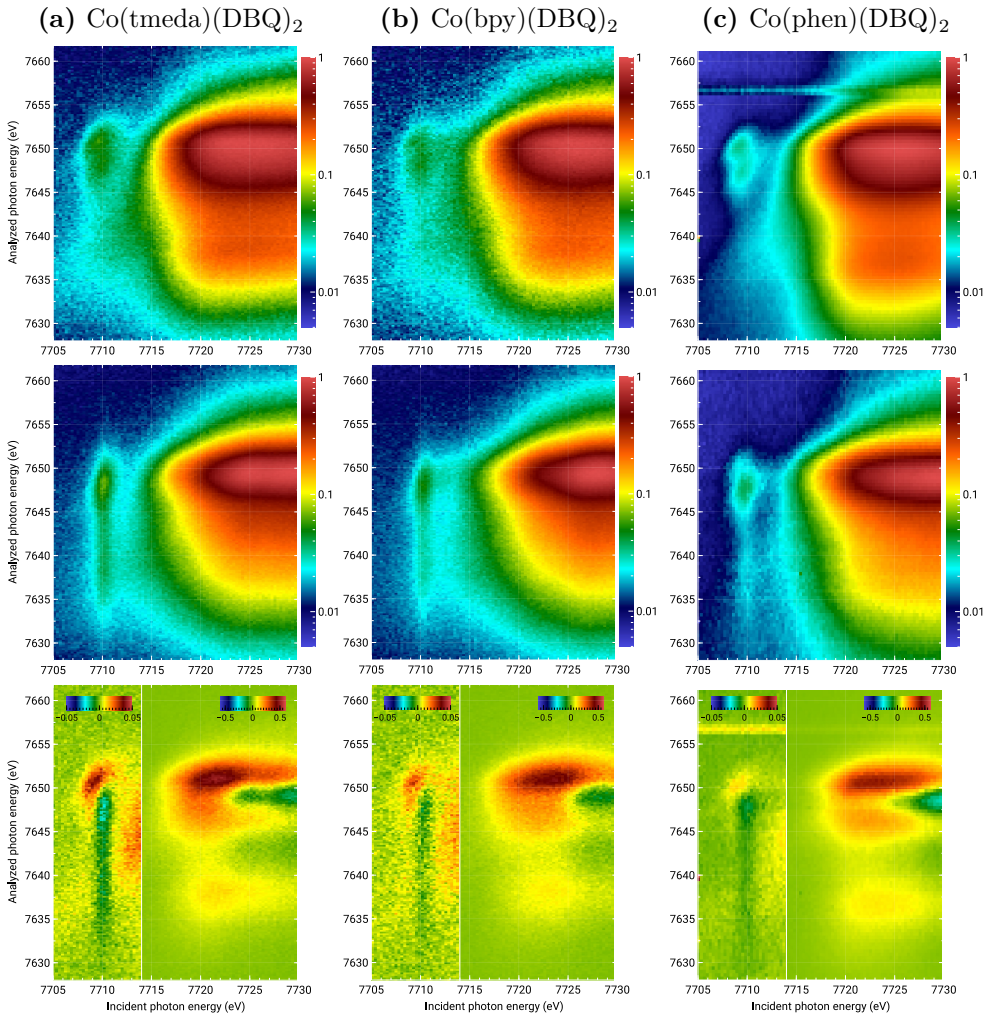

Figure I.1: Resonant XES data on cobalt VT compounds. High-temperature (top), low-temperature (center) and high-low temperature difference (bottom) are presented for three compounds. The color scale for top and center plots is logarithmic. Differences are visualized on a linear color scale. The high-temperature data for $Co(DTB)_2(phen)$ contains a horizontal glitch at 7655 eV analyzed (emitted) photon energy, which is due to differences in the sample concentration during data acquisition.

J DFT and TD-DFT calculations on the benzoquinone ligand

Exemplary ORCA input file for the geometry optimization of 3,5-di-tert-butyl-o-benzoquinone:

```
# Geometry optimization
! B3LYP RIJCOSX def2-TZVP def2/J CPCM(TOLUENE) D3BJ TIGHTSCF Opt
! Freq
% pal nprocs 32
end
%maxcore 20000
* xyzfile 0 1 raw.xyz
```

Inspecting the vibrational frequencies revealed no negative frequencies, indicating that the geometry optimization did not yield a saddle point [127].

The input coordinates (raw.xyz) were taken from the crystal structure of benzoquinone [131] and edited in the Avogadro molecular editor [132].

```
C         -1.12184         0.67348         0.34810
C         -1.09498         2.18199         0.33987
C          0.00000         2.92163         0.00013
C          1.24139         2.17512        -0.38642
C          0.00002         0.00003         0.00022
C          1.22957         0.70496        -0.38224
O          2.26582         2.75783        -0.70559
O          2.22719         0.07167        -0.69229
H          0.02387        -1.08449        -0.00668
H         -1.99998         2.68760         0.62149
C         -2.39076        -0.12592         0.74242
C         -0.01415         4.47925         0.00643
C          0.29079         5.00855        -1.41251
H          1.28642         4.69063        -1.77808
H          0.28091         6.12017        -1.42817
H         -0.47383         4.64408        -2.13224
C         -1.37628         5.08607         0.43291
H         -2.18610         4.78014        -0.26454
H         -1.33515         6.19724         0.42203
H         -1.64523         4.77704         1.46639
C          1.04450         5.00541         1.00111
H          2.07116         4.68813         0.73416
H          0.82550         4.63809         2.02708
H          1.04584         6.11696         1.02275
C         -3.58748         0.78316         1.10925
H         -3.34554         1.42783         1.98180
H         -4.47552         0.17342         1.38477
H         -3.87964         1.42315         0.24863
C         -2.83191        -1.01798        -0.43971
```

H	-3.06251	-0.39380	-1.33005
H	-3.74199	-1.59961	-0.17633
H	-2.04558	-1.74785	-0.72271
C	-2.08587	-1.01019	1.97223
H	-1.77551	-0.38001	2.83370
H	-1.27478	-1.73879	1.76624
H	-2.98444	-1.59217	2.27183

Optimized coordinates for 3,5-di-tert-butyl-o-benzoquinone:

C	-0.98473390393079	0.64166599872335	0.58034826195083
C	-1.04096262508123	2.08274664867333	0.30075898581357
C	0.01117384685215	2.88494019332399	0.04661266471342
C	1.35203227702474	2.25438301979424	0.05195323307612
C	0.20164571413927	0.00288912313653	0.59643231159983
C	1.43693875670507	0.72210681887423	0.34508343578469
O	2.38735023399381	2.84896584222453	-0.15574572346426
O	2.53136620008137	0.19301130173089	0.35313549930862
H	0.29665812956820	-1.05448912126704	0.79574529993587
H	-2.02715784674807	2.51911831023508	0.30195972626604
C	-2.31234300055137	-0.05544023017164	0.84207796450794
C	-0.12125386941600	4.37739840689207	-0.24021844805289
C	0.44017534655815	4.68628541019872	-1.64392054006590
H	1.49512437638292	4.43380802682682	-1.71872173771720
H	0.32449488321436	5.75143562195086	-1.85493112549867
H	-0.10701390654828	4.12878757053565	-2.40729208062267
C	-1.58506425389817	4.83301708218579	-0.20637694473007
H	-2.18819854980681	4.31934885920144	-0.95798590992380
H	-1.62898102727105	5.90183575777635	-0.41976899836837
H	-2.04036060849284	4.67142821980290	0.77300441450627
C	0.65386601326714	5.18068650851039	0.82495016759491
H	1.71453165630938	4.94183404947072	0.81254675905175
H	0.26071769955995	4.97400731962862	1.82281417451889
H	0.53783165719424	6.24876631614428	0.62961276231900
C	-2.98398063574595	0.59378121214572	2.07043791330045
H	-2.35446352917370	0.48657848540789	2.95558251882960
H	-3.93714055292252	0.09891147676801	2.26607340743649
H	-3.18484511144095	1.65488082846493	1.92140880307417
C	-3.21981504850340	0.11263238265354	-0.39436795335787
H	-3.42334594068870	1.15984259582041	-0.61871233946003
H	-4.17595668563930	-0.38102519769342	-0.21123084248332
H	-2.76175625781776	-0.34228663261261	-1.27435395969362
C	-2.13896655172133	-1.55203626823137	1.11845829613457
H	-1.51914167420812	-1.72843219323958	1.99890953294952
H	-1.68787238190273	-2.06882519677213	0.26978690096998
H	-3.11664282934158	-1.99973854711372	1.30191356979610

Optimized coordinates for 3,5-di-tert-butylcatechol:

C	-1.11666659003500	0.71615932361117	0.39006020048350
C	-1.07731893068837	2.10670347360651	0.35348946964214

```
C   0.06773560255207      2.84460046759713      0.00802705018413
C   1.22640292265765      2.12234273047266     -0.31110950850677
C   0.05749092348077      0.03349966623929      0.06210795524968
C   1.20887422507765      0.71934272700530     -0.28093236336879
O   2.43453561713900      2.66616360108850     -0.66527627195653
O   2.37568529589872      0.08015276255576     -0.60438582154303
H   0.09267389934911     -1.05051191025767      0.06913117442841
H   -1.97160051438178      2.65066712117800      0.60288470062319
C   -2.38011965005300     -0.07668672973093      0.76311241823919
C   0.03348287359167      4.38958414215479     -0.01356642059692
C   0.33852997151245      4.92314620977484     -1.43413216030655
H   1.32143652180828      4.64542950861365     -1.81831934430340
H   0.28710398830372      6.01439456793918     -1.43886200737574
H   -0.39889200969406      4.54600450225754     -2.14535294897561
C   -1.35176923285940      4.94636534666232      0.36201986676878
H   -2.12578724185448      4.61765170521936     -0.33343344638200
H   -1.31552794320763      6.03694986301781      0.32508065930296
H   -1.64963587293970      4.65972069307874      1.37197562945643
C   1.03089346608339      4.97011930924823      1.01776746566794
H   2.06865511068904      4.67793112422900      0.85022026250947
H   0.76658508196489      4.64032972125696      2.02441292564584
H   0.99406378286969      6.06186288239730      0.99737739154946
C   -3.55957388040283      0.83739169293997      1.12864239363559
H   -3.32957963051895      1.47122670592107      1.98769118212570
H   -4.42582240307711      0.22607366517476      1.39035812466854
H   -3.84927997868379      1.48166069294889      0.29596720215154
C   -2.80684855885677     -0.95636792660950     -0.43162320714559
H   -3.03235816658331     -0.34128571648969     -1.30571491597562
H   -3.70187354111344     -1.53152414413525     -0.18001500752213
H   -2.02367108729674     -1.66279852488429     -0.71148024606764
C   -2.08458039121955     -0.98252809979322      1.97782746415665
H   -1.78247707181780     -0.38758469550338      2.84272444715126
H   -1.28657827157044     -1.69566340750545      1.76551287820495
H   -2.97647872399886     -1.55219412205738      2.25131049111152
H   2.38102018172300      3.62575978517726     -0.67787898483457
H   2.23858022615193     -0.87340871439930     -0.54622869809596
```

Table 8: Comparison of the DFT-optimized molecular structures of 3,5-di-tert-butyl--o-benzoquinone and 3,5-di-tert-butylcatechol with the crystallographic data on 1,2-benzoquinone [131]. The atomic labels are according to figure 4.18.

	exp.	Q	CAT
O1 – C1	1.216	1.212	1.371
O2 – C2	1.216	1.216	1.369
C1 – C2	1.541	1.562	1.403
C2 – C3	1.463	1.451	1.383
C3 – C4	1.336	1.348	1.397
C4 – C5	1.445	1.469	1.392
C5 – C6	1.336	1.347	1.405
C6 – C1	1.463	1.482	1.402

Exemplary ORCA input file for the TD-DFT calculation on benzoquinone complexes:

```
# TD-DFT XAS
! B3LYP RIJCOSX DEF2-TZVP moread NORMALPRINT
%moinp "opt.gbw"

%tddft
OrbWin[0] = 0,0,-1,-1
NRoots 150
DoQuad true
end

% pal nprocs 32
end
%maxcore 20000

* XYZfile 0 1 opt.xyz
```

K XRS measurement on benzoquinones

The general spectrometer setup at the GALAXIES beamline at SOLEIL was chosen to be in the forward-scattering geometry in the horizontal plane. The sample stage was rotated until the beam hit the sample surface at an incident angle of 15°. On the detection side, a 40 analyzer spectrometer was placed at 1 m distance and under a scattering angle of 2x15° = 30° with respect to the incoming photon beam. The spectrometer analyzer crystals were chosen to be Si(110) in 6th order reflection, yielding a Bragg angle of 87° for the detection of 9699 eV photons. After Bragg-reflection, photons were detected by a 4 module Merlin detector with 55 um pixel size. Out of the 40 analyzers, 38 analyzers gave satisfactory signal on the detector. Samples were

mounted at the end of an He-compressor cryostat head, which was not used during the measurements of this samples.

Figure K.1: Exploratory XRS measurements at the GALAXIES beamline at the SOLEIL synchrotron, France. Top left: The combined setup for detection of both XES and XRS signals by use of a Johann type spectrometer and a dispersive von Hamos type spectrometers. Top right: Sample enviroment; Sample holder and cryostat cap, installed. Bottom right: Detail view of the canted sample holder for reflection geometry simultaneous XES and XRS measurements. Bottom right: Samples after the measurements. In this case, clear signs of radiation induced changes in the sample are visible.

L Assessment of crystal phase changes with XRPD

A standardized diffraction setup was used at BL9, DELTA, Dortmund, Germany, to record powder diffraction data. The sample was positioned inside a horizontally mounted borosilicate 2 mm glass capillary at 1015 mm distance from a Pilatus 100K-S area detector. The detector was fixed at the end of a goniometer arm, which allowed the acquisition of scattering angles ϑ in the range of ca. $2 - 17\ ^\circ$ by scanning the arm

along its elevation angle. This technique essentially samples a vertical slice of the scattering cone, where the width of the slice is given by the horizontal chip size of the detector. The beam size was set to be ca. 1.5 mm x 0.6 mm (H x V) with slits. The incoming photon energy was monochromatized to 15 keV with a Si(1,1,1) double crystal monochromator. The samples were ground and filled into the glass capillaries shortly before the measurement. The sample capillary was mounted onto a pressured air-driven rotation stage which spun the capillary during the measurement along its central axis, thus reducing anisotropy artifacts. VT transitions were induced by cooling with an LN2-operated cryo-jet, which was mounted at a nozzle distance of approximately 5mm above the sample. In this configuration, typical integration times to collect a powder diffraction dataset were around 900 s per sample per temperature point.

A complete dataset was recorded as a series of detector images at different goniometer angles. The diffraction pattern was then obtained by calculating geometrically, for each scan step, (i) the detector chip surface normal based on the goniometer angle, (i) the resulting true scattering angle ϑpix of each pixel position on the detector. The resulting data pairs ϑpix, pixel intensity were then binned along values for ϑpix, i.e., intensities for similar ϑpix values were added up. The final result is a distribution of intensities over ϑ. This approach allowed for fully exploiting the 2D data with minimal resolution or counting statistics loss.

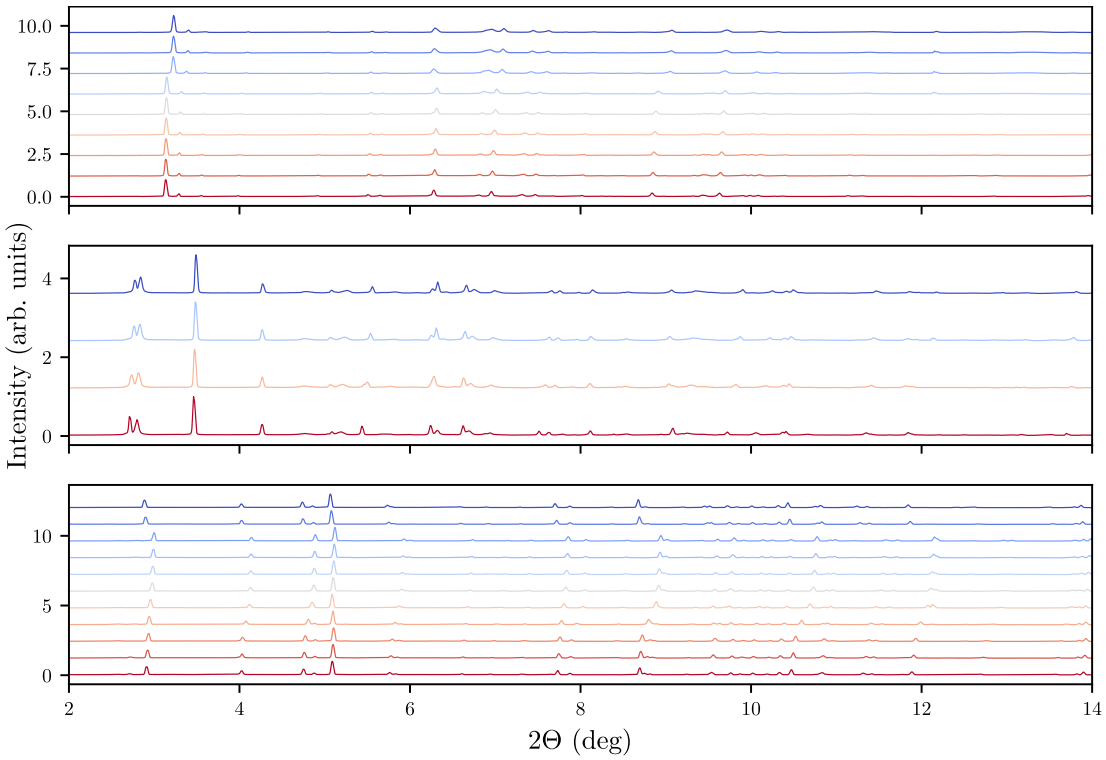

Figure L.1: X-ray powder diffraction on $Co(DTB)_2(tmeda)$, $Co(DTB)_2(bpy)$ and $Co(DTB)_2(phen)$ during temperature induced transition.

M Transient XES measurements at FXE, EuXFEL

M.1 Reconstructed laser-pumped XES spectra

In figure M.1, laser-pumped XES line shapes R of $Co(DTB)_2(tmeda)$ in toluene solution were reconstructed by systematically varying the scaling factor f of the difference spectrum between laser-pumped and laser-unpumped spectra, D, and subsequent addition to the laser-unpumped spectra U

$$R = U + fD. \tag{1}$$

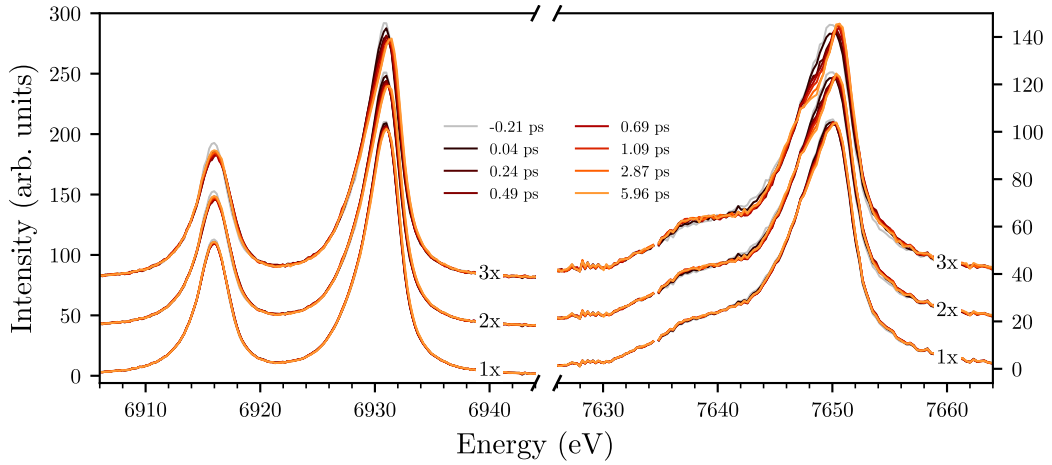

Figure M.1: Excited (laser-pumped) (1x) and reconstructed cobalt XES spectra (2x, 3x), calculated by adding the scaled difference curve between laser-pumped and laser-unpumped spectra to the the GS laser-umpumped spectra.

M.2 Trace fitting

Additional to the trace-fitting analysis presented in section 6.4.8, the results of an individual (i.e., separated by Kα and Kβ traces) approach are given.

Table 9: Fitted time cosnstants for the two-exponential decay model on kinetic traces extracted from the transient differences in the Kα and Kβ region. The Kα and Kβ traces were fitted independently.

Property	Fitted value (Kα)	Fitted value (Kβ)	
t_1	0.19 ± 0.04	0.28 ± 0.08	ps
t_2	0.82 ± 0.09	0.97 ± 0.04	ps

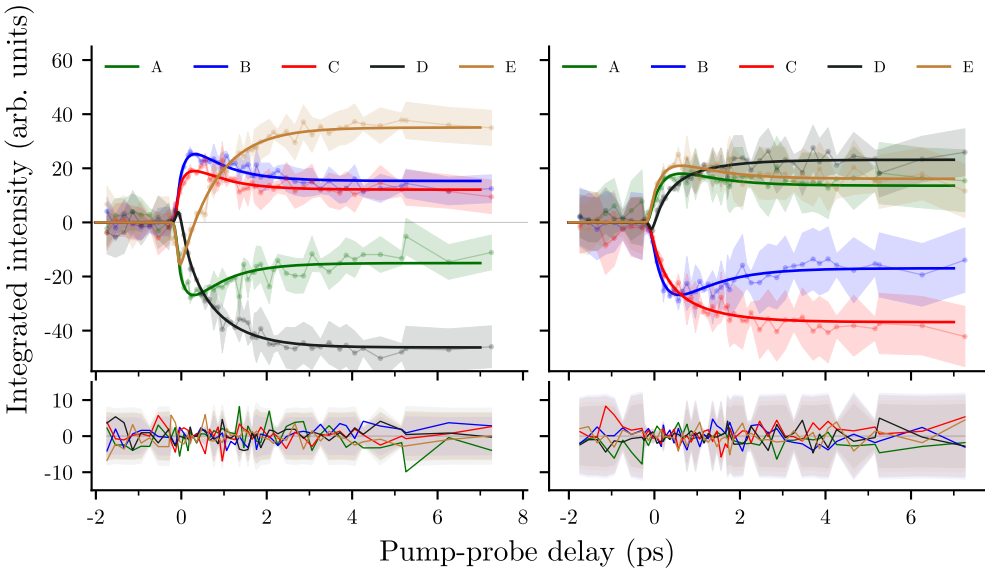

Figure M.2: Separately fitted Kα and Kβ XES traces

Acronyms

CEE Constant emitted energy

CFSE Crystal field stabilization energy

CFT Crystal field theory

CIE Constant incoming energy

DADS Decay associated difference spectra

DFT Density functional theory

EELS Electron energy loss spectroscopy

ESA Excited state absorption

EuXFEL European X-ray free electron laser facility

EXAFS Extended X-ray absorption fine structure

FEL Free electron laser

FWHM Full width at half maximum

GS Ground-state

GSB Ground-state bleach

HERFD High energy resolution fluorescence detected

HOMO Highest occupied molecular orbital

HPLC High-performance liquid chromatography

HS High-spin

IAD Integrated area difference

IRF Instrument response function

IWAE Intensity weighted average energy

LFT Ligand field theory

LMCT Ligand-to-metal charge transfer

LS Low-spin

LUMO Lowest unoccupied molecular orbital

MLCT Metal-to-ligand charge transfer

MO Molecular orbital

NDO Natural difference orbital

NMR Nuclear magnetic resonance

PPODL Pump-probe optical delay line

ROI Region of interest

RXES Resonant X-ray emission spectroscopy

SASE Self-amplified stimulated emission

TD-DFT Time-dependent density functional theory

TM Transition metal

TOAS Transient optical absorption spectroscopy

VT Valence tautomerism / valence tautomer

VtC Valence-to-core

XANES X-ray absorption near edge structure

XAS X-ray absorption spectroscopy

XES X-ray emission spectroscopy

XRS X-ray Raman scattering

Index of chemical compounds

1 $Co(DTB)_2(tmeda)$

1a · toluene $Co(DTB)_2(tmeda)$ 5 mM in toluene

2 $Co(DTB)_2(bpy)$

3 $Co(DTB)_2(phen)$

1a $Co(DTB)_2(tmeda)$, low-temperature

2a $Co(DTB)_2(bpy)$, low-temperature

3a $Co(DTB)_2(phen)$, low-temperature

1b $Co(DTB)_2(tmeda)$, high-temperature

2b $Co(DTB)_2(bpy)$, high-temperature

3b $Co(DTB)_2(phen)$, high-temperature

4 $[Co(bpy)_3]Cl_3 \cdot 4\,H_2O$ / $[Co(bpy)_3]Cl_2 \cdot 5\,H_2O$

4a $[Co(bpy)_3]Cl_3 \cdot 4\,H_2O$

4b $[Co(bpy)_3]Cl_2 \cdot 5\,H_2O$

4b·H_2O 100 mM $[Co(bpy)_3]Cl_2$ 100 mM in water

5 $[Co(phen)_3]Cl_3] \cdot 5\,H_2O$ / $[Co(phen)_3]Cl_2] \cdot 2\,H_2O$

5a $[Co(phen)_3]Cl_3 \cdot 5\,H_2O$

5b $[Co(phen)_3]Cl_2 \cdot 2\,H_2O$

6 $[Co(acac)_3]$ / $[Co(acac)_2]$

6a $[Co(acac)_3]$

6b $[Co(acac)_2]$

6a· toluene $[Co(acac)_3]$ 5 mM in toluene

6aH_2O 21 mM $[Co(acac)_3]$ 5 mM in water

6b· toluene $[Co(acac)_2]$ 5 mM in toluene

7 $[Co(terpy)_2]Cl_2$

8 $[Co(salen)]_2$

9 $[Co(en)_3]Cl_3 \cdot 2\,H_2O$

10 CoF3

11 $Co(DTB)_2(dpbpy)$

11a $Co(DTB)_2(dpbpy)$, low-temperature

11b $Co(DTB)_2(dpbpy)$, high-temperature

12 Co(sep)

12·H_2O 21 mM Co(sep) 21 mM in water

13 Co(II,III) oxide

14 $Co(NH_3)_6$ 230 mM in water

15 $Co(C_2O_4)$

16 Co foil

17 3,5-di-tert-butyl-o-benzoquinone

18 3,5-di-tert-butylcatechol

Bibliography

[1] D. M. Grant and R. K. Harris, eds. *Encyclopedia of nuclear magnetic resonance*. Chichester ; New York: John Wiley, 1996.

[2] L. Antonov, ed. *Tautomerism: concepts and applications in science and technology*. Weinheim: Wiley-VCH Verlag GmbH & Co. KGaA, 2016.

[3] M. Binnewies et al. *Allgemeine und Anorganische Chemie*. Vol. 58. Berlin, Heidelberg: Springer Berlin Heidelberg, 2016.

[4] C. Van Stappen et al. "The Spectroscopy of Nitrogenases". In: *Chemical Reviews* 120.12 (2020), pp. 5005–5081.

[5] C. K. Prier, D. A. Rankic, and D. W. C. MacMillan. "Visible Light Photoredox Catalysis with Transition Metal Complexes: Applications in Organic Synthesis". In: *Chemical Reviews* 113.7 (2013), pp. 5322–5363.

[6] A. H. Proppe et al. "Bioinspiration in light harvesting and catalysis". In: *Nature Reviews Materials* 5.11 (2020), pp. 828–846.

[7] J. D. Slinker et al. "Electroluminescent devices from ionic transition metal complexes". In: *J. Mater. Chem.* 17.29 (2007), pp. 2976–2988.

[8] J. S. Griffith and L. E. Orgel. "Ligand-field theory". In: *Quarterly Reviews, Chemical Society* 11.4 (1957), p. 381.

[9] C. Janiak, H.-J. Meyer, and E. Riedel, eds. *Riedel, moderne anorganische Chemie*. 5. Auflage. De Gruyter Studium. Berlin: De Gruyter, 2018.

[10] S. F. A. Kettle. *Physical Inorganic Chemistry*. Berlin, Heidelberg: Springer Berlin Heidelberg, 1996.

[11] R. J. Lancashire. *Tanabe-Sugano diagrams via spreadsheets*. URL: `http://wwwchem.uwimona.edu.jm/courses/Tanabe-Sugano/TSspread.html` (visited on 06/19/2022).

[12] D. A. Shultz. "Valence Tautomerism in Dioxolene Complexes of Cobalt". In: *Magnetism: Molecules to Materials II*. Vol. 7. Weinheim, FRG: Wiley-VCH Verlag GmbH & Co. KGaA, 2015, pp. 281–306.

[13] P. Gütlich and H. A. Goodwin. "Spin Crossover—An Overall Perspective". In: *Spin Crossover in Transition Metal Compounds I*. Ed. by P. Gütlich and H. Goodwin. Vol. 233. Berlin, Heidelberg: Springer Berlin Heidelberg, 2004, pp. 1–47.

[14] D. N. Hendrickson and C. G. Pierpont. "Valence Tautomeric Transition Metal Complexes". In: *Spin Crossover in Transition Metal Compounds II*. Vol. 234. Berlin, Heidelberg: Springer Berlin Heidelberg, 2004, pp. 63–95.

[15] D. M. Adams et al. "Controlling Valence Tautomerism of Cobalt Complexes Containing the Benzosemiquinone Anion as Ligand". In: *Angewandte Chemie International Edition* 32.6 (1993), pp. 880–882.

[16] D. M. Adams et al. "Bistability in the [Co^{II}(semiquinonate)$_2$] to [Co^{III}(catecholate)(semiquinonate)] valence-tautomeric conversion". In: *Journal of the American Chemical Society* 115.18 (1993), pp. 8221–8229.

[17] R. M. Buchanan and C. G. Pierpont. "Tautomeric catecholate-semiquinone interconversion via metal-ligand electron transfer. Structural, spectral, and magnetic properties of (3,5-di-tert-butylcatecholato)(3,5-di-tert-butylsemiquinone)-(bipyridyl)cobalt(III), a complex containing mixed-valence". In: *Journal of the American Chemical Society* 102.15 (1980), pp. 4951–4957.

[18] W. Liang et al. "Charge and Spin-State Characterization of Cobalt Bis(o -dioxolene) Valence Tautomers Using Co Kβ X-ray Emission and L-Edge X-ray Absorption Spectroscopies". In: *Inorganic Chemistry* 56.2 (2017), pp. 737–747.

[19] O. Sato et al. "Photo-induced Valence Tautomerism in Co Complexes". In: *Accounts of Chemical Research* 40.5 (2007), pp. 361–369.

[20] L. Leroy et al. "Controlled Light and Temperature Induced Valence Tautomerism in a Cobalt-o-Dioxolene Complex". In: *Inorganic Chemistry* 60.12 (2021), pp. 8665–8671.

[21] C. Roux et al. "Pressure-Induced Valence Tautomerism in Cobalt o -Quinone Complexes: An X-ray Absorption Study of the Low-Spin [Co III (3,5-DTBSQ)(3,5-DTBCat)(phen)] to High-Spin [Co II (3,5-DTBSQ) 2 (phen)] Interconversion". In: *Inorganic Chemistry* 35.10 (1996), pp. 2846–2852.

[22] A. Caneschi et al. "Pressure- and Temperature-Induced Valence Tautomeric Interconversion in ao-Dioxolene Adduct of a Cobalt-Tetraazamacrocycle Complex". In: *Chemistry - A European Journal* 7.18 (2001), pp. 3926–3930.

[23] G. Poneti et al. "Soft-X-ray-Induced Redox Isomerism in a Cobalt Dioxolene Complex". In: *Angewandte Chemie International Edition* 49.11 (2010), pp. 1954–1957.

[24] T. M. Francisco et al. "Hard x-ray-induced valence tautomeric interconversion in cobalt-o-dioxolene complexes". In: *Journal of Physical Chemistry Letters* 8.19 (2017), pp. 4774–4778.

[25] D. M. Adams et al. "Photoinduced Valence Tautomerism in Cobalt Complexes Containing Semiquinone Anion as Ligand: Dynamics of the High-Spin[CoII(3,5-dtbsq)2] to Low-Spin[CoIII(3,5-dtbsq)(3,5-dtbcat)] Interconversion". In: *Angewandte Chemie International Edition* 34.1314 (1995), pp. 1481–1483.

[26] E. Evangelio et al. “Solvent effects on valence tautomerism: A comparison between the interconversion in solution and solid state”. In: *Solid State Sciences* 11.4 (2009), pp. 793–800.

[27] P. Gütlich and A. Dei. “Valence Tautomeric Interconversion in Transition Metal 1,2-Benzoquinone Complexes”. In: *Angewandte Chemie International Edition* 36.24 (1997), pp. 2734–2736.

[28] C. G. Pierpont and C. W. Lange. “The Chemistry of Transition Metal Complexes Containing Catechol and Semiquinone Ligands”. In: *Progress in Inorganic Chemistry*. John Wiley & Sons, Ltd, 1994, pp. 331–442.

[29] M. P. Bubnov et al. “Photo- and Thermosensitive Molecular Crystals. Valence Tautomeric Interconversion as the Cause of the Photomechanical Effect in Crystals of Bis(dioxolene)cobalt Complex”. In: (2020), pp. 1–4.

[30] D. M. Adams, L. Noodleman, and D. N. Hendrickson. “Density Functional Study of the Valence-Tautomeric Interconversion Low-Spin [Co III (SQ)(Cat)(phen)] - High-Spin [Co II (SQ) 2 (phen)]”. In: *Inorganic Chemistry* 36.18 (1997), pp. 3966–3984.

[31] T. Tezgerevska, K. G. Alley, and C. Boskovic. “Valence tautomerism in metal complexes: Stimulated and reversible intramolecular electron transfer between metal centers and organic ligands”. In: *Coordination Chemistry Reviews* 268 (2014), pp. 23–40.

[32] S. Bruni et al. “Ferromagnetic Coupling between Semiquinone Type Tridentate Radical Ligands Mediated by Metal Ions”. In: *Journal of the American Chemical Society* 116.4 (1994), pp. 1388–1394.

[33] C. G. Pierpont and R. M. Buchanan. “Transition metal complexes of o-benzoquinone, o-semiquinone, and catecholate ligands”. In: *Coordination Chemistry Reviews* 38.1 (1981), pp. 45–87.

[34] J. T. Janetzki et al. “A Convenient DFT-Based Strategy for Predicting Transition Temperatures of Valence Tautomeric Molecular Switches”. In: (), pp. 1–63.

[35] D. M. Adams and D. N. Hendrickson. “Pulsed Laser Photolysis and Thermodynamics Studies of Intramolecular Electron Transfer in Valence Tautomeric Cobalt o -Quinone Complexes”. In: *Journal of the American Chemical Society* 118.46 (1996), pp. 11515–11528.

[36] O. Sato et al. “Photo-induced reverse valence tautomerism in a metastable Co compound”. In: *Chemical Physics Letters* 355.1-2 (2002), pp. 169–174.

[37] C. Boskovic. “Valence Tautomeric Transitions in Cobalt-dioxolene Complexes”. In: *Spin-Crossover Materials*. Oxford, UK: John Wiley & Sons Ltd, 2013, pp. 203–224.

[38] P. T. Touceda et al. “Transient infrared spectroscopy: a new approach to investigate valence tautomerism”. In: *Phys. Chem. Chem. Phys.* 14.2 (2012), pp. 1038–1047.

[39] L. Lohmeyer, E. Kaifer, and H.-J. Himmel. "Solvent-Induced Redox Isomerism of Cobalt Complexes with Redox-Active Bisguanidine Ligands". In: *Inorganic Chemistry* (2022), acs.inorgchem.1c03983.

[40] A. Panja et al. "Solvent-Triggered Cis/Trans Isomerism in Cobalt Dioxolene Chemistry: Distinguishing Effects of Packing on Valence Tautomerism". In: *Inorganic Chemistry* 55.17 (2016), pp. 8331–8340.

[41] F. d. Groot and A. Kotani. *Core level spectroscopy of solids*. Advances in condensed matter science v. 6. Boca Raton: CRC Press, 2008.

[42] C. J. Cramer and D. G. Truhlar. "Density functional theory for transition metals and transition metal chemistry". In: *Physical Chemistry Chemical Physics* 11.46 (2009), p. 10757.

[43] J. Als-Nielsen and D. McMorrow. *Elements of Modern X-ray Physics*. 1st ed. Wiley, 2011.

[44] A. Thompson et al. *X-ray data booklet*. Third edition. Lawrence Berkely National Laboratory, 2009.

[45] S. P. Cramer. *X-Ray Spectroscopy with Synchrotron Radiation: Fundamentals and Applications*. Biological and Medical Physics, Biomedical Engineering. Cham: Springer International Publishing, 2020.

[46] C. J. Sahle et al. "Planning, performing and analyzing X-ray Raman scattering experiments". In: *Journal of Synchrotron Radiation*. 2015.

[47] M. O. Krause. "Atomic radiative and radiationless yields for K and L shells". In: *Journal of Physical and Chemical Reference Data* 8.2 (1979), pp. 307–327.

[48] C. T. Chantler. "Detailed Tabulation of Atomic Form Factors, Photoelectric Absorption and Scattering Cross Section, and Mass Attenuation Coefficients in the Vicinity of Absorption Edges in the Soft X-Ray (Z=30–36, Z=60–89, E=0.1 keV–10 keV), Addressing Convergence Issues of Earlier Work". In: *Journal of Physical and Chemical Reference Data* 29.4 (2000), pp. 597–1056.

[49] U. Bergmann and P. Glatzel. "X-ray emission spectroscopy". In: *Photosynthesis Research* 102.2-3 (2009), pp. 255–266.

[50] U. Bergmann et al. "Chemical dependence of interatomic X-ray transition energies and intensities – a study of Mn Kβ" and Kβ2, 5 spectra". In: (1999), p. 6.

[51] C. J. Pollock and S. DeBeer. "Valence-to-Core X-ray Emission Spectroscopy: A Sensitive Probe of the Nature of a Bound Ligand". In: *Journal of the American Chemical Society* 133.14 (2011), pp. 5594–5601.

[52] C. J. Pollock and S. DeBeer. "Insights into the Geometric and Electronic Structure of Transition Metal Centers from Valence-to-Core X-ray Emission Spectroscopy". In: *Accounts of Chemical Research* 48.11 (2015), pp. 2967–2975.

[53] A. Beheshti Askari et al. "In situ X-ray emission and high-resolution X-ray absorption spectroscopy applied to Ni-based bimetallic dry methane reforming catalysts". In: *Nanoscale* 12.28 (2020), pp. 15185–15192.

[54] R. G. Castillo et al. "Kβ X-Ray Emission Spectroscopic Study of a Second-Row Transition Metal (Mo) and Its Application to Nitrogenase-Related Model Complexes". In: *Angewandte Chemie International Edition* 59.31 (2020), pp. 12965–12975.

[55] M. Rovezzi and P. Glatzel. "Hard x-ray emission spectroscopy: a powerful tool for the characterization of magnetic semiconductors". In: *Semiconductor Science and Technology* 29.2 (2014), p. 023002.

[56] G. Vankó et al. "Picosecond Time-Resolved X-Ray Emission Spectroscopy: Ultrafast Spin-State Determination in an Iron Complex". In: *Angewandte Chemie International Edition* 49.34 (2010), pp. 5910–5912.

[57] K. O. Kvashnina and A. C. Scheinost. "A Johann-type X-ray emission spectrometer at the Rossendorf beamline". In: *Journal of Synchrotron Radiation* 23.3 (2016), pp. 836–841.

[58] A. Kalinko et al. "A von Hamos-type hard X-ray spectrometer at the PETRA III beamline P64". In: *Journal of Synchrotron Radiation* 27.1 (2020), pp. 31–36.

[59] E. Kleymenov et al. "Five-element Johann-type x-ray emission spectrometer with a single-photon-counting pixel detector". In: *Review of Scientific Instruments* 82.6 (2011).

[60] K. D. Finkelstein et al. "Dual-array valence emission spectrometer (DAVES): A new approach for hard x-ray photon-in photon-out spectroscopies". In: New York, NY USA, 2016, p. 030009.

[61] W. Malzer et al. "A laboratory spectrometer for high throughput X-ray emission spectroscopy in catalysis research". In: *Review of Scientific Instruments* 89.11 (2018), p. 113111.

[62] R. Jenkins et al. "IUPAC—nomenclature system for x-ray spectroscopy". In: *X-Ray Spectrometry* 20.3 (1991), pp. 149–155.

[63] C. J. Pollock et al. "K β Mainline X-ray Emission Spectroscopy as an Experimental Probe of Metal - Ligand Covalency". In: *J. Am. Chem. Soc* 136 (2014), p. 9453.

[64] S. Lafuerza et al. "Chemical Sensitivity of Kβ and Kα X-ray Emission from a Systematic Investigation of Iron Compounds". In: *Inorganic Chemistry* 59.17 (2020), pp. 12518–12535.

[65] E. Stavitski and F. M. de Groot. "The CTM4XAS program for EELS and XAS spectral shape analysis of transition metal L edges". In: *Micron* 41.7 (2010), pp. 687–694.

[66] G. Hölzer et al. "$Ka_{1,2}$ and $Kb_{1,3}$ x-ray emission lines of the 3d transition metals". In: *Physical Review A* 56.6 (1997), pp. 4554–4568.

[67] K. Tsutsumi, H. Nakamori, and K. Ichikawa. "X-ray Mn Kβ emission spectra of manganese oxides and manganates". In: *Physical Review B* 13.2 (1976), pp. 929–933.

[68] G. Vankó et al. “Probing the 3D spin momentum with X-ray emission spectroscopy: The case of molecular-spin transitions”. In: *Journal of Physical Chemistry B* 110.24 (2006), pp. 11647–11653.

[69] P. Glatzel and U. Bergmann. “High resolution 1s core hole X-ray spectroscopy in 3d transition metal complexes - Electronic and structural information”. In: *Coordination Chemistry Reviews* 249.1-2 (2005), pp. 65–95.

[70] G. Smolentsev et al. “X-ray Emission Spectroscopy To Study Ligand Valence Orbitals in Mn Coordination Complexes”. In: *Journal of the American Chemical Society* 131.36 (2009), pp. 13161–13167.

[71] P. Glatzel et al. “Reflections on hard x-ray photon-in/photon-out spectroscopy for electronic structure studies”. In: *Journal of Electron Spectroscopy and Related Phenomena* 188 (2013), pp. 17–25.

[72] J. K. Kowalska et al. “A Practical Guide to High-resolution X-ray Spectroscopic Measurements and their Applications in Bioinorganic Chemistry”. In: *Israel Journal of Chemistry* 56.9-10 (2016), pp. 803–815.

[73] G. Geloni et al. “Coherence properties of the European XFEL”. In: *New Journal of Physics* 12.3 (2010), p. 035021.

[74] T. Tschentscher et al. “Photon Beam Transport and Scientific Instruments at the European XFEL”. In: *Applied Sciences* 7.6 (2017), p. 592.

[75] P. J. Emma et al. “First lasing and operation of an ångstrom-wavelength free-electron laser”. In: *Nature Photonics* 4.9 (2010), pp. 641–647.

[76] D. Khakhulin et al. “Ultrafast X-ray Photochemistry at European XFEL: Capabilities of the Femtosecond X-ray Experiments (FXE) Instrument”. In: *Applied Sciences* 10.3 (2020), p. 995.

[77] T. Johansson. “Über ein neuartiges, genau fokussierendes Röntgenspektrometer: Erste Mitteilung”. In: *Zeitschrift für Physik* 82.7-8 (1933), pp. 507–528.

[78] H. H. Johann. “Die Erzeugung lichtstarker Röntgenspektren mit Hilfe von Konkavkristallen”. In: *Zeitschrift für Physik* 69.3-4 (1931), pp. 185–206.

[79] S. Rani, J. H. Lee, and Y. Kim. “200-mm segmented cylindrical figured crystal for von Hamos x-ray spectrometer”. In: *Review of Scientific Instruments* 91.1 (2020), p. 013101.

[80] R. M. Buchanan, B. J. Fitzgerald, and C. G. Pierpont. “Semiquinone radical anion coordination to divalent cobalt and nickel. Structural features of the bis(3,5-di-tert-butyl-1,2-semiquinone)cobalt(II) tetramer”. In: *Inorganic Chemistry* 18.12 (1979), pp. 3439–3444.

[81] S. O. Shapovalova et al. “Temperature and Time-resolved XANES Studies of Novel Valence Tautomeric Cobalt Complex”. In: *Chemistry Letters* 50.11 (2021), pp. 1933–1937.

[82] A. A. Guda et al. "Valence tautomeric transition of bis(o-dioxolene) cobalt complex in solid state and solution". In: *Journal of Physics: Condensed Matter* 33.21 (2021), p. 215405.

[83] B. Bozic-Weber et al. "Copper(i) dye-sensitized solar cells with [Co(bpy)3]2+/3+ electrolyte". In: *Chemical Communications* 49.65 (2013), p. 7222.

[84] Y. Sasaki, H. Kato, and A. Kudo. "$[Co(bpy)_3]^{3+/2+}$ and $[Co(phen)_3]^{3+/2+}$ Electron Mediators for Overall Water Splitting under Sunlight Irradiation Using Z-Scheme Photocatalyst System". In: *Journal of the American Chemical Society* 135.14 (2013), pp. 5441–5449.

[85] S. Sreekantan Nair Lalithambika et al. "Electronic Structure of Aqueous $[Co(bpy)_3]^{2+/3+}$ Electron Mediators". In: *Inorganic Chemistry* 58.8 (2019), pp. 4731–4740.

[86] M. Guo, X. Liu, and R. He. "Restricted active space simulations of the metal L-edge X-ray absorption spectra and resonant inelastic X-ray scattering: Revisiting [CoII/III(bpy)3]2+/3+ complexes". In: *Inorganic Chemistry Frontiers* 7.9 (2020), pp. 1927–1938.

[87] Y. Ishii et al. "Alkane Oxidation with Molecular Oxygen Using a New Efficient Catalytic System: *N* -Hydroxyphthalimide (NHPI) Combined with $Co(acac)_n$ ($n = 2$ or 3)". In: *The Journal of Organic Chemistry* 61.14 (1996), pp. 4520–4526.

[88] M. R. Buchmeiser and M. G. Marino. "Co(acac)2-Mediated Radical Polymerization of Acrylonitrile: Control Over Molecular Weights and Copolymerization With Methyl Methacrylate". In: *Macromolecular Materials and Engineering* 297.9 (2012), pp. 894–901.

[89] J. Burgess et al. "Monomeric bis(2,4-pentanedionato)cobalt(II)". In: *Acta Crystallographica Section C Crystal Structure Communications* 56.6 (2000), pp. 649–650.

[90] P. Pietrzyk et al. "Spin Ground State and Magnetic Properties of Cobalt(II): Relativistic DFT Calculations Guided by EPR Measurements of Bis(2,4-acetylacetonate)cobalt(II)-Based Complexes". In: *The Journal of Physical Chemistry A* 115.11 (2011), pp. 2316–2324.

[91] J. S. Judge and W. Baker. "On the spin equilibrium in bis(2,2',2"-terpyridine) cobalt(II) salts". In: *Inorganica Chimica Acta* 1 (1967), pp. 68–72.

[92] I. Krivokapic et al. "Spin-crossover in cobalt(II) imine complexes". In: *Coordination Chemistry Reviews* 251.3-4 (2007), pp. 364–378.

[93] H. Oshio et al. "Electronic Relaxation Phenomena Following $^{57}Co(EC)^{57}$ Fe Nuclear Decay in $[Mn^{II}(terpy)_2](ClO_4)_2 \cdot {}^1/_2\ H_2O$ and in the Spin Crossover Complexes $[Co^{II}(terpy)_2]X_2 \cdot n\ H_2O$ (X = Cl and ClO_4): A Mössbauer Emission Spectroscopic Study". In: *Inorganic Chemistry* 40.6 (2001), pp. 1143–1150.

[94] S. Hayami et al. “Spin-crossover in cobalt(II) compounds containing terpyridine and its derivatives”. In: *Coordination Chemistry Reviews* 255.17-18 (2011), pp. 1981–1990.

[95] S. Kremer, W. Henke, and D. Reinen. “High-spin-low-spin equilibriums of cobalt(2+) in the terpyridine complexes Co(terpy)2X2.nH2O”. In: *Inorganic Chemistry* 21.8 (1982), pp. 3013–3022.

[96] A. A. Isse, A. Gennaro, and E. Vianello. “Mechanism of the electrochemical reduction of benzyl chlorides catalysed by Co(salen)”. In: *Journal of Electroanalytical Chemistry* 444.2 (1998), pp. 241–245.

[97] Y.-M. Shen, W.-L. Duan, and M. Shi. “Chemical Fixation of Carbon Dioxide Catalyzed by Binaphthyldiamino Zn, Cu, and Co Salen-Type Complexes”. In: *The Journal of Organic Chemistry* 68.4 (2003), pp. 1559–1562.

[98] R. L. Paddock and S. T. Nguyen. “Chiral (Salen)CoIII Catalyst for the Synthesis of Cyclic Carbonates.” In: *ChemInform* 35.47 (2004).

[99] A. Werner. “Zur Kenntnis des asymmetrischen Kobaltatoms. V”. In: *Berichte der deutschen chemischen Gesellschaft* 45.1 (1912), pp. 121–130.

[100] H. Groult et al. “Nano-CoF_3 prepared by direct fluorination with F_2 gas: Application as electrode material in Li-ion battery”. In: *Journal of Fluorine Chemistry* 196 (2017), pp. 117–127.

[101] D. S. Crocket and H. M. Haendler. “Synthesis of Fluorometallates in Methanol. Some Structure Relationships”. In: *Journal of the American Chemical Society* 82.16 (1960), pp. 4158–4162.

[102] P. Kashinath C. and E. A. Secco. “Complex Fluorides with Perovskite Structure: Thermal Analyses, Calorimetry, and Infrared Spectra”. In: *Canadian Journal of Chemistry* 50.10 (1972), pp. 1529–1530.

[103] J. S. Dailey and T. J. Pinnavaia. “Intercalative reaction of a cobalt(III) cage complex, Co(sep)3+, with magadiite, a layered sodium silicate”. In: *Journal of Inclusion Phenomena and Molecular Recognition in Chemistry* 13.1 (1992), pp. 47–61.

[104] X. Wang et al. “Cobalt(ii,iii) oxide hollow structures: fabrication, properties and applications”. In: *Journal of Materials Chemistry* 22.44 (2012), p. 23310.

[105] S. Jeon et al. “Redox Chemistry and Valence Tautomerism of Cobalt-Quinone Complexes in Nonaqueous Solvents”. In: *Bulletin of the Korean Chemical Society* 19.2 (1998), pp. 212–217.

[106] O. S. Jung and C. G. Pierpont. “Bistability and Low-Energy Electron Transfer in Cobalt Complexes Containing Catecholate and Semiquinone Ligands”. In: *Inorganic Chemistry* 33.10 (1994), pp. 2227–2235.

[107] B. Henderson, G. F. Imbusch, and G. F. Imbusch. *Optical spectroscopy of inorganic solids*. 1st publ. in paperback, repr. Monographs on the physics and chemistry of materials 44. Oxford: Oxford Univ. Press, 2010.

[108] E. Evangelio, D. N. Hendrickson, and D. Ruiz-Molina. "Intramolecular electron transfer in the mixed-valence [Co(3,5-DTBCat)(3,5-DTBSQ)(bpy)] complex: Beyond valence tautomerism". In: *Inorganica Chimica Acta* 361.12-13 (2008), pp. 3403–3409.

[109] A. Cui et al. "Mechanism and relaxation kinetics of photo-induced valence tautomerism of [Co(phen)(3,5-DBSQ)2] · C6H5Cl". In: *Journal of Photochemistry and Photobiology A: Chemistry* 167.2-3 (2004), pp. 69–73.

[110] O. Sato, J. Tao, and Y. Z. Zhang. "Control of magnetic properties through external stimuli". In: *Angewandte Chemie International Edition* 46.13 (2007), pp. 2152–2187.

[111] D. W. Scott et al. "Toluene: Thermodynamic Propoerties, Molecular Vibrations, and Internal Rotation". In: 66 (1962), pp. 911–4.

[112] J. K. Rogalinski. "Transition Metal-centered Valence Tautomeric Complexes: X-Ray and Optical Studies". Bachelor thesis. Hamburg: Universität Hamburg, 2020.

[113] O. Kahn. *Molecular magnetism*. Revised republication. Garden City, New York: Dover Publications, 2021.

[114] T. Nakamoto, Z.-C. Tan, and M. Sorai. "Heat Capacity of the Spin Crossover Complex [Fe(2-pic) $_3$]Cl $_2$ · MeOH: A Spin Crossover Phenomenon with Weak Cooperativity in the Solid State". In: *Inorganic Chemistry* 40.15 (2001), pp. 3805–3809.

[115] F. Otte et al. "Unveiling intramolecular magnetic exchange interactions and spectroscopic properties of valence tautomers". Manuscript in preparation. 2022.

[116] L. Simonelli et al. "CLÆSS: The hard X-ray absorption beamline of the ALBA CELLS synchrotron". In: *Cogent Physics* 3.1 (2016). Ed. by N. L. Saini, p. 123198.

[117] E. R. Hall et al. "Valence-to-Core-Detected X-ray Absorption Spectroscopy: Targeting Ligand Selectivity". In: *Journal of the American Chemical Society* 136.28 (2014), pp. 10076–10084.

[118] C. J. Pollock et al. "Experimentally Quantifying Small-Molecule Bond Activation Using Valence-to-Core X-ray Emission Spectroscopy". In: *Journal of the American Chemical Society* 135.32 (2013), pp. 11803–11808.

[119] V. A. Safonov et al. "Valence-to-Core X-ray Emission Spectroscopy Identification of Carbide Compounds in Nanocrystalline Cr Coatings Deposited from Cr(III) Electrolytes Containing Organic Substances". In: *The Journal of Physical Chemistry B* 110.46 (2006), pp. 23192–23196.

[120] N. Lee et al. "Probing Valence Orbital Composition with Iron Kβ X-ray Emission Spectroscopy". In: *Journal of the American Chemical Society* 132.28 (2010), pp. 9715–9727.

[121] K. M. Lancaster et al. “X-ray Emission Spectroscopy Evidences a Central Carbon in the Nitrogenase Iron-Molybdenum Cofactor”. In: *Science* 334.6058 (2011), pp. 974–977.

[122] M. U. Delgado-Jaime et al. “Identification of a Single Light Atom within a Multinuclear Metal Cluster Using Valence-to-Core X-ray Emission Spectroscopy”. In: *Inorganic Chemistry* 50.21 (2011), pp. 10709–10717.

[123] M. A. Beckwith et al. “Manganese Kβ X-ray Emission Spectroscopy As a Probe of Metal–Ligand Interactions”. In: *Inorganic Chemistry* 50.17 (2011), pp. 8397–8409.

[124] A. M. March et al. “Probing Transient Valence Orbital Changes with Picosecond Valence-to-Core X-ray Emission Spectroscopy”. In: *The Journal of Physical Chemistry C* 121.5 (2017), pp. 2620–2626.

[125] K. Ledbetter et al. “Excited state charge distribution and bond expansion of ferrous complexes observed with femtosecond valence-to-core x-ray emission spectroscopy”. In: *The Journal of Chemical Physics* 152.7 (2020), p. 074203.

[126] F. Neese. “Software update: The ORCA program system - Version 5.0”. In: *WIREs Computational Molecular Science* (2022).

[127] F. Neese et al. *ORCA - An ab initio, DFT and semiempirical SCF-MO package - Version 5.0.2*. 2021.

[128] S. DeBeer George, T. Petrenko, and F. Neese. “Prediction of Iron K-Edge Absorption Spectra Using Time-Dependent Density Functional Theory”. In: *The Journal of Physical Chemistry A* 112.50 (2008), pp. 12936–12943.

[129] D. E. Wheeler, J. H. Rodriguez, and J. K. McCusker. “Density Functional Theory Analysis of Electronic Structure Variations across the Orthoquinone/Semiquinone/Catechol Redox Series”. In: *The Journal of Physical Chemistry A* 103.20 (1999), pp. 4101–4112.

[130] F. Frati, M. O. J. Y. Hunault, and F. M. F. de Groot. “Oxygen K-edge X-ray Absorption Spectra”. In: *Chemical Reviews* 120.9 (2020), pp. 4056–4110.

[131] A. L. Macdonald and J. Trotter. “Crystal and molecular structure of o-benzoquinone”. In: *Journal of the Chemical Society, Perkin Transactions 2* 4 (1973), p. 476.

[132] M. D. Hanwell et al. “Avogadro: an advanced semantic chemical editor, visualization, and analysis platform”. In: *Journal of Cheminformatics* 4.1 (2012), p. 17.

[133] C. Weis et al. “Combining X-ray Kβ $_{1,3}$, valence-to-core, and X-ray Raman spectroscopy for studying Earth materials at high pressure and temperature: the case of siderite”. In: *Journal of Analytical Atomic Spectrometry* 34.2 (2019), pp. 384–393.

[134] J.-P. Rueff et al. "The GALAXIES beamline at the SOLEIL synchrotron: inelastic X-ray scattering and photoelectron spectroscopy in the hard X-ray range". In: *Journal of Synchrotron Radiation* 22.1 (2015), pp. 175–179.

[135] G. Poneti et al. "X-ray Absorption Spectroscopy as a Probe of Photo- and Thermally Induced Valence Tautomeric Transition in a 1:1 Cobalt-Dioxolene Complex". In: *ChemPhysChem* 10.12 (2009), pp. 2090–2095.

[136] R. Ash, K. Zhang, and J. Vura-Weis. "Photoinduced valence tautomerism of a cobalt-dioxolene complex revealed with femtosecond M-edge XANES". In: *The Journal of Chemical Physics* 151.10 (2019), p. 104201.

[137] C. Colliex, T. Manoubi, and C. Ortiz. "Electron-energy-loss-spectroscopy near-edge fine structures in the iron-oxygen system". In: *Physical Review B* 44.20 (1991), pp. 11402–11411.

[138] A. Caneschi, A. Cornia, and A. Dei. "Valence Tautomerism in a Cobalt Complex of a Schiff Base Diquinone Ligand". In: *Inorganic Chemistry* 37.13 (1998), pp. 3419–3421.

[139] J. Szlachetko et al. "A Dispersive Inelastic X-ray Scattering Spectrometer for Use at X-ray Free Electron Lasers". In: *Applied Sciences* (2017).

[140] W. Gawelda, J. Szlachetko, and C. J. Milne. "X-Ray Spectroscopy at Free Electron Lasers". In: *X-Ray Absorption and X-Ray Emission Spectroscopy*. Ed. by J. A. Van Bokhoven and C. Lamberti. Chichester, UK: John Wiley & Sons, Ltd, 2016, pp. 637–669.

[141] M. Roemelt et al. "Manganese K-edge X-ray absorption spectroscopy as a probe of the metal-ligand interactions in coordination compounds". In: *Inorganic Chemistry* 51.1 (2012), pp. 680–687.

[142] J. A. Rees et al. "Experimental and theoretical correlations between vanadium K-edge X-ray absorption and K β emission spectra". In: *Journal of Biological Inorganic Chemistry* 21.5-6 (2016), pp. 793–805.

[143] F. De Groot. "High-resolution X-ray emission and X-ray absorption spectroscopy". In: *Chemical Reviews* 101.6 (2001), pp. 1779–1808.

[144] C. Pollock. *PIPOXS Beamline — CHESS*. URL: `https://www.chess.cornell.edu/users/pipoxs-beamline` (visited on 05/02/2022).

[145] M. Al Samarai et al. "1s3p Resonant Inelastic X-ray Scattering of Cobalt Oxides and Sulfides". In: *Journal of Physical Chemistry C* 120.42 (2016), pp. 24063–24069.

[146] V. Vaz da Cruz et al. "Targeting Individual Tautomers in Equilibrium by Resonant Inelastic X-ray Scattering". In: *The Journal of Physical Chemistry Letters* 13.10 (2022), pp. 2459–2466.

[147] J. A. Rees et al. "Comparative electronic structures of nitrogenase FeMoco and FeVco". In: *Dalton Transactions* 46.8 (2017), pp. 2445–2455.

[148] M. Newville. "Fundamentals of XAFS". In: *Reviews in Mineralogy and Geochemistry* 78.1 (2014), pp. 33–74.

[149] P. Glatzel, R. Alonso-Mori, and D. Sokaras. "Hard X-Ray Photon-in/Photon-out Spectroscopy: Instrumentation, Theory and Applications". In: *X-Ray Absorption and X-Ray Emission Spectroscopy*. John Wiley & Sons, Ltd, 2016, pp. 125–153.

[150] W. Zhang et al. "Tracking excited-state charge and spin dynamics in iron coordination complexes". In: *Nature* (2014).

[151] N. Azzaroli et al. "Valence Tautomerism in Co–Dioxolene Complexes: Static and Time-Resolved Infrared Spectroscopy Study". In: *The Journal of Physical Chemistry B* 117.49 (2013), pp. 15492–15502.

[152] A. Beni et al. "Characterization of photo-induced valence tautomerism in a cobalt-dioxolene complex by ultrafast spectroscopy". In: *Journal of Physics: Conference Series* 21.1 (2005), pp. 124–129.

[153] P. L. Gentili et al. "Time-resolved spectroscopic characterization of photo-induced valence tautomerism for a cobalt–dioxolene complex". In: *Chemical Physics* 314.1-3 (2005), pp. 9–17.

[154] W. Gawelda et al. "Electronic and molecular structure of photoexcited $[RuII(bpy)_3]^{2+}$ probed by picosecond X-ray absorption spectroscopy". In: *Journal of the American Chemical Society* 128.15 (2006), pp. 5001–5009.

[155] C. Bressler et al. "Solvation dynamics monitored by combined X-ray spectroscopies and scattering: Photoinduced spin transition in aqueous [Fe(bpy)3]2+". In: *Faraday Discussions* (2014).

[156] M. Nazari Haghighi Pashaki et al. "Two-dimensional ultrafast transient absorption spectrograph covering deep-ultraviolet to visible spectral region optimized for biomolecules". In: *Journal of Physics: Photonics* 3.3 (2021), p. 034014.

[157] M. Nazari Haghighi Pashaki. "Long-Range Energy Transfer in DNA-Hosted Multichromophoric Systems by Ultrafast 1D and 2D fs UV-Vis Transient Absorption Spectroscopy". PhD thesis. Bern, 2018.

[158] N. Vân Anh and R. M. Williams. "Bis-semiquinone (bi-radical) formation by photoinduced proton coupled electron transfer in covalently linked catechol–quinone systems: Aviram's hemiquinones revisited". In: *Photochemical & Photobiological Sciences* 11.6 (2012), p. 957.

[159] A. Mozzanica et al. "The JUNGFRAU Detector for Applications at Synchrotron Light Sources and XFELs". In: *Synchrotron Radiation News* 31.6 (2018), pp. 16–20.

[160] A. Galler et al. "Scientific instrument Femtosecond X-ray Experiments (FXE): Instrumentation and baseline experimental capabilities". In: *Journal of Synchrotron Radiation* 26 (2019), pp. 1432–1447.

[161] J. H. Lee et al. “Filming the Birth of Molecules and Accompanying Solvent Rearrangement”. In: *Journal of the American Chemical Society* 135.8 (2013), pp. 3255–3261.

[162] K. S. Kjær et al. “Introducing a standard method for experimental determination of the solvent response in laser pump, X-ray probe time-resolved wide-angle X-ray scattering experiments on systems in solution”. In: *Physical Chemistry Chemical Physics* 15.36 (2013), pp. 15003–15016.

[163] G. Palmer et al. “Pump–probe laser system at the FXE and SPB/SFX instruments of the European X-ray Free-Electron Laser Facility”. In: *Journal of Synchrotron Radiation* 26.2 (2019), pp. 328–332.

[164] S. Redford et al. “First full dynamic range calibration of the JUNGFRAU photon detector”. In: *Journal of Instrumentation* 13.01 (2018), pp. C01027–C01027.

[165] E. O. Lebigot. *Uncertainties: a Python package for calculations with uncertainties.* 2021.

[166] Y. Mulyana et al. “Solvation effects on the valence tautomeric transition of a cobalt complex in the solid state”. In: *Dalton Trans.* 39.20 (2010), pp. 4757–4767.

[167] I. H. van Stokkum, D. S. Larsen, and R. van Grondelle. “Global and target analysis of time-resolved spectra”. In: *Biochimica et Biophysica Acta (BBA) - Bioenergetics* 1657.2-3 (2004), pp. 82–104.

[168] M. Diez. “A Self-Referenced Timing-Tool for High Repetition X-ray Free-Electron Laser Sources”. PhD thesis. Hamburg, 2021.

[169] Y. Kalambet et al. “Reconstruction of chromatographic peaks using the exponentially modified Gaussian function”. In: *Journal of Chemometrics* 25.7 (2011), pp. 352–356.

Acknowledgements

At this point, I would like to thank those that made this thesis possible. I want to begin with Prof. Metin Tolan and Prof. Christian Bressler, who fostered my interest in synchrotron (and ultimately FEL) science and enabled me to come to Hamburg for this exciting project. I sincerely appreciate this opportunity, and I thank them for assuming the thesis supervisor and referee role. I sincerely thank Christian for welcoming me into the FXE family and his contagious enthusiasm.

This thesis would not exist without the amazing and uncompromising care of Frederico Alves Lima from FXE, with whom I worked on the VT project and who always had advice helping me through countless challenges. I now share with him a vast stream of interesting, inspiring, and outright crazy memories, of which I am very fond. I greatly profited from his well-rounded scientific network and baking skills.

I am deeply indebted to Christian Sternemann from TU Dortmund, who put things on the right track on so many levels and made the distance to Dortmund feel smaller. I especially appreciated the virtual discussions during lockdown phase.

I was privileged to visit the wonderful people from the group of inorganic synthesis & spectroscopy at the Max-Planck Institute for chemical energy conversion. I am incredibly thankful to Sergio Jannuzzi, who, with his technician Fabian Otto, synthesized the samples for this study and from whose expertise I have greatly profited, last but not least, during beamtimes. I want to thank the head of the group, Prof. Serena DeBeer, for enabling this collaboration, and to Rebeca Gomez Castillo for hands-on support with ORCA early in my project.

I am thankful to Tae-Kyu, Christina, and Michael, with whom I shared the longest part of my Ph.D. journey at FXE and who have supported and shaped me in many ways. I will deeply cherish the friendly atmosphere at FXE toward me and miss the fantastic shared breakfast with the engineers! I also wholeheartedly thank the other people from my facility's Ph.D. program, especially Karina and Tim; they all became my student family in the wondrous world of European XFEL. I want to extend thanks to Julia Rogalinski, who valiantly contributed to the Valence Tautomer project during beamtimes and data analysis in the framework of her Bachelor thesis at FXE.

Despite my rare physical presence in Dortmund, I always felt welcome at my Lehrstuhl of Experimentelle Physik E1a. I want to thank Jan Latarius, Christian Albers, Robin Sakrowski, Jessica Bolle, Kevin Lehninger, Mirco Elbers and Michael Paulus for help with several experiments. Thorsten Witt helped me keep the analyzer database webtool available when it needed a new home. I am very grateful for his fast and

generous help.

I sincerely thank Chris Pollock for his overwhelming support during the remote beamtime at CHESS and his resilient efforts during the COVID pandemic-related restrictions. James Ablett from the GALAXIES beamline at SOLEIL synchrotron is greatly acknowledged, as he and Jean-Pascall Rueff made the SOLEIL experiment possible.

The extensive help of Prof. Andrea Cannizzo with acquiring optical transient absorption spectroscopy data on cobalt VT complexes is greatly acknowledged. I am deeply indebted to Mayam Nazari and Aaron Riede, who supported me with the transient absorption measurements and the numerous questions that arose during my stay in Bern.

I am very grateful for help and inspiration with the global fitting approach from Maria Naumova.

Finally, I want to say thank you to my friends and my family. The largest thank I owe Josi, my idol and partner in crime.